Crashworthiness Assessment of the Flying-V

Under Complex Crash Scenarios with Partially Detailed Structures

MSc Thesis

Tiago Ferreira da Costa

Delft University of Technology

TU Delft

This page intentionally contains no content.

Crashworthiness Assessment of the Flying-V

Under Complex Crash Scenarios with Partially Detailed Structures

by

Tiago Ferreira da Costa

Student Number
5635241

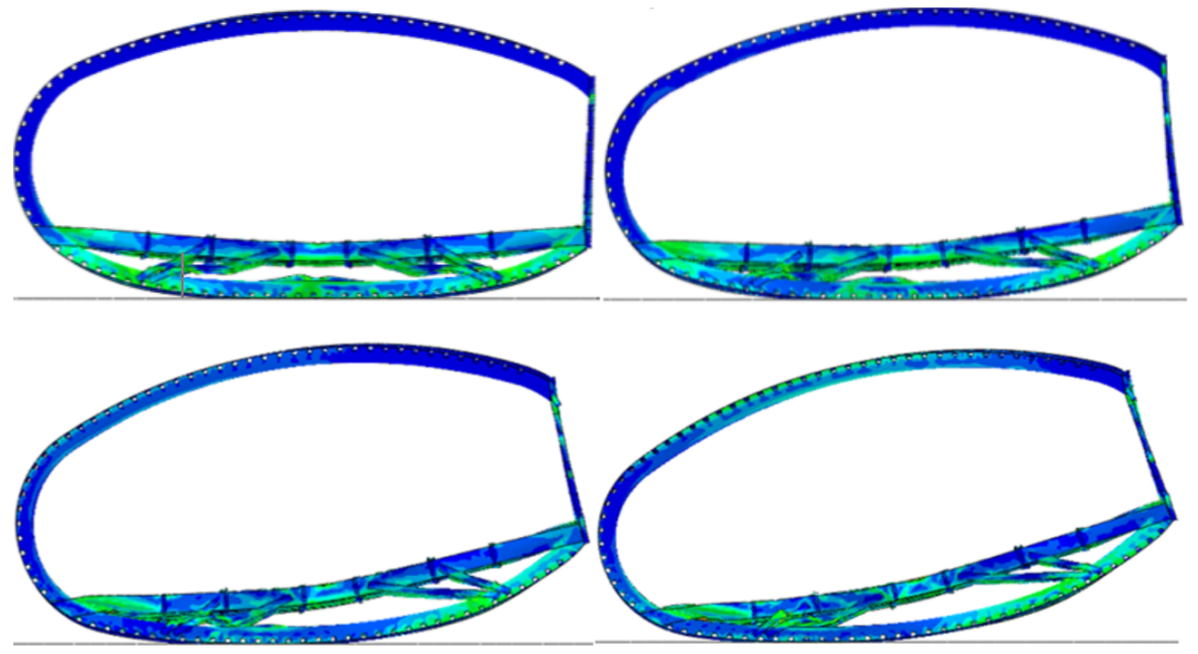

Supervisors:	Dr. S.G.P. Castro, Dr. Calvin Rans
Co-supervisor:	Andrea Villa
Place:	SIMULIA Team at Dassault Systèmes Office, Milan
Project Duration:	May, 2023 - March, 2024

TU Delft

This page intentionally contains no content.

I

Front Matter

This page intentionally contains no content.

Preface and Acknowledgments

Dear reader,

Slightly more than two years ago, in August 2021, I embarked on a journey to Delft, in the Netherlands, to pursue my Master of Science in Aerospace Engineering. Those early days hold a special place in my heart, for they introduced me to a vibrant community of inspiring, kind, and genuine friends. While the future may hold different paths for us, the impact of these friendships in shaping the person I have become is immeasurable. As I now prepare to continue my studies in Italy, new personal connections were again formed, but I carry with me the memories and bonds forged in Delft, cherishing the friendships for life that I have had the privilege to make.

As my Master's program draws to a close, I find myself reflecting on the incredible journey I've undertaken. This master thesis marks the culmination of a thrilling project that explores the crashworthiness of the Flying-V, a novel and intriguing aircraft configuration. The research builds upon the foundation laid by Marco's previous work and paves the way for further exploration into this fascinating and critical aspect of aircraft development.

Delving into the realm of aircraft crashworthiness, I discovered a complex field where unconventional aircraft knowledge meets uncharted territory. It is both humbling and exciting to contribute to the growing body of knowledge in this domain.

I extend my heartfelt gratitude to the individuals who have been instrumental in this endeavor. Dassault Systèmes provided me with the ideal platform for honing my structural analysis skills, and I am particularly thankful to my company supervisor, Andrea Villa, whose unwavering support and expertise have been invaluable.

I would also like to express my sincere appreciation to Dr. Saullo Castro and Dr. Calvin Rans for their steadfast guidance, their ability to grasp and address challenges swiftly, and the enriching discussions that have fueled my progress. Special thanks go to Marco and Rowan for their extensive collaboration and insightful contributions to our research on the Flying-V's crashworthiness. Also, to my dear friends at Dassault Systèmes, I want to express my heartfelt gratitude for the countless cups of coffee and the meaningful conversations during those challenging moments when none of us felt like working.

Finally, in times of personal trials, my family has been my rock, exemplified by my resilient grandmother who, despite health challenges, has remained a constant source of inspiration and support.

As I look ahead, I embark on the next leg of this adventure with boundless excitement. The journey so far has been nothing short of remarkable, and I eagerly anticipate the months to come. Thank you for joining me on this academic path.

Warm regards,

Tiago Ferreira da Costa
Milan, April 2024

This page intentionally contains no content.

Abstract

Addressing the persistent concern of aircraft crashworthiness, this research delves into the complexities associated with unconventional aircraft designs, with a primary focus on the innovative Flying-V configuration. Against the backdrop of a declining trend in fatalities below 50% over the past two decades, the aviation industry's commitment to safety improvement propels an in-depth exploration of crashworthiness in novel designs.

Despite its fuel efficiency and aerodynamic advantages, the Flying-V's unique V-shaped fuselage poses challenges to ensuring passenger safety during crash scenarios. Traditional vertical drop tests, the staple of crashworthiness assessments, encounter applicability concerns due to the Flying-V's unconventional geometry and mass distribution. This research addresses these challenges by proposing modelling approaches to assess the crashworthiness behaviour under various scenarios, when only certain regions are detailed. For the Flying-V, past research on structures have focused on the typical wing-fuselage cross section, which extends from the central to the outboard region, and where most of the passengers and payload are located. However, for the central part of the Flying-V where the two half wing-fuselages are joined, no detailed information concerning the structural layout is available.

An investigation unfolds across various modelling approaches, commencing with examinations of the Flying-V's non-linear, explicit-dynamic finite element model developed in the previous work, which serves as the foundational framework for subsequently analysis. Drop tests validate optimal section designs, emphasizing a minimum vertical impact velocity of 26 ft/s. The exploration of Dynamic Response Index (DRI) and Severity Index (SEV) spatial variations highlights asymmetries, prompting nuanced studies on impact scenarios and potential passenger side loads.

As the analysis progresses into more dynamic scenarios, the extension of the computational domain becomes imperative for a reliable study. Analysis of extended Flying-V fuselage sections reveals important insights into weight distribution imbalances, asymmetrical floor deformations, and challenges associated with corrective measures.

Spatial fluctuations in DRIs and SEVs indicate potential areas of concern, emphasizing the need for a balanced approach between computational time, result realism, energy efficiency, and passenger safety. Additionally, the study highlights the role of the Severity Index in complex crash scenarios, especially when lateral accelerations are prominent. The introduction of sliding boundary conditions and subsequent incorporation of structural components in both rear and front sections of the complete passenger fuselage further refines crashworthiness assessments, enhancing stability and yielding outcomes akin to those observed in more realistic crash scenarios.

Comparative evaluations led to the selection of the extended model with seven passenger rows as the foundational framework for subsequent analysis. This choice is influenced by an improved balance achieved between computational efficiency, result authenticity, and simulation simplicity.

A newly introduced modelling technique that leverages moments of inertia of other sections of the Flying-V, without accounting for their FEM representations, is subsequently implemented on the chosen model. This approach takes advantage of the fact that the mass distribution is known in regions where the structural details are not yet defined. The method demonstrates its effectiveness in vertical drop-test simulations, yielding more realistic results for straightforward scenarios and significantly reducing the simulation time by almost half, when compared with the full model.

The crashworthiness characteristics of the Flying-V are examined under more intricate landing scenarios that incorporate varying roll and pitch angles into the analysis. The inclusion of roll angles, though it represented an initial assessment of the implicit moments of inertia technique, emphasizes the importance of incorporating moments of inertia to uphold structural integrity, alleviate rotation, and impact acceleration patterns.

An analysis of pitch angle variations and the subsequent comparison between the full passenger model and the extended/reduced model emphasizes notable differences in deformations, especially at elevated pitch angles. The reduced model, relying on moments of inertia without accounting for mass, exhibits substantial increases in DRI and SEV values.

Recognizing the limitations of this simplified methodology, a submodelling technique is proposed to address extreme crash scenarios. This involves an initial drop test of the entire available model with a coarser mesh, followed by replicating the test using submodelling focused on refining the engine section. Visual inspection of crash scenarios and a study of spatial variations in DRIs and SEVs reveal a striking similarity in outcomes between the submodel and the full passenger model, indicating the submodelling approach's efficacy in capturing engine section dynamics with a significant reduction in computational time.

While the application of reduced modelling techniques has yielded generally positive results, this study concludes by recognizing the impracticality of the implicit moments of inertia approach in evaluating the crashworthiness of the Flying-V under more intricate crash conditions. The emphasis is on the need for a more comprehensive and ideally full finite element method representation of the Flying-V. Successive simulations with a coarse overall mesh are recommended to pinpoint critical regions in the Flying-V. Following this, the submodelling technique could be employed to subject these critical areas to a more detailed and comprehensive assessment.

Contents

Nomenclature

Abbreviations

Abbreviation	Definition
AMC	Acceptable Means of Compliance
ARAC	Aviation Rulemaking Advisory Committee
BWB	Blended Wing Body
CFR	Code of Federal Regulations
CG	Center of Gravity
CIRA	Italian Aerospace Research Center
CS	Certification Specifications
CTW	Conventional Tube-and-Wing
DLR	German Aerospace Center
DRI	Dynamic Response Index
EASA	European Union Aviation Safety Agency
FAA	Federal Aviation Administration
FEM	Finite Element Method
FMVSS	Federal Motor Vehicle Safety Standard
FV	Flying-V
HIC	Head Injury Criterion
LISA	Laboratory for Impact Tests on Aerospace Structures
MTOW	Maximum Take-Off Weight
NASA	National Aeronautics and Space Administration
NTSB	National Transportation Safety Board
OEMs	Original Equipment Manufacturers
PMHS	Post Mortem Human Surrogates
RP	Reference Point
SEV	Severity Index
TACDWG	Transport Airplane Crashworthiness and Ditching Working Group
US	Unitated States
USAF	United States Air Force

Symbols

Symbol	Definition	Unit
a	Acceleration	ms^{-2}
b	Span length	m
b	Rigid body	-
c_r	Root chord length	m
c_t	Tip chord length	m
DRI	Dynamic Response Index	-
E	Identity matrix	-

Symbol	Definition	Unit
F	Force	N
g	Earth gravitational acceleration	ms^{-2}
h	Height	m
H	Angular momentum	kgm^2s^{-1}
HIC	Head Injury Criterion	-
I	Inertia tensor	-
I_{xx}, I_{yy}, I_{zz}	Moments of inertia about the x, y and z-axis	kgm^2
I_{xy}	Product of inertia from x and y coordinates	kgm^2
I_{xz}	Product of inertia from x and z coordinates	kgm^2
I_{yz}	Product of inertia from y and z coordinates	kgm^2
K_{eg}	Kinetic Energy	J
l	Length	m
m	Mass	kg
M_{xy}, M_{xz}, M_{yz}	Moments in the z, y and x-directions	Nm
r	Length vector to cg location	-
R	Rotation matrix	-
s	Length vector	-
S	Wing integration coefficient	-
SEV	Severity Index	-
t	Thickness	m
t	Time	s
T	Kinetic Energy	J
U	Potential energy	J
V	Volume	m^3
W	Weight	N
$\bar{x}, \bar{y}, \bar{z}$	Coordinates of the center of gravity	m
x_a, y_a	Coordinates in the airfoil coordinate frame	m
μ	Airfoil thickness distribution	-
ω	Angular velocity	$rads^{-1}$
ρ	Density	kgm^{-3}
Γ	Dihedral angle	$^\circ$
δ	Left/right wing sign coefficient	-
τ_m	Percent maximum airfoil thickness	%
Λ	Quarter-chord sweep angle	$^\circ$
τ_r	Root airfoil thickness	m
θ	Rotation matrix angle	$^\circ$
v_0	Thickness distribution coefficient	-
τ_t	Tip airfoil thickness	m
v	Velocity	ms^{-1}
κ	Wing planform coefficient	-

This page intentionally contains no content.

List of Figures

This page intentionally contains no content.

List of Tables

This page intentionally contains no content.

Introduction

Aircraft crashworthiness has been an enduring concern in the aviation industry since the inception of air travel. Ensuring the safety of occupants during emergency landings or unforeseen accidents has become paramount in the pursuit of safer commercial air transportation. Over the past two decades, significant progress has been made, with the proportion of accidents resulting in fatalities dropping below 50%. This positive trend underscores the industry's commitment to enhancing aviation safety.

The focus on crashworthiness extends to novel aircraft configurations such as the Flying-V, a revolutionary design featuring a distinctive V-shaped fuselage. While this innovative design offers advantages in terms of fuel efficiency and aerodynamics, it poses unique challenges in ensuring passenger safety during crash scenarios. Traditionally, aircraft crashworthiness assessments involve vertical drop tests on a specific segment of the fuselage section that replicate landing impact dynamics. However, the Flying-V's unconventional geometry and mass distribution raise questions about the applicability of such simplified crash scenario to assess its crashworthiness. Past research has focused on providing detailed structural design information only at the wing-fuselage region of the Flying-V [28, 26, 27], where most of the passengers and payload is located, but little or no information exists about the structural design of the central and outboard regions of the Flying-V. Furthermore, there are mass estimates for those regions, which have been used in recent studies investigating the Flying-V family concept, and its projected fuel efficiency when compared with the A350 [52].

The primary objective of this research project is then to develop a methodology that enables the assessment of more complete crash scenarios, especially in unconventional aircraft such as the Flying-V. This will be achieved by suggesting simplified modelling approaches that effectively capture the essential kinematics of various sections of the Flying-V without the need of a detailed physical representation of the entire aircraft, or, in other words, when only the regions of interest are detailed.

Nonetheless, in order to achieve so, a literature study has been first performed as part of this research. The scope of the literature study was to provide insights into 1) regulatory requirements and crash injury criteria to evaluate aircraft crashworthiness; 2) propose new crashworthiness requirements for the Flying-V; 3) provide an overview of crashworthiness behavior of conventional aircraft designs at different impact angles; 4) and introduce the reader to the simplified modelling techniques proposed. While the literature study report was a separate deliverable, in this report, a small extract on the most relevant parts of the literature study will be presented. This dissertation will document all the activities performed in the context of the research, present the obtained results and lay down the groundwork for future crashworthiness developments. The report is structured in multiple parts, with each part being constituted by multiple Chapters.

Part I consists of the front matter, including the Preface and Introduction. Successively, highlights from the literature study report will be presented in Part II.

Part III will present the methodology, results, and conclusions drawn from different modelling approaches conducted. It starts by, in Chapter 6, presenting an understanding of the procedures employed in establishing, verifying, and validating the non-linear, explicit-dynamic finite element model used in the previous research, serving as the foundational framework for subsequent analyses. Before delving into more dynamically complex scenarios, expanding the computational domain to encompass larger fuselage sections becomes essential for a more reliable study. This is the goal of Chapter 7, to examine an extended fuselage section size before incorporating the kinematics of other Flying-V sections. Unrealistic side deformations were obtained, so Chapter 8 and Chapter 9 introduced respectively lateral sliding boundary conditions and structural constraints. Ultimately, the effect of both approaches in minimizing the free boundary deformations is compared. Furthermore, for a better analysis of potential Flying-V crash scenarios without oversimplifying, and for the subsequent validation of a modelling technique introduced in upcoming Chapters, the crashworthiness assessment is extended to the full passenger fuselage in Chapter 9. Part III ends with an overall comparative assessment of all the crashworthiness modelling approaches previously discussed. Based on the outcomes of this analysis, one of the modelling approaches is subsequently chosen to model possible Flying-V crash scenarios with the simplified technique introduced in the literature, establishing the foundation for Part IV.

Titled ”Modelling Unique Flying-V Crash Scenarios”, Part IV begins with an optimization attempt of the vertical drop test of the fuselage section chosen in Chapter 10, by leveraging the moments of inertia of subsequent sections of the FV. This initiates, in Chapter 11, the main core of this research, by finally studying the modelling technique formerly proposed. Expanding on this investigation, in Chapter 12, the current study is focused on evaluating the crashworthiness performance of fuselage sections under varying roll angle impact conditions. Drop tests are performed with and without the inclusion of moments of inertia of subsequent sections, and their outcomes are discussed. Finally, Chapter 13 takes a progressive step, introducing a variable centerline orientation to the full passenger section: instead of remaining horizontal, a pitch angle is present. This case study aims to provide an understanding of how different orientations affect crash responses. Subsequently, the implicit moments of inertia approach will be re-evaluated by a verification and validation plan. The Chapter ends with the proposal and testing of an alternative methodology capable of increasing the results accuracy.

To conclude, Part V encompasses the Conclusions, Recommendations, and References derived from the findings of this research. Finally, Part VI incorporates Appendices.

Research Objective and Questions

The primary aim of this project is to enhance the crashworthiness evaluation. This entails proposing simplified modelling approaches that capture the essential kinematics of various sections of the Flying-V without the need for detailed physical representation of all regions. Simultaneously, the project endeavours to enhance the crashworthiness assessment of the Flying-V when exposed to more intricate crash scenarios. As a result, the central research question emerges:

”How can reduce modelling techniques be effectively employed to capture the fundamental kinematics of different sections of the Flying-V without a detailed physical representation, and how do these approaches contribute to improving the crashworthiness assessment of the aircraft in unique and complex crash scenarios?”

To address this, the central research question has been broken down into several sub-questions:

1. **Implementing Different Modelling Approaches:**
    - How can a balance between computational efficiency and result accuracy be achieved within finite element models, especially when delving into more intricate dynamic scenarios?
    - Which criteria should guide the selection of an appropriate modelling approach for crashworthiness evaluation of the FV, considering the complex interplay among passenger distribution, structural configuration, and overall structural behavior across different approaches?
    - To what extent is it essential to expand the computational domain, encompassing larger fuselage sections, to enhance the reliability of analyses in such assessments?
2. **Modelling Unique Flying-V Crash Scenarios:**
    - Given that aircraft crashes typically involve non-straightforward vertical descents, what possible crash scenarios can be incorporated to provide a comprehensive understanding of the Flying-V’s crashworthiness?
    - How can simplified modelling techniques be effectively employed and validated when addressing the challenge of evaluating the crashworthiness of the Flying-V under more complex crash scenarios?

II

Literature Study

This page intentionally contains no content.

1

Relevance of the Research Topic

One of the main challenges in designing the Flying-V, a novel aircraft configuration with a V-shaped fuselage, is to ensure its crashworthiness in case of an emergency landing. A technique commonly employed to assess the crashworthiness of a traditional airplane involves conducting vertical drop tests that replicate the vertical aspects of a landing impact. However, this method has some limitations and drawbacks that need to be considered before applying it to the Flying-V. For example, in case of blended wings body designs, the constant cross section of the wings' fuselage creates a certain angle with the landing direction, and this might refute the viability of vertical drop tests for such unconventional designs.

Also, vertical drop tests fail to capture the complexity and dynamics of realistic landing scenarios that involve horizontal, rotational, and vertical components. The unique geometry and mass distribution of the Flying-V may impact its behavior during a landing in ways that vertical drop tests do not account for.

In addition, these tests may not provide sufficient information about the failure modes and energy absorption mechanisms of the Flying-V structure. The large and flexible fuselage of the Flying-V can deform and buckle in various ways depending on the impact conditions. A vertical drop test may not be able to capture these details and provide useful insights for improving the design.

Therefore, this research will question the viability of traditional procedures used in conventional airplane designs when studying the crashworthiness of the Flying-V.

To that extent, it is proposed to use a combination of numerical simulations to evaluate and optimize the design of the Flying-V for crashworthiness. These can provide detailed information about the stress and strain distributions, failure modes, and energy absorption mechanisms of the Flying-V structure under various impact scenarios. Moreover, reduced modelling techniques will be suggested to streamline the analysis and decrease the computational time required for simulations.

Sub-scale experiments should also be conducted to validate and calibrate the numerical models and provide experimental data that are more reliable and repeatable than those from a full-scale vertical drop test but, due to insufficient funds and lack of Flying-V's physical models, this cannot be accomplished.

This master's thesis then tries to enhance the understanding of the crashworthiness of the Flying-V and design it to meet future aviation safety requirements.

To acquaint the reader with the significance of this work, it is crucial to first discuss previous research conducted on the topic (Section 1.1), and later emphasize the basic principles of crashworthy design, along with the primary distinctions between conventional aircraft design and blended wing body (BWB) design.

These two aspects will be highlighted in Section 1.2 and Section 1.3, respectively.

1.1. Previous Work Done on the Subject

This master's thesis builds upon the prior research conducted by Marco Desiderio [26], focusing on the design and crashworthiness assessment of the Flying-V concept aircraft.

In order to introduce the reader to the relevance of this work, it is crucial to outline the methodologies and conclusions presented by Desiderio, as a starting point.

To establish a crash concept for FV aircraft, Desiderio has commenced by gathering and documenting existing advanced research on the crashworthiness of aircraft, primarily focused on traditional aircraft designs. Additionally, design requirements have been established as part of this phase, specifically a maximum equivalent dynamic response index of 16 units that has been determined as a criterion to define a representative section that exhibits crashworthiness (this injury criteria and design requirements will be discussed more in detail in Chapter 2).

Subsequently, a sequence of studies have been conducted on a representative section of the Fokker F-28 airliner to investigate the impact of increased fuselage eccentricity and variations in floor beam height on the mean accelerations and dynamic response index (DRI) experienced by occupants during a crash. The findings indicate that both these factors have a notable influence on the crash characteristics, particularly on mean accelerations.

Significantly eccentric sections exhibited a substantial increase in DRI compared to conventional circular sections. This was mainly due to:

- a decrease in crushable length, resulting in a shorter impact time duration, which significantly affected the DRI;
- the oval shape of the fuselage frames, leading to a loss in their capacity to absorb energy.

Desiderio came to the conclusion that a reduction of 7.5% in the amount of absorbed energy has been noted when comparing the sections with zero eccentricity to the most oval sections that were tested.

Regarding the floor beam height, a slight increase resulted in a longer impact duration, which in turn led to a decrease in DRI values. However, the floor beam height had minimal to no impact on the overall amount of energy absorbed.

In terms of crash concepts for the FV aircraft, four different concepts were explored, two of which resembled those used in conventional aircraft. These concepts aimed to create a plastic hinge on the frames to absorb energy. The evaluation of these concepts considered DRI and absorbed energy. One concept with six floor struts (6S) was discarded due to excessive stiffness, resulting in high DRIs. Another concept with four floor struts (4S) performed well, with a significant portion of initial kinetic energy dissipated, but still had DRIs slightly above the required threshold of 16 units (reaching 18.2 units). Despite this, it was ultimately deemed the optimal design choice. The concept involving horizontal and vertical struts (HB) had a measured DRI of 22.2 and the concept involving many vertical crushable elements (HBH) exhibited structural instability, resulting in the lowest rate of energy absorption and the highest DRI.

Throughout the studies, Desiderio came to the conclusion that a good balance between rigidity and flexibility is necessary for effective crushing behavior. Overly rigid sections led to high DRIs, while structural instability caused large elastic deformations, which increased the risk of spinal injury.

A sensitivity analysis on the best concept, 4S-5, revealed that floor beam thickness had a significant impact on crash properties, with a more compliant floor beam allowing for greater energy absorption through plastic deformations. The analysis also emphasized the importance of accurately modelling frame bending stiffness (17% reduction in the frames bending stiffness yielded a DRI of 16.6 units).

Although Desiderio wasn't able to design a crashworthy typical section based on his current research, the collected data provided assurance that this objective can be achieved with further investigation. His recommendation to pursue a crashworthy typical section is the 4S concept, with an emphasis on optimizing the positioning and dimensions of the floor struts as design variables.

Building upon Desiderio's work, this MSc thesis attempts to further explore the crashworthiness evaluation of the Flying-V aircraft. This involves delving into the more intricate dynamics of real-world landing scenarios, which encompass horizontal, rotational, and vertical components, aspects these that are not adequately captured by the vertical drop tests.

To begin the study, the fundamental principles of crashworthiness will be introduced as a foundation.

1.2. Basic Principles of Crashworthiness

Since the introduction of aircraft and all other modes of transportation, accidents have been a persistent concern. These accidents have often been characterized as catastrophic events, prompting aircraft designers and the entire aerospace industry to progressively prioritize the safety of commercial air travel. Undoubtedly, aircraft crashes can result in devastating outcomes. However, the proportion of accidents leading to fatalities has decreased to less than 50 % over the past two decades, as depicted in Figure 1.1. Furthermore, a significant number of accidents are survivable for passengers, particularly those that culminate in emergency landings.

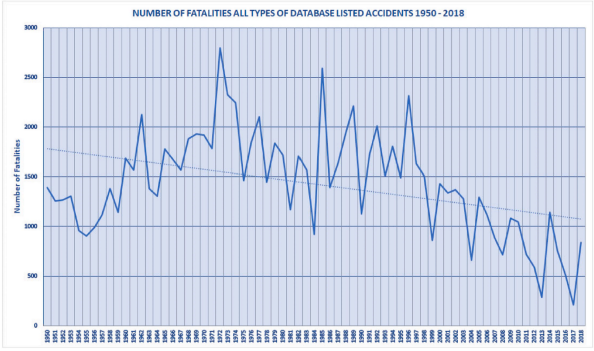

Figure 1.1: Number of fatal accidents of commercial aviation per year [1]

According to several studies [45], a significant portion of accidents (56%) occur during the approach and landing phases of a typical flight mission. Additionally, 20% of accidents happen during take-off and climb, as shown in Figure 1.2. Surprisingly, accidents during these phases have a higher likelihood of being survivable. However, accidents occurring in other flight phases often result in a greater number of casualties due to high-energy impacts or mid-air explosions. Therefore, two factors strongly contribute to this observation: aircraft speed and the distance from airports.

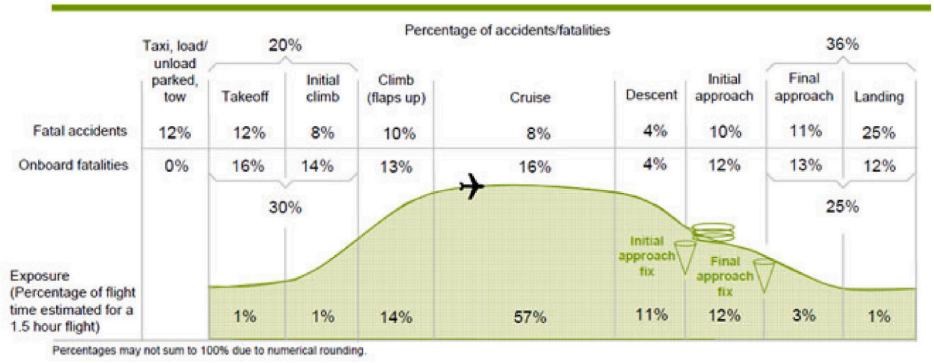

Figure 1.2: Percentage of fatalities by phase of flight [45]

In recent years, collaborative efforts between U.S. federal agencies and aircraft manufacturers have been dedicated to studying accidents and compiling a comprehensive database. The primary objective has been to identify and establish guidelines and regulations for creating a crash environment that maximizes survivability [33].

Extensive analysis of the collected data has revealed that, typically, injuries resulting from aircraft crashes can be attributed to three primary factors:

- excessive forces of acceleration;
- direct trauma caused by contact with hazardous surfaces;
- exposure to environmental elements like fire, smoke, water, and chemicals, leading to burns, drowning, or asphyxiation.

Therefore, effective crashworthiness designs must account for all potential injury sources and aim to eliminate or minimize them within practical limits for a given design impact threshold [63]. These research endeavors have provided the groundwork for the emergence of a new design philosophy commonly referred to as ”crashworthiness” [33]. This involves assessing the:

- structural integrity of the cockpit and cabin;
- adequacy of seats and restraint systems;
- effectiveness of energy absorption mechanisms;
- presence of potentially harmful objects near occupants;
- post-crash considerations, particularly fire prevention and the availability of safe escape routes [63].

The crashworthy aircraft needs to take into account all these things while possessing the ability to withstand and effectively manage high, sudden decelerations from various directions that occur during impacts on different types of crash landing conditions [39].

1.2.1. Implementing Crashworthiness

The designer’s aim is to eradicate injuries and deaths caused by less severe collisions, reduce injuries and fatalities in severe crashes that are still survivable, and minimize the harm inflicted on the aircraft structure in any crash scenario. As a result, based on the CREEP criteria, a successful design is achieved by maximizing the dissipation of impact energy, ensuring the preservation of a volume that allows for occupants survival. This involves converting the impact energy into plastic deformation and fracture energy of the structural components that are affected during the crash [33].

Most of the strike energy is absorbed by the structure, and when the fuselage impacts the terrain, it will transmit significant acceleration forces in different directions that are applied to both the cabin floor and seats. To properly implement crashworhtiness into an airplane, different impact angles caused by dissimilar crash landing events must be considered, to capture the intricate nature and dynamic aspects of an authentic landing situation. These fundamental requirements must then be accomplished:

- The majority of the impact energy needs to be absorbed through controlled plastic deformation of components in order to minimize the load transmitted to the passenger. Unlike traditional aircraft with cylindrical fuselages and wings, the Flying-V cabin exhibits a notable eccentricity due to its dual function as a passenger seating area and lifting surface. This unique configuration poses a design challenge when it comes to ensuring crashworthiness. Conventional full-metal fuselages are capable of offering adequate protection to passengers due to the generous crumple zone situated beneath the seating area. However, for the Flying-V aircraft, the available space for such protective measures is constrained;
- After the impact, it is essential to maintain a minimum volume that allows for survival;
- The deceleration experienced by the passenger due to the crash must not result in any injuries. Regulatory guidelines prescribe various injury criteria that must not be surpassed. These will be touched upon in Chapter 2;
- The objective is to minimize the harm to the occupants following an impact. It should be imperative in the future to assess all potential seat arrangements within the cabin, encompassing forward-facing, aft-facing, and side-facing configurations. This becomes particularly critical for the Flying-V, given its unique seat orientation that does not directly face forward or aft. Such a deviation from conventional layouts may present challenges in adhering to established regulations set forth by the European Union Aviation Safety Agency (EASA) and the Federal Aviation Administration (FAA). Consequently, it will be necessary to propose additional special conditions to address this discrepancy.

With that being said, to properly implement crashworthiness into the Flying-V’s design process, the reader must be well informed about the main structural differences between conventional transport airplanes and blended wing body designs ones, especially the Flying-V configuration.

1.3. Aircraft Design and Its Effects on Crashworthiness

In recent decades, the environmental impacts of aviation have become a key challenge for the aeronautical community [17]. In order to address this issue, aircraft fuel efficiency has been enhanced primarily with the implementation of advanced aerodynamics, utilization of new materials, optimization of aircraft structure, and improvement of engine performance [66].

However, the aviation industry continues to face significant pressure to enhance its sustainability. As a result, there is a strong motivation to explore alternative aircraft options in order to minimize environmental emissions and reduce direct operating cost [17]. The blended wing body (BWB) design and Flying-V configurations holds further potential for a more environmentally friendly aircraft, thanks to its advanced aerodynamic design and reduced weight [66], but the different configurations poses a challenge in terms of crashworthiness regulations.

When certifying new aircraft configurations, airworthiness authorities demand evidence of safety standards that are at least comparable to those of traditional transport aircraft. In the case of BWB and the Flying-V configurations, it is necessary to demonstrate adequate crashworthiness for emergency landings on both rigid surfaces and water [66]. Due to time constraints, the ditching behaviour is out of the scope of this Msc thesis.

1.3.1. The Flying-V Aircraft Configuration

The Flying-V is an innovative aircraft design that offers significant advancements in fuel efficiency compared to traditional aircraft. It features a unique V-shaped flying wing configuration that seamlessly integrates the passenger cabin and cargo space into the main lifting surface. The cabin takes on an oval shape, and the engines are positioned along the trailing edge (Figure 1.3).

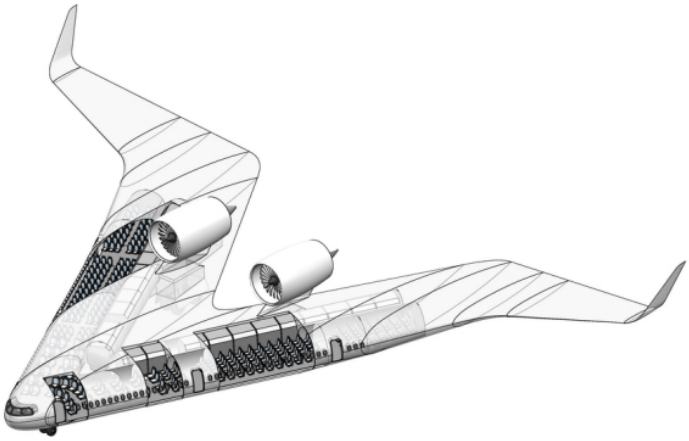

Figure 1.3: Flying-V 3D geometry resulting from the conceptual study [42]

This configuration offers improved aerodynamic efficiency compared to conventional tube-and-wing (CTW) aircraft. It achieves this by reducing the wetted area, thereby minimizing friction drag, and increasing the effective wingspan, which reduces lift-induced drag. Nonetheless, the significant eccentricity in the Flying-V cabin's typical section leads to a reduction in crushing distance, making the crashworthiness aspect unique and the design more challenging.

Extensive research has been conducted on various aspects of the Flying-V, including its aerodynamics and structural integrity, all of which confirm its substantial potential for reducing fuel consumption, up to 20% compared to an Airbus A350 for the same flight [25].

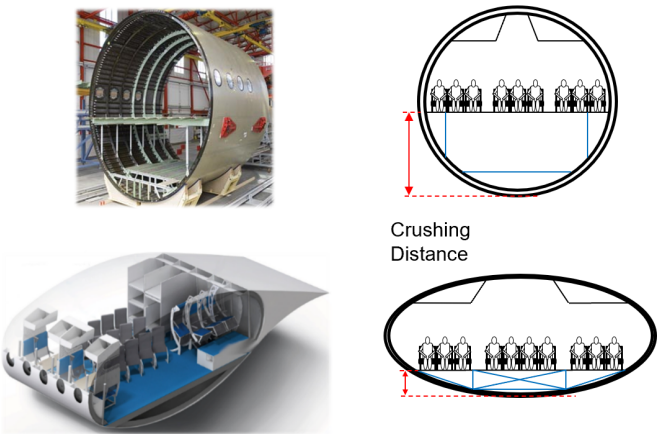

Figure 1.4: Differences in crushing distance from convantional and the Flying-V aircraft design

Oosterom [52] gathered a lot of information focused on the feasibility of developing a family of Flying-V aircraft, which can be a large advantage with respect to blended wing body designs. Previous investigation on the later suggested that developing a family is difficult due to its lack of a constant cross-section.

Liebeck [42] made a statement regarding the blended wing body (BWB), which bears some resemblance to the Flying-V aircraft configuration: ”commonality may be the key to provide the incentive and courage to proceed to develop this new airplane concept.” On the contrary, according to Mike Sinnett [34], a blended wing body (BWB) design is not suitable for being extended or reduced in size. “You take the most expensive part of the airplane, the non-constant section, and growing it in a non-constant way, or shrinking it in a non-constant way. It’s really hard.”

It should also be noted that the Flying-V configuration positions the center of gravity further forward compared to a BWB configuration, which can increase even more the stability and help prevent excessive nose-up pitching. This is achieved by eliminating the ”triangle in the back” of the aircraft, effectively increasing the moment arm of the movable components even further. Additionally, the initial design of the Flying-V incorporates emergency exits on both sides of the cabins, whereas the BWB configuration does not offer this feature [52].

Oosterom then compared the three variants of the Flying-V’s family performance to the reference Airbus A350 family (the -800, -900 and -1000).

Since one of the main contrasts between both models lied in the utilization of an elliptical fuselage, the systems, operational components, landing gear, engines, cabin provisions, and payload items did not differ much from conventional aircraft layouts. To limit computational complexity, Oosterom used Class II weight estimation methods, based on empirical formulas employed to compute the mass of each essential component. This led to the final mass breakdown for the component group weights estimations seen in Table 1.5 for the -900 variant.

Group	subgroup	Part	Group Mass	Sub Mass	Part Mass	Location
$MTOW$			266 000	[-]	[-]	Overall CG
$W_{payload}$			34 000	[-]	[-]	Cabin CG
W_{fuel}			103 000	[-]	[-]	Fuel CG
OEW	Landing Gear	Nose	[-]	[-]	1 800	NG CG
		Main*	[-]	[-]	4 650	MG CG
		Total	[-]	11 100	[-]	[-]
	Engines	Left	[-]	[-]	10 950	L. Eng. CG
		Right	[-]	[-]	10 950	R. Eng. CG
		Total	[-]	21 900	[-]	[-]
	Operational Items		[-]	6 400	[-]	Cabin CG
	Furniture		[-]	16 700	[-]	Cabin CG
	Remaining (Structure + Systems)		[-]	73 400	[-]	Structural CG
	Total OEW		129 500	[-]	[-]	[-]

All masses are represented in [kg]
** mass per individual gear*

Figure 1.5: Flying-V Mass Breakdown

For the -800 and -1000 variants, the overall weight was estimated to be 207 ton and 278 ton, respectively.

While the conceptual design performed by Oosterom led to a rough overall mass estimation of the Flying-V, there's still a big gap of structural design information, except for the typical wing-fuselage cross section developed by Desiderio [26], which extends from the central to the outboard region. Nonetheless, the mass and parts subdivision already estimated for the whole aircraft will be further used to enable a technique proposed in Chapter 5, enhancing the crashowrthiness understanding of the FV.

As an introductory step, some important data and conclusions to analyze the crashworthiness of the Flying-V can already be inferred, providing a foundational understanding of its potential performance in various impact scenarios.

First of all, the leading edge sweep of the inboard wing of the FV can have an impact on the accelerations encountered by passengers during a crash landing. The extent of leading edge sweep affects the aerodynamic characteristics of the wing, which in turn affects the distribution of forces and loads during impact [13].

A greater leading edge sweep can also help by dissipating and absorbing energy upon impact. It can contribute to a smoother distribution of forces along the wing structure [73], reducing the concentration of stress at specific points. By deflecting some of the air and debris away from the fuselage, impact forces can be mitigated. This results in a smoother deceleration and lower peak accelerations experienced by passengers.

A higher leading edge sweep may also enhance the torsional stiffness of the wing, reducing deformation and bending during a crash [67].

Additionally, the leading edge sweep can influence the aerodynamic stability and control of the aircraft during the crash sequence, which might influence the trajectory and attitude of the airplane before impact. It can affect the generation of lift and the ability of the wing to maintain stability, potentially impacting the aircraft's ability to maintain a level attitude and minimize the forces experienced by the passengers [13].

Lastly, a notable feature of the Flying-V is its superior rigidity and strength in comparison to traditional fuselages. This structural robustness implies that the aircraft may demonstrate unique crash dynamics. For instance, in a tail-first impact scenario, the outer wings of the Flying-V could sustain damage or separate from the main body, leading to a dissipation of energy distinct from conventional designs and directly impacting the aircraft's crashworthiness.

However, the stiff and robust fuselage section of the Flying-V is expected to undergo significant rigid-body rotation upon contact of the wingtips with the ground. This rotation may introduce upward forces, generating a strong pitch-down moment on the aircraft, followed by further rotation. As a result, different segments of the passenger cabin may encounter varying vertical impact velocities, potentially causing disparate occupant accelerations.

Furthermore, impact scenarios involving different roll angles can induce additional rigid-body rotations. As the Flying-V tilts during impact, sections of the passenger cabin situated further from the initial contact point with the ground may experience heightened vertical impact velocities, further complicating the assessment of passenger safety.

In light of these intricacies, it becomes evident that a comprehensive examination of the crashworthiness of the Flying-V is imperative before certifying its operational safety and ensuring the protection of passengers and crew during potential crash scenarios.

This page intentionally contains no content.

2

Regulatory Approaches and Injury Criteria Regarding Crashworthiness for Conventional Aircraft Design

Throughout the history of federal civil aircraft certification standards, the primary focus has been on designing aircraft to be safe for flying. Initially, the emphasis was on ensuring airworthiness, and static load tests were preferred over dynamic ones. This emphasis on airworthiness was justified because early airplane designs often had structural and handling issues. Moreover, there wasn't enough theoretical or technical knowledge available at the time to establish meaningful crash survival parameters. Similarly, determining dynamic criteria for aircraft design has always been challenging [10].

In the early stages of aircraft design, little attention was given to crashworthiness, except for certain aspects like seat belts, seat static load requirements, and exits. A significant shift occurred in 1967 when the Federal Aviation Administration (FAA) introduced a series of crashworthiness standards specifically for transport category airplanes.

These rule changes demonstrated that the FAA's approach to crashworthiness mainly revolved around three key concerns: protecting occupants from crash impact, minimizing the risk and severity of fires resulting from crashes, and facilitating the swift evacuation of occupants. These factors have remained central to the periodic updates and enhancements of regulatory standards over time [10].

For a considerable period, the FAA and the aviation industry have collaborated extensively to enhance the safety of occupants in transport airplanes during accidents that are deemed survivable. This collaborative effort has encompassed the investigation of aircraft accidents, the execution of crash simulations in testing, and the utilization of analytical modelling to study various crash scenarios. The primary objective of these endeavors has been to gain deeper understanding regarding the factors that impact occupant safety. The outcomes of this ongoing endeavor have played a vital role in effecting targeted modifications to regulatory standards and design methodologies, all aimed at enhancing occupant safety [59].

However, when it comes to crashworthiness, there is currently no overall standard specifically for the crashworthiness of the aircraft structure. Instead, the FAA has established standards that focus on protecting occupants at the level of seat installations. The assumption is that the aircraft structure itself inherently offers an acceptable level of crashworthiness [59].

Additionally, while current airworthiness standards and regulatory guidance for part 25 were being developed, the FAA made assumptions about the predominant use of metal and the skin-stringer-frame architecture in constructing airframe structures for transport airplanes. As a result, certain requirements either fail to address all the issues related to nonmetallic materials or are based on experiences with large metallic airplanes designed in a traditional configuration [7].

To asses this problem, the FAA assigned the Aviation Rulemaking Advisory Committee (ARAC) with a new assignment. Their goal was to provide recommendations regarding the inclusion of crashworthiness and ditching standards at the airframe level into Title 14, Code of Federal Regulations (14 CFR) part 25. They were also responsible for developing associated advisory material [7].

With that in mind, the Transport Airplane Crashworthiness and Ditching Working Group (TACDWG) was born in order to rationalize, modernize, and harmonize the regulatory environment, by proposing new rulemaking and advisory material to incorporate updated crashworthiness standards. Their work will be discussed in more detail in subsequent sections of this Chapter.

As such, before proposing new regulatory approaches regarding the crashworthiness of the Flying-V (which will be addressed in Chapter 3), the well established certification requirements from regulatory agencies will be discussed in Section 2.1, as well as some of the significant work done by the TACDWG so far. Towards the end of this chapter, in Section 2.3, some injury criteria will be briefly discussed.

2.1. Current Requirements from Regulatory Agencies

The Federal Aviation Administration (FAA) in the United States and the European Union Aviation Safety Agency (EASA) are leading authorities when it comes to certification specifications [8, 11]. The Flying-V aircraft is classified under the 'part 25' and 'CS-25' categories in the regulatory requirements of both the FAA and EASA. These categories specifically apply to "turbine powered Large Aeroplanes."

Given the similarities between the regulations of both authorities, and knowing that the FV will be designed in the European Union [69], this section's discussion will primarily focus on the requirements and acceptable means of compliance outlined by the European regulator. This simplification is adopted for the sake of clarity and ease of understanding.

The baseline requirements established by regulations dictate the necessary conditions that an aircraft must meet in order to obtain certification. As a result, compliance with these regulations is a crucial aspect discussed in this report, as it determines the eligibility of the Flying-V for operational purposes.

The regulations are enforceable guidelines that can be regarded as rigid legal requirements. However, they are frequently less precise and explicit when it comes to a particular type of aircraft, where some flexibility needs to be provided by the regulatory system through the use of non-binding standards (soft law) [11]. Therefore, EASA created Certification Specifications (CS) and Acceptable Means of Compliance (AMC) that provide detailed information regarding the implementation of regulations, which are commonly explained using legal terminology that can be challenging to comprehend.

EASA defines certain requirements for aircraft crashworthiness, as well as AMC, in the CS-25 SUBPART C – STRUCTURE: Emergency Landing Conditions regulation. These can also be found in Desiderio's dissertation but, for sake of comprehension, it will be outlined in the next subsection. Moreover, CS-25 describes design requirements for seats and safety belts in SUBPART D - DESIGN AND CONSTRUCTION: Seats, Berths, Safety Belts and Harnesses.

2.1.1. SUBPART C – STRUCTURE: Emergency Landing Conditions

The present standards for determining the impact conditions utilized in the development of safety systems for aircraft occupants can be found within CS-25, Subpart C-Structure, specifically outlined in Section 25.561 ("General") and Section 25.562 ("Emergency Landing Dynamic Conditions") [11]. These regulations primarily focus on assessing the robustness and effectiveness of seat and restraint systems, although some consideration is given to the immediate environment of the occupants and the structural integrity of the fuselage [33].

CS-25.561

The general provision CS-25.561, mandates that the aircraft structure should be designed in a manner that offers occupants a reasonable opportunity to prevent serious injuries during a minor crash landing, assuming that all safety measures such as seat belts and other provisions are used correctly. This requirement is further detailed in CS-25.561(b)(3), which specifies the ultimate inertia forces that occupants should encounter in a configuration where the landing gear is retracted:

- Upward - 3.0 g;
- Forward - 9.0 g;
- Sideward - 3.0 g on the airframe and 4.0 g on the seat and their attachments;
- Downward - 9.0 g;
- Backward - 1.5 g.

Furthermore, CS-25.561 stipulates that seats, objects of significant mass, and their supporting structures must not undergo any deformation under the previously mentioned loads that would hinder the quick evacuation of occupants [33]. As Desiderio emphasized in his study [26], it's important to note that the mentioned conditions typically pertain to a standard fuselage segment. However, because of other factors such as the section housing the central wing box and considerations of rigid body dynamics, the actual accelerations encountered by passengers during a crash event will vary depending on their seating position. Furthermore, these load factors are to be applied in static analyses, and do not reflect the impact nature of crash impacts.

CS-25.562

Section 25.562 outlines the requirement for conducting a minimum of two dynamic tests to evaluate the performance of an aircraft seat, its restraints, and the associated interior systems. These tests must be successfully completed.

In Test I, the system's performance is assessed when the primary force component acts along the occupant's spinal column, along with a forward force component. During this test, the aircraft's longitudinal axis is inclined 30° downwards relative to the horizontal plane [11].

In Test II, the primary force component is directed along the aircraft's longitudinal axis, in combination with a lateral force component. The longitudinal axis remains horizontal, but it is yawed either 10° to the right or 10° to the left. Test II evaluates the seat structure's performance, permanent deformation, and also analyzes the behavior and loads on the restraint systems [11].

Figure 2.1a illustrates the seating arrangement for both Test I and Test II, with an arrow indicating the direction of the inertial load, while Figure 2.1b depicts the idealized test pulse simulating the aircraft floor deceleration, where the maximum deceleration (measured in G) occurs at the rise time t_1.

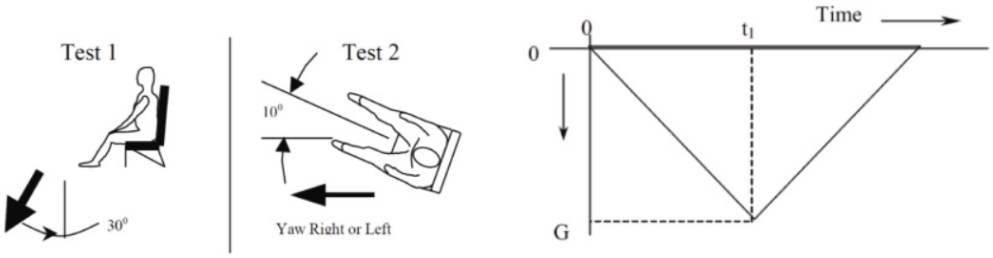

(a) CFR 25.562 Test I and Test II setup **(b)** CFR 25.562 acceleration pulse

Figure 2.1: CFR 25.562 test setups and acceleration pulse [33]

Finally, Table 2.1 provides details about the test conditions, including the minimum impact velocity (V_1), maximum impact duration (t), minimum peak deceleration (G), and the roll and pitch angles of the seat.

Table 2.1: CS-25.562 Test I and Test II conditions [33]

	Test I	Test II
Min $V_1(m/s)$	10.67	13.41
Max t (s)	0.08	0.09
Min G	14	16
Roll (deg)	0	10
Pitch (deg)	0	10

Following the dynamic conditions discussed, a set of performance criteria must be met, as outlined in CS-25.562(c)(1) through CS-25.562(c)(5). It's important to highlight the maximum allowable compressive load between the pelvis and the lumbar column, that should not exceed 1500lbs (680kg), and the Head Injury Criterion (HIC). When there is a potential for contact between an occupant's head and the surrounding structure, there must be adequate safeguards in place to ensure that the impact on the head does not exceed an HIC of 1000 points. The HIC will be introduced later in Section 2.3.2.

Nevertheless, as previously mentioned, the regulatory framework does not provide specific details regarding the dynamic crash landing conditions at the aircraft level.

This omission is recognized by the TACDWG [9]. Also, the criteria mentioned in CS-25.562(c)(1) to CS-25.562(c)(5) requires a model for the seat when performing a numerical simulation, as well as an anthropomorphic dummy, in order to obtain meaningful results. To solve this issues, TACDWG proposes alternative crash injury criterias as a valid methods of compliance. One such criterion is the Dynamic Response Index (DRI), a commonly utilized metric in the aviation sector for demonstrating compliance with aircraft crashworthiness standards [26]. The DRI is a risk-based injury criterion calculated based on the accelerations recorded at the connection point between the passenger seat and the floor, without the need for a specific seat model to be incorporated. Additional information about the DRI will be presented in Section 2.3.3.

2.1.2. SUBPART D - DESIGN AND CONSTRUCTION: Seats, Berths, Safety Belts and Harnesses

CS 25.785 dictates relevant information about the seats and safety seat belts, but the main focus of this subsection is given to the seat orientation. This is an important topic to be addressed, due to the Flying-V's cross section exhibiting a yaw angle of 25.5° with respect to the flight direction. As it will be seen later, the initial proposal was to optimize the seat orientation by studying the effect of the misalignment and the subsequent introduction of side loads to passengers. However, due to time constraints, such tests could not be conducted, and are left has a recommendation for future research. Nonetheless, due to its importance in assessing passenger safety for the Flying-V, it was deemed appropriate to introduce this matter within the current dissertation.

According to CS-25.785(d), occupants seated at an angle exceeding 18° from the aircraft's centerline vertical plane must be safeguarded against head injuries. This protection can be achieved through a combination of a safety belt and an energy-absorbing rest that supports the arms, shoulders, head, and spine. Alternatively, a safety belt and shoulder harness can be utilized to prevent the head from making contact with any harmful objects. For occupants seated in other positions, head protection against injury is ensured through the use of a safety belt. The specific measures taken for head protection depend on factors such as the seat type, location, and facing angle.

Therefore, $\pm 18°$ is the maximum allowed angle with the direction of the flight when using conventional belts, otherwise additional protection systems will have to be added. With respect to seats other than forward-facing, the performance measures of CS 25.562(c) have proved to adequately address the injury criteria for occupants of aft-facing seats but not for occupants of oblique-facing seats, which might introduce distinctive safety concerns due to the differing occupant kinematics and loading experienced during emergency landing situations.

More recently, to guarantee that novel seat designs offer an equivalent level of safety, the FAA created additional guidelines known as Special Conditions. These guidelines are intended to supplement the existing design and performance requirements.

Also, EASA has actively participated in the development of SAE ARP6316 [15], which establishes updated criteria for occupant injury assessment when certifying the installation of oblique seats on large airplanes. Within the framework of ARP6316, the facing direction of the occupant is defined as follows:

- Forward facing seats - Seats installed into the aircraft where the occupant facing direction is at $0° \pm 18°$ relative to the aircraft longitudinal axis.
- Aft facing seats - Seats installed into the aircraft where the occupant facing direction is at $180° \pm 18°$ relative to the aircraft longitudinal axis.
- Side facing seats - Seats installed into the aircraft where the occupant facing direction is at 90° relative to the aircraft longitudinal axis.
- Oblique facing seats - Seats installed into the aircraft where the occupant angle relative to the aircraft longitudinal axis is other than those described above.

Special Conditions on CS 25.785(d): Installation of Angled Seats

To circumvent the use of additional protection systems, some companies have requested special conditions, namely Airbus [4, 50].

Airbus introduced a "Proposed Equivalent Safety Finding on CS 25.785(d): Installation of Angled Seats" [4] for the Airbus A350-941 aircraft, allowing seats at angles exceeding 18 degrees without the need for an energy-absorbing rest or shoulder harness.

This proposal suggests that an equivalent level of safety can be achieved if the seat design enables occupants to align during the impact with the deceleration vector specified in CS 25.562(b).

This approach was supported by dynamic tests demonstrating that angled seat installations can replicate the behavior of a forward-facing impact for the upper torso of an anthropomorphic test device (ATD). The seat surroundings facilitate the forward alignment of the test dummy's upper torso during impact.

Furthermore, Airbus demonstrated that typical forward-facing seating was shown to have no obstructions that pose risks or cause significant twisting forces to the upper dummy body during impact.

Based on development tests, when the seat design allows for alignment of the ATD's upper torso and legs with the deceleration vector, there is no requirement for an energy-absorbing rest for the arms, shoulders, head, and spine, as mandated by CS25.785(d).

Alternatively, in cases where the occupant is unable to realign adequately, an acceptable design solution to address misalignment is the installation of an airbag-belt system. This alternative approach must also incorporate measurements of internal forces and moments on the anthropomorphic test device, in addition to the requirements specified in CS 25.562(c), for comparative analysis.

Another special condition on the installation of angled seats was also introduced by Airbus [50], but this time applicable to the A330 NEO. In addition to the injury criteria stipulated in CS 25.562(c), when performing the horizontal test as specified in CS 25.562(b)(2), the occupant injury criteria presented in Appendix A should be added.

Nonetheless, the primary challenge associated with this specific method of compliance is the requirement to incorporate a seat model and an anthropomorphic dummy into the numerical simulation to obtain meaningful results, both of which were excluded from the current work.

Responses and Injuries in Side-Facing and Oblique Seats per CS25.562

The FAA has recently launched a program to investigate the impact of obliquely oriented seats on occupant loading and injuries. This program aims to achieve two objectives:

- comprehend the injury mechanism in different body regions;
- and establish human tolerances for multi-axis loading conditions resulting from oblique orientations.

Previous studies predominantly employed Post Mortem Human Surrogates (PMHS) to examine pure lateral and oblique side impacts (Cavanaugh, et al., [21, 22]; Maltese, et al., [44]; Pintar, et al., [3]; Viano, [20]; Yoganandan, et al., [70, 72, 71]). However, these studies are mainly applicable to automotive environments and scenarios involving relatively smaller changes in velocities compared to those generated by the longitudinal impact pulse specified in FAA regulations [8].

One significant distinction between aircraft and automobile crashes is that, in the aviation environment, there is a need to evacuate the cabin after a crash occurrence.

To that extent, Humm et al. [36] conducted oblique side impact sled tests utilizing whole-body PMHS exposed to impact scenarios and severities relevant to aviation. The study examined injuries, patterns, and mechanisms, and also identified associated kinematic measurements for various body regions.

4 specimens with different seat configurations and restraint systems were subjected to horizontal longitudinal accelerations according to CS25.562(b)(2) emergency landing conditions, as seen in Figure 2.2.

Table 2.2 summarizes the test conditions applied for each specimen.

Table 2.2: Test Conditions used by Humm et al.[36]

Load direction	Yaw angle deg	Seat belt restraint type	Arm rest	Leg restraint	Specimen ID
Side	-90	Body centered lap belt; near side shoulder belt	Yes	None	1
Oblique	45	Body centered lap belt; standard frontal lap belt	No	Femur and tibiae restrained	2
Oblique	45	Standard frontal lap belt	Yes	Femur and tibiae restrained	3
Oblique	30	Body centered lap belt; standard frontal lap belt	No	None	4

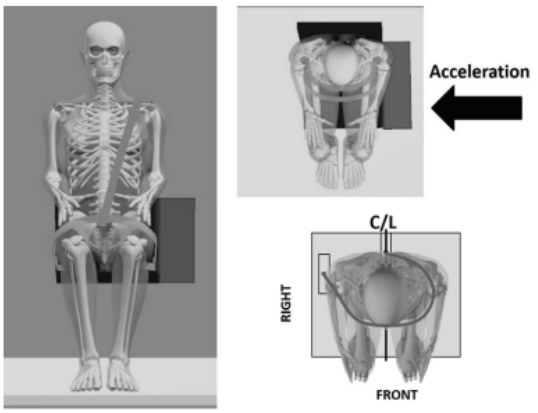

(a) Test condition for Specimen 1 (side-facing seat, 90-degree orientation to acceleration vector)

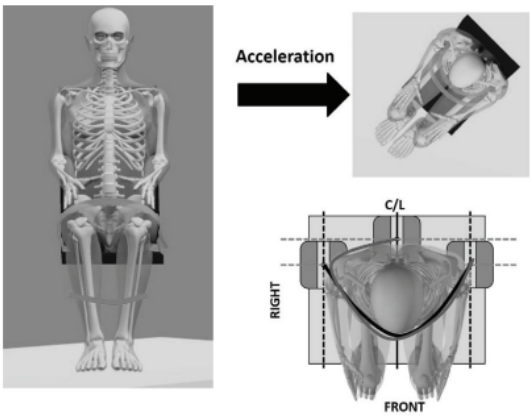

(b) Test condition for Specimen 2 (oblique seat, 45-degree orientation to acceleration vector)

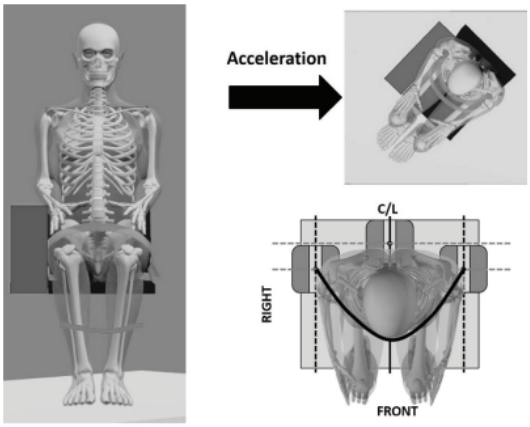

(c) Test condition for Specimen 3 (oblique seat with right side armrest, 45-degree orientation to acceleration vector)

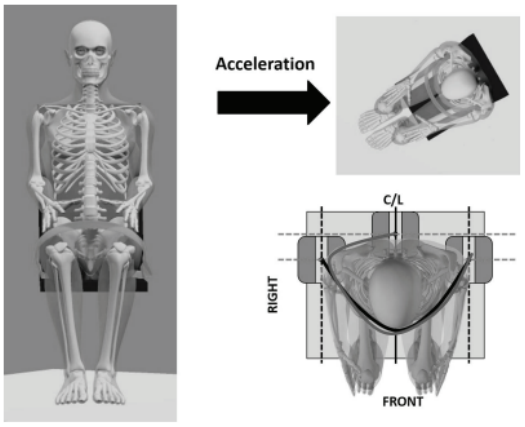

(d) Test condition for Specimen 4 (oblique seat, 30-degree orientation to acceleration vector)

Figure 2.2: 4 specimens with different seat configurations and restraint systems

The mean age, stature, total body mass, and body mass index of the four specimens were 59.5 ± 6.9 years, $1.8 \pm 0.1m$, $74.5 \pm 7.1kg$, and $24.0 \pm 4.3kg/m^2$.

As previously seen, CS25.562(b)(2) horizontal emergency landing condition specify a pulse with a peak of 16 g, a velocity of 13.4 m/s (4ft/s), and a rise time of 90 milliseconds [11]. This sled pulse simulates the frontal impact conditions that an aircraft may experience during takeoff or landing. Due to constraints within the test laboratory during the testing of specimen 1, the EASA's prescribed dynamic condition for horizontal impact during emergency landings, characterized by a triangular-shaped pulse, was not attained. Instead, a rectangular pulse with comparable energy was employed. Tests conducted by Phillippens, et al. [55] at the FAA Civil Aerospace Medical Institute indicated that this rectangular pulse generated occupant kinematics similar to those produced by the triangular pulse. However, for specimen tests 2-4, the triangular pulse shape was utilized.

Each of these initial tests conducted on PMHS represented a potential worst-case loading scenario and served the purpose of identifying particular loading conditions that should be taken into account when conducting further tests. These subsequent tests aimed to gather statistically significant data for the development of injury criteria, specifically in the form of risk curves.

Based on the results obtained, Humm et al. came to the conclusion that all specimens sustained spinal injuries, although variation existed by vertebral level. Cervical spine injuries were associated with the tension mechanism, while thoracolumbar spine injuries resulted from bending and tension. Fractures in the ribcage were caused by compression due to the seatbelt restraint, the presence of the armrest, and/or severe movements of the unconstrained torso. Pelvic injuries were attributed to the restraint provided by the lap belt on the accelerating torso-pelvis complex in the absence of an armrest. Leg injuries occurred as a result of the flailing mechanism.

According to the following deductions and avoiding the use of extra additional protection systems, it is proposed, for future work, that the passenger seats will have an angle of $\pm 18^{\circ}$ or less with respect to the longitudinal axis of the Flying-V.

2.2. Coordinate Systems

Research has demonstrated that the tolerance of the human body to sudden acceleration is influenced by several factors, including the magnitude and duration of the applied force, as well as the direction and rate at which it is applied. During a crash, injuries occur due to how the human body responds to the application of those forces [63]. To provide a description, both the aircraft and the seated human are assigned coordinate axes, which are arbitrarily depicted in Figure 2.3.

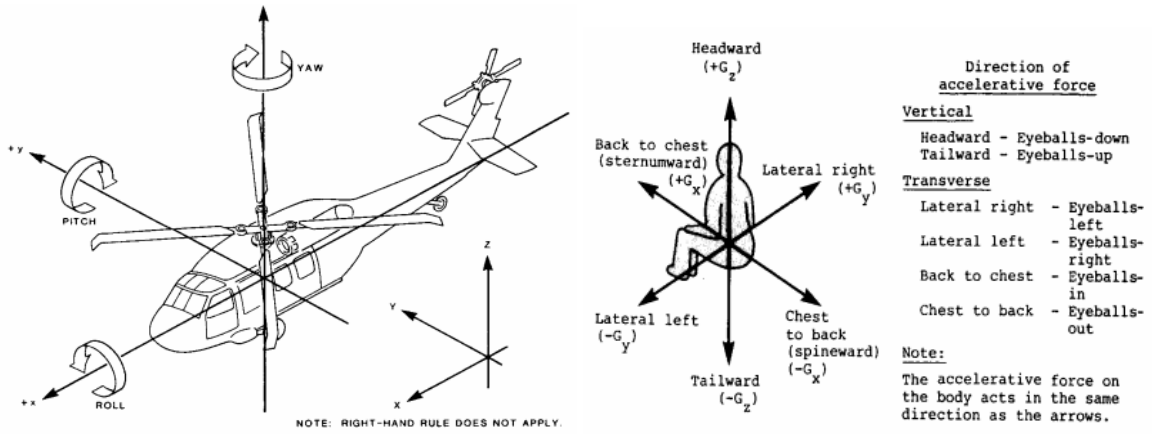

(a) Aircraft coordinates [63] **(b)** Human coordinate system [63]

Figure 2.3: Coordinate Systems

The applied force or acceleration can be described by its individual components along each of the perpendicular axes [63]. Figure 2.3b illustrates a widely used coordinate system that is applied to the seated human. The mention of the movement of the eyeballs refers to the body's inertial reaction to the applied acceleration. This reaction is in the opposite direction and equal in magnitude to the applied acceleration [63]. It is this inertial response of the body to acceleration that leads to injuries.

2.3. Human Tolerance to Impact

Although a significant number of experiments have been carried out and a considerable amount of information has been gathered, there have been limited efforts in developing and confirming useful criteria for system design [24]. This section introduces some of the criteria that are widely acknowledged for practical purposes in evaluating the crash resistance of an aircraft system. As explained in this section, these criteria can be employed to assess the suitability of an aircraft or its components, such as seats and restraint systems, by analyzing the outcomes of dynamic testing using anthropomorphic dummies or computer simulations. Only criteria with established quantitative values are presented here.

However, in the present study, the aim is to expand upon the initial crashworthiness assessment of the Flying-V aircraft, focusing on the fuselage structure. Thus, it would be inadequate to center attention on any particular body region when evaluating passenger injuries until a final design of the cabin interior, seats, and corresponding restraint system has been established. Also, no numerical model which included ATDs has been done so far and, consequently, only the most widely used and recognized injury criteria will be introduced and discussed in this section. Subsequently, two of these criteria will be applied to evaluate passenger injury in this research.

2.3.1. Whole-Body Tolerance (Eiband Curves)

In 1959, Eiband gathered the existing knowledge regarding the ability of a restrained person to withstand sudden accelerations [24]. This information was primarily derived from the studies conducted by Colonel John Stapp, who conducted experiments on human tolerance using acceleration sleds and other devices, involving both himself and his colleagues as volunteers. Eiband's compilation also incorporated experiments conducted on surrogate humans. Figure 2.4 represents the Eiband Curve for occupants having upper torso restraint when subjected to accelerations along the $+G_z$ axis. This axis corresponds to the direction of forces encountered in situations such as ejection seats or vertical crashes of helicopters.

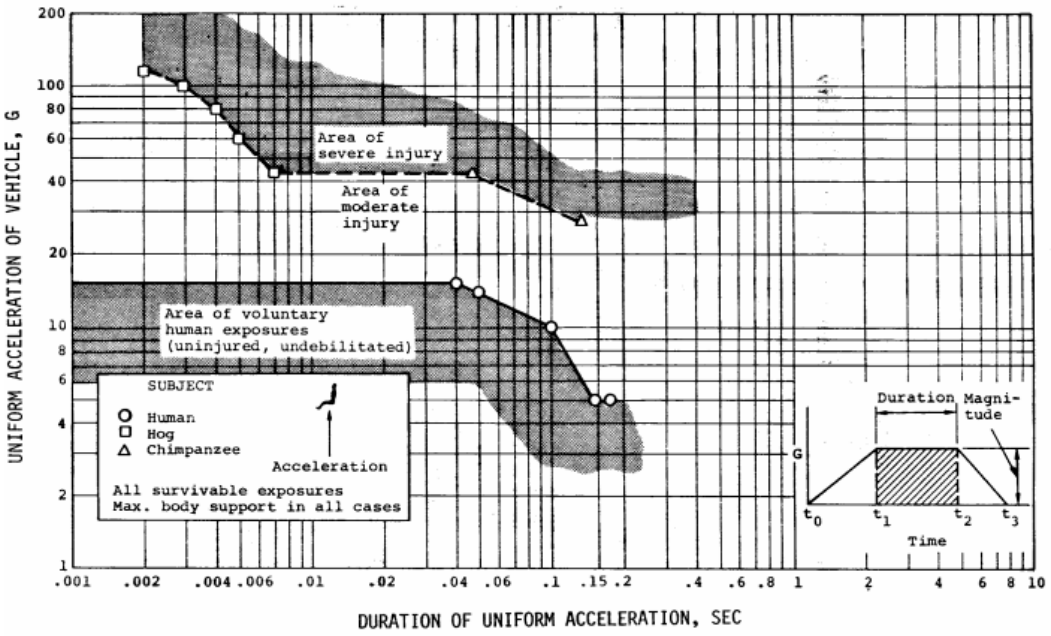

Figure 2.4: Eiband Curve for $+G_Z$ [63]

The graph demonstrates that individuals can tolerate accelerations of up to approximately 18 G without experiencing any injuries. Furthermore, spinal injury is not observed at accelerations below approximately 20-25 G.

Comparable curves are accessible for the remaining axes. A summary of estimated human tolerance in all axes is presented in Table 2.3.

Table 2.3: Human Tolerance Limits (0.10 second time duration of crash pulse; full restraint [63])

Direction of Accelerative Force	Occupant's Inertial Response	Tolerance Level
Headward (+Gz)	Eyeballs Down	$20-25$G
Tailward (-Gz)	Eyeballs Up	15G
Lateral Right $(+$Gy$)$	Eyeballs Left	20G
Lateral Left (-Gy)	Eyeballs Right	20G
Back to Chest $(+$Gx$)$	Eyeballs Out	45G
Chest to Back $(-$Gx$)$	Eyeballs In	45G

For Army aircraft, a personnel restraint system that is deemed acceptable should incorporate upper torso restraint, regardless of the orientation of the seat. However, in situations where enhanced comfort is prioritized, such as in commercial airplanes, a lap belt alone is typically employed as the passenger restraint system. In such cases, it is advisable to adhere to a human tolerance level of 20 G in the spineward (-Gx) direction and 10 G laterally (G) when using lap-belt-only restraints. These levels are derived from experiments conducted with human subjects who experienced minor injuries [74].

Another drawback of utilizing Eiband diagrams is their lack of sensitivity to diverse acceleration pulse shapes.

Furthermore, while the tolerance levels presented in Figure 2.4 provide information about acceptable regions of acceleration and rate of onset within the aircraft interior, they do not enable a comprehensive assessment of protective systems like restraint systems, energy-absorbing seats, or protective padding. To address questions regarding the adequacy of seat stroking distance or the acceptability of shoulder belt webbing stiffness, injury criteria for critical body parts such as the head and spinal column must be employed [24].

2.3.2. Head Injury Criteria

Protection against severe injuries is necessary in areas where head impacts can occur [33]. To that extent, the evaluation of head injury risk can be conducted using the Head Injury Criterion (HIC). Developed by Versace as an alternative interpretation of the Wayne State University Tolerance Curve (that relates effective acceleration with its time duration) [24], this criteria was first incorporated into the Federal Motor Vehicle Safety Standard 208 (FMVSS 208) as a specification for head impact tolerance [24].

The HIC is calculated by:

$$HIC = \left\{ (t_2 - t_1) \left[\frac{1}{(t_2 - t_1)} \int_{t_1}^{t_2} a(t)dt \right]^{2.5} \right\}_{\max} \tag{2.1}$$

where t_1 and t_2 represent the initial and final times at which the HIC reaches its maximum value, while a(t) denotes the resultant acceleration (measured in G) at the center of gravity of the head [62].

In 1985, Prasad and Mertz [58] analyzed test data collected from human surrogates to establish the correlation between the HIC and injuries to the skull and brain. The results are shown in Figure 2.5.

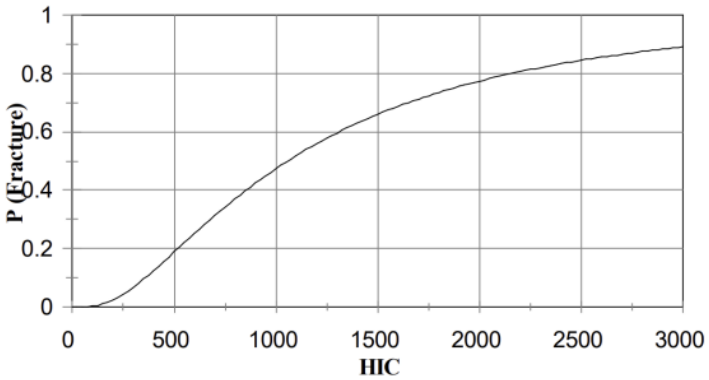

Figure 2.5: Head injury risk probability vs. HIC value [58]

While the effectiveness of the HIC in accurately predicting actual injuries may not be as successful as desired, it remains one of the most widely utilized criteria for assessing head injury protection [24].

2.3.3. Dynamic Response Index (DRI) and Severity Index (SEV)

In conformity with CS-25.562(c) a series of performance parameters need to be satisfied. Worthy to mention is the previously seen head injury criterion (should not exceed 1000 points) and the maximum allowable compressive load between the pelvis and the lumbar column (should be limited to 1500 lbs). The main challenge with this particular method of means of compliance is the necessity to incorporate a seat model and an anthropomorphic dummy during a numerical simulation to acquire significant findings.

To overcome this issue, various mathematical models have been developed for prediction of spinal response, especially in the +Gz loading. A clear cause of injury is the pressure exerted on the vertebrae due to inertia, leading to compression fractures. Consequently, the initial models focused on one-dimensional spring-mass systems, assuming that the vertebral body carries the entire load.

A widely utilized model is the dynamic response index (DRI) [24]. It is a well-established crash injury criterion, already used as alternative means of compliance for CS-25.562 and it is the injury criterion used in Desiderio's studies.

Since the 1970s, the Dynamic Response Index has been employed by the US Air Force (USAF) as a technique to estimate the likelihood of spinal injuries in pilots who experience high-amplitude and short-duration accelerations caused by ejection seats [18].

From a physical standpoint, the calculation of the DRI involves mathematically representing the human body using an analogous mechanical model that includes lumped parameters such as mass, spring, and damper [46]. Figure 2.6 depicts such model and its variables.

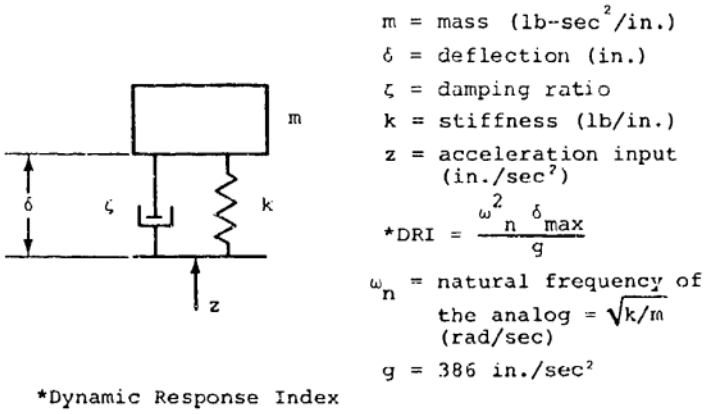

Figure 2.6: Spinal injury model [65]

The DRI is derived from the following differential equation [24]:

$$\frac{d^2\delta}{dt^2} + 2\zeta\omega_n\frac{d\delta}{dt} + \omega_n^2\delta = \frac{d^2z}{dt^2} \tag{2.2}$$

and it is defined as the third term in the equation, which involves the spinal deformation, δ, divided by the gravitational acceleration, g:

$$DRI = \frac{w_n^2\delta_{\text{max}}}{g} \tag{2.3}$$

In the study conducted by Stech and Pain [65], they examined the 50th percentile of USAF pilots at that time and determined that the values of ω_n were 52.9 rad/s, and ζ was 0.224. The spring stiffness for the model was determined from tests of human cadaver vertebral segments [24].

A thorough analysis was carried out by Brinkley and Shaffer [18] to assess the level of correlation between the spinal injury model and injuries occurring in ejection seats of operational aircraft. Figure 2.7 illustrates the connection between the acceleration environments experienced during operations and the actual rates of spinal injuries.

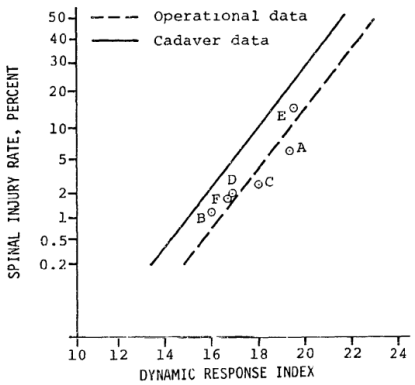

Aircraft type	Nonfatal ejections
A*	64
B*	62
C	65
D*	89
E	33
F	48

*Denotes rocket catapult

Figure 2.7: Probability of spinal injury estimated from laboratory data compared to operational experience [18]

The model's response is measured in DRI values. The data reveals that the likelihood of injury does vary depending on the DRI, but the cadaver data indicates a higher probability of injury compared to the operational data. This outcome can be expected since the intact vertebral column embedded in a living torso is likely to be stronger than segments from cadavers [24]. To account for other accelerations rather than the vertical, the Air Force has implemented a system that combines acceleration components and the DRI to determine the acceptable acceleration environments for ejection seats. This system is outlined in Specification MIL-S-9479 [46], where the levels of acceleration experienced by the occupant of the seat are regulated based on factors such as acceleration, time, and DRI. Given the complexity of injury assessment, this more sophisticated criterion will be known as Severity Index (SEV) and will be employed in subsequent analyses, together with the DRI. The SEV is determined by the following expression:

$$SEV = \left(\frac{\text{DRI}}{DRI_L}\right)^2 + \left(\frac{G_x}{G_{xL}}\right)^2 + \left(\frac{G_y}{G_{yL}}\right)^2 \tag{2.4}$$

Here G_x and G_y represent the magnitudes of acceleration along the x and y axes respectively, which are derived using the methodology explained in Appendix B. This technique is used to determine the acceleration time history for each axis.

G_{xL} is the limit value for the x axis (fore and aft) of figures B.3, B.4, and B.5 in Appendix B. G_{yL} is the limit value for the y axis (sideways) of figure B.6, also in Appendix B.

DRI is the dynamic response index value computed from Equation 2.3 for the positive z direction. DRI_L is the limit value of the DRI and its value is set to 16 units. Regulatory bodies have already deemed a DRI value below 16 as an acceptable means of compliance for crashworthiness.

The calculated value from Equation 2.4 should not surpass one, otherwise the passengers will sustain injuries.

Lastly, when there are acceleration components present in the $-G_z$ direction, the equation should be solved using $\frac{-G_z}{-G_{zL}}$ in place of $\frac{\text{DRI}}{DRI_L}$ where:

- $-G_z$ is the -z direction;
- $-G_{zL}$ is the limit value for the -z direction of figures B.7 and B.8 in Appendix B.

The DRI has proven to be effective in predicting the potential for spinal injury in situations involving $+G_z$ acceleration environments in ejection seats [24]. However, it is important to recognize that the DRI is a simplified model of a complex dynamic system, and the correlations established are specifically for acceleration-time profiles associated with ejection seats, which can differ from those experienced during crashes. In particular, the rate of acceleration onset in crashes can be significantly higher, sometimes by an order of magnitude, compared to ejection seat pulses.

Additionally, the position of the spine at the moment of impact can significantly impact the vulnerability to vertebral damage. Consequently, a passenger who is leaning forward in their seat would likely react differently from an upright occupant in a well-restrained ejection seat, potentially exhibiting lower tolerance to impact [24]. Another concern is that the currently used coefficients for the DRI are based on data from USAF pilots from about 50 years ago, specifically the 50th percentile. This poses a significant issue considering that the physical characteristics of the average passenger differ significantly from those of fighter jet pilots. Despite these concerns, regulators already accept a DRI value lower than 16 as a satisfactory measure for crashworthiness. The accumulated experience thus far indicates that such a DRI threshold is adequate, regardless of the methodology used to determine the coefficients and the DRI itself.

3

Proposed Crashworthiness Requirements for the Flying-V

Unlike traditional aircraft with cylindrical fuselages and wings, the Flying-V integrates the lifting surface and fuselage into a single integrated structure. Its cabin also presents a significant eccentricity, posing a design challenge in terms of ensuring crashworthiness.

In contrast, conventional aircraft with full-metal fuselages also have a generous crumple zone below the passenger seating area that offers substantial protection to passengers, and the available space for the Flying-V aircraft is more limited.

Furthermore, the Flying-V's innovative design lacks a well-established operational history for this unique aircraft concept. Its distinct feature of offering notably greater seat rotation compared to a vertical plane containing its center line also complicates alignment with standard regulations for conventional aircraft.

Consequently, it's likely that the crashworthiness standards necessary for its certification will be more stringent than those currently in place.

As a response to these challenges, the discussion herein will try to propose crashworthiness requirements for the Flying-V aircraft, having has foundation the already well established regulatory requirements for conventional aircrafts. In Section 3.1, potential velocities and angles for the emergency landing of the Flying-V aircraft are suggested. Ultimately, Section 3.2 outlines the conclusive crashworthiness requirements that will be employed in this study to further evaluate the crashworthiness of the Flying-V and to test the simplified modelling techniques later proposed in Chapter 5.

3.1. Flying-V: Impact Velocity & Attitude Considered for Crashworthiness Analysis

The impact velocity considered for crashworthiness analysis is typically determined based on factors such as:

- Emergency landing scenarios: The impact velocity may be based on emergency landing conditions, such as touchdown speeds or descent rates, which can vary depending on the specific circumstances;
- Certification requirements: Regulatory bodies specify the impact conditions that aircraft must demonstrate compliance with during certification. These requirements may include specific impact velocities or conditions to evaluate crashworthiness;
- Structural limitations: The impact velocity should be within the structural capabilities of the aircraft. The aircraft's design, materials, and structural integrity will influence the acceptable impact velocities for crashworthiness analysis;
- Historical data and safety assessments: Analysis of previous incidents or accidents can inform the determination of acceptable impact velocities. Safety assessments and risk analyses play a

crucial role in establishing appropriate criteria. Certainly, such data is currently unavailable for the Flying-V. However, charts resembling the one illustrated in Figure 3.1 offer a solid foundation for conducting analysis.

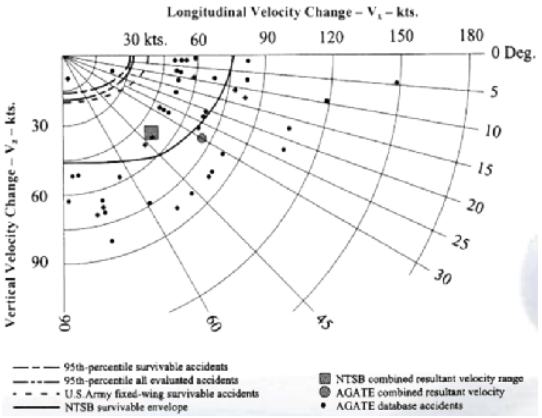

Figure 3.1: An example of historical crash data [30]

It's important to note that the determination of an acceptable impact velocity for crashworthiness analysis is a complex process that involves various stakeholders, including aircraft manufacturers, regulatory authorities, and safety experts. These entities collaborate to ensure that the crashworthiness requirements are robust, considering the safety of passengers and crew in the event of an emergency landing or impact.

The absence of data concerning these aspects for the FV limits the scope of the analysis; however, a few propositions will still be put forward.

3.1.1. Flying-V's Impact Velocity

One of the main sub-question regarding the crashwothiness of the Flying-V is the landing velocity that one should consider in case of an emergency landing.

This is one of the gaps in legislation even for conventional transport aircrafts and is already acknowledged by TACDWG, established by the Aviation Rulemaking Advisory Committee (ARAC), with the purpose of providing recommendations pertaining to new airframe-level crashworthiness and ditching standards [26, 27]. These recommendations are intended for inclusion in CS-25 and other relevant advisory materials [9]. The members of TACDWG comprise industry experts (including Boeing, Airbus, Embraer, and others) and representatives from research institutions (such as NASA and the German Aerospace Center - DLR).

Although the final report was submitted to ARAC in October 2018, as of the present time, the implementation of these recommendations into CS-25 and similar regulations is still pending [9].

Nonetheless, vertical drop tests have been regarded has one of the main experimental tests to evaluate the crashworthiness of conventional aircraft design.

Back in 2007, the FAA issued special conditions for the Boeing Model 787-8 airplane [59]. This aircraft was going to incorporate innovative or unconventional design aspects when compared to the state of technology outlined in the airworthiness standards for transport category airplanes. These unique design elements pertained to the incorporation of carbon fiber reinforced plastic in the fuselage construction. Given these distinctive design attributes, the existing airworthiness regulations lacked sufficient or suitable safety standards pertaining to impact response characteristics to ensure a crashworthy survivability. To that extent, FAA introduced special conditions that encompassed supplementary safety standards that the administrator deemed essential to establish a safety level comparable to the standards already in place.

Both the FAA and the aviation industry have gathered substantial experimental data, along with information from actual crashes involving transport category aircraft.

These data sets demonstrate a notable rate of occupant survival when subjected to vertical descent velocities of up to 30 ft/sec.

Based on this information, the FAA finds it appropriate and necessary for an assessment of the crashworthiness to span a range of airplane vertical descent speeds up to 30 ft/sec [59]. Also, according to the FAA [59], if there are significant differences in the impact characteristics of the 787 compared to a previously approved large aircrafts, it will be necessary to adhere to higher load factors than those specified in 14 CFR 25.561. These increased load factors will be required to ensure the same level of safety for the occupants, in terms of retention of items of mass [59]. In the case of acceleration and loads experienced by the passengers, means must be integrated to reduce the load levels experienced by these passengers to meet the injury standards outlined in CFR 25.562. Alternatively, the load levels could be adjusted to match those of a previously certified similar aircraft, all to uphold the same level of passenger safety.

Following the same line of thought and by working with Original Equipment Manufacturers (OEMs), TACDWG also concluded that almost all of the considered aircraft that fall under the CS-25 regulations possess the capability to safeguard passengers within a vertical impact velocity range of 20 to 30 ft/s, depending on the aircraft's size [9]. A prevailing pattern is noted, where wide-body aircraft from the same manufacturer demonstrate an ability to endure higher speed impacts. This is probably attributed to the presence of a larger deformation area, which aids in diminishing the forces transferred to the occupants [26]. To that extent, the proposed vertical impact velocity requirement by TACDWG becomes a function of the aircraft's Maximum Take-Off Weight (MTOW), as depicted in Figure 3.2. In his examination of the Flying-V family design, Oosterom [52] estimated the Flying-V's MTOW to span from 207 tons (456,000 lbs) for the FV-800 variant to 278 tons (613,000 lbs) for the FV-1000 model. This variance in MTOWs is also visually indicated in Figure 3.2, represented by the red hatched pattern.

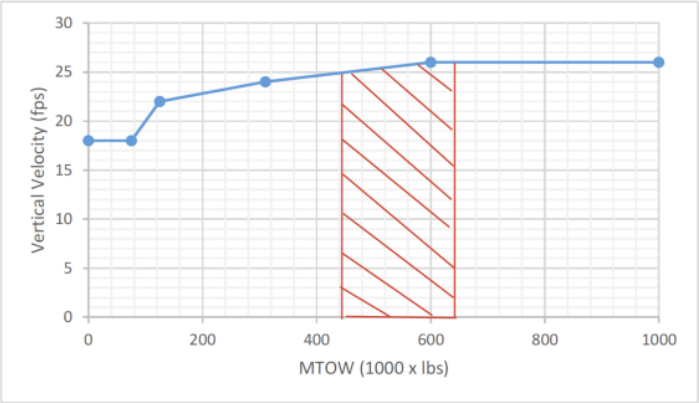

Figure 3.2: Vertical impact velocity requirement vs. MTOW, adapted from TACDWG [9]. The hatched pattern was created by Desiderio [26] and indicates the estimated range of MTOW for the Flying-V family, as determined by Oosterom [52]

Certainly, one of the primary benefits of having an aircraft family lies in the potential to relatively easily extend the fuselage without extensive alterations to the geometry [52]. As a result, the standard cross-section of the Flying-V must attain certification for the most rigorous loading scenario, which in this specific instance corresponds to the FV-1000 setup. For the MTOW of the FV-1000, TACDWG proposes a vertical impact velocity of 26 ft/s. Consequently, this was the stipulated requirement for vertical impact velocity used by Desiderio [26], and it will also be the vertical velocity to be met in the scope of this research.

Interesting information about the vertical velocity can also be extracted from the FAA document DOT/FAA/CT-TN90/23 [64], a research paper written by Soltis that provides an overview of the reasoning employed to establish crash impact attributes for a variety of aircraft sizes, with a focus on formulating standards for the dynamic performance of seats suitable for commuter-category-sized aircraft. Instead of plotting the vertical velocity over the MTOW, Soltis [64] proposed to replace the MTOW with the distance between the aircraft floor and the lower mold line of the aircraft. This distance, which is the available structural depth or vertical impact stopping distance, sets a tangible boundary that would be employed to delineate the crash impact attributes across various aircraft sizes. This adjustment aligns well with the crashworthiness analysis of the Flying-V, as its elliptical fuselage entails less crushing distance, effectively minimizing the proposed vertical velocity for certification.

The vertical impact velocity information extracted from [64] is illustrated in Figure 3.3. The graph portraying vertical impact velocity against crush depth was deduced by combining accident data with drop tests conducted on fuselage segments of transport aircraft. The vertical impact velocity at the airframe level was determined by TACDWG by deducting the energy absorption contribution of the landing gears, which amounted to 12 ft/sec, from the overall vertical impact velocity of the aircraft.

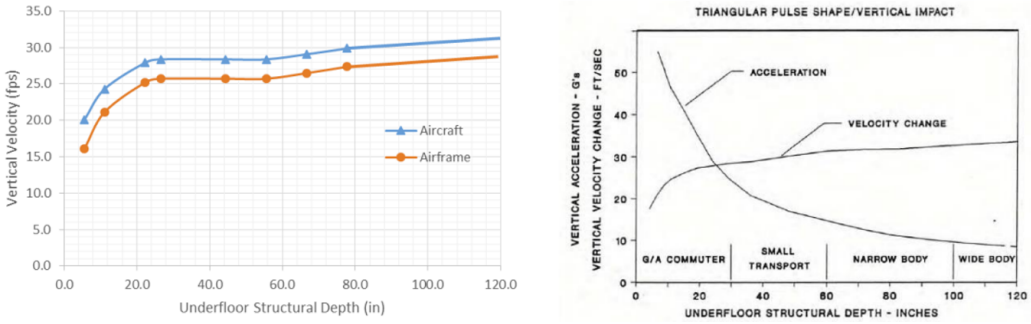

Figure 3.3: Part 25 Aircraft Vertical Impact Velocity based on Subfloor Depth [9, 64]

Nonetheless, the proposed velocity of 26 ft/s remains the same for a wide range of underfloor depth, in which the Flying-V is included (24 in to 68 in, as depicted in Figure 3.3).

During the literature review phase, prior studies also explored the incorporation of a horizontal component of velocity, as depicted in Figure C.2.

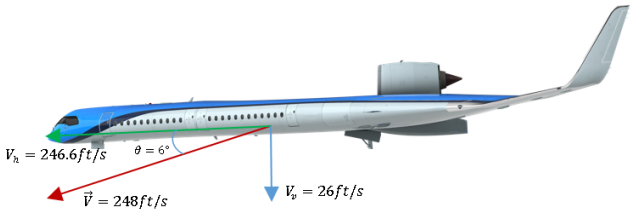

Figure 3.4: Lateral view of the FV with the velocity vector used [25]

The literature revealed valuable findings and conclusions endorsing this approach. Unfortunately, due to time constraints, the initial idea had to be abandoned and only the vertical impact velocity will be considered to further assess the crashworthiness of the Flying-V. However, readers curious about the rationale behind calculating the horizontal velocity component can refer to Appendix C for further insight.

3.1.2. Possible Flying-V's Approach Attitude

An additional factor that should be taken into account for crash scenarios is the aircraft's orientation upon impact. In the event of an emergency landing, the primary objective remains the safety of passengers and crew, prompting the pilot to execute necessary maneuvers for aircraft control and impact force reduction. These maneuvers could encompass adjusting the pitch, roll, and yaw angles to sustain control, stabilize the aircraft, and align it with the landing surface [9].

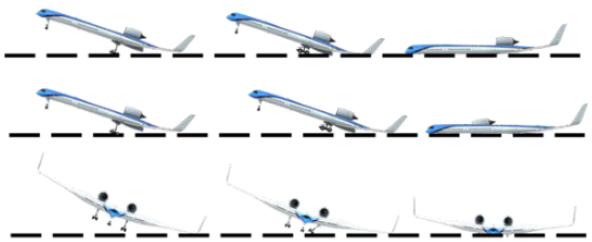

Figure 3.5: Possible crash sequences for the Flying-V

However, there exist no fixed predetermined angles for such landings, given the considerable variability driven by elements like available landing space, wind conditions, aircraft model, and the pilot's expertise and judgment.

In accordance with TACDWG [9], the majority of part 25 aircraft exhibit limited tolerance for minor roll or pitch deviations before the fundamental dynamics of the event undergo notable alterations. A collision with a wingtip can trigger an unpredictable tumbling motion of the airplane, as exemplified by incidents like the Asiana 777 in San Francisco and the United DC-10 in Sioux City [9]. Striking the nose or tail first results in a combination of vertical and longitudinal accelerations, with designs being more sensitive to the vertical component. While yaw can be taken into consideration, its impact on the loading of the fuselage structure is relatively negligible [9]. The greater concern with yaw pertains to the lateral velocity's influence on passengers and the behavior of seats in such conditions, a matter of heightened importance when considering the Flying-V design.

The Aircraft Crash Survival Design Guide [24] and the Army's military standard MIL-STD-1290, "Light Fixed- and Rotary-Wing Aircraft Crash Resistance" [2] provide some information on impact angles and attitudes to be employed by aircraft designers to ensure that structures meet crash-resistance requirements. These standards for the development of new aircraft were initially validated through the use of actual crash data and engineering test results. The main source of these data is primarily derived from both Fixed- and Rotary-Wing Aircraft with light characteristics. However, the outcomes they present can be used as a reference point for understanding the crash behavior of the Flying-V.

Figure D.1 in Appendix D, show the aircraft impact attitudes envelopes for different pitch, roll and yaw angles. MIL-STD-1290 [2] outlines a comprehensive set of pitch and roll angles that should be taken into account by designers. When dealing with vertical impacts, Figure D.1A illustrates that pitch can vary from +15° to -5°, and roll can vary from +10° to -10°. Nevertheless, when pitch and roll are combined, there are limitations on the extremes, as indicated in the Figure. For instance, designers are not required to consider scenarios such as +15° pitch combined with +10° roll, due to their lower likelihood and the significant weight penalties on the fuselage associated with extreme pitch and roll combinations [24]. Although MIL-STD-1290 doesn't prescribe specific angles for off-axis orientations in longitudinal and lateral impacts, MIL-STD-1290 [2] advises to consider impact attitude ranges during the design phase to ensure survivability in such situations involving pitch, yaw, or roll. Figures D.1B and D.1C display recommended impact attitude ranges for longitudinal and lateral impacts, respectively.

Yaw and Roll Angles

Torenbeek [68] infered that variations of $\pm 10°$ yaw angles can be observed in modern transport aircraft's attitude during approach landing. Oosterom [52] also came to the conclusion that during landing in maximum crosswind conditions, the required rudder deflection of the Flying-V should not exceed 20 degrees, leading more or less to a yaw angle of $\pm 20°$.

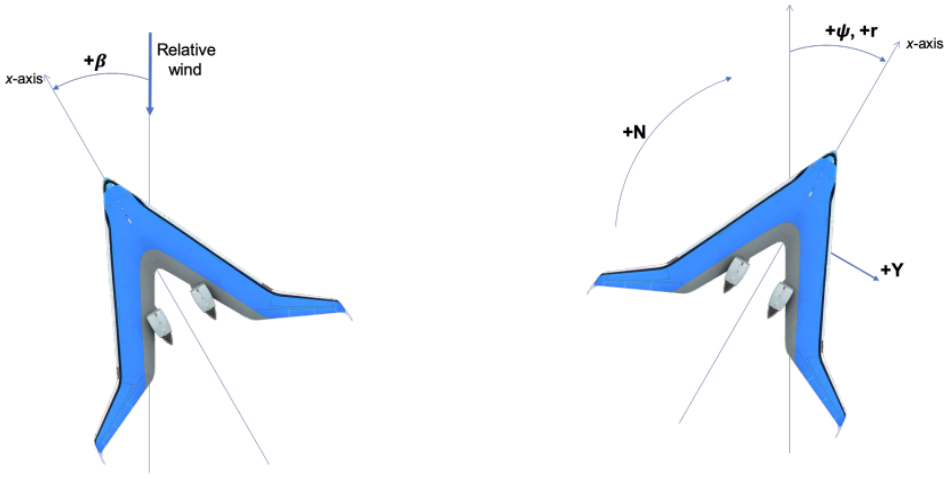

(a) Sideslip angle (β) convention

(b) Yaw angle (ψ) and yawing moment (N) conventions

Figure 3.6: Yaw angles and their conventions. The yaw rate (r) and and side force (Y) conventions are also depicted in the right image [35]

Regarding roll angles, Torenbeek presumed that the optimal angle for transport airplanes is 8°. Van Oene [51] and Bourget [16] also opted for this particular angle to be attained by the Flying-V.

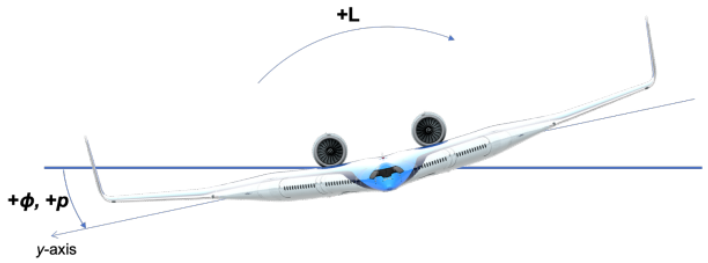

Figure 3.7: Bank angle (ϕ), rolling moment (L), and roll rate (p) convention, viewed from nose [35]

However, for a more comprehensive evaluation of the Flying-V's crashworthiness and potential passenger injuries, a fixed roll angle won't be assumed. Instead, the initial assessment will focus on a reduced section of the Flying-V, spanning roll angles from 0° to 15° in 5° increments without considering any yaw.

It is worth noting that in real crash scenarios, the Flying-V's cross section exhibits a yaw angle of 25.5° with respect to the flight direction (see Figure 3.8). Nonetheless, constrained by time limitations and the complexity of simulations, the evaluation will only include drop tests incorporating vertical velocity, coupled with roll and later pitch angles. In these scenarios, consideration will be given to the induced longitudinal and lateral velocities resulting from the section's rotation, with the natural yaw of the Flying-V not being taken into account.

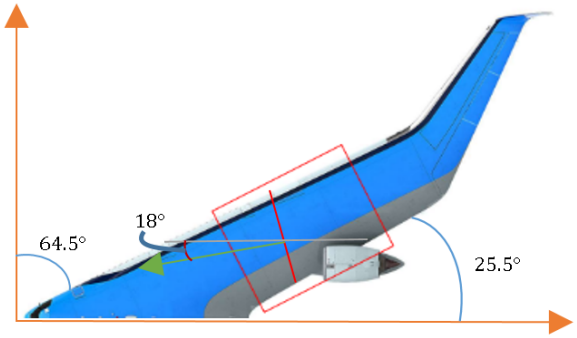

Figure 3.8: The red box indicates an approximation of the FV's fuselage section being investigated and possible passenger seats orientation [25]

Pitch Angle

According to Torenbeek [68], for jet aircraft, the highest pitch angle encountered during landing typically falls within the range of 12° to 14°, which is generally smaller than that observed during takeoff. This discrepancy can be attributed to the extension of flaps during landing, resulting in a reduced critical angle of attack for the wing by a few degrees compared to the takeoff configuration.

However, the Flying-V, as noted by Nikki [43] and Bourget [16], does not feature high lift devices, meaning that the maximum lift coefficient remains constant for both takeoff and landing phases.

In the investigation conducted by Bourget [16] regarding the takeoff and landing angles of the Flying-V in relation to gear design, the curves in Figure 3.9 were computed. The wind tunnel outcomes utilized for calculating the curves were approximated using the more convenient polynomial model developed by Ruiz-Garcia [31].

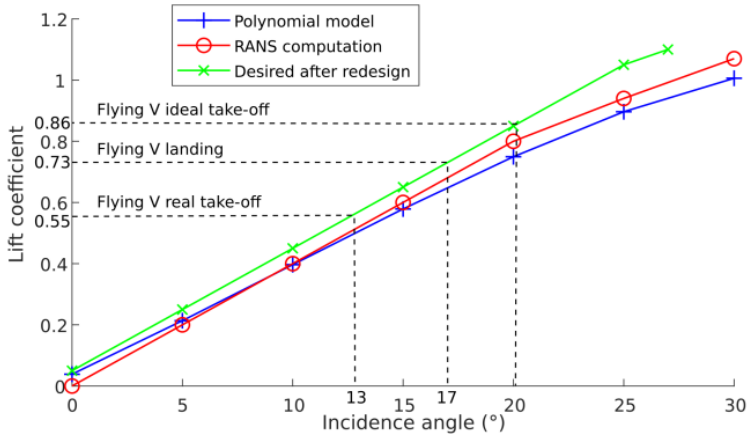

Figure 3.9: Experimental lift curves of the Flying V sub-scaled model [31, 53] superimposed with desired lift curve, out of ground effect [16]

From Equations 3.1, the maximum lift coefficient for landing is 0.73, providing a landing incidences of 17°.

$$C_{\text{L,ldg}} = \frac{C_{\text{L,max}}}{1.18^2} \tag{3.1}$$

Finally, in order to analyze the necessary view-field during landing for the Flying-V, Pluijm [56] employed the angle of attack value of $\alpha = 17°$ calculated by Bourget [16]. This implies that a pitch angle of $\theta = 14.5°$ is required if a glide slope of 2.5° [68] is attained.

An illustration depicting a possible landing approach of the Flying-V is provided in Figure 3.10.

Again, to offer a more thorough understanding evaluation of the Flying-V's crashworthiness and facilitate future validation of potential reduced modelling techniques, a constant pitch angle will not be presumed. Alternatively, pitch angles ranging from 0 to 15 degrees with 5-degree increments will be incorporated. The effects of introducing roll and pitch angles will be analyzed separately in the current study, and the assessment of crashworthiness considering both combined effects will be left as a recommendation for future work.

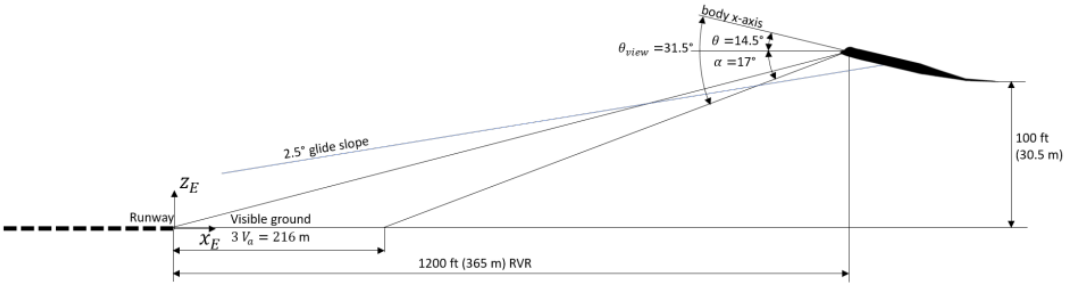

Figure 3.10: : Required view angle at the pilot seat during landing [16]

3.2. Final FV Crashworthiness Requirements for the Current Work

Following the review of existing and potential future crashworthiness regulations by airworthiness authorities and the formulation of general requirements to assess the crashworthiness of the Flying-V, a formal set of criteria for the outcomes of this research can be delineated. Building on prior work, the crashworthiness characteristics of proposed sections of the Flying-V aircraft will be initially evaluated through drop tests, employing a minimum vertical impact velocity of 26 ft/s, with the fuselage centerline in a horizontal orientation. Whereas previous studies considered an equivalent DRI not greater than 16 units to make the Flying-V section crashworthy, the analysis will encompass a spatial examination of Dynamic Response Index distributions along the analyzed sections, incorporating the Severity Index to address injuries in directions other than the vertical.

The current objective is not to optimize the design to minimize injury criteria but to explore how various modelling approaches and crash scenarios influence spatial injury patterns among passengers. Accordingly, a DRI and SEV above 16 and 1, respectively, will be considered hazardous, with greater danger associated with higher values. Conversely, values below 16 and 1 for DRI and SEV, respectively, will be deemed safe.

Subsequently, the introduction of roll angles and pitch angles, ranging from 5 to 15 degrees in 5-degree increments, will be integrated to scrutinize the simplified modelling techniques introduced in Chapter 5 and enhance the understanding of the Flying-V's crashworthiness.

In the scope of this research, it's imperative to note that the cabin interior will not be taken into consideration. Also, ATDs models would provide a better understanding of the passenger behaviour and injury risk during emergency landings, but due to time constraints and following the previous method used by Desiderio, the dummies weren't modelled. The consideration of forward velocity combined with the crash attitude seen in Figure 3.10 is postponed for future studies due to the absence of FEM representation for the entire Flying-V aircraft. Furthermore, the initial plan to investigate passenger seat orientation and its impact on side loads and potential injuries had to be abandoned because of time limitations.

4

Crashworthiness Behavior of Conventional Aircraft Designs at Different Impact Angles

The significance of crashworthiness design and certification for civil transport aircraft lies in enhancing aviation safety by improving the crashworthy performance of aircraft fuselage structures, cabin layout, and internal facilities [6, 75]. Aircraft crashes occur in diverse and complex environments with varying crash postures, making a comprehensive evaluation of fuselage section crashworthiness contingent upon analyzing structural responses under various crash conditions [19].

Conventional aircraft designs have been rigorously tested and refined to ensure their resilience in the face of various collision scenarios, but the emergence of novel aircraft concepts demands a fresh perspective on crashworthiness evaluation.

The Flying-V's groundbreaking layout presents an intriguing opportunity to rethink crashworthiness strategies. As this innovative design challenges traditional norms, it becomes imperative to explore how the crashworthiness behavior of conventional aircraft, when subjected to impacts at different angles, can inform and guide the crashworthiness considerations for the Flying-V.

With that being said, this Chapter focus on the response of conventional aircraft designs to impacts at varying angles (Section 4.1 and Section 4.2). As the investigation into crashworthiness within conventional aircraft progresses, connections to the Flying-V design naturally become apparent. By deriving knowledge from analyses of crashworthiness in conventional aircraft, the groundwork is established for the preliminary creation of a framework dedicated to assessing and enhancing the crashworthiness capabilities of the Flying-V, in Section 4.3.

4.1. Impact of Roll Angles on Civil Aircraft Fuselage Crashworthiness

While previous experimental and simulation analyses primarily concentrated on the vertical impact crashworthiness of fuselage sections, the aircraft crash itself doesn't not involve a straightforward vertical descent; instead, it typically occurs with different degrees of rolling inclination [47]. By 1997, NASA Langley Research Center had designed a scaled-down model, one-fifth the size of a light aircraft fuselage section, and performed drop experiments and simulation investigations for roll angles of 0 degrees and 15 degrees [37]. The research program aimed to reduce impact forces transferred to occupants and uphold the structural integrity of the fuselage to ensure a safe minimum space, although the impact of roll angle on the crashworthiness of the fuselage section wasn't explored [38]. The current experimental and simulation investigations predominantly concentrated on assessing the crash resistance of fuselage sections exposed to vertical impacts, paying limited attention to the implications of roll angle on the crashworthiness of civil aircraft fuselage sections.

Nonetheless, an investigation delved into NTSB (National Transportation Safety Board) accident reports covering the period from 1999 to 2011, extracting data concerning aircraft accidents that encompassed different roll angles from a total of 26 accident [47].

The incidents were categorized based on the extent of roll angle, and the resultant aviation accidents and occupant injuries were tabulated in Table 4.1 [47]. Notably, aircraft predominantly crashed with roll angles ranging from -30 degrees to 30 degrees, constituting 17 instances or 65.4% of the total accidents. In cases where roll angles exceeded 30 degrees, there were 9 accidents, accounting for 34.6% of the total, with only one instance of survival. Higher roll angles during impact corresponded to reduced occupant survivability, whereas lower roll angles were associated with higher survivability rates.

Table 4.1: Injuries chart [47] (Note: Roll to left is negative, roll to right is positive)

Roll Angle	Number of Accidents	Fatal	Serious	Minor	None
$x < -90$	0	/	/	/	/
$-90 \leq x < -60$	2	281	0	0	0
$-60 \leq x < -30$	1	8	0	0	0
$-30 \leq x < 0$	5	137	6	102	57
$x = 0$	7	300	33	3	124
$0 < x \leq 30$	5	80	11	60	74
$30 < x \leq 60$	0	/	/	/	/
$60 < x \leq 90$	3	5	3	5	0
$x > 90$	3	104	0	0	0
Total	26	915	53	170	255

To investigate the crashworthy performance of fuselage sections under varying roll angle impact conditions, Mou et al. [47] conducted a study employing the nonlinear finite element code LS-DYNA. A comprehensive 3-dimensional finite element model of a five-frame fuselage section equipped with waved-plates beneath the cargo floor was developed (Figure 4.1).

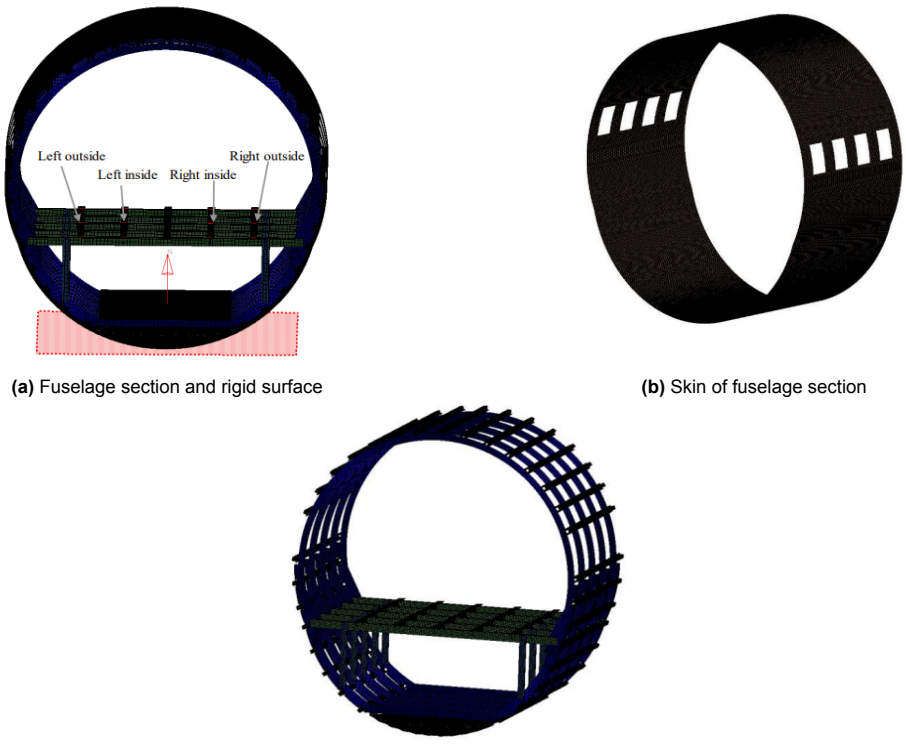

(a) Fuselage section and rigid surface

(b) Skin of fuselage section

(c) Main frame of fuselage section

Figure 4.1: Finite element model of fuselage section [47]

The occupant-seat arrangement was regarded as a concentrated mass distributed across the cabin floor.

Within the fuselage section, 12 distinct masses were accounted for by Mou et al., with each mass set at 88 kg as per the specifications of Federal Airworthiness Regulation 25.562(b). Through this model, the failure modes, acceleration responses, and energy absorption of the fuselage section at roll angles of 0 degrees, 5 degrees, 10 degrees, and 15 degrees were assessed.

4.1.1. Finite Element Model Simulation Results and Discussion

Failure Modes

Mou et al. [47] acquired a comprehensive understanding of the failure modes of the aircraft's subfloor structures, proving valuable for the crashworthiness design of civil aircraft. The examination of failure modes performed by Mou et al. for fuselage sections at 100 ms, under various conditions, is presented in Figure H.1.

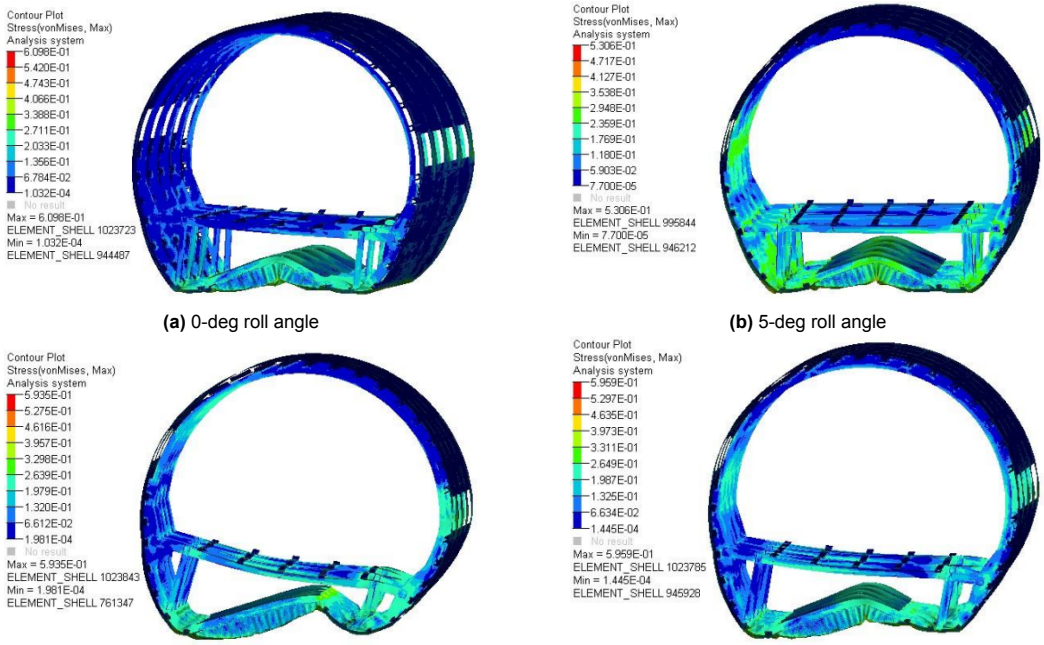

(a) 0-deg roll angle **(b)** 5-deg roll angle

(c) 10-deg roll angle **(d)** 15-deg roll angle

Figure 4.2: Deformation and stress cloud of fuselage section at 100 ms [47]

Upon comparing the displayed figures, Mou et al. observed that distinct failure modes and stress distributions emerge within fuselage sections. When fuselage sections collide with rigid ground at roll angles of 0 degrees, 5 degrees, and 10 degrees, heightened initial in-plane loads result in the fracturing and displacement of fuselage frames and skin toward the cabin floor. During these instances, the waved-plates also undergo bending and deformation. The fractured frames manifest three plastic hinges, while the triangular region formed by fuselage frames, floor beams, and oblique struts features plastic hinges on both sides [47]. Positioned at the bottom of the fuselage frame, the third plastic hinge is perceptible. Importantly, the post-crash survival space for occupants remains at least 85% of the original volume. As the fuselage section inclines rightward with increasing right roll angles, the waved-plates bend and shift to an offset right position, amplifying the severity of deformation in right oblique struts. When subjected to a 15-degree roll angle crash, minimal bending is observable in the waved-plates, and three plastic hinges reappear within the frames, with the fuselage section undergoing pronounced rightward tilting [47].

Mou et al. also highlighted that the deformation of waved-plates leads to a reduction in energy absorbed, primarily due to the decrease in effective energy-absorbing areas as roll angles increase.

Acceleration Responses

The acceleration profile is a pivotal factor in ensuring occupants' safety and can be evaluated by assessing the acceleration at the seat-floor junctions. Given the fuselage section's symmetry, Mou et al.'s [47] study focused on acceleration responses for seats on the right outside and left outside. A sampling frequency of 100 Hz was applied. As depicted in Figure 4.3, acceleration responses for fuselage sections with various roll angles — namely, 0 degrees, 5 degrees, 10 degrees, and 15 degrees — were presented.

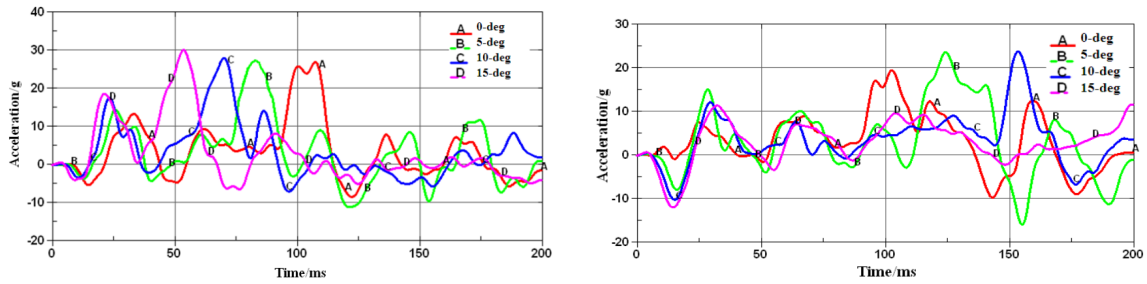

(a) Right outside **(b)** Left outside

Figure 4.3: Acceleration responses of junctions between seats and floor with different roll angles [47]

Results shown in both Figure 4.3 and Table 4.2 illustrate the impact of roll angle on acceleration pulses for the seat tracks on the left and right sides.

Table 4.2: Maximum peak acceleration and corresponding time [47]

Roll angle	Right outside		Left outside	
	Maximum peak acceleration	Time	Maximum peak acceleration	Time
0-deg	26 g	110 ms	19.5 g	105 ms
$5-$ deg	27 g	80 ms	25 g	125 ms
$10-$ deg	29 g	70 ms	25 g	160 ms
15-deg	32 g	52 ms	12 g	200 ms

A right roll angle led to an increase peak acceleration response on the right side while decreasing it on the left side. Simultaneously, the timing of acceleration pulses altered, with earlier occurrences on the right side as the roll angle increased, and delayed occurrences on the left side. Mou et al.'s [47] denoted that these fluctuations in peak acceleration also influenced seat behavior, potentially leading to the collapse of right-side seats. It's evident that as the roll angle intensified, the initial, secondary, and maximum peak accelerations escalated, accompanied by an earlier arrival of the acceleration pulse. The occurrence of a substantial acceleration response within a brief timeframe can result in occupant injuries.

Energy Absorption

Mou et al.'s work also demonstrates the kinetic energy histories of the fuselage section under the different conditions of 0-deg, 5-deg, 10-deg and 15-deg roll angles, as depicted in Figure 4.4.

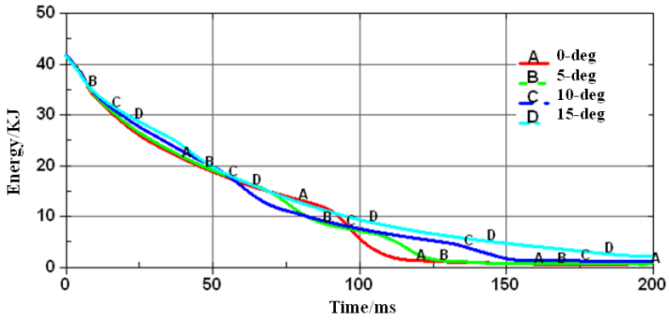

Figure 4.4: Kinetic energy histories of fuselage section with different roll angles [48]

Notably, the initial total kinetic energy of the fuselage sections remained the same at 42KJ when the fuselage sections experienced impacts with different roll angles against rigid ground. The reduction in kinetic energy showcased greater consistency and smoothness before the 60 ms mark across all four cases [47]. However, after this point, as referenced by Mou et al., distinct patterns emerged. For instance, when the fuselage section collided with rigid ground at a 0-degree roll angle, the kinetic energy experienced rapid decay, reaching its lowest point at 110 ms. Similarly, under a 5-degree roll angle scenario, the kinetic energy reduced swiftly, reaching its lowest point at 125 ms. The case of a 15-degree roll angle demonstrated a smoother kinetic energy decay, yet it had yet to reach its lowest point at 200 ms. It's evident that the time taken for kinetic energy to reach its minimum value extended progressively with increasing roll angles, reflecting a slowly energy absorption during crashes that could lead to occupant injuries.

In accordance with the findings by Mou et al., impact energy dissipation primarily relied on substantial plastic deformations within fuselage structures during impact accidents. However, the energy-absorbing capacities of the main fuselage structures exhibited variance. The energy-versus-time curves of diverse fuselage structures are detailed in Figure 4.5, while Table 4.3 lists the steady-state times and energy absorbed by waved-plates for the four different cases.

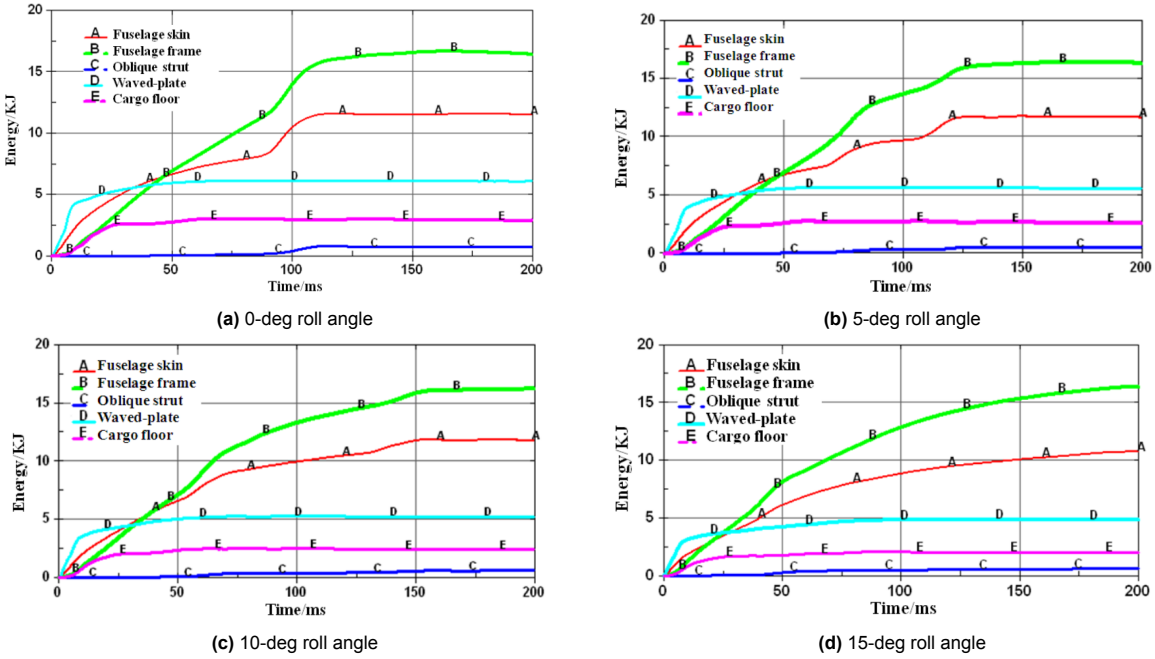

(a) 0-deg roll angle

(b) 5-deg roll angle

(c) 10-deg roll angle

(d) 15-deg roll angle

Figure 4.5: Energy absorption of main structures of fuselage section with different roll angles [47]

Table 4.3: Time of steady state and energy absorbed by waved-plates [47]

Roll angle	Time of steady state	Energy absorbed by waved-plates
$0-$ deg	110 ms	6.3KJ
$5-$ deg	130 ms	6KJ
$10-$ deg	150 ms	5.2KJ
$15-$ deg	200 ms	5KJ

As apparent from Figure 4.5 and Table 4.3, waved-plates and skin were the main energy-absorbing structures during the initial impact stages, with fuselage frames subsequently assuming this role owing to unique design features. The case of a 0-degree roll angle reached a steady-state energy absorption for components at approximately 110 ms, while the 5-degree roll angle case reached stability at around 130 ms. In scenarios involving a 10-degree roll angle, component energy absorption stabilized at approximately 150 ms, whereas for a 15-degree roll angle, it occurred around 200 ms [47]. Clearly, as roll angles escalated, energy absorbed by waved-plates gradually diminished, and the time required for each component's internal energy to reach stability extended.

4.2. Impact of Pitch Angles on Civil Aircraft Fuselage Crashworthiness

Impacts at different pitch angles in a crash analysis is vital for understanding the complex dynamics of aircraft crashes, assessing structural integrity, evaluating passenger safety, and ensuring regulatory compliance. It provides a more complete picture of how an aircraft responds to crashes under various conditions, enabling improved safety measures and emergency response protocols.

This was exactly the goal behind the study done by Riccio et al. [60], where a drop test of a composite fuselage section was investigated, focusing on the impact angle with the rigid ground. The drop test involved inducing an impact angle by rotating the fuselage pitch during its descent, a condition brought about by imbalanced masses on the floor beams. To facilitate a comprehensive analysis of the impact event, Riccio et al. employed numerical simulations utilizing the ABAQUS explicit software. The pitch angle was incorporated into these simulations by introducing a rotation to the rigid plate that simulated the ground, enhancing the fidelity of the investigation.

Two analysis were carried out. Initially, an analysis was conducted involving a direct impact perpendicular to the ground and the fuselage section. Subsequently, another simulation was performed, this time introducing an estimated pitch angle of around 3 degrees. The simulations had an initial velocity of 9.9 m/s (32.5 ft/s). This velocity was determined based on a drop height of 5 meters.

4.2.1. Finite Element Model Simulation Results and Discussion

The experimental test was performed at the Crash Laboratory LISA, owned by the Italian Aerospace Research Centre (CIRA). The test article impacted the ground with a pitch angle of about 3°, as highlighted in Figure 4.6a. The initiation of impact between the fuselage section and the ground revealed that the lack of balance in the fuselage caused the impact to start within a limited area [60].

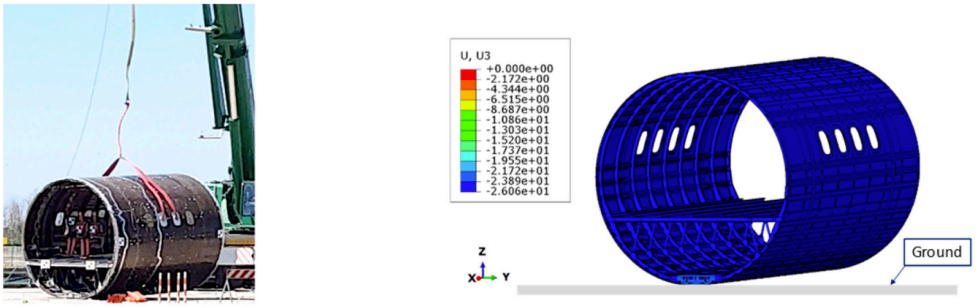

(a) Experimental test **(b)** Numerical simulation (units in mm)

Figure 4.6: First phase of the fuselage section impact with ground [60]

A comparison between the photograph captured during the experimental test is present in Figure 4.7.

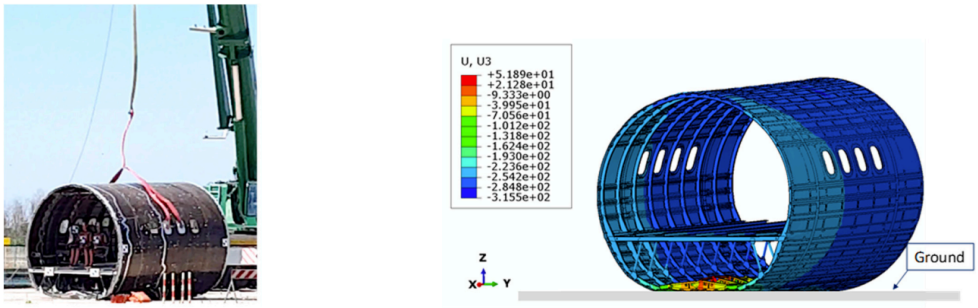

(a) Experimental test **(b)** Numerical simulation (units in mm)

Figure 4.7: Frame of the fuselage section impact with ground [60]

It shows the rear portion of the fuselage section making contact with the ground (depicted in Figure 4.7a), and the corresponding state shown in the numerical simulation under the same circumstances (illustrated in Figure 4.7b). Finally, Figure 4.8 depicts a numerical analysis simulating the impact between the fuselage section and the ground with no pitch angle. Uniform damage on all the lower frames and reinforcements can be observed in the perpendicular impact between the rigid ground and the fuselage section.

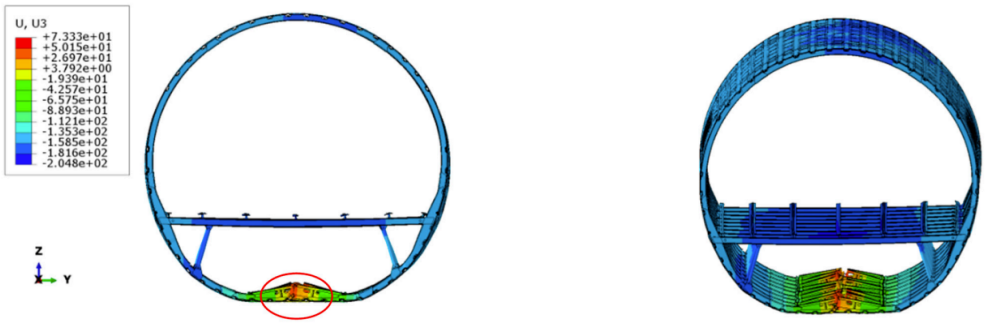

(a) Frontal view **(b)** Rotated view (units in mm)

Figure 4.8: Fuselage section impact parallel to the ground [60]

A concise overview of the damage energy graphs for both configurations is provided in Figure 4.9a by Riccio et al. [60]. The assessment of damage energies involved calculating the cumulative dissipated damage energy for each element, across various failure modes. In reference to the work by Riccio et al., Figure 4.9a clearly illustrates that the 10 kJ threshold for damage energy (represented by the traced line) was attained at different time intervals for the two examined configurations. Specifically, the configuration without an impact angle reached the 10 kJ damage energy mark at approximately 9 ms, while the configuration with a 3° impact angle achieved the same level of damage energy at around 14 ms. These observed trends align with expectations, given that the configuration with a perpendicular impact exhibited a more extensive damaged area. This broader damage area led to a rapid dissipation of energy through fracture processes [60].

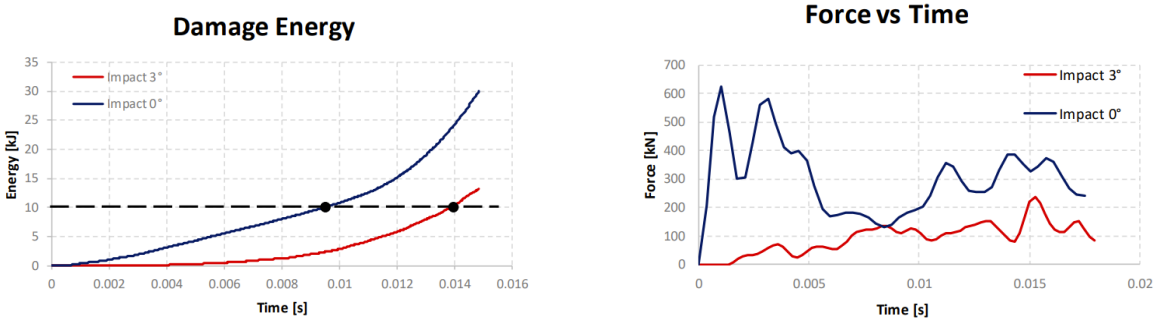

(a) Damage energy graph **(b)** Force vs. time graph

Figure 4.9: Plots of damage energy and force vs. time [60]

Figure 4.9b presents force vs. time trends for two analyzed configurations. The force, measured as a reaction force in the z-direction on a rigid plane, displayed distinct behaviors for these configurations [60]. In the case of the zero-impact angle configuration, a peak force of approximately 200 kN was achieved, whereas the configuration with a 3° impact angle reached a peak force of around 150 kN. According to Riccio et al., this disparity in behavior was representative of the deformations experienced by the two configurations. Specifically, the perpendicular impact configuration underwent a gradual deformation due to energy distribution along the entire fuselage length. Consequently, residual stiffness during impact resulted in a force peak, whereas the 3° angle impact configuration experienced an abrupt deformation on one edge, causing stiffness degradation and the absence of force peaks initially.

Lastly, Figures 4.10 provide a comparison of deformed fuselage sections at specific time intervals for the two configurations. Riccio et al. pointed out that, despite dissipating the same amount of fracture energy (10 kJ energy), the configuration with a normal impact exhibited a notably more extended damaged area compared to the configuration with a 3° impact angle.

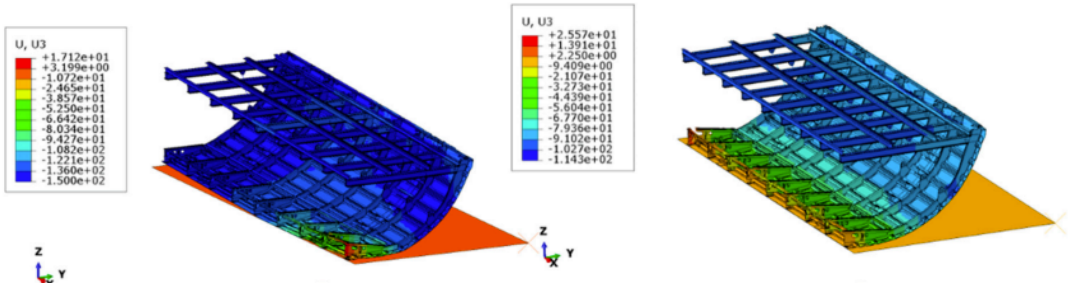

(a) 3° impact angle **(b)** Normal angle (units in mm)

Figure 4.10: Initial phases of sub-cargo area impact [60]

4.3. Introduction to the Impact of Roll, Pitch and Yaw Angles on Flying-V Crashworthiness

In the event of a crash, whether it be a controlled landing or an emergency situation, the behavior of an aircraft can significantly impact the safety of its occupants. Traditional aircraft with their cylindrical fuselages, as seen in previous sections, have been studied extensively in terms of crashworthiness, yielding valuable insights into impact angles, structural integrity, and passenger safety.

On the other hand, the Flying-V, while offering numerous advantages, presents a departure from conventional design principles, namely the enhanced rigidity and strength of its fuselage. This structural robustness suggests that the aircraft may exhibit unique crash dynamics. For instance, during a tail-first impact, the outer wings of the Flying-V could be damaged or even separate from the main body. Such an event would dissipate energy differently from conventional designs and directly affect the aircraft's crashworthiness. However, the stiff and robust fuselage section of the Flying-V is likely to undergo significant rigid-body rotation when the wingtips make contact with the ground. This rotation introduces upwards forces, resulting in a strong pitch-down moment on the aircraft, followed by further rotation. Consequently, different sections of the passenger cabin may experience varying vertical impact velocities, potentially leading to uneven occupant accelerations.

Moreover, impact scenarios involving different roll angles can also induce rigid-body rotations. As the Flying-V tilts during impact, sections of the passenger cabin located farther from the initial point of contact with the ground may experience higher impact velocities, further complicating the assessment of passenger safety.

While the FV FEM representation is initially limited to a small fuselage section for the current work, an overly complex model would also entail absurd amounts of computational time, so an equilibrium between these two factors have to be accomplish.

In light of these observations, it becomes evident that the crashworthiness of the Flying-V demands further examination. Numerical simulations can provide valuable insights, but the necessity to validate such results with analytical equations governing rigid-body rotation becomes apparent. The development of simplified yet accurate modelling approaches to study the Flying-V's crash dynamics is also essential to enhance the crashworthiness understanding and improve safety measures for this innovative aircraft design.

5

Simplified Modelling Techniques

The complex interaction between fundamental aircraft characteristics and structural dynamics significantly influence the overall functionality and safety of the Flying-V.

The finite element method model established by Desiderio's previous research [26] plays a vital role as the foundation for analysis. Nevertheless, its limited scope, covering only a specific segment of the fuselage, present a notable challenge, particularly in situations where velocity components extend beyond the vertical axis. In such cases, the model can experience rotations and unrealistic motions due to its incomplete representation of the entire aircraft. This calls for innovative strategies to ensure accurate and comprehensive analyses that reflect real-world dynamics.

Additionally, adopting a simplified modelling approach that captures the essential kinematics of other sections of the FV without requiring physical representation would notably decrease the overall modelling complexity and, consequently, alleviate associated computational costs. With that being stated, the objective of the upcoming sections is to prioritize the development of streamlined methodologies, aiming to address the absence of FEM representations for other parts of the Flying-V.

This chapter commences by offering the reader a full depiction of the Flying-V aircraft, detailing its subdivisions and outlining the positions of the analyzed models within the aircraft. This information is presented in 5.1.1. In Section 5.1.2, a suggested solution is presented to capture the fundamental kinematics of various sections of the Flying-V without the need for physical representation. It also provides details on a preliminary assessment for extracting moments of inertia for other sections of the FV. Similarly, an analytical presentation of inertial estimate for the outer-wing can be found in Appendix F.Subsequently, Section 5.2 proposes another simplified modelling technique that avoids overly simplified models to refine analyses in specific areas without overwhelming computational resources.

5.1. Implicit Moments of Inertia Approach

5.1.1. Flying-V Parts Subdivision and Inertial Properties Estimation

Oosterom [52] and Claeys [23] conducted a thorough subdivision of the Flying-V aircraft, as outlined in the Literature Study. These subdivisions formed the basis for mass breakdowns using various weight estimation methods. However, the use of class II methods, consisting of basic analytical structural evaluations, prevailed in estimating only the weights of primary and secondary structures, as well as non-structural elements. This choice was necessitated by the absence of finite element method representations for different sections of the Flying-V.

Marloes developed a FEM representation of the outer wing to apply the class III weight estimation method, recognized for providing a more accurate assessment of structural weight. Nevertheless, this model, created using ANSYS, was not readily available for the present thesis work. Alongside the FEM section crafted by Desiderio, these were the only FEM models accessible for the Flying-V.

While Desiderio's model played a crucial role in the preliminary crashworthiness assessment of the Flying-V, its scope was limited to a specific fuselage section, comprising five frames with a length of approximately 2.9 meters, presented in Figure 5.1.

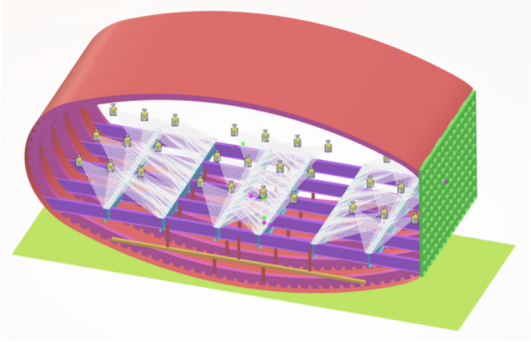

Figure 5.1: View of the FEM of the FV aircraft. Different colors are qualitatively representative of different section assignments [26]

This constraint posed challenges, particularly in scenarios involving different landing dynamics or velocity components beyond the vertical axis. Although a comprehensive representation of the entire Flying-V is not imperative for an accurate crashworthiness assessment, considerations arise regarding how extending the fuselage length could yield more precise results without significantly compromising computational efficiency.

To that extent, an exploration of augmenting the baseline section up to the full passenger fuselage will be undertaken along the current study. Additional modelling approaches, such as introducing sliding boundary conditions, will also be employed to enhance the realism of the analysis. However, the representation of the Flying-V aircraft will still remain far from complete, presenting difficulties for an accurate crashworthiness assessment due to its distinctive design.

This incomplete portrayal of the entire aircraft, compounded by the absence of moments of inertia for other sections, could result in rotational issues and unrealistic outcomes.

To address this challenge, a strategy involves further manipulation of existing resources. The fuselage section maintains consistent along the longitudinal axis from the nose section to the outer wing (see Figure 5.2). This approach ensures continuity in both material and modelling techniques, as detailed in the forthcoming section Section 6.1.

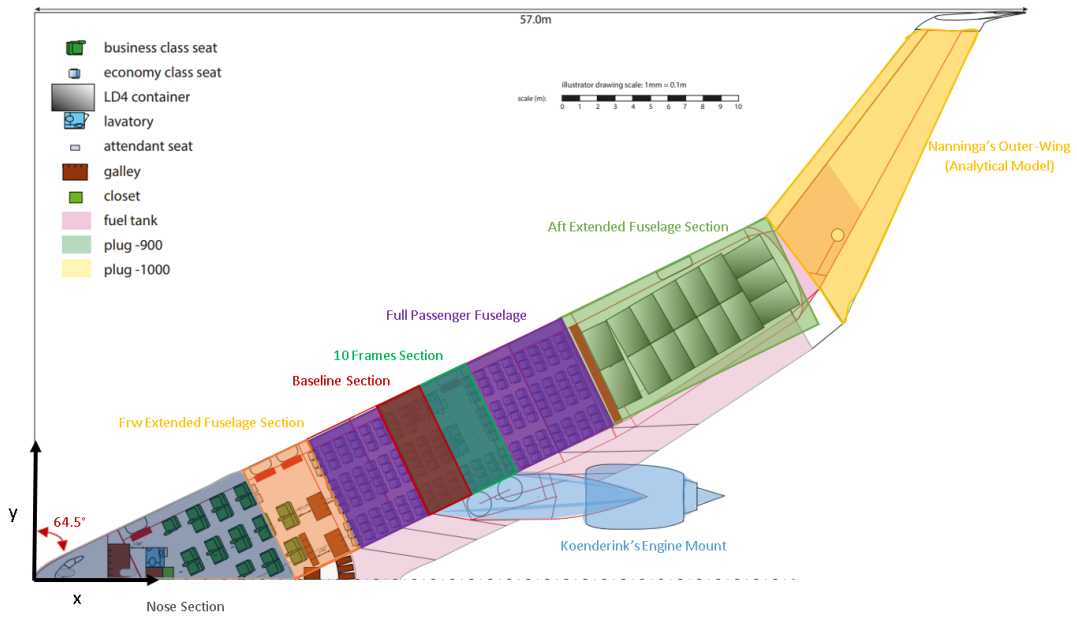

Figure 5.2: Proposed Part Subdivision for the Flying-V

Leveraging the known cross-section from Desidario's model, the fuselage section can be extended beyond the full passenger model to encompass the entire fuselage.

The forward and aft segments (depicted in orange and green, respectively) are created using 3DEXPERIENCE. This application of Class III methods facilitates the computation of weight and moments of inertia for each segment.

The nose section, as depicted in Figure 5.2, poses distinctive challenges. Previous research by Pluijm solely focused on cockpit design and integration into the Flying-V, excluding structural analysis. Recognizing the significance of mass and moments of inertia for this study, it was proposed to extend the fuselage forward section until the origin of the global coordinate system (see Figure 5.3a) and subsequently making a cut along the global x-direction, leading to the creation of the model depicted in Figure 5.3b. While this method is somewhat rudimentary, it provides preliminary insights into the potential moments of inertia for that section.

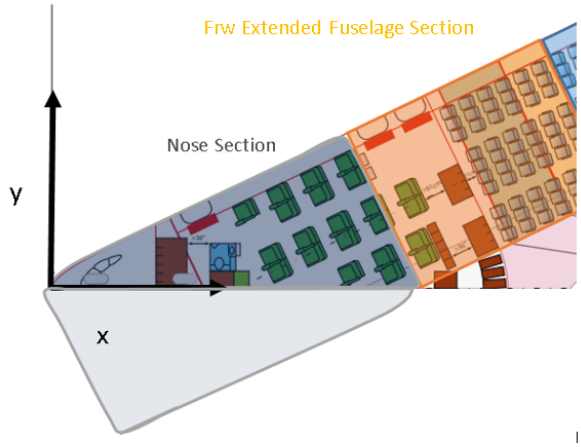

(a) Fuselage extension. The shaded lower part was then removed

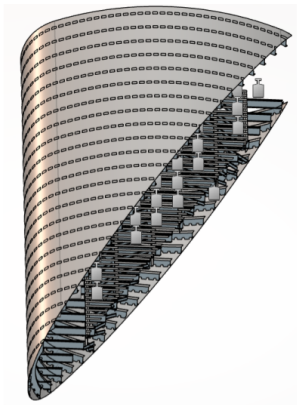

(b) FEM model of the nose section created with 3DEXPERIENCE

Figure 5.3: Nose section development process

Also, prior investigations performed by Koenderink [41], led to the creation of a FEM model of the engine mount (illustrated in Figure 5.2 and situated next to the 10-frame Flying-V section). A mass study on the possible engine weight was conducted, although this work remains unpublished up to this point.

For the outer wing, only the weight information was available from Marloes' research ($6{\times}10^3$ kg). Analytical equations introduced in Appendix F were employed to calculate its center of gravity and moments of inertia, as a FEM representation was not accessible.

Ultimately, a FEM model of all the parts in Figure 5.2, excluding the outer wing, was developed. Using Class III methods, the primary weight of each part's fuselage was determined, along with the respective moments of inertia about their centers of gravity. Initially, these values were computed in relation to the local coordinate frame of each subdivision. Subsequently, upon the application of the rotation matrix seen in 13.6 and discussed later in Section 13.2.1, the moments of inertia were recalculated, considering the respective centers of gravity within the global coordinate system illustrated in Figure 5.2. The analysis also accounted for passenger and seat weights, while the cargo in the aft section of the green segment (in Figure 5.2) was simplified as a large parallelepiped, facilitating the calculation of its moments of inertia and center of gravity.

5.1.2. Moments of Inertia Solution and Super-Position

A nearly comprehensive model was now available. However, despite implementing numerous simplifications in the process, the model consisted of a substantial number of elements, resulting in computationally intensive simulations.

The solution was to simplify the model by making use of the inertia properties previously estimated for the various parts of the Flying-V. Currently, all sections have been condensed into a singular point, encompassing their cumulative inertial properties.

To further streamline the model, Figure 5.4 outlines a solution. By applying the principle of superposition and the parallel axis theorem:

$$J_{ij} = \sum \left(I_{ij} + m \left(|\mathbf{R}|^2 \delta_{ij} - R_i R_j \right) \right) \tag{5.1}$$

where $\mathbf{R} = R_1\hat{\mathbf{x}} + R_2\hat{\mathbf{y}} + R_3\hat{\mathbf{z}}$, moments of inertia calculated at the centers of gravity of each section were computed at reference points within a specified distance from the global coordinate system.

To ensure comprehensive information, the coordinates of both the left and right reference points are provided as follows:

$$\begin{array}{lll} X_L = 21.45m & Y_L = 6.61m & Z_L = -0.37m \\ X_R = 27.92m & Y_R = 9.63m & Z_R = -0.37m \end{array}$$

The final inertial properties applied to the RPs are:

$$J_L = \begin{bmatrix} 0.2352 & -0.4316 & -0.0006 \\ -0.4316 & 1.4141 & -0.0010 \\ -0.0006 & -0.0010 & 1.6305 \end{bmatrix} \cdot 10^6 kgm^2 \quad J_R = \begin{bmatrix} 0.7971 & -1.2917 & -0.0198 \\ -1.2917 & 3.0291 & -0.0109 \\ -0.0198 & -0.0109 & 3.7692 \end{bmatrix} \cdot 10^6 kgm^2$$

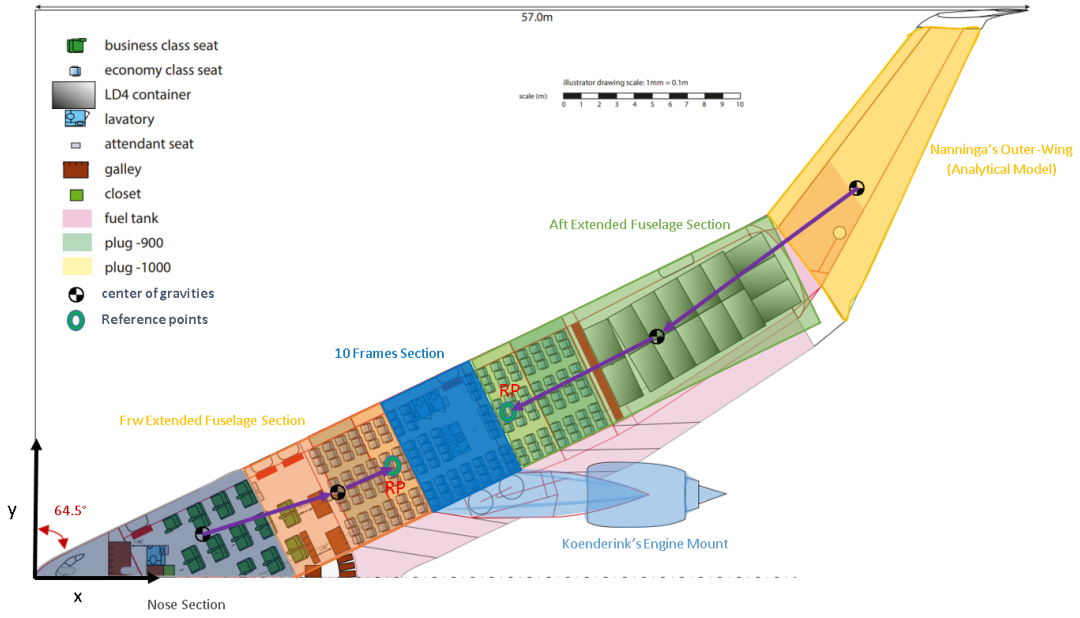

Figure 5.4: Possible location of the CGs of each section and RP's representation

Utilizing these moments of inertia at designated reference points facilitated distributed coupling between the reference points and cross sections of the 10 frames Flying-V section, situated in proximity to the engine (refer to Figure 5.4). Given that this is a novel and previously unexplored methodology, this section was selected over the baseline and full passenger section, aligning with the conclusions that will be drawn in Chapter 10. This choice achieved a commendable balance between computational efficiency and result accuracy in the conducted simulations.

Also, the distributed coupling allowed for the natural deformation of secondary nodes, thereby preserving the authenticity of the simulation.

As a concluding remark, it's worth noting that only inertias are incorporated into the model, while the mass is omitted to prevent potential acceleration increases without taking into account the crash dynamics and energy absorption by other components representations. The examination of the validity and effectiveness of this approach will be a primary focus in the subsequent Chapters of Part IV titled "Modeling Unique Flying-V Crash Scenarios".

5.2. Submodelling

As a possible alternative to the implicit modelling approach previously presented, other alternative was considered, capable of maitaining accuracy and efficiency while streamlining finite element models and reducing computational time. Submodelling, a practical solution gaining prominence, avoids overly simplified models to refine analyses in specific areas without overwhelming computational resources. Employed in software like Abaqus, it offers a straightforward strategy by isolating and scrutinizing targeted regions within a larger structural model, facilitating a detailed examination where it matters most.

Initiating with a comprehensive structure assessment through global analysis allows the identification of critical areas responsive to loading. A refined local submodel is then crafted for these zones, incorporating enhanced geometric representation and/or mesh refinement. This targeted submodel provides heightened accuracy compared to the global model, eliminating the need for extensive remeshing and reanalysis of the entire structure. This approach not only reduces analysis expenses but also preserves intricate details in pivotal regions, offering an efficient and cost-effective strategy for structural evaluation [32].

5.2.1. Theory Behind

The submodelling process relies on St. Venant's principle, asserting that "The difference between the effects of two different but statically equivalent loads becomes very small at sufficiently large distances from load". This concept is grounded in the strategy of establishing a coarse finite element mesh for a component or assembly. It is assumed that minor geometric details exert negligible influence on the overall system response, allowing for their omission during mesh discretization.

The underlying assumption is that the local stiffness has no discernible impact on the strain beyond its immediate vicinity. Following the computation of the structure with a coarse mesh using the finite element method, a highly refined finite element model is crafted for the region of interest. Results from the coarse mesh (typically displacements in structural analysis) are then transferred to the submodel nodes as boundary conditions through interpolation based on element shape functions. The original loads, if present in the region of interest, are reapplied, and the finite element model is rerun to obtain a precise and refined response within the specified area [32].

Figure 5.5 from the work by Nath et al. [32] offers a depiction of the submodelling process. On the left side, a step-by-step presentation guides through each sequential stage, while the right side provides a visual representation, offering a clear illustration of the involved steps in achieving a precise and detailed analysis.

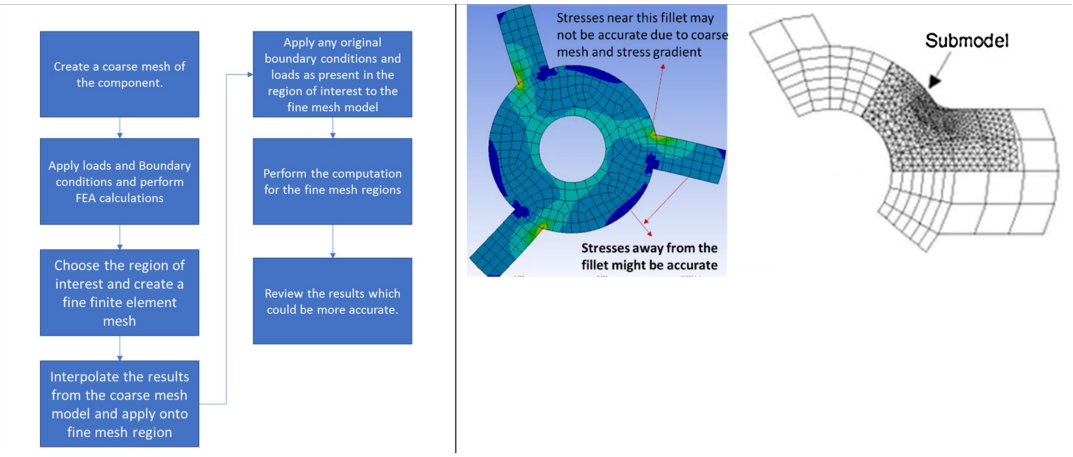

Figure 5.5: Description of the submodelling process step by step and pictorially [32]

5.2.2. Submodelling Techniques in Abaqus

In the realm of Abaqus, two distinct submodelling techniques exist: node-based and surface-based submodelling [14]. The node-based approach involves interpolating the nodal results field from the global model onto submodel nodes, representing the more general and commonly employed method. Conversely, surface-based submodelling entails interpolating the stress field onto the submodel surface integration points, primarily applicable to solid-to-solid scenarios in static analyses [14]. For all other purposes, the node-based submodelling technique is recommended [14]. Depending on the characteristics of the model, either technique or a combination of both can be utilized within an analysis.

The surface-based technique proves advantageous in static analyses when there is a substantial difference in average stiffness between the submodel region and the globally loaded model subjected to force-controlled loading. On the other hand, when stiffness in the regions is comparable, node-based submodelling yields similar results to surface-based submodelling while minimizing potential numerical issues arising from rigid-body modes [14].

In cases involving large displacements or rotations, node-based submodelling enhances accuracy in transmitting these deformations to the submodel. Nonetheless, the choice between node-based and surface-based submodelling depends on the desired output results. Node-based submodelling ensures more accurate transmission of the displacement field in the submodel, while surface-based submodelling excels in accurately transmitting the stress field, thereby determining reaction forces in the submodel more precisely.

5.2.3. Future Applicability

Submodelling will be employed later to explore alternative simplified modelling techniques, ensuring accurate results while reducing computational time in the simulation.

Given that the FV section analyzed in the present study undergoes large displacements and rotations and comprises only shell elements, the node-based technique will be employed for optimal results.

The global model will encompass the complete passenger fuselage, where drop tests will be conducted with a coarser mesh. The variables manipulated within the global model will then be used as outputs at common boundaries for the submodel. Here, the submodel refers to the extended model positioned in the center of the complete passenger section.

In conclusion, two sets of analysis results will be obtained: the first from the global model, providing an approximate behavioral overview, and the second from a refined local model, offering a more precise representation of detailed output.

This page intentionally contains no content.

III

Modelling Approaches

This page intentionally contains no content.

6

Baseline FV Typical Section

Prior to embarking on the creation of novel models designed to assess the distinct impact scenarios of the Flying-V, it is imperative to formulate a robust point of comparison.

This is the main goal of this Chapter: to present an understanding of the procedures employed in establishing, verifying, and validating Desiderio's non-linear, explicit-dynamic finite element model, serving as the foundational framework for subsequent analyses. The initial focus will be on providing an overview of Desiderio's finite element model, as detailed in Section 6.1. It is followed, in Section 6.2, by a verification and validation of the best-performing FV design concept (4S-5). Building upon this analysis, Section 6.3 delves into a more comprehensive evaluation of the DRI. Additionally, an expanded injury criteria, briefly introduced in Chapter 2, is thoroughly explored to provide a nuanced understanding. To conclude the Chapter, Section 6.4 presents a synthesis of the results obtained, accompanied by conclusions drawn from the findings.

6.1. CAD and FEM Model

Desiderio's previous research [26] investigated the optimization of a fuselage segment of the Flying-V, specifically exploring the incorporation and spatial arrangement of crushable elements beneath the floor structure. In the preceding thesis, the finite element model for the Flying-V's aircraft section was meticulously constructed using the 3DX platform, facilitating the seamless integration of computer-aided design and FE models. The computational analysis was executed employing Abaqus/Explicit on TU Delft's cluster computer.

Figure 6.1 offers a three-dimensional view of the CAD model illustrating the fuselage segment of the Flying-V that exhibited superior performance in reducing equivalent DRIs (incorporating 4 struts per floor beam, 2 on each side, arranged obliquely). This detailed CAD depiction includes essential components, including frames, wing spar, skin, floor beams, and floor supporting structures.

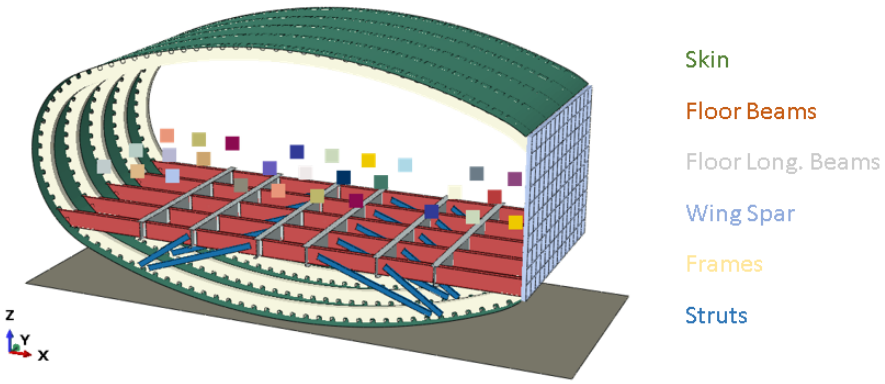

Figure 6.1: View of the FEM model of the FV aircraft in Abaqus. Different colors are qualitatively representative of different section assignments

Additionally, Figure 6.1 visually represents passengers as mass elements within the model. To optimize the efficiency of the finite element model, certain simplifications were incorporated. Notably, the exclusion of stiffeners from the analysis was deemed appropriate, given their negligible impact on the crash characteristics of the Flying-V. However, attention was paid to retaining the mouse holes in the frames within the analysis.

It is noteworthy that the analyzed section was confined to a configuration comprising five frames; nonetheless, subsequent Chapters of this study will scrutinize and potentially challenge this specific choice.

6.1.1. Section Allocation & Element Dimensions

Desiderio implemented a mesh primarily consisting of quad elements employing S4 elements (first-order shell). The specific thickness assignments and overall general element sizes are outlined in Table 6.1, while additional clarification on component nomenclature in Figure 6.1. Notably, the floor beam was modelled as an I-beam structure. It is crucial to highlight that the details presented in this section, as well as the subsequently assigned materials, will remain unchanged in the upcoming Chapters.

Also, a mesh analysis has been previously undertaken, and as a result, the mesh size for all structural elements will remain consistent. Conducting a mesh convergence study is beyond the scope of this master's thesis.

Table 6.1: Element dimensions for various structural elements used in the 4S-5 desing concept

Component	Thick. [mm]	Elem. size [mm]	Component	Thick. [mm]	Elem. size [mm]
Skin	2.5	60	Ground	1	200
Frames	5.7	20	Floor beams	var	30
Floor long. beams	2	20	Floor struts	var	10
Spar skin	3	20	Spar stiffeners	4	20

6.1.2. Material Assignment

The material used in the preceding thesis was 2024-T3 aluminum alloy. The properties of the mentioned alloy, extracted from literature, are outlined in Table 6.2.

Table 6.2: Parameters employed for the JC elastic-plastic model, encompassing damage aspects [40]. All measurements are expressed in kg, N, and mm

Variable	Value	Variable	Value
A	420	D_1	0.112
B	683	D_2	0.123
c	0	D_3	1.5
n	0.73	D_4	0
m	0	D_5	0

The selected material model for simulation purposes is the Johnson-Cook (JC), an elastic-plastic model capable of incorporating temperature and strain-rate dependencies. Widely employed in industry for impact damage simulations [40], the JC model defines flow stress through the relation:

$$\sigma_y = \left(A + B\bar{\varepsilon}^{p^n}\right)\left(1 + c\ln\dot{\varepsilon}^*\right)\left(1 - T*^m\right), \tag{6.1}$$

with A and B representing the material yield strength and hardening modulus, respectively. $\bar{\varepsilon}^p$ represents the plastic strain, n is the hardening parameter, $\dot{\varepsilon}^*$ denotes the strain rate, c stands for the strain-rate dependency parameter, T^* signifies the dimensionless temperature (calculated as $T^* = \frac{T - T_{\text{room}}}{T_{\text{melt}} - T_{\text{room}}}$), and *m* represents the temperature dependency parameter.

In this model, the failure mechanism is strain-based, expressed as:

$$\varepsilon_{\text{failure}} = \left[D_1 + D_2 \exp\left(D_3\sigma^*\right)\left[1 + D_4 \ln\left(\varepsilon^*\right)\left[1 + D_5 T^*\right]\right.\right. \tag{6.2}$$

Here, σ^* is the pressure-to-effective stress ratio $\sigma^* = \frac{\text{pressure}}{\bar{\sigma}}$, and D_1 to D_5 are empirically-determined failure parameters.

The fracture occurs in the JC model when the damage parameter D exceeds 1, where D is the ratio between effective plastic strain and the failure strain determined using Equation 6.2:

$$D = \sum \frac{\Delta \bar{\varepsilon}^p}{\varepsilon_{\text{failure}}} \tag{6.3}$$

6.1.3. Interaction and Contact Properties

All riveted connections were represented using tie constraints to prevent joint failure. To mitigate any unrealistic element penetration, Desiderio [26] established general contact interaction property. This property incorporates hard contact for normal behavior and employs a penalty friction formulation to define tangential behavior, specifying a friction coefficient of 0.5 (independent of slip rate). This coefficient is considered a reliable estimate for contact interfaces involving both aluminum/aluminum and aluminum/asphalt.

6.1.4. Passenger and Seating Representation

An assumed mass for an individual passenger equivalent to the 95th percentile male was estimated at approximately 90 kg [57]. To accommodate the seat mass, an additional 10 kg was assigned by Desiderio, as shown in Figure 6.1. Consequently, the entire mass of the passenger and seat system amounted to 100 kg and was represented as a point inertia in the finite element model.

The seat itself was modelled with a flexible coupling to the floor structure, utilizing a chosen spring constant of 3924 N/mm in the FEM. To ensure a realistic configuration, the vertical distance between the point mass and the floor beams was adjusted to align roughly with the lumbar region of a seated passenger. For more in-depth insights, Desiderio's thesis work serves as a comprehensive reference [26].

6.1.5. Drop Test Conditions

The crashworthiness characteristics of the section of the Flying-V aircraft were assessed through a drop test, conducted at a minimum vertical impact velocity of 26 ft/s (7.925 m/s), with the fuselage centerline in a horizontal orientation. The selection of this velocity is supported by prior literature and in line with Desiderio's research. These conditions for the drop test will remain consistent unless otherwise specified.

6.2. Best Concept Verification and Validation

6.2.1. The 4S-5 Design Concept

As previously mentioned, a comprehensive exploration of various conceptual designs for the Flying-V's typical sections was conducted. The primary objective of these designs was to minimize the Dynamic Response Index introduced in Chapter 2 as much as possible. Following a thorough analysis, particularly involving modifications to the crushable elements beneath the floor, Desiderio identified the 4S concept (depicted in Figure 6.1) as the optimal design. Geometric variables such as the orientation and horizontal positioning of the floor struts, their thickness, and the floor beam thickness were key factors considered in achieving a viable design.

For the sake of comprehension, Figure 6.2, extracted from Desiderio's thesis work, illustrates the equivalent DRI plotted against the dissipated energy normalized by the pre-impact kinetic energy for all the tested variants, but special attention will be given to the 4S design concept.

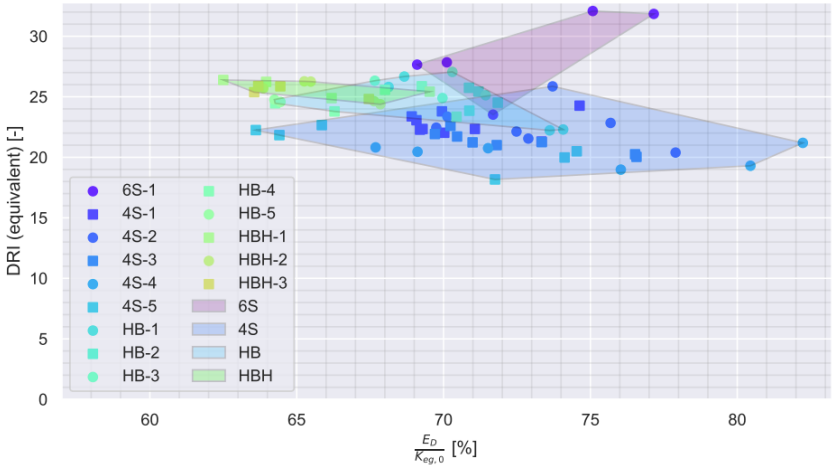

Figure 6.2: Equivalent DRI versus the dissipated energy normalized by the pre-impact kinetic energy, for all the tested variants [26]

The initial observation from 4S-1, the first evolution, revealed challenges in achieving a plastic hinge, with the passenger floor beam susceptible to bending instability. The second iteration, 4S-2, aimed to localize the load on the frames, promote the creation of a plastic hinge, and reduce the internal load on the passenger floor beam by bringing the floor struts closer together.

Subsequent modifications, such as making the floor struts more shallow and centralized in 4S-3, were implemented to increase the load in the floor struts and, consequently, enhance the bending load in the frames. A key alteration in 4S-4 involved raising the floor structure by 100 mm to increase the floor beam length and the length of the frame under the floor structure. This was anticipated to enhance energy absorption and decrease the DRI, as validated by the results in Figure 6.2.

In the evolution to 4S-5, the coupling between the point inertia and the floor structure was made flexible to model seat compliance. This became the distinguishing factor between 4S-4 and 4S-5.

Notably, the overall best-performing concept across all tested variants, with an equivalent DRI of 18.2, was identified as 4S-5 (refer to Figure 6.2).

Based on these findings, this concept design was selected to continue the crashworthiness research in this dissertation.

6.2.2. Model Validation

As mentioned earlier, the selected design concept plays a pivotal role in securing the subsequent crashworthiness study. Therefore, a validation process, involving a thorough evaluation of the model's fidelity, is imperative to ensure its accurate reflection of the intricacies inherent in the chosen design.

Prior to confirming the precision and dependability of the current model, Figure 6.3 provides a front view comparison of the deformed 4S-5 concept design from Desiderio's thesis work (Figure 6.3a) and the present study (Figure 6.3b).

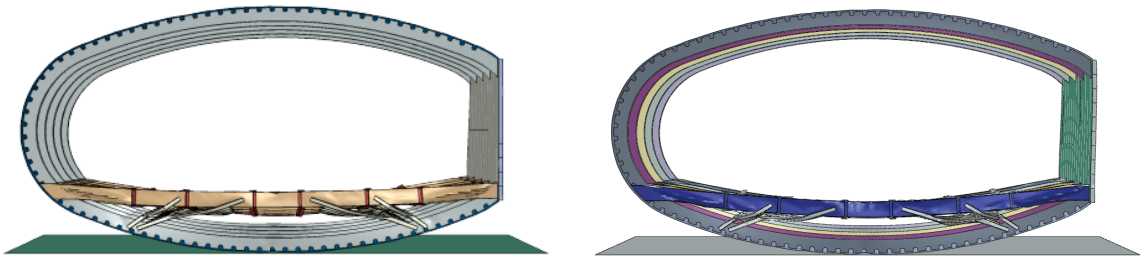

(a) Deformed baseline section, from Desidario's thesis work [26]

(b) Deformed baseline section, current thesis work

Figure 6.3: Qualitative comparison, 4S-5 design concept ($t_s = 2.5mm, t_s = 1.0mm$)

A visual inspection reveals striking similarities in deformations between the two models. Notably, the fuselage frames exhibit minimal deformation owing to their high bending stiffness in both instances. Consequently, the impact is efficiently dissipated through the buckling of the floor beam and floor struts, showcasing nearly identical behavior on both models.

When scrutinizing the distribution of energy absorption across components, a more consistent resemblance emerges. Three distinct 4S-5 models, each featuring varying thicknesses for the struts and floor beams, underwent simulations once again. The resulting data was subsequently compared with that acquired by Desiderio. Figure 6.4 illustrates the distribution of component energy absorption normalized by initial kinetic energy, while Figure 6.5 delineates the fraction of total dissipated energy attributed to each component. Given the information gathered from these three simulations, there was no deemed necessity to conduct simulations for all six 4S-5 design concepts; the selected trio proves adequate for validation purposes.

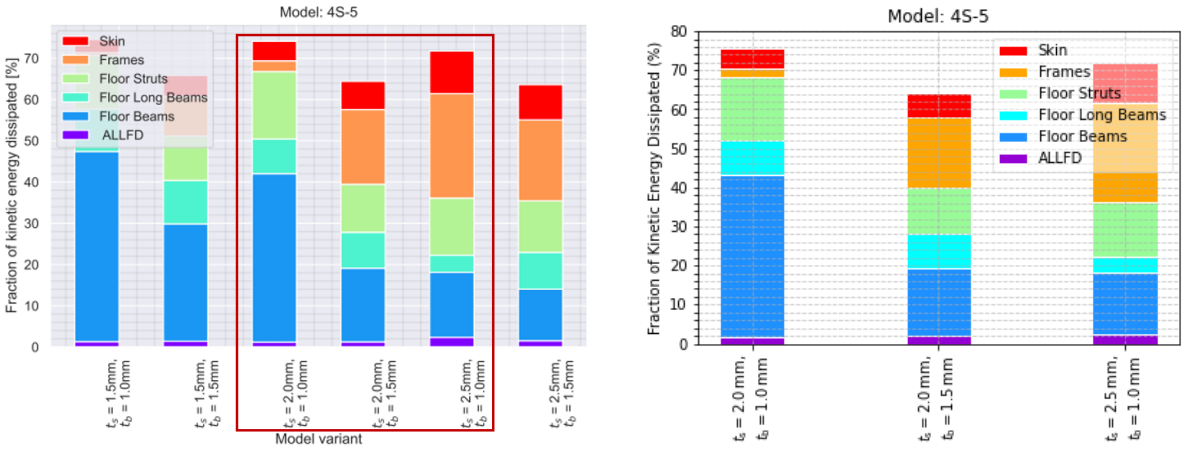

(a) Component energy absorption distribution, normalized by initial kinetic energy, from Desiderio's work [26]

(b) Component energy absorption distribution, normalized by initial kinetic energy, current work

Figure 6.4: Comparison of component energy absorption distribution, normalized by initial kinetic energy, from previous and current 4S-5 concept design

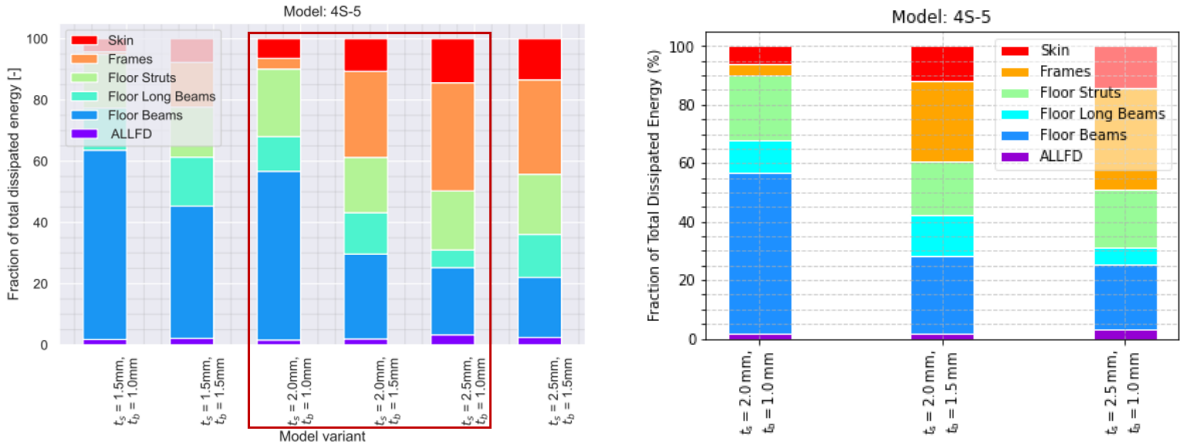

(a) Component energy absorption distribution, from Desiderio's work [26]

(b) Component energy absorption distribution, current work

Figure 6.5: Comparison of component energy absorption from previous and current 4S-5 concept design

In the concluding analysis, Table 6.3 examines the energy dissipation by component for the optimal 4S-5 design concept, employing a thickness of 2.5 mm for the struts and 1 mm for the floor beams. Once again, a substantial resemblance is evident, with the minimal variation observed possibly attributed to Desiderio's methodology. Specifically, Desiderio constructed the FE/CAD coupled model in 3DEXPERIENCE and then exported it to Abaqus/CAE for preprocessing.

In contrast, in the present study, both the FE/CAD model and preprocessing were executed within 3DEXPERIENCE, utilizing Abaqus solely for postprocessing.

Table 6.3: Energy dissipated, by component, for the best 4S-5 design concept ($t_s = 2.5mm, t_s = 1.0mm$)

Energy Dissipated	Desiderio	Current
Initial K_{eg}[kJ]	125.25	125.34
Plastic Energy Dissipated [kJ]	91.31	91.34
- Skin	13.28	13.28
- Frames [kJ]	31.98	31.99
- Floor Struts [kJ]	18.13	18.14
- Floor Long Beams [kJ]	5.49	5.49
- Floor Beams [kJ]	20.12	20.13
Friction [kJ]	3.06	3.06
Equivalent DRI [-]	18.20	18.22

As a final remark, it's noteworthy to mention that Desiderio's work provided limited information regarding data extracted from the 4S-5 design concept. As a result, the validation process was confined to the available data, highlighting the importance of working within the constraints of the information provided in the previous study.

To simplify matters, from now on the preferred 4S-5 design concept will be denoted as the "baseline model".

6.3. Spatial DRI and SEV Variation

6.3.1. Introducing the DRI

Structural optimization and crashorthiness assessement for each concept design was previously attained using the equivalent DRI which, essentially, is a weighted average of DRIs for different seats. This ensures that the overall likelihood of spinal injury is equivalent to having a DRI of the same value measured at each seat location. The spinal injury rate, represented as a percentage in Figure 2.7 in Section 2.3.3, was utilized to derive the equivalent DRI.

However, this fundamental method fails to offer insights into how the spatial positioning of passengers influences the DRIs, making it more challenging to assess the distinct impact scenarios of the Flying-V. Also, an improved comprehension would form the foundation for a more thorough optimization process in subsequent studies.

Taking that into consideration and for improved visual clarity, Figure 6.6 represents spatial position labels for passengers within the baseline FV section. Proceeding from the left (exterior) to the right (interior), each longitudinal row is assigned a letter from A to J, with a numerical range from 1 to 3, encompassing a total of 30 passengers.

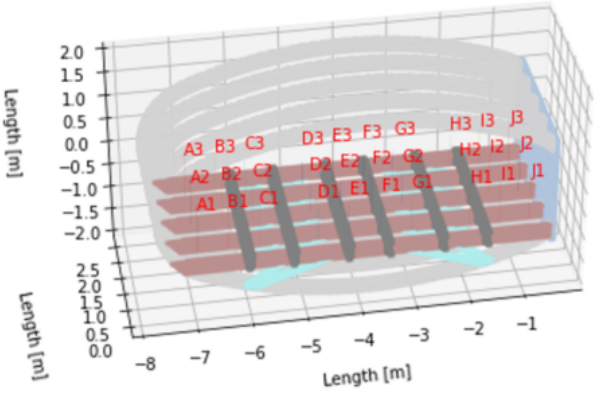

Figure 6.6: Labels indicating the spatial positions of passengers within the baseline model, consisting of 5 frames

The simplified model depicted in the plot is generated using a Python script, which reads the nodes and elements from a Nastran file exported directly from 3DEXPERIENCE. Distinct colors are used to signify various components of the fuselage section.

For the baseline section, Table 6.4 displays the DRI values associated with each passenger ID.

Table 6.4: DRI values corresponding to each Passenger ID within the baseline FV section

Pass. ID	DRI	Pass. ID	DRI	Pass. ID	DRI	Pass. ID	DRI	Pass. ID	DRI
A3	21.76	*B3*	18.84	*C3*	15.92	*D3*	11.99	*E3*	12.21
A2	23.63	*B2*	20.56	*C2*	17.55	*D2*	14.18	*E2*	14.41
A1	23.79	*B1*	21.32	*C1*	19.19	*D1*	16.03	*E1*	16.23
F3	12.57	*G3*	12.96	*H3*	18.12	*I3*	19.79	*J3*	22.12
F2	14.64	*G2*	14.87	*H2*	19.50	*I2*	21.29	*J2*	23.93
F1	16.50	*G1*	16.82	*H1*	20.73	*I1*	20.99	*J1*	22.45

Subsequently, bar plots illustrate the DRI values at each passenger location in Figure 6.7. Additionally, on the left side of Figure 6.7, a box plot visually illustrates the distribution, spread, and skewness of all 30 DRIs, along with the median (approximately 18.2, the same value of the equivalent DRI). On the right side of the same Figure, a color palette is presented, showcasing the maximum (J2 location) and minimum (D3 location) DRIs attained.

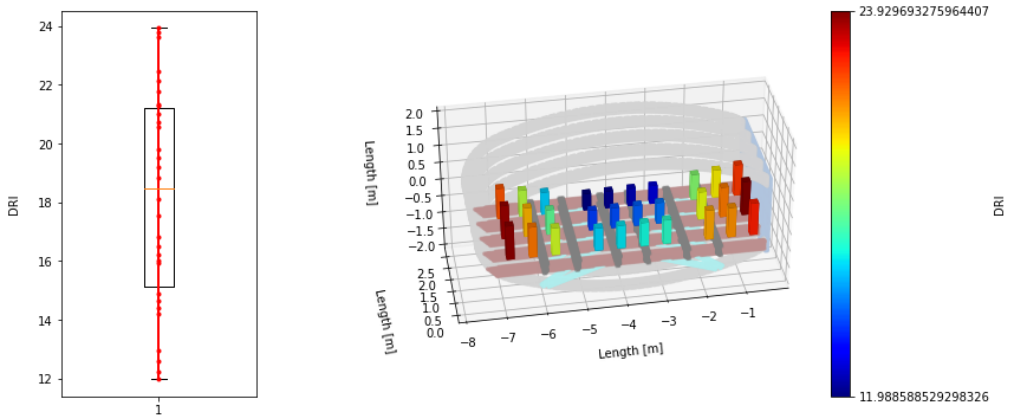

Figure 6.7: Spatial variation of the DRI along the baseline FV section

Valuable insights can be derived from the analysis of Figure 6.7. Notably, within the central section, the Dynamic Response Index values are smaller, gradually increasing as one moves away from the midpoint towards the sides. This spatial variation in DRIs is attributed to the plastic deformation of the underlying structural elements. The middle section, providing more room for components to deform, exhibits a more pronounced effect. Approaching the sides, there is a notable increase in structural stiffness, resulting in reduced deformations and consequently lower energy absorption during impacts in those specific areas.

Furthermore, moving from the front to the back, a decrease in DRI is observed. This phenomenon is attributed to the fuselage section's crushing and twisting behavior, initiated by the upward folding frames towards the central floor longitudinal beam. The asymmetrical cross-section of this beam induces lateral deflection of the frames, initiating the crushing-twisting motion.

A more in-depth exploration of this crushing-twisting motion, particularly its heightened manifestation in longer fuselages, will be elucidated in the subsequent Chapter.

6.3.2. Introducing the SEV

While the DRI serves adequately for evaluating injury probability in the vertical direction, especially during vertical drop tests, it is not sufficient to comprehensively assess the full spectrum of potential impact scenarios faced by the Flying-V.

Its unique design, coupled with the fuselage's angle concerning the longitudinal direction during landing, challenges the exclusive reliance on the DRI for a proper crashworthiness assessment: it fails to account for potential side loads that passengers may experience.

To achieve a more thorough evaluation of potential injuries, it becomes imperative to consider additional acceleration components and their potential impact. This is where the Severity Index (SEV) becomes crucial.

As briefly introduced in Section 2.3.3, the SEV, given by equation 6.4, provides a more comprehensive assessment of the Flying-V, taking into account the combined effects of various accelerations on potential injuries.

$$\left(\frac{\text{DRI}}{DRI_L}\right)^2 + \left(\frac{G_x}{G_{xL}}\right)^2 + \left(\frac{G_y}{G_{yL}}\right)^2 = SEV \tag{6.4}$$

As a reminder, throughout this work, the x-direction signifies the lateral direction (positive as right and negative as left). The y-direction represents the backward (positive, through the screen) or forward (negative), while the z-direction indicates the vertical component (positive as up and negative as down). G_x and G_y then denote the magnitudes of acceleration along the x and y axes, respectively, determined using the methodology outlined in Appendix B. This approach is employed to ascertain the acceleration time history for each axis and was automated using Python. An illustration of this automated process is depicted in Figure 6.8, where the temporal variations of acceleration in the x, y, and z directions for passenger B2 are exhibited. Notably, it includes the calibration time, 10% and 90% peak lines, and the peak acceleration. Additionally, dashed lines connect specific points in the plots, serving as the basis for calculating plateau duration and rise time – essential values for determining G_{xL} and G_{yL} in different scenarios.

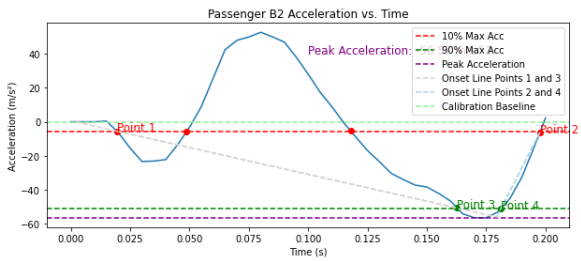

(a) Acceleration suffered by passenger B2 in the x direction

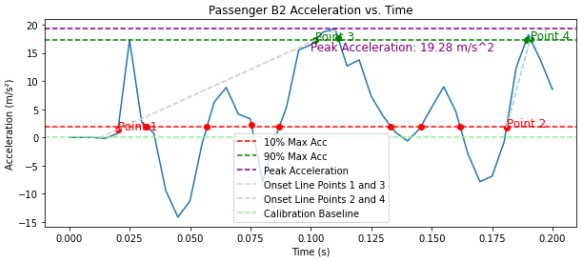

(b) Acceleration suffered by passenger B2 in the y direction

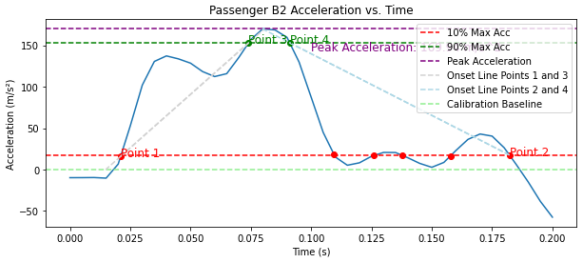

(c) Acceleration suffered by passenger B2 in the z direction

Figure 6.8: Acceleration vs. time plots for passenger B2

These values signify the limit for the x-axis (fore and aft) and y-axis (sideways), respectively, and, depending on the computed rise time and plateau duration, distinct plots are utilized to calculate them. These plots are accessible in the literature and are featured in figures B.3, B.4, B.5, and B.6 of Appendix B.

The DRI in the equation stands for the Dynamic Response Index value calculated from Equation 2.3 for the positive z direction, while DRI_L is the limit value for DRI, set at 16 units.

In cases where acceleration components exist in the $-G_z$ direction, the equation should be solved using $\frac{-G_z}{-G_{zL}}$ instead of $\frac{\text{DRI}}{DRI_L}$, where:

- $-G_z$ denotes the -z direction.

- $-G_{zL}$ is the limit value for the -z direction in figures B.7 and B.8 of Appendix B.

For every passenger, analogous plots to those shown in Figure 6.8 are generated for all three directions. The corresponding plateau durations and rise times are computed, enabling the derivation of the appropriate values for G_{xL} and G_{yL}.

Using this data, in conjunction with the DRI and peak acceleration values, the Severity Index for each passenger can be determined and are presented in Table 6.5.

Table 6.5: SEV values corresponding to each Passenger ID within the baseline FV section

Pass. ID	SEV	Pass. ID	SEV	Pass. ID	SEV	Pass. ID	SEV	Pass. ID	SEV
A3	1.48	*B3*	1.29	*C3*	1.13	*D3*	0.78	*E3*	0.79
A2	1.50	*B2*	1.30	*C2*	1.15	*D2*	0.92	*E2*	0.93
A1	1.56	*B1*	1.38	*C1*	1.26	*D1*	1.02	*E1*	1.02
F3	0.81	*G3*	0.84	*H3*	1.28	*I3*	1.34	*J3*	1.47
F2	0.94	*G2*	0.95	*H2*	1.26	*I2*	1.36	*J2*	1.53
F1	1.04	*G1*	1.06	*H1*	1.31	*I1*	1.33	*J1*	1.44

Just like the DRIs, bar charts showcase the SEV values corresponding to each passenger's location in Figure 6.9. Moreover, on the left portion of Figure 6.9, a box plot provides a visual representation of the distribution, spread, and skewness of all 30 SEVs, along with the median. On the opposite side of the same figure, a color palette is displayed, highlighting the maximum (A1 location) and minimum (D3 location) attained SEVs.

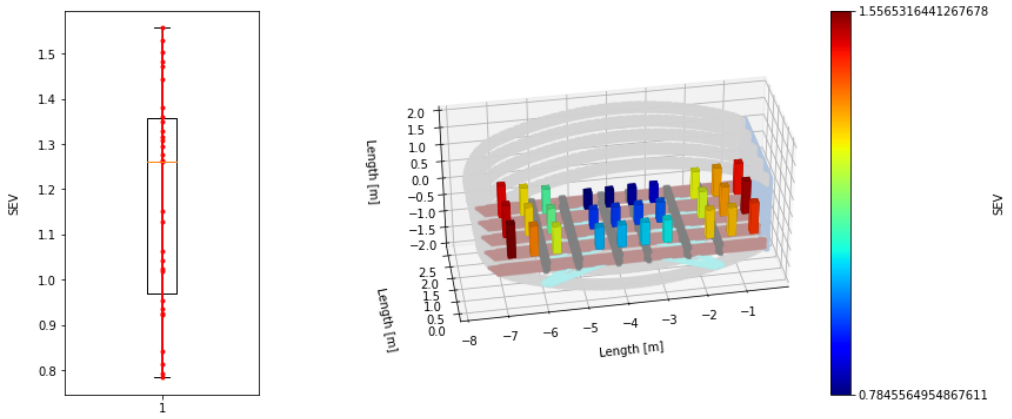

Figure 6.9: Spatial variation of the SEV along the baseline model

The distribution of the Severity Index mirrors the pattern observed in the Dynamic Response Index. This correlation is attributed to the drop test's exclusive emphasis on vertical velocity. Since the DRI plays a pivotal role in SEV calculation, particularly in the context of the drop test's limitation to vertical velocity, it significantly influences the overall SEV. Accelerations in the x and y directions are nearly negligible when compared to those in the z direction.

Once again, SEV values are lower for passengers situated in the central region and progressively increase towards the sides. This alignment with the DRI trend can be explained by the previously mentioned factors: heightened plastic deformations in the central area and increased stiffness towards the sides, resulting in reduced energy absorption laterally.

The results of exploring SEV variation without considering z-direction accelerations (by removing the first fraction in equation 6.4) can be seen in Figure 6.10. The same trend persists, but SEVs are more pronounced, particularly on the sides of the rear section. It will be elaborated further, in Chapter 7, that, upon impact and rebound, the structure tilts backward. This backward lean induces an increase in out-of-plane displacement (y direction), consequently elevating the accelerations experienced by passengers in the y direction.

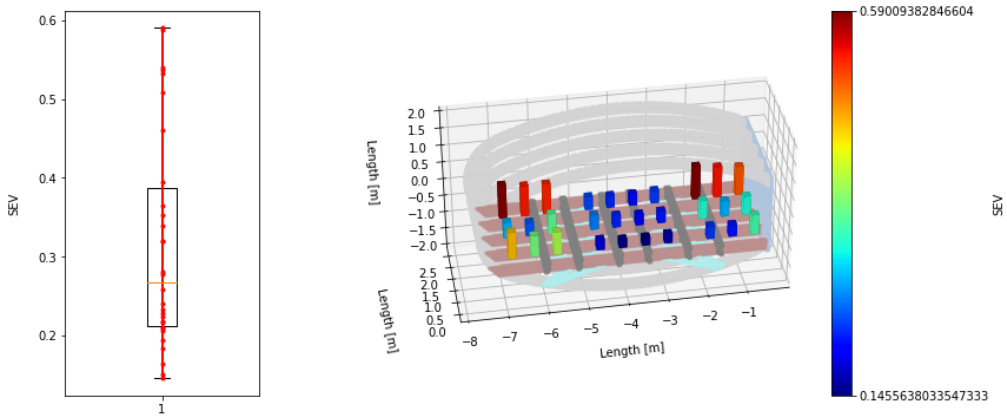

Figure 6.10: Spatial variation of the SEV along the baseline FV section, disregarding accelerations along the z-axis

6.4. Conclusions

The visual comparison of the deformed 4S-5 concept design between Desiderio's thesis and the present study reveals good similarities in deformations. Additionally, the analysis of energy absorption distribution across components in three simulations of varying 4S-5 models, when compared with previous data, demonstrates a consistent pattern. This consistency serves to validate the chosen trio of simulations as representative for the study.

The conventional use of the equivalent Dynamic Response Index (DRI) for structural optimization and crashworthiness assessment falls short in providing insights into the impact of spatial passenger positioning on DRIs. This limitation complicates the evaluation of distinct impact scenarios for the Flying V. Therefore, it is recommended to shift focus towards studying the spatial variation of DRIs for enhanced visual clarity, aiming to identify areas where passengers may sustain more damage. This approach will serve as the foundation for a more comprehensive analysis process in future studies.

The observed variations in passenger damage along the fuselage section are attributed to the plastic deformation of underlying structural elements. Within the central area, DRI values are smaller, gradually increasing towards the sides. The middle area, allowing more room for components to deform, exhibits a pronounced effect, contributing to a reduction in passenger injury. Approaching the sides, there is a notable increase in structural stiffness, resulting in diminished deformations and lower energy absorption during impacts in those specific areas. This, in turn, leads to higher passenger accelerations.

Moreover, a distinct decrease in DRI is noted when moving from the front to the back of the fuselage section. This phenomenon is linked to the crushing and twisting behavior initiated by upward folding frames towards the central floor longitudinal beam. The asymmetrical cross-section of this beam induces lateral deflection of frames, initiating the crushing-twisting motion, further emphasizing the intricate dynamics influencing passenger injury likelihood throughout the aircraft.

When examining the Severity Index (SEV), a similar pattern to that observed in the DRI emerges, as the drop test predominantly emphasizes vertical velocity. However, while the DRI effectively assesses injury probability in the vertical direction, the SEV takes into account lateral, forward, and backward acceleration components, providing a more comprehensive evaluation of the injuries sustained by each passenger. It is therefore concluded that a balanced consideration of both injury criteria is essential for a better understanding of fuselage crashworthiness.

The analysis also acknowledges the need for further exploration, especially in considering possible rotations and out-of-plane displacements, highlighting the importance of an improved understanding of impact scenarios and the potential side loads passengers may experience.

7

Augmented FV Fuselage Section

Achieving a satisfactory equilibrium between computational efficiency and result accuracy is imperative in the finite element model. However, as the analysis delves into more dynamically complex scenarios, expanding the computational domain to encompass larger fuselage sections becomes essential for a more reliable study.

This Chapter addresses this necessity by examining an extended fuselage section size before incorporating the kinematics of other Flying-V sections, as proposed in the Literature. Initiating with a visual inspection of the crash sections in Section 7.1.1, the subsequent step involves delving into the locations of centers of gravity in Section 7.1.2, aiming to provide an explanatory framework for the observed events during the crash scenarios. Nevertheless, recognizing the limitations of relying solely on visual observations for a comprehensive understanding of the crash event, a correlation between absolute energy absorption values, categorized by component, is conducted in Section 7.1.3.

In the following Section 7.1.4, the exploration of kinetic energy variation is undertaken, and the results are compared to the baseline model. To facilitate a more effective comparison between the extended and baseline model, the spatial variation of the DRIs and SEVs is further scrutinized in Section 7.1.5.

Finally, Section 7.2 consolidates and analyzes the findings derived from this Chapter, drawing comparisons with the benchmark model to yield conclusive insights.

7.1. Extended Baseline Model: 5 Frames vs. 10 Frames

To validate the FEA model to assess the crashworthiness of the Flying-V, Desiderio conducted a study to determine the minimum fuselage section size that should be considered. This investigation initially focused on the fuselage of the Fokker F-28, with the finite element model of the F-28 being verified through a mesh convergence study and validated by comparing it to both physical tests and simulations conducted by NASA.

Subsequently, the modelling techniques employed for the FEA model of the Fokker F-28 were adapted to perform a virtual drop test for the typical section of the FV.

Generally, for certification purposes, a six-frame section is conventionally used to assess the crashworthiness of traditional aircrafts. However, Desiderio explored the possibility of analyzing a shorter section for the Fokker F-28 to reduce model size and computational costs.

In this context, the energy absorbed by each component was evaluated for sections with four, five, and six frames. It was concluded that the difference between these three sections is negligible, and a five-frame section was deemed sufficient for assessing the crashworthiness of the FV.

However, this minimum fuselage section size analysis solely considered the energy absorbed by each component and involved a simple qualitative assessment, visually inspecting a crushing-twisting motion in the four-frame section. Other crucial parameters, such as Dynamic Response Index and accelerations, were not considered. Additionally, this analysis was specific to the Fokker F-28, with subsequent results from the minimum section size being translated to the Flying-V.

Also, longer fuselage sections may be more prone to buckling or significant deformation during a crash due to increased bending moments and structural flexing, a factor that needs to be accounted for.

Before expanding the length of the FEM model to cover the entire passengers' fuselage section, the validity of the minimum fuselage section size was questioned. The results for fuselage section with 10 frames for the Flying-V were then extracted and compared to those obtained for the baseline (5 frames) configuration.

7.1.1. Visual Inspection of the Crash Sections

The discernible contrast between the two sections becomes evident upon visual examination of the outcomes (refer to Figures 7.1a and 7.1b). This was unexpected, since the extension of the Flying-V was thought to have little influence as additional mass and surface area were added in an identical manner as the baseline model. Nonetheless, it is apparent that the structural components of the floor exhibit significantly greater deformation towards the rear in the case of 10 frames. This observed phenomenon may be attributed to an uneven distribution of weight along the fuselage section.

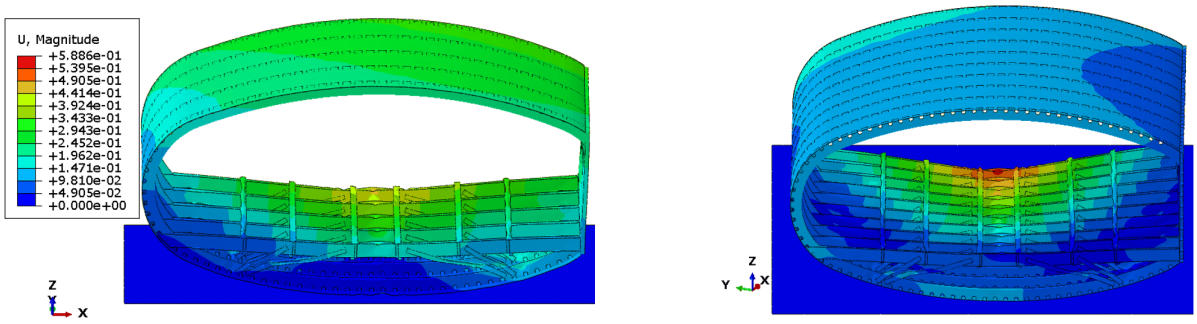

(a) 5 frames model **(b)** 10 frames model

Figure 7.1: Displacement variation for the baseline and extended model

In Figure 7.2, an aerial perspective of the elongated fuselage segment is presented, where the yellow box encloses the baseline FV section, constituting roughly half of the extended model. The red dots signify individual passengers distributed across the section. In the hypothetical division of the extended fuselage into two halves, the front would accommodate 30 passengers, while the rear would host the remaining 40, augmenting the weight borne by the rear floor elements. Additionally, the last row at the back is positioned directly at the section's end, introducing extra momentum without adequate structural support to counterbalance it.

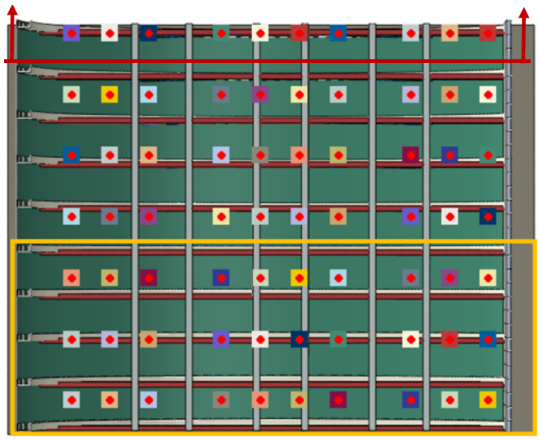

Figure 7.2: Fuselage extension; the yellow box limits the baseline section. Up the red line is the row to be removed

Furthermore, the spacing between passengers and the system comprising struts, floor beams, and frames (all positioned in the same frontal plane) varies. This results in some passengers being seated directly above the frames, while others occupy the spaces between two consecutive frames. The disparate seating arrangements likewise contribute to the observed differences in structural behavior.

Lateral contractions and expansions may also be significant factors influencing fuselage behavior during drop tests, particularly under asymmetrical loading or deformation conditions. Also, the presence of free edges results in subsequent unrestrained contraction in those regions. Figure 7.3 illustrates this effect, as shown in research conducted by Dotman[29]. This, combined with a slight shift in weight towards the rear, could potentially trigger greater localized deformations.

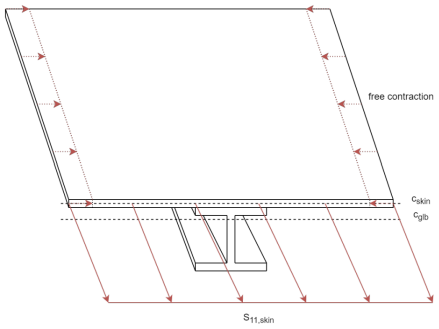

Figure 7.3: Possible free contraction of the frames and skin [29]

In the baseline model, fewer frames provide more lateral flexibility during contraction and expansion, leading to more symmetrical deformations due to reduced resistance.

Conversely, a model with 10 frames imposes more constraints on lateral contraction and expansion, causing asymmetrical and further localized deformations, particularly when there are variations in loading or impact forces along the fuselage length. Taking for instance the current case, an increase in weight at the rear part apply greater force on the rear side, causing the frames to resist lateral movement more strongly and resulting in asymmetrical deformations.

The limitations on lateral movement in the middle frames can also contribute to higher passenger accelerations. Asymmetric deformation, induced by restricted lateral movement and subsequent increased resistance to changes in motion, can generate additional dynamic forces on passengers, leading to elevated accelerations.

Thus, the disparities in lateral contraction and expansion between fuselage models with 5 frames and 10 frames may also contribute to the observed variations in deformation behavior and future passenger accelerations.

It's also important to highlight that the 5-frames section consists of 3 rows, while the 10-frames section encompasses 7 rows. This variation in row configuration leads to a twofold increase in structural weight from one model to the other, a contrast that does not parallel the rise in passenger weight. This observation naturally raises the question: What impact would be observed if the back row was removed?

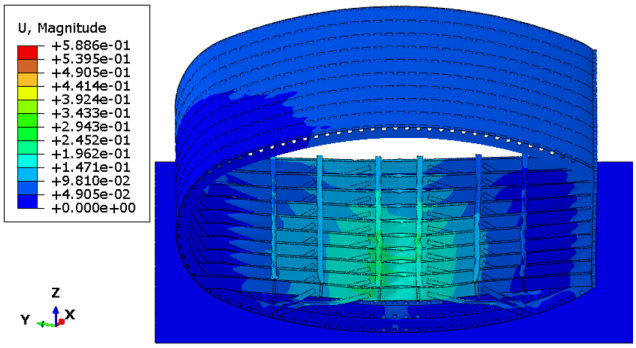

Figure 7.4: Displacement variation for the 10 frames, 6 passenger rows model

Notably, a contrasting trend emerges in comparison to the preceding sections. While the earlier configurations exhibited greater floor deformations towards the rear (particularly pronounced in the extended, 7 rows model), the floor deformation in the 6-row section remains relatively constant along the longitudinal direction, with a slightly heightened deformation at the front part. This divergence finds elucidation by referring to Figure 7.4.

Upon removing the last row (depicted in Figure 7.2) while maintaining the length of the 10 frames fuselage section, a more balanced distribution between structural and passenger weight is attained. However, it is crucial to acknowledge that passenger weight becomes more concentrated in the forward portion, leading to a subtle shift in the center of gravity towards the front. This, in turn, contributes to increased deformations in the front section.

7.1.2. Centers of Gravity Location

The insights derived from visually examining the crash sections are further supported by an analysis of the spatial positions of the structural and passengers' Centers of Mass (CM), as illustrated in Figures 7.5 and 7.6. The structural CM coordinates were directly obtained from Abaqus. However, determining the passengers' CM posed a unique challenge due to the treatment of each passenger plus seat system as a point inertia, making direct extraction unfeasible within the FEM software. Despite this limitation, the CM was determined by identifying the intersection point of the two dashed diagonal lines in Figure 7.5 and 7.6, considering the consistently distributed spacing between passengers in a rectangular/squared pattern.

(a) 10 frames, 6 rows section

(b) 10 frames, 7 rows section

Figure 7.5: CMs' position for the different extended models

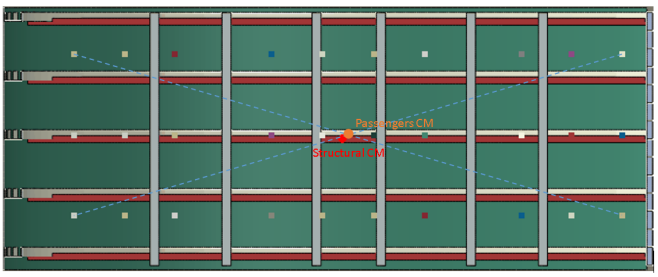

Figure 7.6: Location of the structural and passengers CMs for the 5 frames (baseline) section

Upon examining the CMs' locations, it becomes evident that for the baseline case and the extended 7-rows section, the passengers' CM is slightly positioned above the structural one, resulting in an upward shift of the overall CM. Conversely, for the 10 frames, 6-rows model, the opposite occurs, with the passengers' CM positioned below the structural one, leading to a downward shift of the overall center of mass.

7.1.3. Energy Absorption Distribution by Component

Relying solely on visual observations cannot provide a comprehensive understanding of the crash event. To either substantiate or challenge theories related to the involved energy-absorbing mechanisms, a correlation was established between absolute energy absorption values, categorized by component, and visual inspections. Figure 7.7 serves as a valuable representation, illustrating the percentage of energy absorption for each component. This metric offers a straightforward means of identifying critical structural elements responsible for dissipating crash energy.

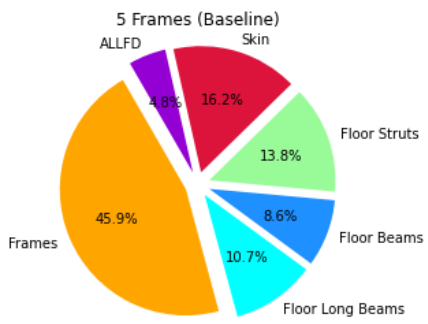

(a) Component energy absorption distribution, 5 frames section

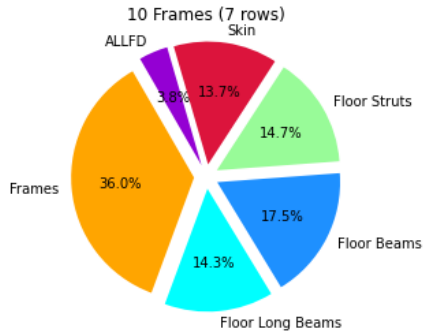

(b) Component energy absorption distribution, 10 frames, 7 rows section

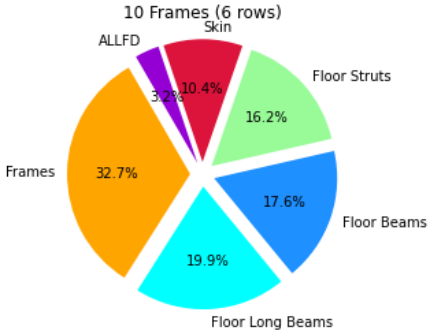

(c) Component energy absorption distribution, 10 frames, 6 rows section

Figure 7.7: Comparison of component energy absorption, 5 frames (2.9 m) vs. 10 frames (5.8 m) with and without row removal

Some differences are evident, with a significant decrease in energy absorption by the frames and a notable increase in absorption by the floor components within the extended FV models when compared to the baseline section. For the 7 rows section case, this phenomenon aligns with the visually observed increase in the coupling between the crushing and twisting behavior of the fuselage section, originating from the upward folding frames impacting the central floor longitudinal beam (refer to Figure 7.8b). The asymmetrical cross-section of this beam induces lateral deflection of the frames, initiating the crushing-twisting motion.

It is worth emphasizing that longer sections seems to display diminished stability against the crushing-twisting mode. As the length increases, there is a higher tendency for the section to bend and become more vulnerable to torsional forces during drop tests, particularly when the load distribution is uneven or if the impact doesn't align precisely with the fuselage's longitudinal axis. Consequently, the frames are not confined to stay centralized, resulting in a more forceful impact with the floor beams. This behaviour might lead to reduced deformation of the frames and increased deformation of the floor beams, manifesting as a noticeable shift in energy absorption and structural behavior between these two components.

In contrast, in the baseline model, the frames consistently steer clear of engaging with the structural elements on the floor, as seen in Figure 7.8a. Consequently, it is the frames themselves that predominantly absorb the impact energy, as this energy doesn't disperse directly through contact with the floor structural elements.

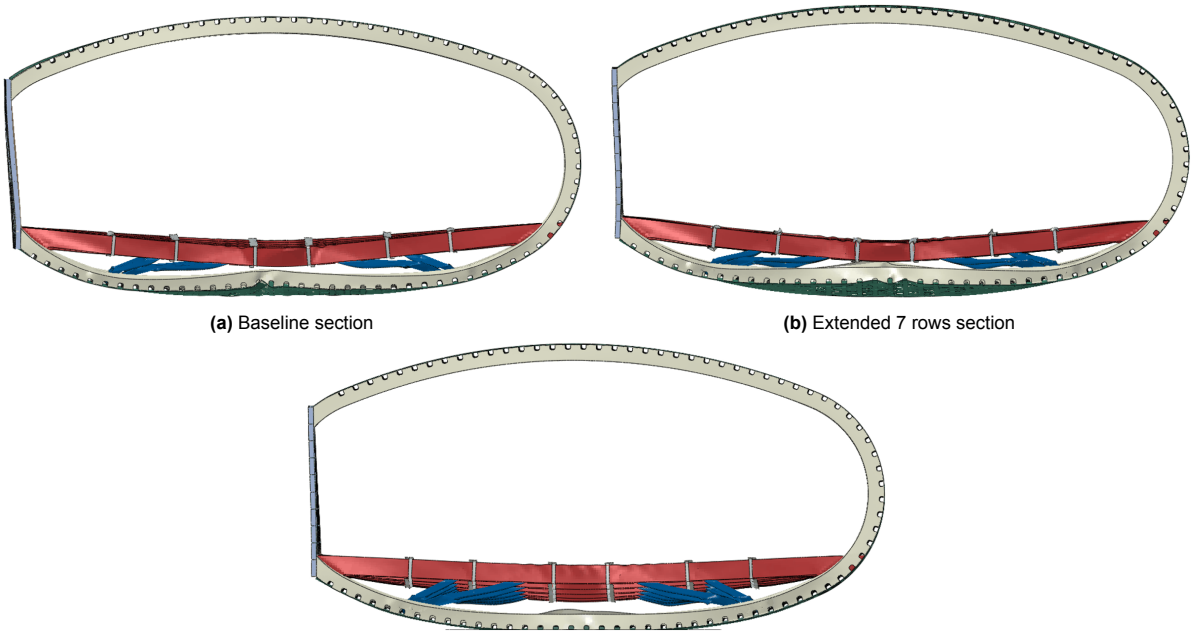

(a) Baseline section

(b) Extended 7 rows section

(c) Extended 6 rows section

Figure 7.8: Back view comparison of the maximum structural deformation between different models

As mentioned earlier, the 10 frames, 6 rows section exhibits more consistent floor deformation. This phenomenon may be ascribed to the comparatively heightened energy absorption by the floor longitudinal beams. These beams deform uniformly along the longitudinal axis, contributing to a sustained structural integrity in that direction, helping to maintain a more stable and constant overall structural profile.

7.1.4. Kinetic Energy Time History

Figure 7.9 displays the time history plots of kinetic energy for the three cases. Initially, it's evident that the baseline fuselage section exhibits significantly lower K_{eg} compared to the extended models. Despite having the same initial velocity, its mass is approximately half that of the other two sections, resulting in roughly half the kinetic energy. The impact of removing the last passenger row is also evident in Figure 7.9, displaying a lower initial kinetic energy compared to its 7-rows counterpart.

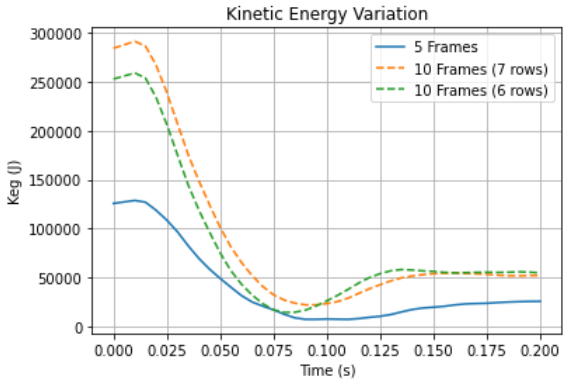

Figure 7.9: Model kinetic energy vs. time; different lines indicate different fuselage sections

Initially, all three models undergo an increase in energy due to the initial negative vertical velocity applied when the model is not entirely in contact with the ground.

The subsequent analysis delves into the rate at which the kinetic energy of the fuselage section and occupants converts to elastic and plastic energy, denoted by the slope of the K_{eg} vs. time curve ($\dot{K}_{eg}$).

Extended FV sections demonstrate a higher dissipation rate, suggesting more forceful ground contact and consequently larger acceleration pulses experienced by occupants, a factor that will be examined upon studying the variation of DRIs.

Moving on to the point of maximum deformation, indicating the moment when kinetic energy is minimized, it becomes evident that the baseline FV section deforms the most, followed by the 10 frames 7 rows and, finally, the 10 frames 6 rows - consistent with visual observations. Surprisingly, kinetic energy doesn't reach zero at this point, maintaining some residual energy as different nodes reach zero-velocity at different times.

In the final phase, the rebound occurs, releasing elastic energy stored in the structure and converting it back into kinetic energy or dissipating it through vibrations in the case of material failure. Rebounds are generally undesirable as they prolong the duration of acceleration pulses experienced by occupants. Upon analysis of Figure 7.9, a higher rebound is observed in the 10 frames, 6 rows FV section, followed by a decrease in the extended 7 rows section, and the least rebound occurs in the baseline FV model. This trend could be attributed to the gradual reduction in plastic deformation for the sections, resulting in more elastic energy stored in the structure.

A summary of the energy extractions for the three models is provided in Table 7.1. Of particular interest is the examination of total plastic dissipation divided by the initial kinetic energy for each section, supporting the conclusions drawn from the point of maximum deformation. Again, the 5 frames FV section exhibits the highest deformation, followed by the 10 frames 7 rows, and lastly, the 10 frames 6 rows.

Table 7.1: Fraction of energy dissipated, by component, for the 5 and 10 frames sections

Energy	5 Frames	10 Frames (7 Rows)	10 Frames (6 Rows)
Initial K_{eg}[kJ]	128.83	291.28	291.21
Final E_D[kJ]	91.10	200.12	171.28
Total $\frac{E_D}{K_{cg}}$[%]	70.71	68.66	58.82
-Skin [%]	12.03	9.54	6.22
-Frames [%]	34.00	25.16	19.56
-Floor Struts [%]	10.17	10.23	9.67
-Floor Long Beams [%]	7.92	10.02	11.91
-Floor Beams [%]	6.39	12.26	10.56
Friction [kJ]	4.59	7.79	1.92

7.1.5. DRIs and Severity Indexes Analysis

Following a methodology akin to the assessment applied to the baseline FV section, an examination of the spatial variation of DRIs and SEVs was conducted for the two extended models. In Figure 7.10, spatial position labels for passengers within the 10 frames FV section are depicted. While the longitudinal row remains consistent (ranging from A to J), the numerical range now spans from 1 to 7 rows for one model (comprising 70 passengers) and 1 to 6 rows for the other model (involving 60 passengers).

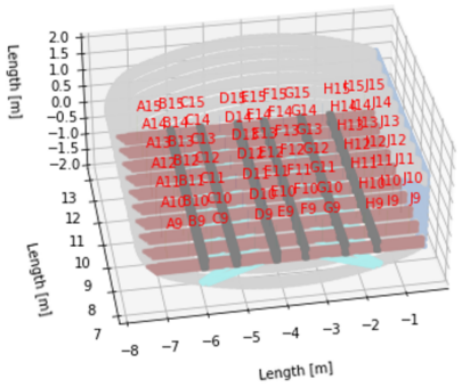

Figure 7.10: Labels indicating the spatial positions of passengers within the fuselage section consisting of 10 frames

Figure 7.11a and Figure 7.11b illustrate the spatial variation of DRIs and SEVs for the 10-frame, 7-passenger-row section. In comparison to the baseline model results (depicted in Figures 6.7 and 6.9), the minimum DRI and SEV persistently remain at 11.93 and 0.77, respectively, situated in the middle rear area. Notably, outliers A2 and J2 exhibit abnormally high DRI and SEV values (nearly 28 and 2, respectively) compared to neighboring locations. However, the skewness and median of both injury criteria remain consistent with those of the 5-frame baseline section.

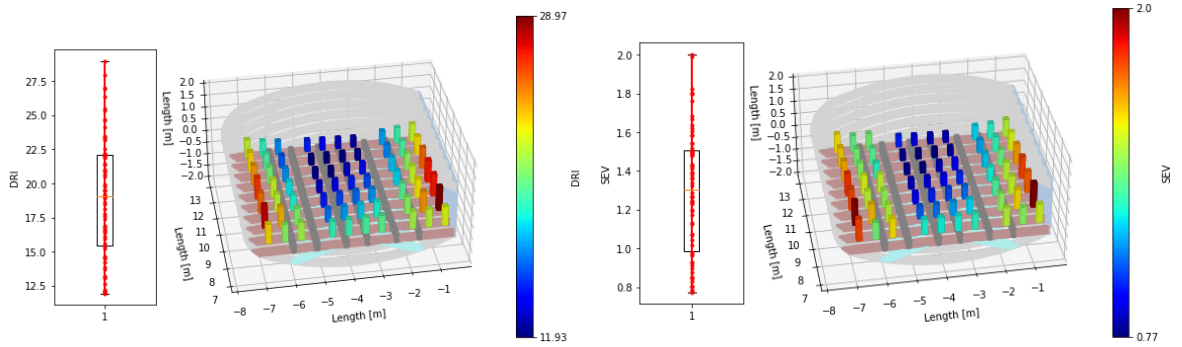

(a) Spatial variation of the DRI **(b)** Spatial variation of the SEV

Figure 7.11: Spatial variation of the DRI and SEV along the extended, 7 rows FV section

The longitudinal variation of DRIs and SEVs aligns with the baseline model, showing an overall decrease from front to back, with higher values at the sides (stiffer region) and lower values in the middle (providing more crushing space, leading to increased plastic deformation). The longitudinal decrease in DRI and SEV is more pronounced than in the 5-frame section.

These results reinforce the observations in Figure 7.1b and the earlier conclusions: the weight distribution is more concentrated towards the back, and the last row at the rear is directly positioned at the end of the section, introducing additional momentum without sufficient structural support to counteract it. As a notable observation, the first three and last three passengers in the front row exhibit abnormally smaller values compared to the overall trend, where values abruptly increase in the second row and gradually decrease towards the back of the section.

Moving forward, upon scrutinizing Figure 7.12a and 7.12b, and building on the insights from Figure 7.4 regarding the 10-frame, 6-row sections, a contrasting pattern emerges. Slightly elevated deformations are observed at the front of the section, substantiated by lower DRIs and SEVs in that region. This phenomenon results from a minor shift of the center of gravity towards the front, prompted by the removal of the last back row. Nevertheless, longitudinally, the values remain relatively constant due to the more uniform floor deformation. Both the maximum and minimum DRI and SEV, along with the median, experience an increase compared to the other two models.

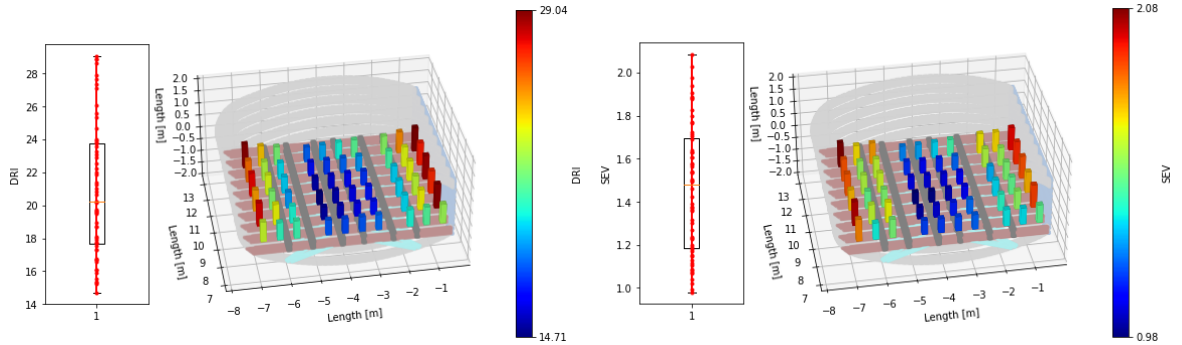

(a) Spatial variation of the DRI **(b)** Spatial variation of the SEV

Figure 7.12: Spatial variation of the DRI and SEV along the extended, 6 rows FV section

As mentioned earlier, the spacing between passengers and the system composed of struts, floor beams, and frames positioned in the same frontal plane exhibits variation.

Passengers are distributed such that some are directly above frames, while others occupy spaces between consecutive frames. This spatial discrepancy is evident in the longitudinal arrangement of side rows in DRIs and SEVs for the 10-frame, 6-row section, where higher DRIs correspond to passengers seated directly above the frames, alternating with lower values linked to those occupying spaces between consecutive frames.

7.2. Discussion on the Results

The visible deformation contrast between the baseline and extended section was initially unexpected, as the extension of the Flying-V was thought to have little influence as additional mass and surface area were added in an identical manner as the baseline fuselage. Nonetheless, the observed distinct imbalance in weight distribution along the fuselage, particularly pronounced in the 10 frames section, may explain these differences. Occupants concentration towards the rear half of the extended fuselage introduced asymmetry, leading to significant floor deformations in the same region. This phenomenon was exacerbated by variations in spacing between passengers and structural components, contributing to differences in structural behavior.

Lateral contractions and expansions could also significantly influence fuselage behavior during drop tests, especially under asymmetrical loading or deformation conditions, such as when weight is concentrated more heavily at the back. In a fuselage model with 5 frames, the fewer frames afford greater lateral freedom during contraction and expansion. This reduced constraint may lead to less resistance to lateral movement during deformation, resulting in more uniformly distributed deformations and symmetrical behavior overall.

Conversely, a model with 10 frames places more restrictions on lateral contraction and expansion. This heightened constraint can result in asymmetrical deformations, particularly when there are variations in loading or impact forces along the fuselage length. For example, a concentration of weight at the rear may exert greater force on the back side, causing the frames to resist lateral movement more vigorously and leading to asymmetrical deformations.

The removal of the last row in the 10 frames fuselage section aimed to address the weight distribution imbalance and lead to closer resemblances with the deformations of the baseline model. By doing so, a more balanced load on the structure could be achieved, along with maintaining the same ratio of structural and passenger mass as the baseline model. However, this adjustment resulted in a new challenge, concentrating passenger weight towards the front and inducing a subtle shift in the center of gravity. This shift led to a different crash behaviour with slightly elevated deformations at the front section. Also, an increase in overall structural stiffness was achieved as a result of the less deformed fuselage, explaining the higher DRIs and SEVs obtained.

In an effort to clarify the varied structural responses to dynamic loading, an examination was undertaken to compare the energy absorption patterns between the extended 7-row FV model and the baseline section. It was observed that the elongation of the model was associated with a decrease and subsequent increase in energy absorbed by the frames and floor structural components, respectively. The longer section appeared to demonstrate decrease stability against crushing-twisting modes, leading to contact between the frames and floor beams, potentially explaining the shift in energy absorption between these elements. Furthermore, the extended model's more forceful ground impact, supported by a higher dissipation rate derived from kinetic energy analysis, may corroborate the subsequent impact of these structural elements and the overall increase in DRIs and SEVs values.

In the 10-frame, 6-row case, the heightened energy absorption by the floor longitudinal beams may explain the distinctive floor deformation along the longitudinal direction, ensuring a more sustained and uniformly distributed structural integrity overall. Also, the increased residual kinetic energy during the rebound phase carried significant implications for occupant safety, prolonging the acceleration pulses and further increasing the DRIs and SEVs.

This analysis aimed to address discrepancies in crash behaviors and the consequent rise in DRIs and SEVs when longer fuselage sections are examined. Despite offering some potential explanations for the observed phenomena, substantial differences in energy absorption by component still remain unclear with increasing frame numbers. To provide further clarity, upcoming Chapters will introduce new modeling approaches to better understand these differences and attempt to mitigate out-of-plane buckling and induced lateral contractions and expansions, particularly noticeable at the rear free cross-sectional edges.

8

Dynamic Boundary Conditions: Modelling Sliding Interfaces for Enhanced Simulations

In real-world emergency landing scenarios, the entire airplane would typically experience impact. However, conducting experimental drop tests for the entire aircraft is cost-prohibitive and, as a result, smaller section of the fuselage is often chosen for such tests. Nonetheless, it's important to note that in these cases, each side of the fuselage section lacks constraints and can deform freely. This free deformation is unlike what would occur structurally if other components of the subsequent sections were present to counteract lateral deformations.

As an alternative, this Chapter investigates the impact of sliding boundary conditions on the structural dynamics of fuselage sections during simulated emergency landing scenarios. It commences by, in Section 8.1.1, examining the influence of these condition on the deformation behavior of fuselage sections. Following this, the analysis delves into stability considerations in Section 8.1.2, with specific attention to lateral perspectives and the role of sliding boundary conditions in minimizing accelerations at key points. Subsequently, in Section 8.1.3 energy absorption distribution by component is examined to discern the alterations induced by constraining lateral movements.

The kinetic energy time history studied in Section 8.1.4 provides an overview of mass and velocity variations with and without sliding boundary conditions. Subsequently, Section 8.1.5 explores the variation of Dynamic Response and Severity Indexes, revealing the implications of constrained out-of-plane displacement and lateral accelerations on the overall structural response. Finally, Section 8.2 concludes this Chapter by giving an interpretation of the findings.

8.1. Introducing Sliding Boundary Conditions

Previously it was seen that the unrestricted edges of the studied model may lead to unrealistic buckling effects, resulting in unclear discrepancies in component energy absorption and undesirable crushing and twisting behaviors. This, in turn, contributed to an uneven distribution of DRIs and SEVs longitudinally, particularly near one of the free cross sections, effects which became apparent during visual inspections of deformation modes and the spatial variation of the injury criteria along the fuselage sections.

Lateral contractions and expansions may also contribute to the asymmetrical deformation conditions. Research conducted by Dotman [29] has highlighted that tensile stresses are notably high in the outer skin and spar, whereas compressive stresses are predominant in the floor. The Poisson's effect induces significant contraction in components like the skin and spar, while expansion occurs in the floor (see Figure 7.3). If left unaddressed, this phenomenon can lead to a shape resembling an hourglass, as depicted in Figure 8.1.

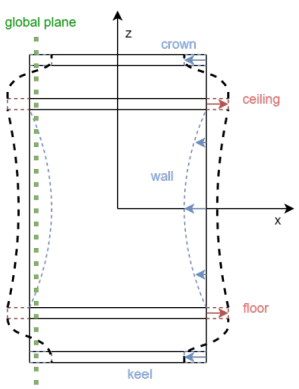

(a) Hourglassing effect by unrestricted expansion and contraction

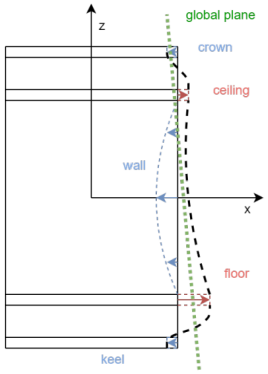

(b) Asymmetric hourglassing due to different lateral expansions, causing a change in angle about y

Figure 8.1: Possible hourglassing effects [29]

According to Dotman's work, it is crucial to effectively resist this "hourglassing" effect through adjacent structural elements. Therefore, ensuring that all edges lie on a single contraction plane is imperative. With that being said, to address these issues and promote more consistent deformation without firstly adding neighboring structure to the free edges, a modification is proposed. Specifically, the deformation in the longitudinal direction (y-axis) is constrained to zero at the two free cross sections, aiming to mitigate unrealistic effects caused by uncontrolled lateral deformations and enhance the overall accuracy of the simulation.

8.1.1. Visual Inspection of the Crash Sections

Figure 8.2 illustrates the deformed state of the different sections, showcasing differences with and without boundary conditions.

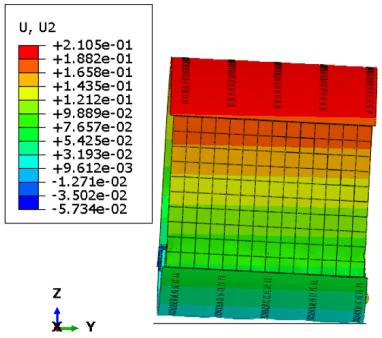

(a) Baseline section, without BC

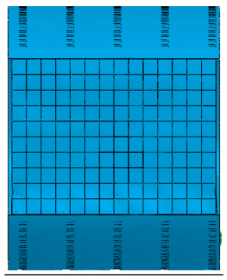

(b) Baseline section, with BC

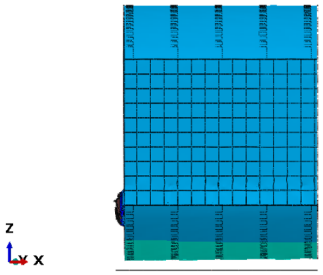

(c) Extended, 7 rows section, with same length as baseline model

Figure 8.2: Side view of different models, with and without BC

In Figure 8.2a, the section exhibits a slight forward lean. However, when a sliding boundary condition is implemented to restrict out-of-plane displacement (in the lateral y-direction), the section maintains perpendicularity to the ground (refer to Figure 8.2b). The inclination observed without the boundary condition is attributed to the section's uneven weight distribution, small longitudinal size, inherent asymmetry in the model and possibly different components' lateral expansions along the free cross sections. Notably, the floor struts connect to the front faces of the floor beams and, after the model's collision with the ground, they internally deform (from left to right in the side view depicted in Figure 8.2a). The deformation is affected by the C-shaped configuration of the struts, where the open side typically exhibits lower bending stiffness, determining the direction of eventual strut distortion. Subsequent contact with the floor beams intensifies this internal distortion. As the struts are linked to the floor beams and frames, the lateral deformation propagates to the connected components.

Following the initial impact, the structure rebounds, causing a more pronounced shift in the center of mass towards the interior (again from left to right). This asymmetry, coupled with the asymmetric hourglassing behaviour, results in a leaning effect which is alleviated when out-of-plane displacement is constrained.

Figure 8.2c illustrates a scaled-down version of the extended, 7-rows model, aligning its length with that of the baseline section. In comparison to the 5-frame section with boundary conditions, the out-of-plane displacements exhibit remarkable similarity. In one scenario, the lateral deformations are restricted by the subsequent structural elements, which have been omitted in the current depiction. In the alternative case, this limitation is imposed by the inclusion of boundary conditions.

On the contrary, Figure 8.3 presents a lateral perspective of the 10-frame, 7-rows section, both with and without boundary conditions. Due to its greater weight and extended longitudinal dimension in comparison to the 5-frame section, the model demonstrates increased stability, diminishing the impact of the out-of-plane constraint on post-impact behaviour. Consequently, the lateral deformations exhibit a higher degree of similarity with and without boundary conditions.

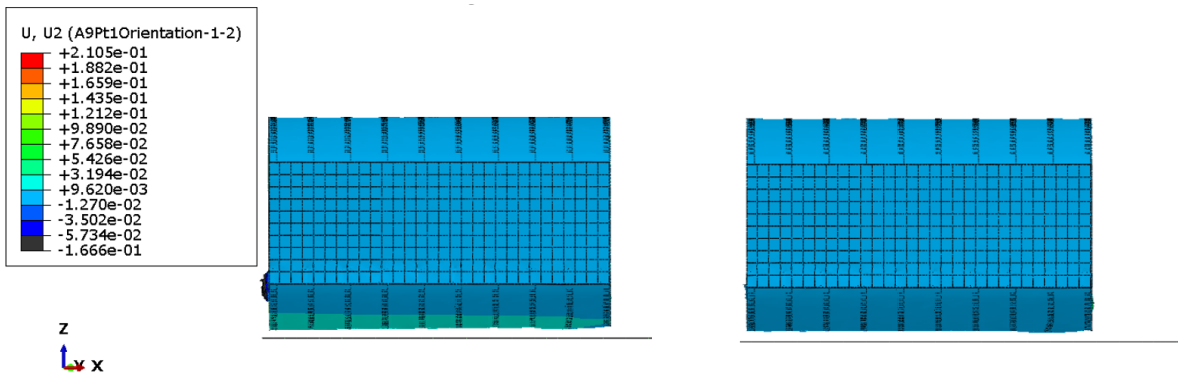

(a) Extended section, without BC

(b) Extended section, with BC

Figure 8.3: Side view of the extended 10 frames section, with and without BC

The visual examination of Figure 8.4 provides a clearer understanding of the deformations in the sections, when both the baseline and extended models incorporate sliding boundary conditions.

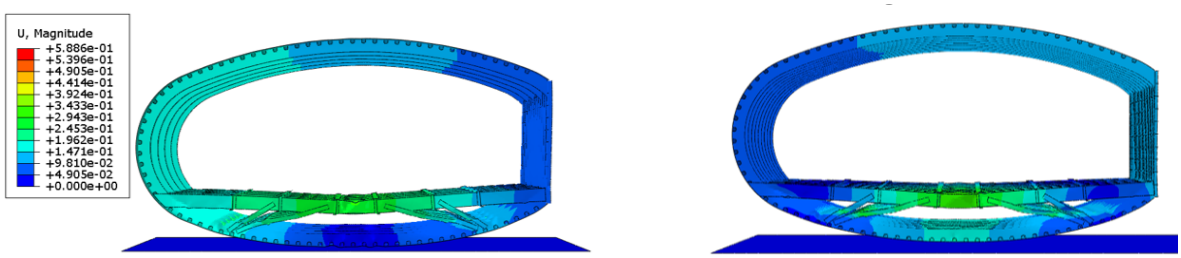

(a) Front view of the baseline section

(b) Front view of the extended section

Figure 8.4: Front view of the two sections being analysed, with BC applied

A noticeable resemblance can be observed. In contrast to previous findings where drop tests resulted in higher deformations at the rear part of both models, the present scenarios reveal a consistent deformation along the floor elements. This observation already offers good insights into the effectiveness of the boundary conditions in mitigating buckling effects and subsequent undesirable twisting behaviors, as well as constraining lateral contractions and expansions located at the free edges.

8.1.2. Acceleration Analysis

An improved understanding of the boundary condition's effect emerges when examining accelerations at a common point across the three models. The rationale behind this analysis is to provide insights into the correlation of results when applying a boundary condition versus having other structural elements in subsequent sections, both aiming to restrict deformations at the analyzed points. The specific point chosen for analysis is depicted in Figure 8.5, where a longitudinal cut was executed for the 10-frame section to make it identical to the 5-frame one (the cut was made along the upper limit of the yellow box in Figure 7.2 and it is represented in Figure 8.2c).

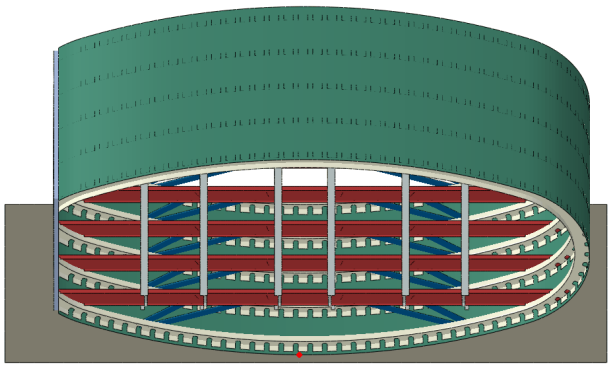

Figure 8.5: Location of the point where the accelerations were extracted

Figure 8.6 displays the temporal variations in magnitude, x, y, and z accelerations at that point for the three different models.

Upon analysing the results, it becomes evident that the 5-frame model without a boundary condition exhibits nearly four times higher magnitude acceleration than the model with the applied boundary condition (refer to Figure 8.6a). In terms of out-of-plane displacement (y-direction), the 5-frame model with boundary condition shows zero displacement, resulting in zero accelerations in that direction. The 10-frame model without boundary condition displays minimal out-of-plane displacement since subsequent structural elements restrict such deformations. In contrast, the 5-frame section without a boundary condition exhibits a pronounced initial peak.

Moreover, given the constrained out-of-plane displacement when implementing the boundary conditions, the structure is compelled to move more significantly in the alternative available direction, namely the x-direction. This observation is substantiated by the findings in Figure 8.6b, indicating that the accelerations in the x-direction for the 5-frame section with BC are more pronounced compared to the other two models.

8.1.3. Energy Absorption Distribution by Component

Figure 8.7 displays the energy dissipation by individual components for two models incorporating sliding boundary conditions. A comparison can be made by contrasting these outcomes with those depicted in Figures 7.7a and 7.7b, which present the energy absorption by component for the same two models in the absence of applied boundary conditions. It would be expected that, upon mitigating the out-of-plane buckling for both models, the energy absorption by component would now more closely align. However, this expectation does not hold true.

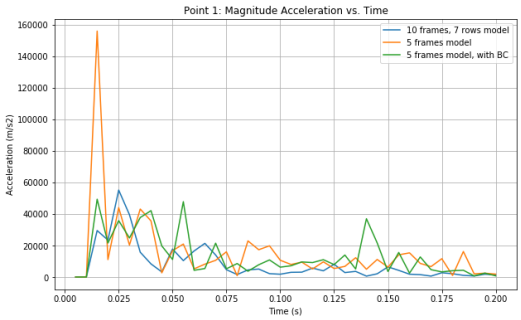

(a) Magnitude acceleration

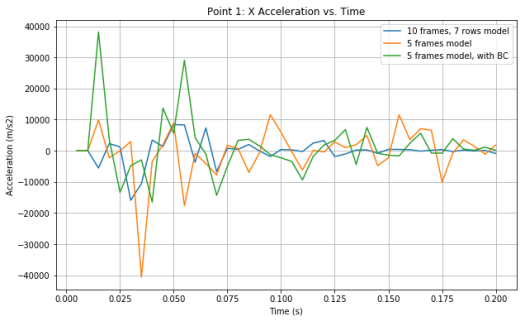

(b) Acceleration in the x-direction

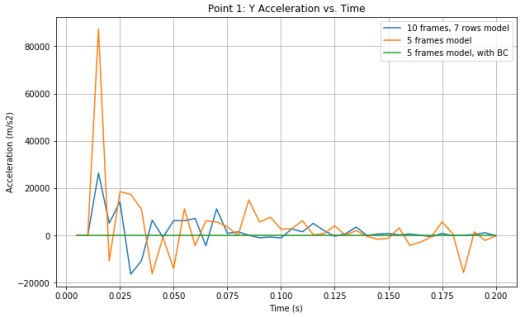

(c) Acceleration in the y-direction

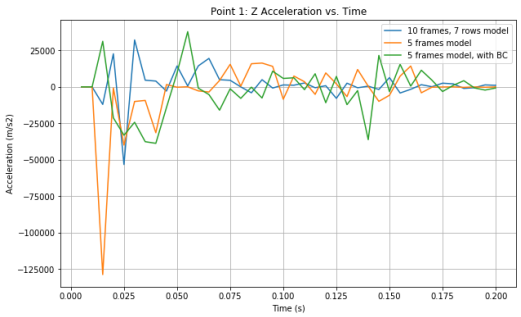

(d) Acceleration in the z-direction

Figure 8.6: Changes in accelerations over time at a specified control point

Nonetheless, across all elements, a consistent trend emerges: in the current analysis, there is an increase in dissipated energy for frames, floor struts, and skin, while there is a decrease for other components, including floor long beams and floor beams, along with a reduction in friction dissipation.

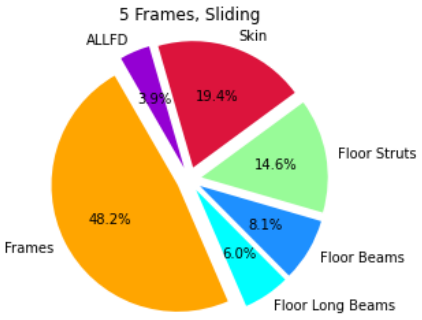

(a) Component energy absorption distribution, 5 frames section with sliding BC

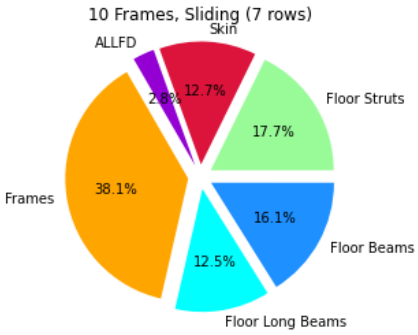

(b) Component energy absorption distribution, 10 frames (7 rows) section with sliding BC

Figure 8.7: Evaluation of the energy absorption capabilities of models featuring sliding boundary conditions

The difference in results might be attributed to the prevention of crushing and twisting behaviors upon the introduction of sliding boundary conditions. The out-of-plane constraints effectively minimize buckling effects, consequently reducing floor deformations, especially near the free edges. This deduction is substantiated by Figures 8.4a and 8.4b, and an examination of the spatial variation of the DRIs and SEVs will provide further support to these conclusions.

Likewise, in the current modelling case, the frames avoid engaging with the structural elements on the floor. This might explain the increased deformation of the frames and decreased deformation of the floor and longitudinal beams, manifesting as a noticeable shift in energy absorption and structural behavior between these components. Moreover, due to the interconnection between frames and struts, distortions extend to subsequent structural elements, possibly escalating the energy absorbed by the struts.

8.1.4. Kinetic Energy Time History

Kinetic energy variations for all the models analysed so far are displayed in Figure 8.8. The newly introduced sections with boundary conditions applied are represented by dashed lines. As anticipated, given that the mass and velocity of the models remained consistent with their predecessors, the curves overlap and, due to this similarity, a reanalysis of the results will not be conducted.

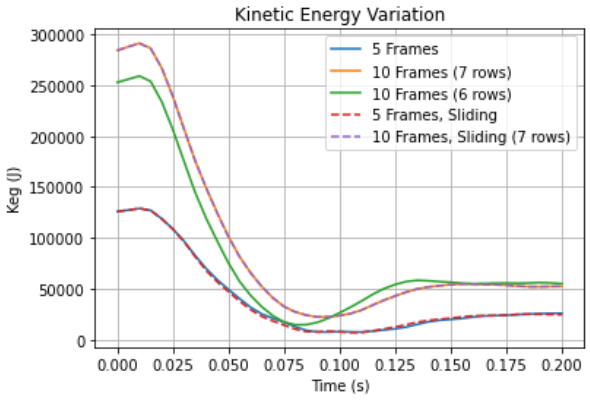

Figure 8.8: Model kinetic energy vs. time; dashed lines indicate the models with the BC applied

8.1.5. DRIs and Severity Indexes Analysis

Good insights can be drawn from the variation in DRIs and SEVs in the base model when subjected to boundary conditions. Departing from previous trends, the structure now maintains perpendicular alignment to the ground, eliminating the leaning effects induced by the asymmetrical structural distribution and rebounding upon impact, as well as previous lateral contractions and expansions more pronounced at the free edges. This alignment is evident in Figures 8.9a and 8.9b, where DRIs and SEVs exhibit a relatively constant values longitudinally. Nevertheless, the application of the boundary conditions adds additional stiffness to the sides. As a result, both the maximum (1.65) and minimum SEV (0.83) experience an increase compared to the baseline model.

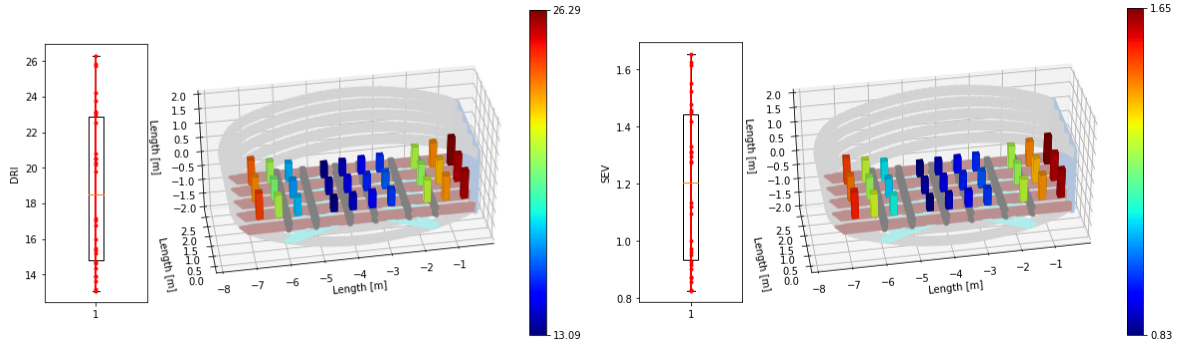

(a) Spatial variation of the DRI

(b) Spatial variation of the SEV

Figure 8.9: Spatial variation of the DRI and SEV along the baseline section, with sliding boundary conditions

The influence of lateral accelerations was also investigated by excluding the z acceleration from equation 6.4 when computing the SEV. Additionally, as the out-of-plane displacement is constrained, the y contribution is minimized. The outcomes of this analysis are depicted in Figure 8.10, revealing that, indeed, the SEV is lower than the baseline case (refer to Figure 6.10). While in the previous scenario, the SEV without the z component still adhered to the overall trend (higher on the lateral sides and lower in the middle), a distinct behaviour unfolds with boundary conditions.

In this case, the x component is significantly higher along the first three longitudinal rows (A to C), diminishes in the middle four rows, and experiences a slight increase in rows H to J.

Upon constraining the out-of-plane displacement, following impact and rebound, the fuselage is limited to upward or sideways movement along the x-direction.

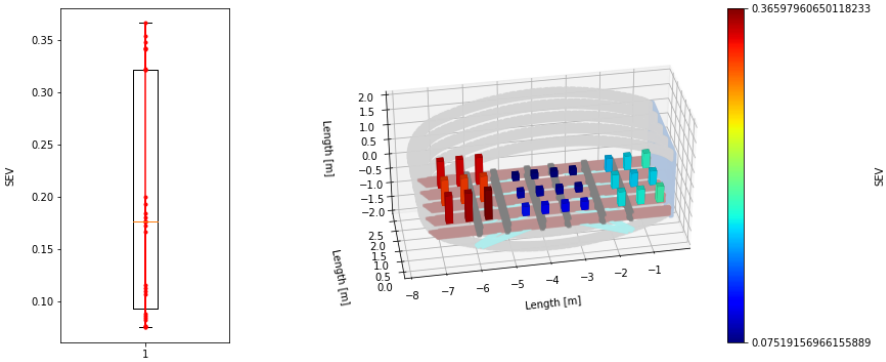

Figure 8.10: Spatial variation of the SEV along the baseline FV section, with sliding boundary conditions applied and disregarding accelerations in the z direction

In the extended, 7 passenger rows section shown in Figure 7.11, there were still slightly reduced DRIs and SEVs values at the back when compared to the front. This disparity was further minimized with the application of boundary conditions. Now, the uniformity in results is accentuated even further, as evident in Figure 8.11a and 8.11b. However, restricting the out-of-plane deformation amplifies the accelerations in the other two possible directions, leading to a peak DRI and SEV (30.4 and 2.1, respectively).

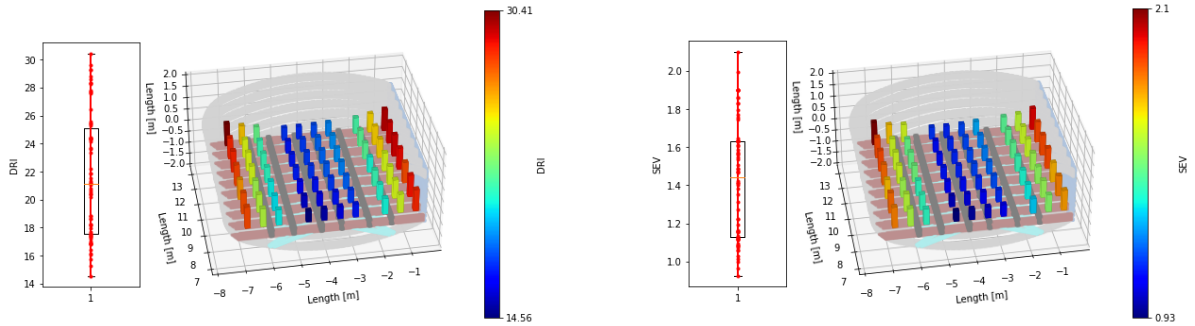

(a) Spatial variation of the DRI

(b) Spatial variation of the SEV

Figure 8.11: Spatial variation of the DRI along the extended section, with sliding boundary conditions

8.2. Interpretation of the Findings

The proposed modification, involving the constraint of longitudinal deformation at free cross sections, effectively minimized the crushing and twisting behaviour, achieving more uniform deformations and enhancing the overall accuracy of simulations. Thus, it can be concluded that the previously hypothesized factor of increased lateral contractions and expansions at the free edges, which was suspected to have a significant impact on the asymmetrical longitudinal deformations, has indeed been validated to some extent. Nonetheless, this was accompanied with stiffer sections at the sides, leading to the overall increase in accelerations sustained by the passengers. Despite this and the closer resemblance between both deformed models, one might assume that by mitigating out-of-plane buckling, the energy absorption by components would align more closely. However, this assumption proved to be incorrect.

In the end, no definitive explanation was found for these differences. Initially, one potential factor could be due to the relatively short length of the baseline model, which might not adequately capture the behavior of the Flying-V's fuselage section during vertical ground impact.

Nonetheless, the lack of longitudinal stability due to the small size and the subsequent lean upon rebouncing, factors these that, before, may had also contributed to the difference in behaviour between baseline and extended models, were solved by constraining the lateral contractions and expansions of the free edges. Yet, despite this intervention, differences persisted in energy absorption by components and in DRIs and SEVs. Additionally, the dynamic response of the fuselage sections during the drop test relies on factors such as material properties, geometry, and damping characteristics. Despite the similar modelling of both sections, slight disparities in these factors could have contributed to differences in dynamic behavior, potentially resulting in varying levels of deformation and accelerations experienced by the passengers.

However, the conclusions drawn earlier do not diminish the value of the remaining simulations. The current method still allows for comparing different cases and drawing conclusions about their effects. While the sliding boundary conditions achieved more realistic and uniform deformations during simulated emergency landing scenarios, there still remains an avenue for further exploration into the impact of introducing additional structural elements to constrain lateral deformations. A more extensive analysis of the distinctions between mitigating lateral deformations through the application of boundary conditions versus incorporating structural elements will be undertaken in subsequent studies.

9

Full Passenger Fuselage Model

Previous investigations expanded the model of the Flying-V section by doubling its length. However, these instances lacked constraints on each side of the fuselage section, allowing for unrestricted deformation that could result in predominantly unrealistic out-of-plane displacement. To address this issue, the preceding Chapter introduced lateral sliding boundary conditions, effectively mitigating uneven longitudinal deformations and leading to closer crash sections between the analysed models. It was emphasized and briefly studied that a similar effect could occur if other components of subsequent sections were present to counteract lateral deformations. Thus, the basis of this Chapter is to examine the crashworthiness of the entire passenger fuselage, with a particular focus on the middle engine section, constituting the extended model. Subsequent analysis will compare results obtained with sliding boundary conditions to assess the consistency of fuselage deformations.

Furthermore, for a better analysis of potential Flying-V crash scenarios without oversimplifying, and for the subsequent validation of a reduced modelling technique introduced in upcoming Chapters, the crashworthiness assessment had to be extended to the full passenger fuselage. The study begins by outlining, in Section 9.1, the finite element method model of the complete passenger fuselage and its resemblances to the extended model. This is followed by a visual inspection of the crash section and an analysis of the centers of gravity location in Section 9.2 and Section 9.2.1, respectively. Energy analysis is then conducted in Section 9.3 and Section 9.4, with the results compared to those obtained from other modelling approaches. The spatial distribution of the DRIs and SEVs is addressed in Section 9.5, and finally, Section 9.6 provides a reflection on the results.

9.1. Geometrical and Numerical FEM Model Description

Illustrated in Figure 9.1 is the passengers' fuselage section, accommodating a total of 210 passengers and with a length of 19000 mm. The spatial positioning of such model along the full Flying-V aircraft can be seen in Figure 5.2.

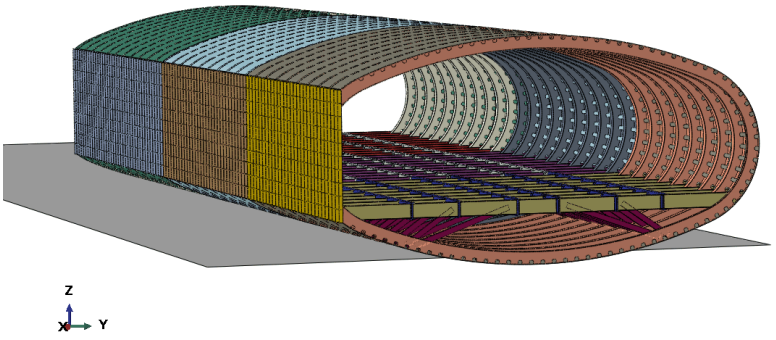

Figure 9.1: Whole passengers' fuselage section

The full model is subdivided into three smaller segments: the back, engine, and front sections. The engine part is essentially the extended model, featuring tie connections with the other two sections. This division is visually highlighted in Figure 9.1 through distinct color representations.

In the event of a ground impact, the sub-cargo floor area emerges as the fuselage region most susceptible to absorbing kinetic energy. For a clearer comprehension of its design, Figure 9.2a visually outlines the components within this specific section.

The complete fuselage section carries a weight of 27252.9 kg. Prior to the drop test, extra masses, as depicted in Figure 9.2b, were introduced following the same procedure applied to previous models.

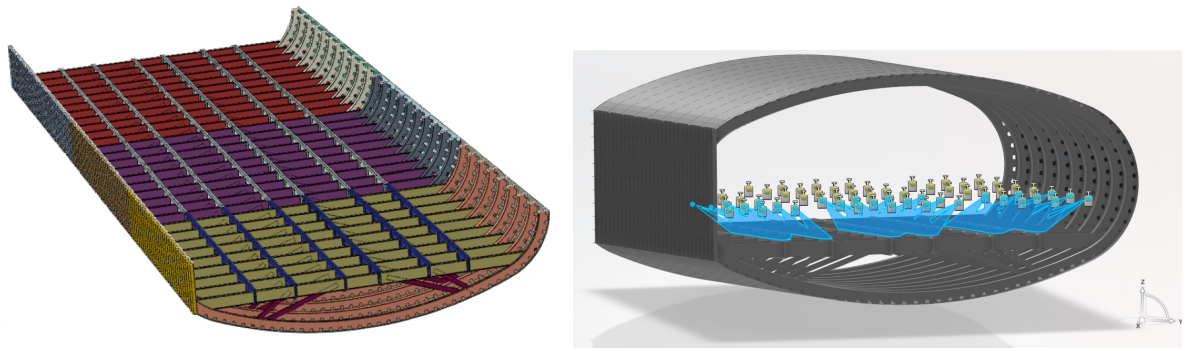

(a) Subsection cargo floor **(b)** Position of seat dummies

Figure 9.2: Representation of cargo floor and seat dummies position

For increased accuracy in replicating ground effects, the plane, fixed in space, was considered rigid, eliminating the need for mesh use. Similarly, the same drop test conditions were maintained, with a starting vertical velocity of 7900 mm/s downwards applied to each point on the fuselage section. As with earlier models, simplification was achieved by removing physical connections, such as rivets and bolts, replaced by a multipoint constraint tie available in Abaqus.

9.2. Visual Inspection of the Crash Section

The outcomes post-impact are illustrated in Figure 9.3 and 9.4a. The displacement magnitude limits were adjusted to align with the limits of both the baseline and extended sections, facilitating a more visually effective comparison.

The representation from both the front and rear perspectives distinctly reveals increased displacement of floor beams and longitudinal floor beams at the center of the section. These observations are substantiated by the diagonal top view in Figure 9.4a. The plastic deformation of the floor remains more or less constant from both the front and back towards the center, gradually diminishing from the sides to the middle. In contrast to the shorter baseline model, where each rebounding phase led to subsequent leaning in the direction of the passengers' center of mass, the increased length of the section now imparts greater stability. The section remains perpendicular to the ground during rebounding, resulting in a more uniform longitudinal deformation.

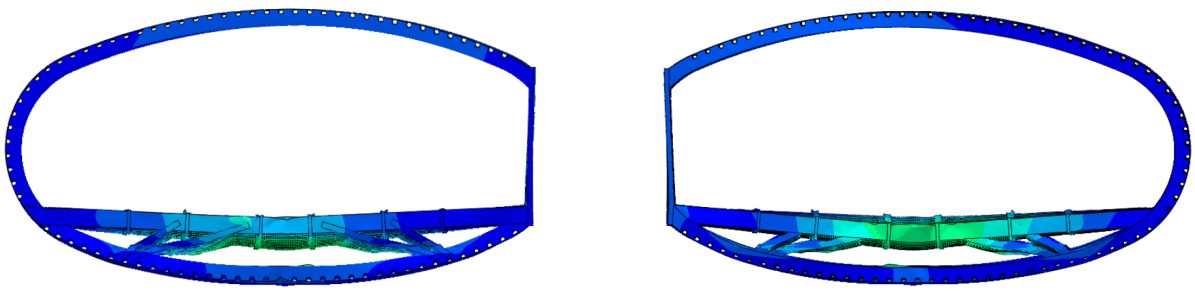

(a) Front view of the full passengers' section **(b)** Different views of the full passengers' fuselage, after impact

Figure 9.3: Different views of the full passengers' fuselage, after impact

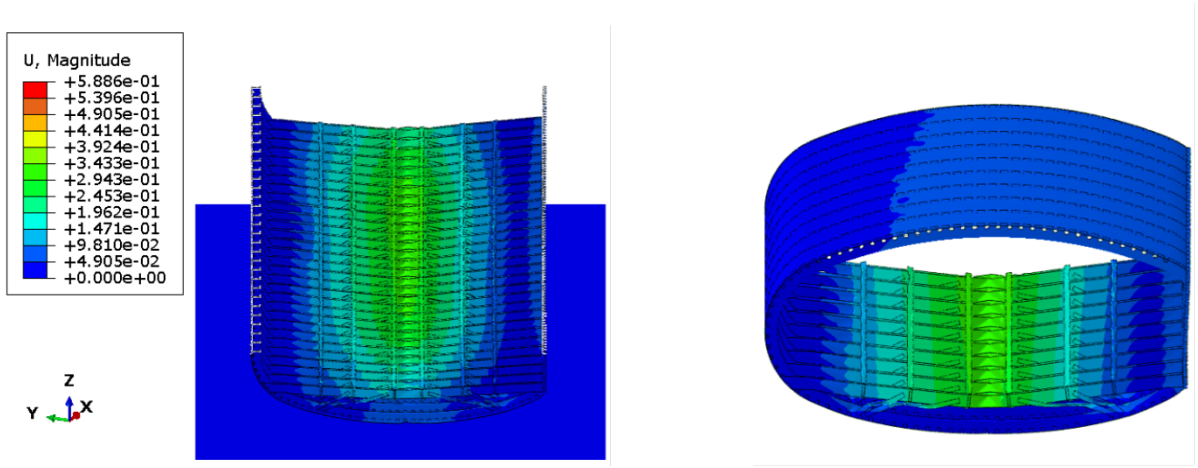

(a) Diagonal view of the full section

(b) Engine section of the passengers' fuselage

Figure 9.4: Diagonl view and engine section of the passengers' fuselage section

For enhanced visualization, Figure 9.4b illustrates the deformation specifically emphasizing the middle engine section, mirroring the extended model analyzed earlier.

Upon visual inspection, significant observations emerge. The prior unrestrained extended model, devoided of side constraints such as boundary conditions or structural elements, displayed, at the free edges, unimpeded deformation in the out-of-plane direction, leading to increased deformations at the rear end. The introduction of sliding boundary conditions facilitated a more uniform deformation along the length of the model. Similarly, incorporating structural components in both the rear and front sections of the complete passenger model enhanced the stability of the engine section's structural elements, yielding similar outcomes.

9.2.1. Centers of Gravity Location

Once again, this time for the entire passengers' fuselage, the coordinates of both the structural and passengers' center of masses were determined, as indicated by the red dot in Figure 9.5.

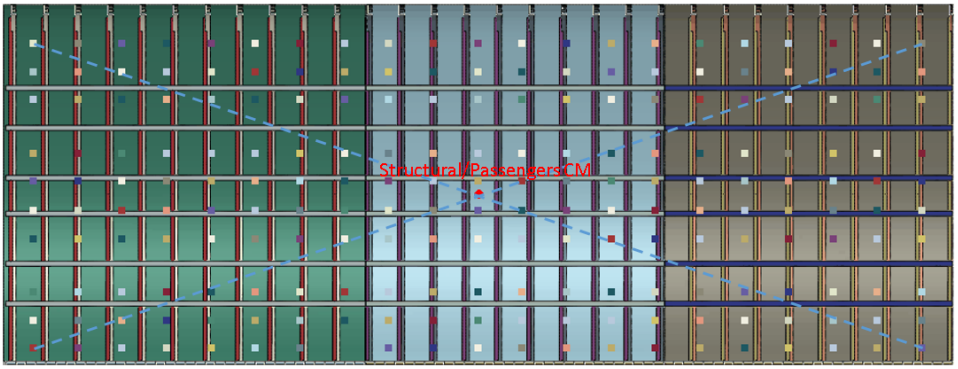

Figure 9.5: Location of the full model's structural and passengers CMs

In this case, both coincide at the same point. This alignment, combined with the substantial length of the model, contributes to enhanced overall structural stability, resulting in the observed deformation uniformity, as depicted in Figure 9.4a. However, slightly less pronounced deformations are evident at the back and front of the complete fuselage section. This might be elucidated by the positioning of the first and final rows, which are not directly above the initial and end frame. Instead, these rows are spatially situated above a region with less structural support (leftmost row) and, in the case of the rightmost row, above the penultimate frame. Following the impact, the additional passenger weight concentrated more towards the interior does not exert force on the outer frames, consequently resulting in reduced structural distortion.

9.3. Energy Absorption Distribution by Component

Figure 9.6 depicts the fraction of energy absorbed by components in the full passenger fuselage. Contrasting with the extended, 7-rows model case (shown in Figure 7.7b), a minor increase in energy absorption due to the frames is observed, coupled with a subsequent decrease in energy absorbed by the floor long beams. This aligns with the visual examination of the crash sections, revealing a more localized plastic deformation in the extended section as opposed to the full passenger model.

When comparing with the energy absorption by component of the extended model with the addition of sliding boundary conditions, depicted in Figure 8.7b, closer resemblances appear, as anticipated. The energy absorbed by the frames and floor long beams remains unchanged, with only a slight decrease and subsequent increase in the energy absorbed by the struts and floor beams, respectively, in the current scenario. Nevertheless, as the structural layout remains consistent in both cases, there are no discernible differences in the overall portion of energy dissipated by the components.

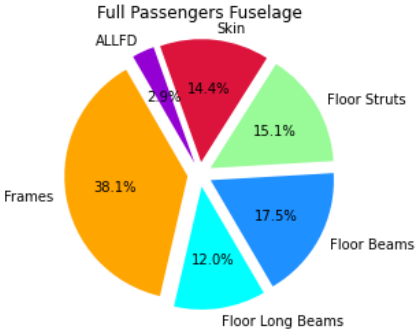

Figure 9.6: Component energy absorption distribution, full passengers' fuselage section

9.4. Kinetic Energy Time History

The kinetic energy variation depicted in Figure 9.7 provides additional support for the analysis. Initially, it rises, again attributed to the negative vertical velocity applied to the model when it is not entirely in contact with the ground. Notably, the full fuselage section demonstrates a significantly higher kinetic energy compared to the other models, due to the full fuselage section's mass being approximately three times that of the other 10-frame sections.

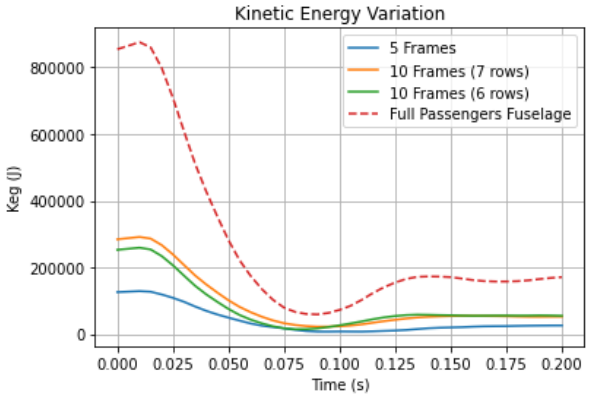

Figure 9.7: Model kinetic energy vs. time; different lines indicate different fuselage sections

Furthermore, it exhibits a considerably steeper slope, indicating a higher rate of plastic dissipation. This, again, is ascribed to an elongated section combined with a more impactful ground contact, leading to larger acceleration pulses experienced by occupants — a factor that will be explored in the analysis of DRIs.

The kinetic energy does not reach zero, retaining some residual energy as different nodes attain zero velocity at different times. Ultimately, the elastic energy stored in the structure is released, converting back into kinetic energy during the substantial rebound phase, thereby prolonging the duration of acceleration pulses experienced by occupants.

9.5. DRIs and Severity Indexes Analysis

In Figure 9.8, the spatial position labels for passengers within the complete passengers' fuselage section are presented. Similar to the previous models, the rows are transversely labeled from A to J, while longitudinally, it spans from 1 to 21.

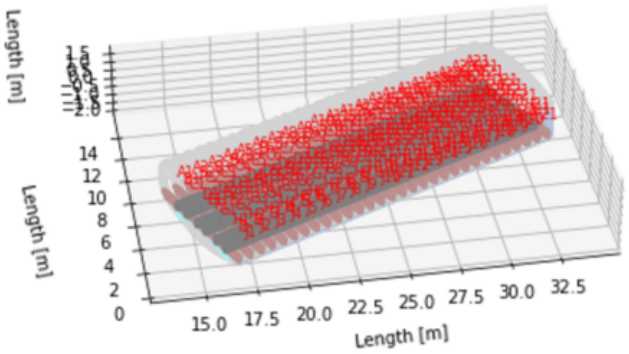

Figure 9.8: Labels indicating the spatial positions of passengers within the full passengers' fuselage section

Consistently, the observed pattern persists, wherein increased plastic deformation in the middle contributes to lower DRIs and SEVs (refer to Figure 9.9a and 9.9b). Longitudinally, the values exhibit more stability due to the superposition of the structural and passengers' centers of mass and subsquent more uniform floor deformation. Both the maximum and minimum DRIs and SEVs exhibit an increase in comparison to the other models without BCs, while the median remains relatively constant, similar to the baseline section.

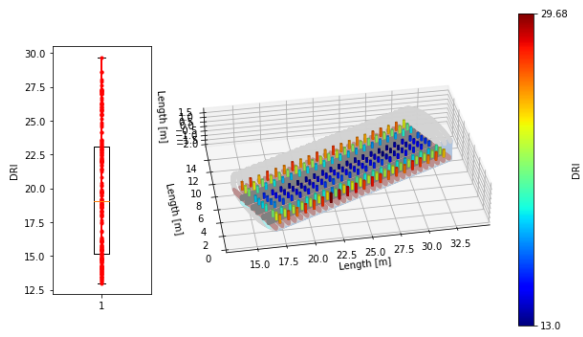

(a) Spatial variation of the DRI

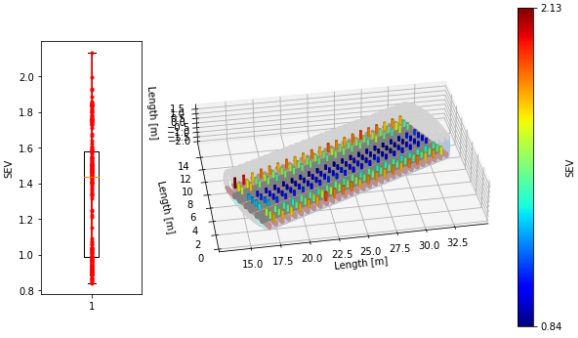

(b) Spatial variation of the SEV

Figure 9.9: Spatial variation of the DRI and SEV along the full passengers' fuselage section

To enhance correlation, Figure 9.10a and 9.10b depict the spatial distribution of dynamic response indexes and SEVs, respectively, specifically focusing on the engine section within the entire fuselage of the passenger compartment. This section serves as a representative model for the 10 frames, 7 rows configuration (refer to Figure 7.11a and 7.11b).

In contrast to the previous scenario, where lower DRI and SEV values were observed in the rear part, the current analysis reveals a more consistent longitudinal pattern in both DRIs and SEVs. Notably, similarities can already be discerned with the application of sliding boundary conditions. In both cases, the free edges remain constrained, once again establishing a correlation between the two modelling techniques in terms of structural behavior during impact.

However, it's essential to note that the computational time between these different techniques is not currently considered. This aspect will be addressed in the next Chapter, where all the models will be comprehensively compared to gain a better understanding of the outcomes achieved thus far.

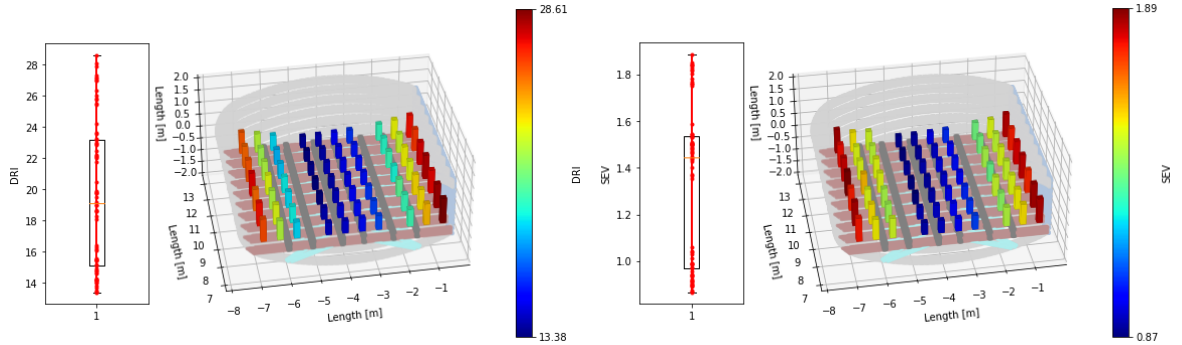

(a) Spatial distribution of the DRI

(b) Spatial distribution of the SEV

Figure 9.10: Spatial distribution of the DRI and SEV when zooming in on the engine section within the entire fuselage of the passenger compartment

9.6. Reflection on the Results

Incorporating structural components in both the rear and front sections notably improved the stability of the engine section, yielding outcomes akin to those observed with sliding boundary conditions. The close resemblance in energy absorption between the full passenger fuselage and the extended model with BCs, which wasn't previously attained when side constraints were added to the baseline and the extended fuselage, underscored the similar effect of both approaches in addressing previously encountered unrealistic buckling effects, thus facilitating a more realistic crashworthiness assessment.

However, the imposition of boundary conditions resulted in an unnatural deformation at the cross sections due to the unrealistic zero out-of-plane displacement at certain component nodes. This controlled lateral constraint increased stiffness in those areas, leading to a more pronounced increase in DRIs and SEVs compared to the engine section of the full passenger model.

The addition of structural elements on the sides of the engine section maintained a more natural side deformation, offering a more realistic alternative to incorporating boundary conditions.

Furthermore, the energy absorption of the extended model remained more or less consistent even without the inclusion of boundary conditions or side structural elements. Conversely, the structural components of the baseline model exhibited markedly distinct energy absorption characteristics. This discrepancy once again prompts questions regarding the reliability of the baseline model, whether it is due to the small size incapable of effectively capturing the behavior of the Flying-V or attributed to some possible modelling error of the FEM model itself.

While the analysis presented here offered an understanding of the results achieved thus far, the computational time of each simulation wasn't already taken into account. This will be further explored in the subsequent Chapter, where a comparison of all models will be provided.

10

Crashworthiness Modelling Approaches: An Overall Comparative Assessment

The preceding Chapters delved into an exploration of various modelling approaches. Initially, the length of the 5-frame section was doubled, resulting in a more pronounced increase in deformation at the rear end compared to the baseline model (Figure 10.1a). This deformation was mitigated by excluding the last passenger row, with prior analyses encompassing energy considerations and passenger-induced accelerations.

Implementing sliding boundary conditions along the free edges of the models effectively reduced buckling and lateral localized contractions and expansions, thereby minimizing undesirable crushing and twisting behaviors (Figure 10.1b). Alternatively, the introduction of additional adjacent structural elements further homogenized longitudinal deformations, as evident in the examination of the engine section within the full passenger model (Figure 10.1c).

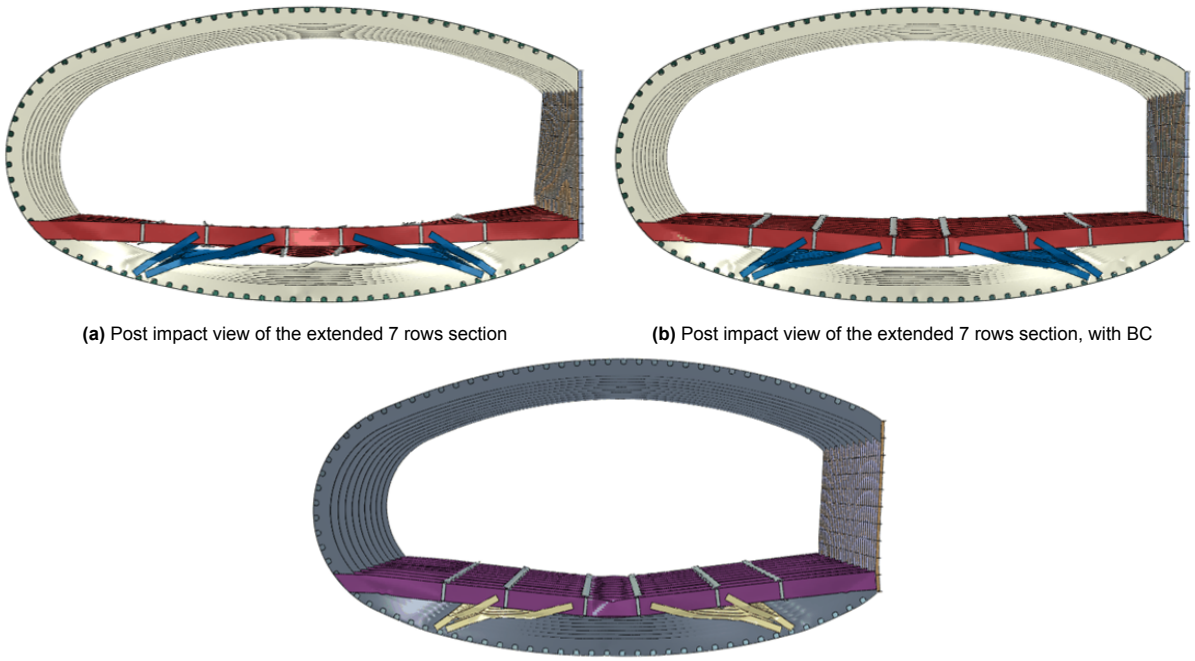

(a) Post impact view of the extended 7 rows section

(b) Post impact view of the extended 7 rows section, with BC

(c) Post impact view of the engine section of the full passenger model

Figure 10.1: Comparison of the structural deformation between different model approaches

However, each modelling technique was examined somewhat independently. This Chapter aims to integrate all these techniques simultaneously.

This integration is important not only to provide an overview of Dynamic Response Indexes, Severity Indexes, and energy absorptions, but also to expand the assessment to encompass the computational time required for each model. Building on the results of this analysis, one modelling approach will be selected to attempt the modelling of potential Flying-V crash scenarios using the simplified technique discussed in the Literature. To set the foundation for comparison, Table 10.1 begins by presenting the average, maximum, median, and minimum values for DRIs and SEVs, along with the time taken for simulations of each analyzed model thus far.

Table 10.1: DRI and SEV comparison for different models

Models	**DRI**				**SEV**				**Comp. Time (h)**
-	Avg	Max	Median	Min	Avg	Max	Median	Min	-
Baseline	18.16	23.93	18.48	11.99	1.18	1.56	1.26	0.78	5.37
Ext. 7 rows	18.95	28.97	19.09	11.93	1.29	2.00	1.30	0.77	6.54
Ext. 6 rows	20.94	29.04	20.23	14.71	1.46	2.08	1.48	0.98	3.54
Baseline BC	18.80	26.29	18.48	13.09	1.19	1.65	1.20	0.83	46.32
Ext. 7 rows BC	21.61	30.41	20.92	14.56	1.42	2.10	1.42	0.93	67.24
Full Fuselage	19.57	29.68	19.06	13.00	1.34	2.13	1.44	0.84	9.3

Additionally, Figure 10.2a and 10.2b present box plots illustrating the variations in DRIs and SEVs, respectively. These plots offer a clearer visualization of how these values fluctuate across all modelling techniques, showcasing the minimum, maximum, and median values for each injury criterion.

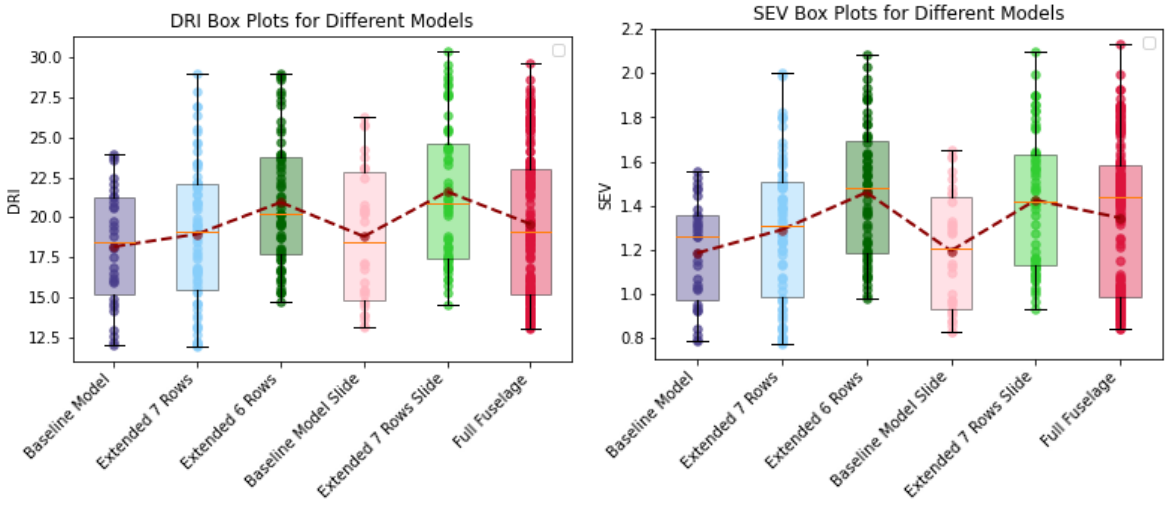

(a) DRI box plots for the different models studied

(b) SEV box plots for the different models studied

Figure 10.2: DRI and SEV box plots for the different models studied

The baseline model stands out as having notably lower values for injury criteria evaluation, exhibiting an average DRI and SEV of 18.16 and 1.18, respectively. The decision to adopt the minimum fuselage section size, determined in prior research on conventional aircraft design, and then extrapolate it for the Flying-V baseline section, was based on five frames. However, as discussed earlier, this minimum section size was qualitatively assessed, without considering other factors that might influence the section's behavior post-impact. Table 10.1 illustrates that the increase in model size led to an overall rise in DRIs and SEVs, raising questions about the reliability of using a smaller section. Nevertheless, with a low computational time, it was considered adequate for evaluating the crashworthiness of the Flying-V in conventional vertical drop tests.

However, as the analysis progresses into more dynamically complex scenarios, it becomes imperative to expand the computational domain to include larger fuselage sections for a more reliable study. In this context, this section acted as the baseline model to validate other modelling approaches and will not be utilized further in the subsequent phases of this work.

When comparing the extended models, the one with 7 rows outperformed in the overall reduction of DRIs and SEVs. Yet, it exhibited an increased computational time compared to its 6-row counterpart.

The decreased computational time of the 6-row extended model, even surpassing the baseline model, was attributed to minimal plastic deformation in the structural components, resulting in a swift simulation of drop tests. The augmented size of the extended model with 7 rows, coupled with increased deformations, contributed to the overall rise in computational time. Nevertheless, the extended model with 6 rows served a unique purpose for comparison and will be discontinued for modelling more realistic Flying-V crash scenarios due to its unrealistic passenger layout, inconsistent with the frame spacing.

The introduction of sliding boundary conditions was a logical step to minimize potential unrealistic deformations. However, as a drawback, it increased the overall stiffness of the model by unnaturally constraining structural distortion in other directions. This effect is evident in the overall increase in DRIs and SEVs compared to other models, reaching a maximum when sliding boundary conditions were applied to the extended model. The unbalanced increase in computational time, compared to its counterparts, complicated the potential use of this approach for further crashworthiness assessments, falling short in the study. Nonetheless, this modelling approach provided valuable insights into the overall study of the Flying-V section.

Finally, the full fuselage section, with approximately three times the length of the extended fuselage, exhibited a slight increase in DRIs and SEVs. Despite this, its larger finite element model produced the most realistic results for the studies conducted thus far. It not only performed well in terms of computational time but is deemed crucial for future investigations into various Flying-V crash scenarios without oversimplification. Furthermore, it serves as validation for upcoming reduced modelling techniques introduced in subsequent Chapters.

For enhanced visualization of DRI and SEV distribution, Figures 10.3 and 10.4 depict bar plots for the middle passenger row in each section, with its normalized counterpart in the right image. The arc shape of this distribution follows the overall trend observed so far: higher central plastic deformations (resulting in lower DRIs and SEVs) and stiffer sides (resulting in higher DRIs and SEVs).

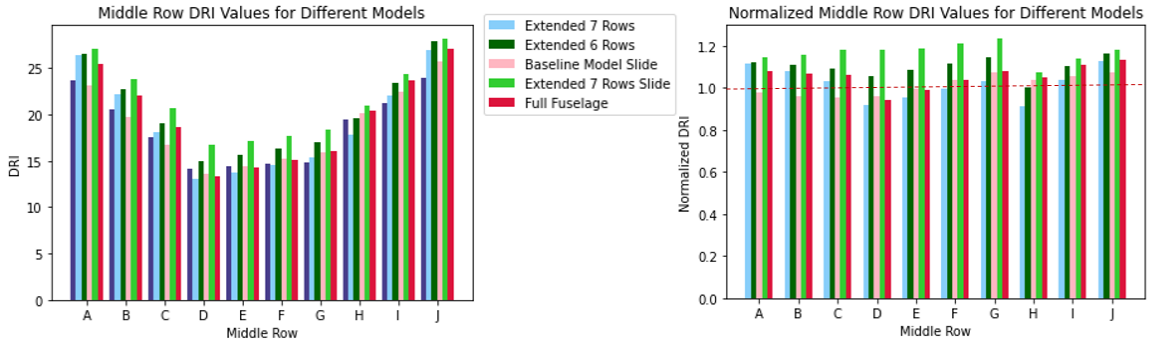

Figure 10.3: Middle row DRI values for the different models analysed. On the right figure, the DRIs are normalized by the baseline model values

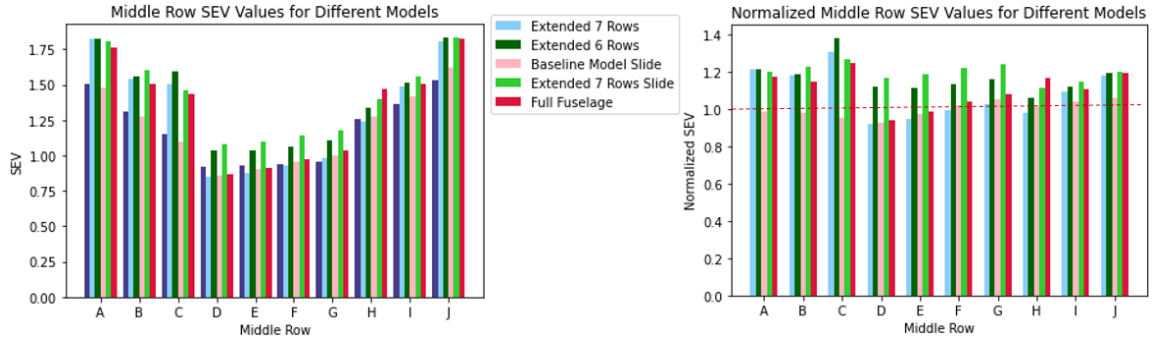

Figure 10.4: Middle row SEV values for the different models analysed. On the right figure, the SEVs are normalized by the baseline model values

The Chapter concludes by presenting, in Figure 10.5, the proportion of total energy dissipated by components for the various modelling approaches. Previously analyzed individually for each case, this visualization provides a clearer overview of the energy dissipation variations across the implemented modifications. As previously discussed and reiterated here, the energy absorption by component of the baseline model significantly diverges from the other models analyzed. One potential explanation for these disparities lies in the observation that frames in the baseline model consistently avoid interacting with the structural elements on the floor. Consequently, it is primarily the frames themselves that absorb the impact energy, as this energy is not directly dispersed through contact with the floor's structural elements. However, this explanation is based solely on visual inspections of the crash sections and lacks further substantiation. The addition of boundary conditions for both the baseline and extended models was proposed to address this issue. While this did result in similar crash sections and longitudinal deformations, the differences in energy absorption persisted, and no definitive explanation was found for these discrepancies.

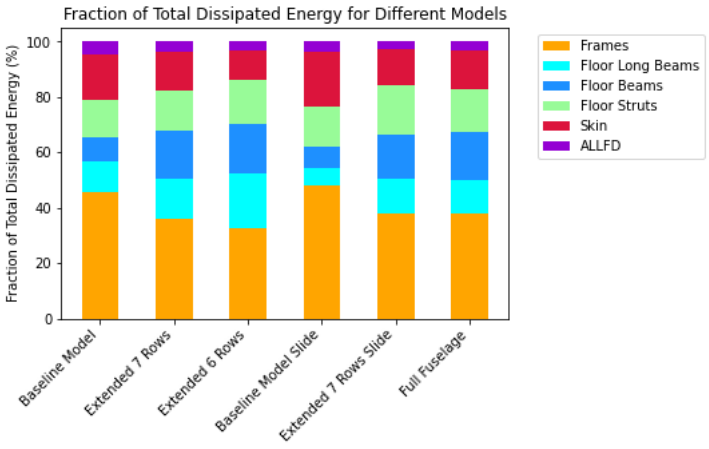

Figure 10.5: Comparison of component energy absorption distribution for the different models studied

However, it was previously observed that the section deformations upon applying the boundary conditions resembled those of the full passenger fuselage. These observations align with the energy absorbed by each component, as evident from the very similar bar plots for both models.

Ultimately, the decision has been made to proceed with the subsequent analysis using the 7-row extended model. This choice was driven by its demonstrated good balance between efficiency and result accuracy, all while preserving simulation simplicity. The full passenger model, achieving the most realistic results within a reasonable computational timeframe, will also serve as a benchmark for validating forthcoming reduced modelling techniques in subsequent Chapters.

This page intentionally contains no content.

IV

Modelling Unique Flying-V Crash Scenarios

This page intentionally contains no content.

11

Optimizing Vertical Drop Tests for the FV: Leveraging Moments of Inertia

Various modelling approaches have been previously juxtaposed, considering factors such as computational time, result realism, energy efficiency, and passenger safety. The consensus favored the extended model with seven passenger rows, which demonstrated a good equilibrium between efficiency and result authenticity while maintaining simulation simplicity. This selected model serves as the foundational framework for subsequent analyses.

Following the replication of simulations under conventional drop-test conditions stipulated by regulatory bodies and utilized in prior research, this study aims to address the challenge of assessing the Flying-V's crashworthiness under alternative crash scenarios. Before delving into this, the proposed simplified methodology from the Literature (Section 5.1) must undergo testing against outcomes from the more complex passenger model. This is what this Chapter is all about: trying to optimize vertical drop tests of the extended section by leveraging the use of moments of inertia.

Beginning with a visual inspection in Section 11.1.1, the newly crashed sections are presented and briefly compared to the previously tested extended sections without the inclusion of moments of inertia. Subsequently, Section 11.1.2 addresses energy absorption by component, aiming for a comparative analysis. The spatial variation of DRIs and SEVs are explored in Section 11.1.3, followed by a more general comparative assessment with previous models in Section 11.1.4. Finally, Section 11.2 undertakes a more intricate analysis, providing a preliminary assessment to showcase the capabilities of the proposed methodology.

11.1. Effects of Moments of Inertia Addition on Previous Models

Due to the displacement of the passengers' center of mass, particularly when considering 7 passenger rows, there was a noticeable increase in deformation at the rear section. The phenomenon was exacerbated by the passengers' CM being less centralized compared to the structural one, as elaborated in Section 7.1.2. However, an interesting shift occurred upon removing the last row of passengers, causing their overall center of mass to move forward. This, in turn, led to a slight rise in plastic deformation at the front part of the structure.

Conversely, when examining the engine section representing the extended model of the full passenger fuselage, a more centralized deformation pattern emerged. Here, the passengers' center of mass coincided with the structural CM. Additionally, the presence of other structural elements from subsequent sections effectively minimized extensive deformations both at the rear and front.

These observations prompted a compelling question: What if, instead of employing the FEM model representation of the front and back sections of the full fuselage, moments of inertia of other sections of the FV were considered? This alternative approach, outlined in Section 5.1, involves applying moments of inertia at reference points attached to the cross section of the extended model, as illustrated in Figure 11.1.

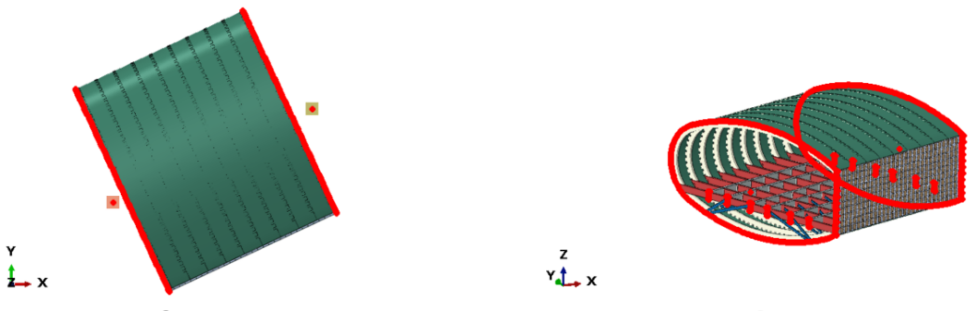

(a) Top view of the extended fuselage section

(b) Isometric view of the extended fuselage section

Figure 11.1: Views of the extended model. The reference points and the cross sections where the distributed coupling was applied are highlighted in red

Also, Figure 11.2 depicts an Abaqus FEM model of the extended fuselage section and its position along the global coordinate system used. The origin of the system coincides with the tip of the FV nose section, as depicted in Figure 5.2.

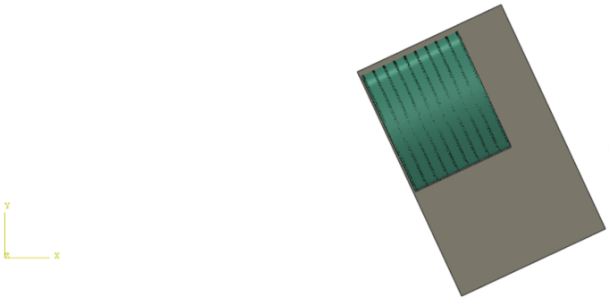

Figure 11.2: Upper view of the Abaqus model, with special attention to its position with respect to the global coordinate system

11.1.1. Visual Inspection of the Crash Section

Applying the described methodology yielded interesting qualitative results. Figure 11.3a displays the displacement magnitude of the 10-frame, 7-passenger-rows section with applied moments of inertia.

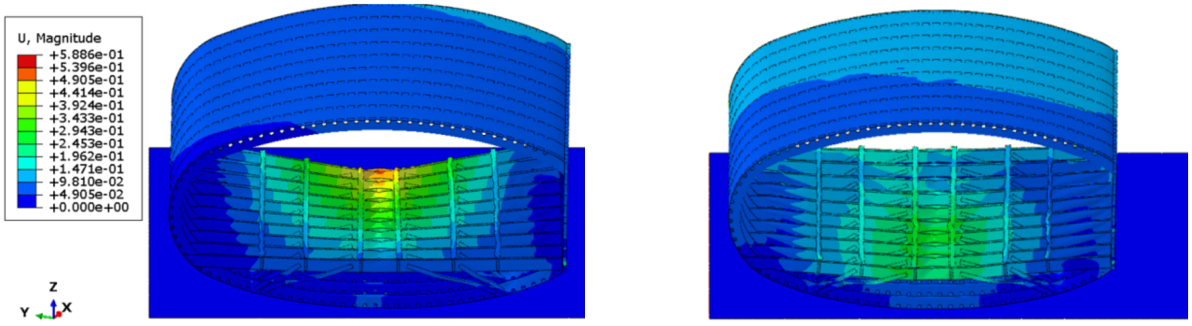

(a) Displacement variation for the 10 frames, 7 rows model

(b) Displacement variation for the 10 frames, 6 rows model

Figure 11.3: Displacement variation for the extended models with moments of inertia applied

Upon visual inspection and referencing the displacement magnitudes of previously analyzed models (Figure 7.1b and 9.4b for the extended model without moments of inertia and the engine section within the full passenger model, respectively), favorable outcomes are evident. The floor deformation is observed to lie between the two cases. In comparison to the extended, 7 rows without moments of inertia, the rear part exhibits less deformation, with increased deformations towards the front part, indicating a more even longitudinal distribution.

This approximation resembles more closely the floor deformations of the engine section within the full passenger model, with the observed deformations being less extensive. When comparing the two 10-frame, 6-passenger-rows models, with and without the application of moments of inertia, the same consistent trend is observed. The floor deformations were already well distributed longitudinally, as depicted in Figure 7.4. However, with the addition of moments of inertia, there is a slight increase in deformations at the rear and front ends, as evident in Figure 11.3b.

From this preliminary visual inspection during vertical drop tests, it can already be inferred that the addition of moments of inertia slightly enhances the simulation's realism, allowing for better comparison with the more complex full model.

11.1.2. Energy Analysis

Building on the previous section's logic, the pie chart in Figure 11.4a supports the provided information.

(a) Component energy absorption distribution, extended (7 rows) section with moments of inertia

(b) Component energy absorption distribution, extended (6 rows) section with moments of inertia

Figure 11.4: Components energy absorption capabilities of models with additional moments of inertia

A comparison with the pie chart for the extended, 7-passenger-rows model (depicted in Figure 7.7b) reveals that, upon the application of moments of inertia, the floor structural elements absorb less energy. Consequently, this results in reduced deformation from these components, as suggested by the earlier visual inspection of the crash section. Meanwhile, the frames, as well as the skin and struts directly connected to them, absorb more impact energy. Also, as opposed to the crash scenario from the 7 rows extended model without moments of inertia, the frames do not impact the floor components, possibly corroborating the fraction of energy absorption observed. On the contrary, when scrutinizing the pie charts in Figure 7.7c for the extended model with 6 passenger rows and those in Figure 11.4b for the same model with applied moments of inertia, fewer distinctions become apparent. Both models exhibit similar longitudinal deformation in their floor elements, with the model incorporating moments of inertia displaying slightly increased deformations at the rear. Nonetheless, bar charts depicting the energy absorption of models with and without moments of inertia will be discussed shortly, allowing for a more convenient side-by-side comparison.

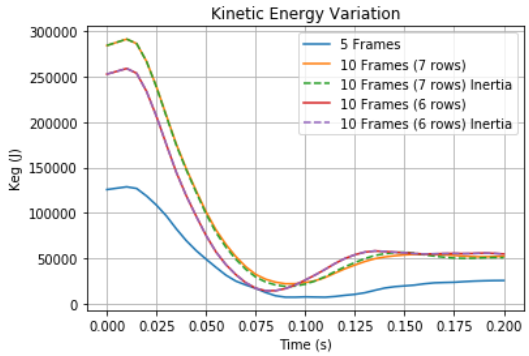

Figure 11.5: Model kinetic energy vs. time; dashed lines indicate the models with the moments of inertia applied

Figure 11.5 displays curves depicting the kinetic energy of both newly introduced models and their predecessors.

For the sake of clarity, the baseline model is also included in the plot. As anticipated, no differences in energy among the models are observed, as the size, masses, and the corresponding velocities applied to each node remain consistent.

11.1.3. DRIs and Severity Indexes Analysis

Upon analyzing the DRIs and SEVs for extended models with 7 and 6 passenger rows, incorporating moments of inertia yields some observations.

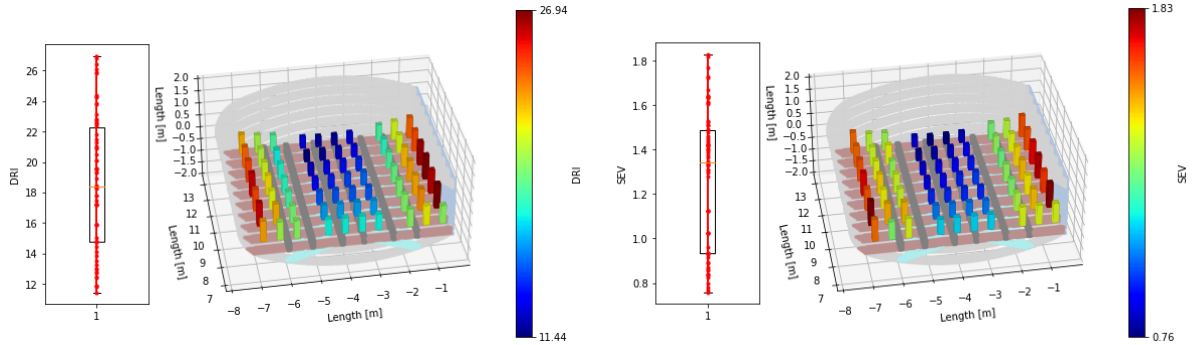

(a) Spatial variation of the DRI **(b)** Spatial variation of the SEV

Figure 11.6: Extended 7 rows FV section with moments of inertia

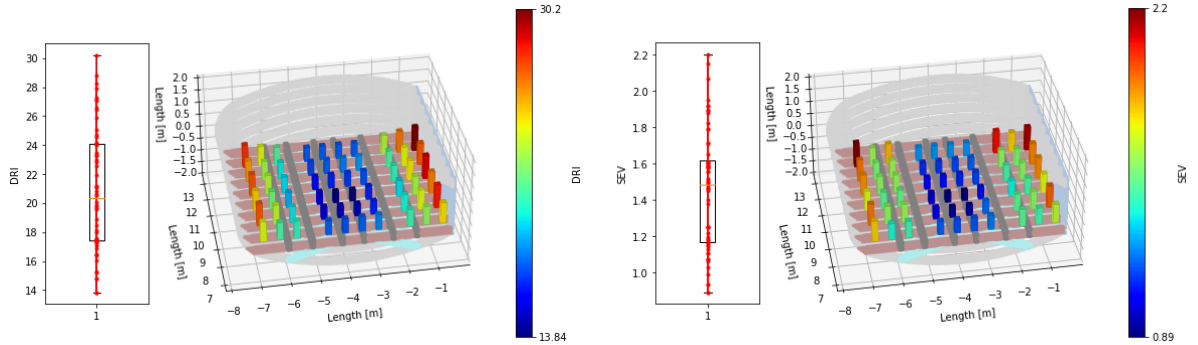

(a) Spatial variation of the DRI **(b)** Spatial variation of the SEV

Figure 11.7: Extended 6 rows FV section with moments of inertia

In comparison to their predecessors (referenced in 7.11 and 7.12), a subtle reduction in injury criteria is evident at the front part, resulting in a more evenly distributed pattern towards the rear of each section. Previously, there existed an imbalance in mass distribution, with more concentration at the back for the 7-row case and at the front for the 6-row case. The application of moments of inertia effectively counterbalances this behavior.

By introducing additional momentum representative of other sections of the Flying-V to the free edges of each section, the kinematic behavior induced by subsequent parts is conveyed to the extended section, eliminating the need for a representative model. The distribution observed in Figure 11.6a and 11.6b aligns with visual observations, bringing it a step closer to the DRIs and SEVs variation studied for the engine section of the full passenger model, as depicted in Figure 9.10a and 9.10b, respectively.

11.1.4. Exploiting Moments of Inertia Addition: A Comparative Assessment

Once again, a comparative analysis of the studies conducted in this Chapter is undertaken. Front views of the extended 7-row model are presented side by side in Figure 11.8, facilitating the visualization of deformations encountered during the discussed approaches. Figure 11.8b illustrates the successful reduction of uneven longitudinal floor deformations upon the incorporation of moments of inertia representing other parts of the Flying-V. This addition prevents the twisting behavior that previously resulted in undesirable backward lean of the floor elements and introduces a more uniformly bent behavior at the front part. The methodology brings the section closer to the impact behavior observed in Figure 11.8c, representing the engine section of the full passenger model. By circumventing the complexities of a more intricate model and the associated computational times, this simplified approach appears to yield more realistic results for simple vertical drop tests.

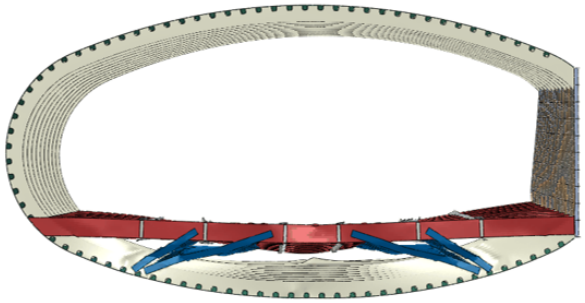

(a) Post impact view of the extended 7 rows section

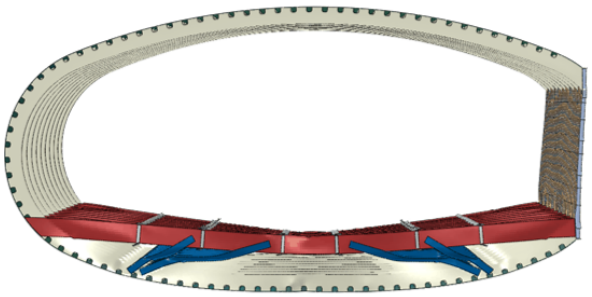

(b) Post impact view of the extended 7 rows section, with moments of inertia

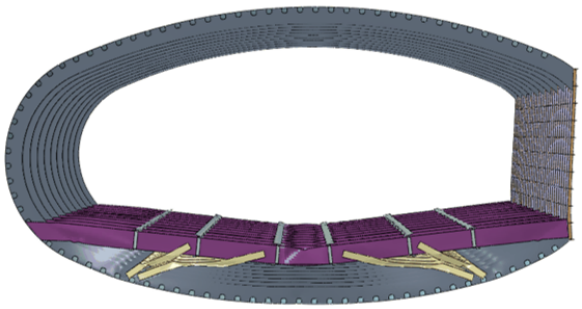

(c) Post impact view of the engine section of the full passenger model

Figure 11.8: Comparison of the structural deformation between different model approaches

To enhance the comparison of models analyzed in this Chapter, Table 11.1 succinctly summarizes important DRI and SEV values, providing insights into computational time. Additionally, boxplots in Figure 11.9 visually facilitate the observation of variations in injury criteria.

Table 11.1: DRI and SEV comparison for models with inertia addition

Models	**DRI**				**SEV**				**Comp. Time**
-	Avg	Max	Median	Min	Avg	Max	Median	Min	**(h)**
Ext. 7 rows	18.95	28.97	19.09	11.93	1.29	2.00	1.30	0.77	6.54
Ext. 7 rows Inertia	18.63	26.94	18.42	11.44	1.27	1.83	1.34	0.76	3.83
Full Model Eng. Section	19.65	28.61	19.09	13.38	1.33	1.89	1.44	0.87	-
Ext. 6 rows	20.94	29.04	20.23	14.71	1.46	2.08	1.48	0.98	3.54
Ext. 6 rows Inertia	20.80	30.20	20.31	13.84	1.45	2.20	1.48	0.89	3.79

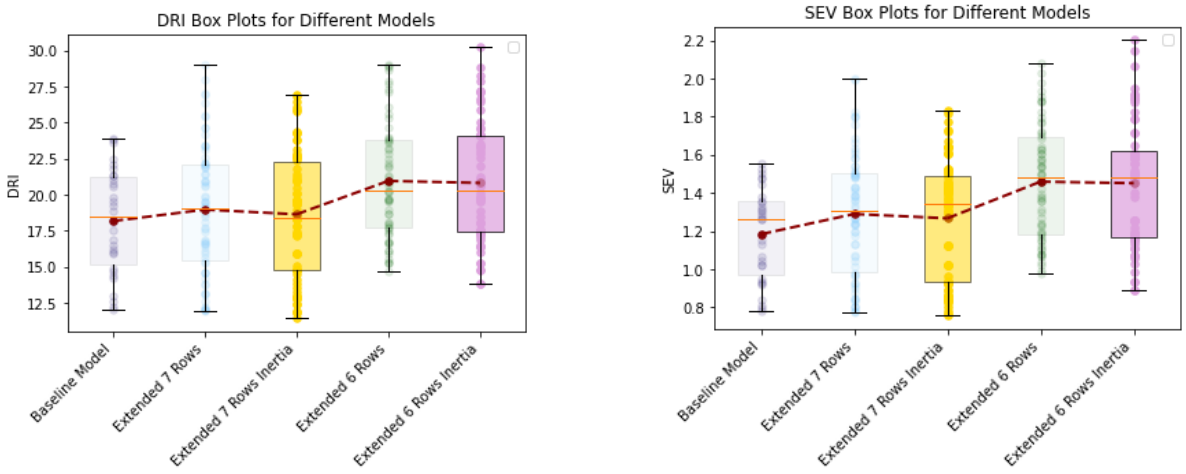

(a) DRI box plots for the different models studied

(b) SEV box plots for the different models studied

Figure 11.9: DRI and SEV box plots for the models with moments of inertia applied

Examining the averages of both DRI and SEV, the incorporation of moments of inertia leads to a reduction in values for both extended models. Although the extended 7-row model initially demonstrated values closer to the engine section of the full model, the introduction of moments of inertia resulted in an overall decrease in these metrics. This shift may indicate enhanced crashworthiness, although with a slight deviation from the average values observed in the more complex model. However, these variations in injury criteria are marginal and can be considered negligible. Additionally, the spatial variation plots for DRIs and SEVs show a closer resemblance to the engine section when moments of inertia are introduced, reinforcing the viability of this approach. Notably, there are interesting outcomes in terms of computational time. The incorporation of moments of inertia for the extended 7-row model significantly reduces the simulation time for the corresponding sections, aligning with expectations as fewer floor deformations lead to a faster solver solution. For the 6-row counterpart, there is no significant distinction, only a minor increase in simulation time due to slightly more plastic deformations of the floor structure. In line with the structure of the previous Chapter, Figure 11.10 and 11.11 visually represent the distribution of DRIs and SEVs as bar plots for the middle passenger row in each section, alongside their normalized counterparts in the right image.

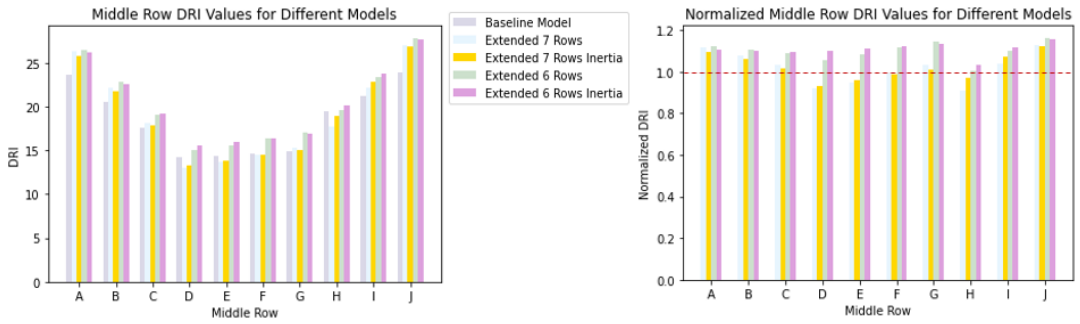

Figure 11.10: Middle row DRI values for the different models analysed. On the right figure, the DRIs are normalized by the baseline model values

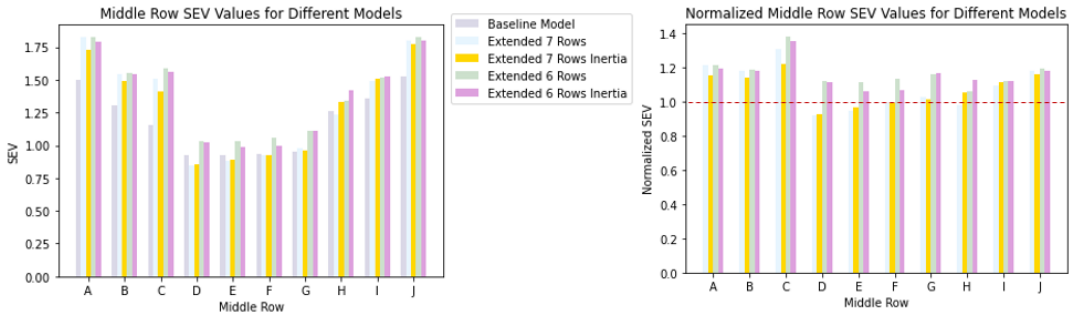

Figure 11.11: Middle row SEV values for the different models analysed. On the right figure, the SEVs are normalized by the baseline model values

For models featuring six rows, the average of the third and fourth rows were taken into consideration. The baseline model is illustrated for comparative purposes, and the normalized right figure more effectively emphasizes the differences in injuries sustained by each passenger across the various models.

Noticeably higher values are observed for the six-row model, while the seven-row variant appears to exhibit greater alignment with the baseline. The incorporation of moments of inertia, as visually evidenced in these Figures, leads to a marginal reduction in both DRIs and SEVs. The arc shape of this distribution follows the consistent trend observed throughout various modelling approaches: higher central plastic deformations leading to lower DRIs and SEVs, and stiffer sides contributing to higher injury criteria values.

Finally, Figure 11.12 illustrates the fraction of energy absorbed by components for different scenarios. Shaded bars represent earlier studies, while the more vivid ones pertain to the models discussed in this Chapter.

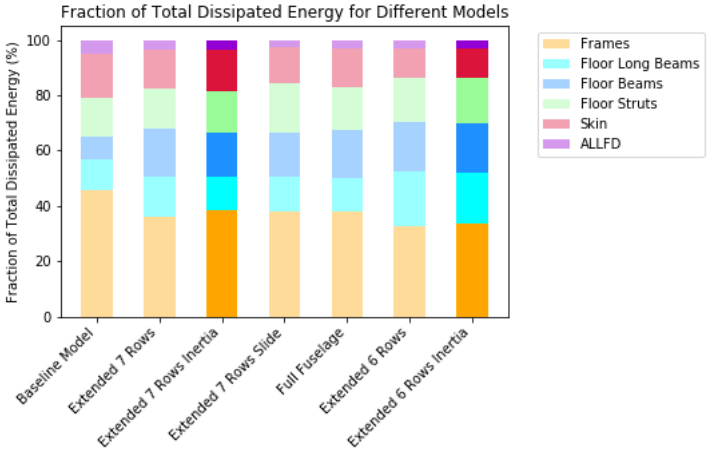

Figure 11.12: Comparison of component energy absorption distribution for different models studied

Additionally, for better comparison, energy bars for the full passenger configuration and the extended 7-rows setup with boundary conditions are included. In the 7-rows model without moments of inertia, heightened floor deformation and frames impacting the floor components led to increased energy absorption by these structural elements. However, the application of moments of inertia counteracted this behavior, resulting in deformations closely resembling those in the full passenger and 7-rows extended models with boundary conditions, evident in their identical bar plots.

Examining the 6-row extended section with and without moments of inertia, the fraction of energy absorbed remains remarkably similar, consistent with nearly analogous visual deformations in their crash sections.

11.2. A Preliminary Analysis: Counteracting the Engine Weight

In the earlier investigation, the primary focus was to evaluate the effects of incorporating moments of inertia during vertical drop tests involving the elongated fuselage. Notably, the results highlighted a reduction in extensive plastic deformation at the rear section. Following this, a subsequent preliminary analysis sought to enhance the fuselage model by incorporating the engine mount model developed by Koenderink, a previous TUDelft student [41]. Figure 11.13 illustrates the initial configuration of the engine mount structure attached to the extended fuselage. Within this structure, two nodes, representing the masses of the engine and landing gear, were interconnected, as depicted in Figures G.1a and G.1b in Appendix G. It's important to highlight that Koenderink's current estimated mass for the complete engine mounting structure, incorporating both landing gear and engine, was approximately 22150 kg. This significantly exceeds the structural mass of the extended fuselage section, even when factoring in the mass of each passenger and seat, which amounts to 7080 kg.

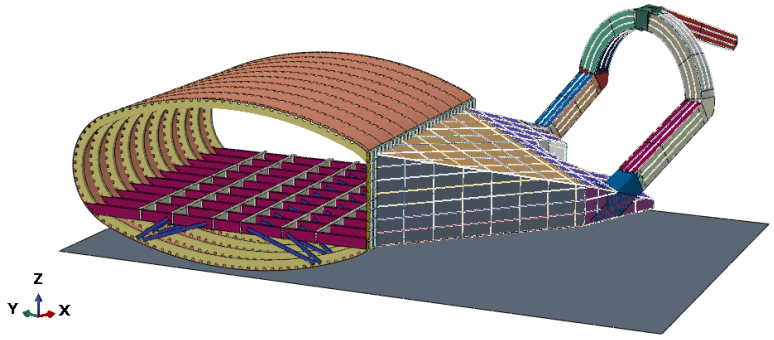

Figure 11.13: Koenderink's engine mount model attached to the fuselage section

The exploration then advanced to, once again, examine the impact of moments of inertia associated with other sections of the Flying-V. This involved conducting drop tests with and without these moments of inertia. Figures 11.14a and 11.14b showcase the deformed state for both scenarios at a time step of 0.3 seconds, a smaller interval chosen to mitigate computational demands.

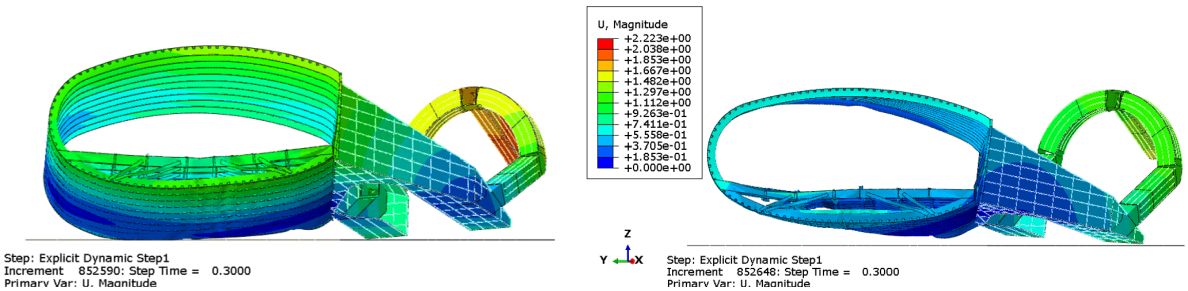

(a) Model's deformed state without considering moments of inertia of other sections of the FV

(b) Model's deformed state when moments of inertia of other sections of the FV are considered

Figure 11.14: Impact of adding moments of inertia from other segments of the Flying-V

Noteworthy insights emerged: in Figure 11.14b, the application of reference points with moments of inertia from other sections effectively countered the rotation induced by the engine's weight. These preliminary findings suggest the potential of this approach, where the overall kinematics of other divisions of the Flying-V are considered without the need for physical representation, thereby enhancing computational efficiency. Examining Figure 11.14a, it reveals the deformed state of the model without the use of reference points. Contrarily, the structure, influenced by the significant momentum from the weight of the engine and engine mount, rotates backward. DRI and SEV variations, along with the position of the structural center of mass, are detailed in Appendix G.

It's crucial to note that the center of mass position in Figure G.2 only considers the structure itself. Due to the substantial mass of the engine, the overall center of mass shifts further backward, adjacent to the engine location. Additionally, it was anticipated that both the DRIs and SEVs values would significantly escalate and shift more towards the spar. However, the average DRI and SEV only exhibited a slight increase. This is attributed to the engine mount deforming when making contact with the ground, thereby absorbing a portion of the energy.

This initial analysis, coupled with insights from the preceding section, offers a promising evaluation of the proposed simplified methodology, laying the ground for a more comprehensive verification of this approach when applied to more complex crash scenarios, forming the central focus of future Chapters.

12

Impact of Roll Angles on FV Fuselage Crashworthiness

While earlier experimental and simulation analyses focused primarily on conventional vertical drop tests to assess the crashworthiness of fuselage sections, it's important to note that aircraft crashes don't typically involve a straightforward vertical descent. Instead, they often occur with varying degrees of rolling inclination. To better evaluate the crashworthiness of aircraft fuselage sections, an examination must be conducted by comparing the structural responses in different initial crash conditions and environments.

Previous crashworthiness studies related to unconventional aircraft designs have been limited, especially when considering simple vertical drop tests. The inclusion of roll angles in these studies is even more scarce. Nevertheless, the impact of adding roll angles has been briefly discussed in the Literature concerning conventional aircraft design. In this context, it will be attempted to correlate relevant data when conducting a similar analysis for the Flying-V.

The former Chapter highlighted the positive effects of integrating moments of inertia near the fuselage cross sections. Expanding on this investigation, the current study focuses on evaluating the crashworthiness performance of fuselage sections under varying roll angle impact conditions. Given that the centerline maintains a horizontal orientation in both analyses, it was considered advantageous to revisit the extended 7-row model further enhanced with additional moments of inertia to capture the dynamics of other Flying-V sections. In Appendix H, some results are presented for the scenario without applied moments of inertia, allowing for a more detailed examination of the differences between the two approaches. The investigation includes the evaluation of failure modes (Section 12.1), followed by acceleration responses, in Section 12.2. The energy absorption analysis is also taken into account in Section 12.3, as well as DRI and SEV spatial variation along the fuselage section under roll angles of 5-deg, 10-deg, and 15-deg (Section 12.4). The drop test conditions remain consistent, featuring a vertical impact velocity of 26 ft/s (7.925 m/s), with the fuselage centerline maintained in a horizontal orientation. Finally, Section 12.5 will highlight the findings and discuss the results.

12.1. Failure Modes

Comprehending the impact responses conveyed to the cabin floor holds crucial importance and is frequently shaped by the inherent failure modes within the subfloor structures of aircraft, as illustrated in Figure 12.1 for the extended model with moments of inertia applied. The analysis conducted without moments of inertia produced results comparable to those obtained with moments of inertia, rendering the presentation of both unnecessary. This consistency in results can be attributed to the analysis concentrating on the identical initial time frame (75ms) within the overall time step of 200ms.

A comparison of the figures reveals distinct failure modes and stress distributions in fuselage sections. However, despite these differences, the structural integrity of the cabin floor is fundamentally maintained during the crash. Similarly to the crash behavior observed in circular cross sections of conventional aircraft, larger initial in-plane loads lead to fuselage frames and skin moving towards the cabin floor when the fuselage sections impact the rigid ground at 5-deg, 10-deg and 15-deg roll angles.

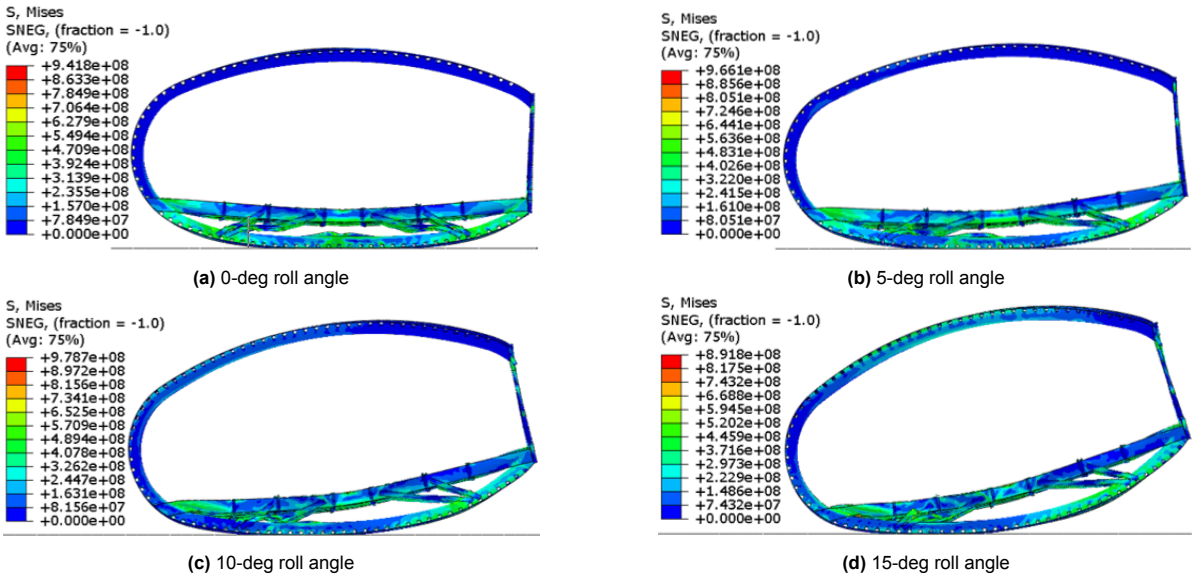

(a) 0-deg roll angle

(b) 5-deg roll angle

(c) 10-deg roll angle

(d) 15-deg roll angle

Figure 12.1: Deformation and stress variation of fuselage section at 75 ms

During these impacts, deformed frames typically exhibit three primary plastic hinges. On both sides, a triangular region formed by fuselage frames, floor beams, and oblique struts contains one plastic hinge, while the third, harder to perceive plastic hinge is located at the bottom of the fuselage frame. The oblique struts yield, yet floor beams remain unpenetrated, effectively supporting the occupant-seat systems. Crucially, the occupant survival space also remains at least 85% of the original space post-crash.

As the fuselage section tilts left with an increasing left roll angle, frames bend offset from the center to the left position, and the deformation of left oblique struts intensifies. The decrease in absorbed energy by the right part of the fuselage section is attributed to the diminishing effective energy-absorbing areas on the right side, resulting from the escalating roll angles.

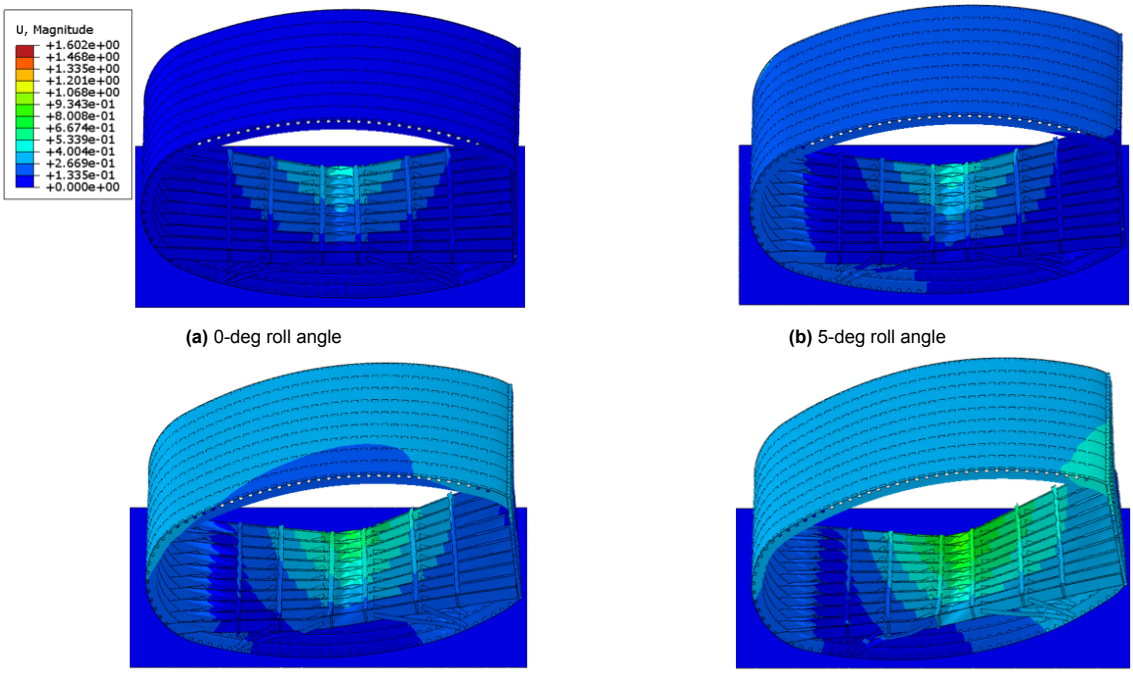

(a) 0-deg roll angle

(b) 5-deg roll angle

(c) 10-deg roll angle

(d) 15-deg roll angle

Figure 12.2: Displacement variation of fuselage section at 200 ms, with moments of inertia

Consequently, more energy is dissipated to the main fuselage structure, leading to an escalation in the deformation of fuselage frames and, mostly, floor beams. Figure 12.2 illustrates the displacement magnitude at the end of the analysis for the section with applied moments of inertia. The corresponding plots without moments of inertia can be found in Figure H.1 in Appendix H. Upon visually inspecting the crashed sections, interesting outcomes emerge. When moments of inertia are considered, they effectively counteract the rotation of the section after ground impact, with this counteraction becoming more pronounced as the roll angle increases. In contrast, in scenarios without moments of inertia, the section continues to roll until the spar aligns more or less perpendicular to the ground. Supporting the rationale for introducing moments of inertia, a brief discussion can be derived from Figure 5.4, showcasing all sections where moments of inertia were considered. The extended parts at the rear of the fuselage section (depicted in green, and the outer wing in yellow) with their increased weight and centers of gravity further away from the current analysed model suggest that, if their FEM representations were available and drop tests were conducted, the structure would exhibit greater deformations at the back while additional momentum would more effectively counteract the rotation of the model.

It's important to note that this analysis is preliminary and lacks sufficient empirical support for validation due to time constraints. Nevertheless, such observed behavior may offer a plausible explanation for the disparities in results between the two sections.

12.2. Acceleration Responses

The assessment of acceleration characteristics plays a pivotal role in ensuring occupants' safety, particularly when evaluating accelerations at nodes representing each passenger. Despite the fuselage section's asymmetry, this study focuses on the acceleration responses of passengers on the middle left and right inside, depicted in Figure 12.3. Figures 12.4 and 12.5 display the acceleration responses of fuselage sections corresponding to the various roll angles: 0-deg, 5-deg, 10-deg, and 15-deg.

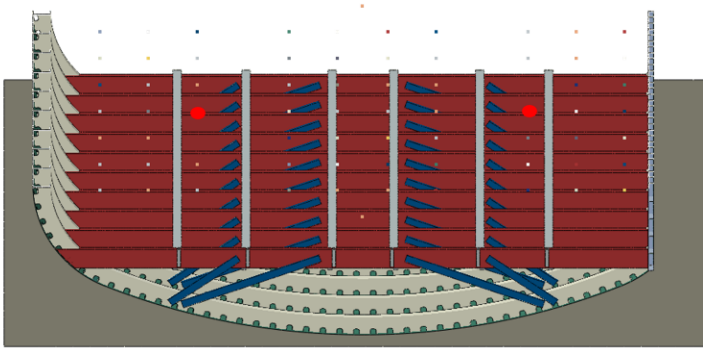

Figure 12.3: The location of passengers where accelerations were recorded

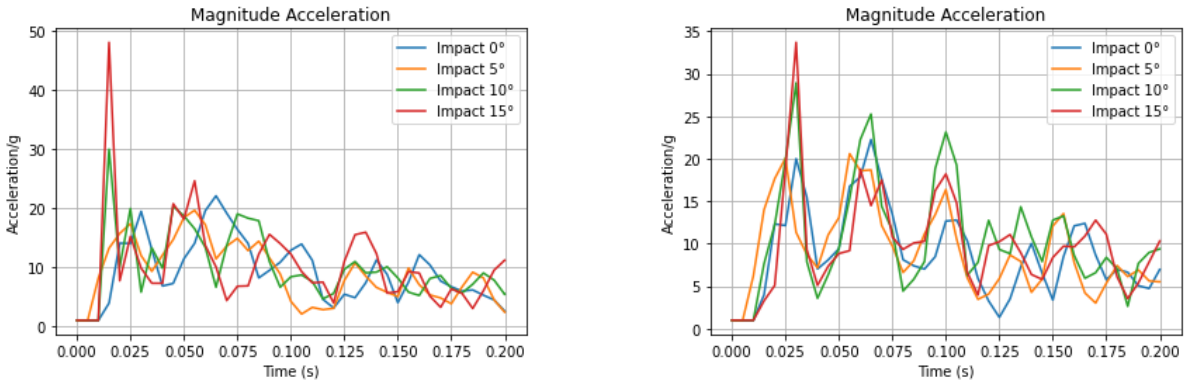

(a) Left inside

(b) Right inside

Figure 12.4: Acceleration responses of two passengers when different roll angles are applied, with moments of inertia

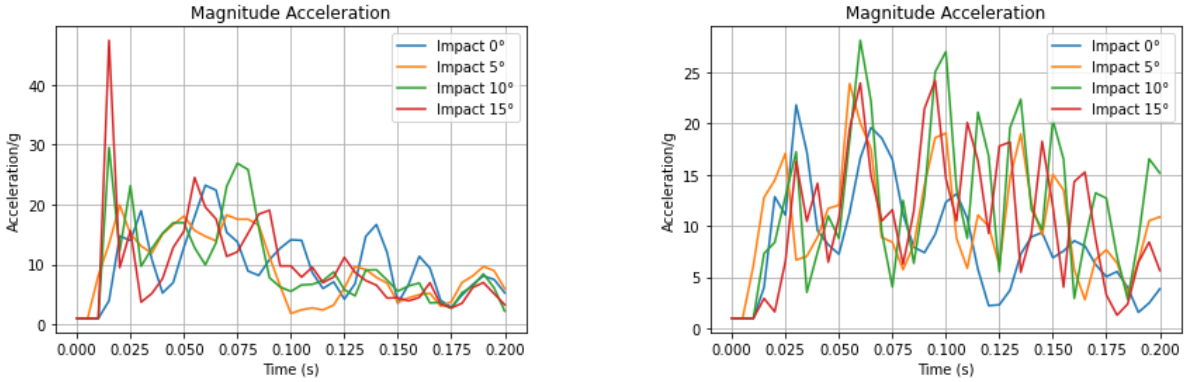

(a) Left inside

(b) Right inside

Figure 12.5: Acceleration responses of two passengers when different roll angles are applied, without moments of inertia

The outcomes highlight the impact of roll angles on acceleration pulses for left and right seat tracks, for both models with and without moments of inertia applied. Table 12.1 summarizes the maximum peak accelerations and their time of occurrence.

Table 12.1: Maximum peak accelerations and corresponding times

Condition	Roll angle	Left inside		Right outside	
		Max peak acc	Time	Max peak acc	Time
Inertia	0-deg	22 g	65 ms	22 g	65 ms
	5-deg	20 g	55 ms	21 g	55 ms
	10-deg	30 g	15 ms	29 g	30 ms
	15-deg	48 g	15 ms	34 g	30 ms
No Inertia	0-deg	23 g	60 ms	22 g	30 ms
	5-deg	20 g	20 ms	24 g	55 ms
	10-deg	30 g	15 ms	28 g	60 ms
	15-deg	47 g	15 ms	24 g	95 ms

A left roll angle results in an increase in peak acceleration response on the left side and a decrease on the right side. Additionally, the timing of acceleration pulses undergoes changes, with left side pulses occurring earlier as the roll angle increases, while right side ones are delayed. These variations in peak acceleration can influence seat behavior, potentially leading to the collapse of left side seats. The effect is more pronounced in cases without moments of inertia, where the impact energy is concentrated on the left part upon ground contact. The introduction of moments of inertia mitigates the rotation of the model, dispersing impact energy throughout the entire section, leading to a more uniform distribution of accelerations sustained by passengers. Once again, the displacement variations depicted in Figures 12.2 and H.1 lend support to these conclusions.

Considering Figure 12.4a as an example, when the fuselage section crashed with a 0-deg roll angle, the corresponding maximum peak acceleration of 22 g occurred at 65 ms. With roll angles of 10-deg and 15-deg, the maximum peak acceleration increased to 30 g and 48 g, appearing at 15 ms for both cases. Clearly, initial, second, and maximum peak accelerations escalate with higher roll angles, and the resulting acceleration pulse arrives earlier. Such a substantial acceleration response in a short time can cause injuries to occupants. The influence of moments of inertia is more obvious on the right side. In cases with, the same pattern as the left side remains consistent: an escalation in the maximum peak aligns with an increase in the roll angle, coupled with a reduction in the corresponding time of occurrence. In contrast, when moments of inertia are absent, the maximum peak remains relatively constant across all angles (22 g for 0° roll and 24 g for 15° roll), but there is a noticeable rise in the time of occurrence (30 ms for 0 roll angle and 95 ms for 15 roll angle).

12.3. Energy Analysis

Figure 12.6 displays the kinetic energy profiles of the fuselage section across the different roll angles. The slight distance between the section and the ground before impact, which is less pronounced in the 5 degrees case, transitions into an initial increase in kinetic energy. However, the initial kinetic energy of the fuselage sections remains constant at 285 kJ for all models, whether moments of inertia are applied or not. The processes of kinetic energy reduction roughly exhibits uniformity and smoothness before 30 ms across the four cases, but divergence is more noticeable after this threshold. The uniformity is less apparent when moments of inertia are omitted, as a more pronounced divergence occurs earlier, approximately at 25 ms (refer to Figure 12.6b).

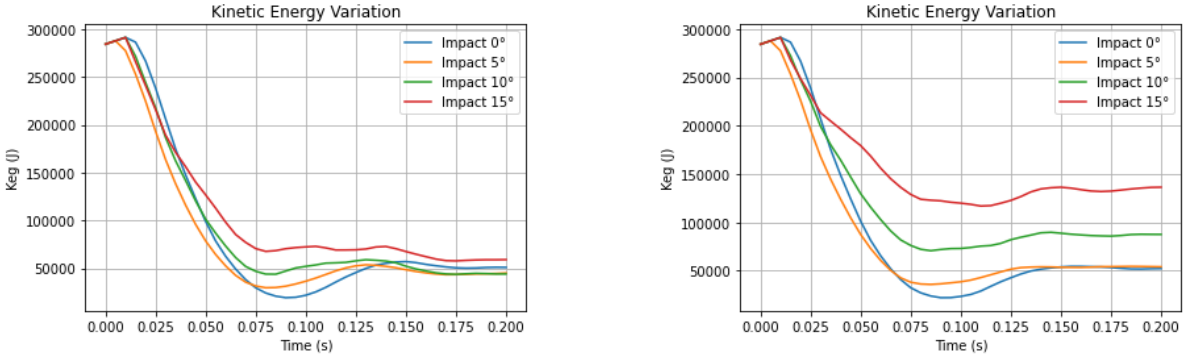

(a) With moments of inertia

(b) Without moments of inertia

Figure 12.6: Kinetic energy histories of fuselage section with different roll angles

The kinetic energy of the fuselage section, whether moments of inertia are included or not, rapidly diminishes, reaching its lowest point at 90 ms during a 0-degree roll angle crash and at 80 ms during a 5-degree roll angle crash. However, as roll angles increase, the divergence between cases with and without moments of inertia becomes more pronounced, notably in the dissipation rate represented by the slope of the curves.

The incorporation of moments of inertia results in distributed energy absorption throughout the entire section, leading to a swift dissipation of energy, evident in the more steep curves. However, the increased roll angles reduce further the rate of energy being dissipated. As it was previously seen, a higher rate of dissipation will imply harder contact with the ground, and, consequently, larger acceleration pulses felt by the occupants. This will be touched upon when analysing the spatial variation of the DRIs and SEVs. Conversely, the absence of moments of inertia concentrates impact energy on the left part of the section, diminishing effective energy-absorbing areas on the right side, therefore decreasing the energy being dissipated by the overall structure. The subsequent kinetic energy present in the structure is attributed to the angular momentum generated by the section's rotation, explaining why kinetic energy is not significantly minimized and maintains high values after impact. Also, the point of maximum deformation, indicating the moment when kinetic energy is minimized, decreases with increase roll angle. This reveals that the perpendicular impact section deforms the most, decreasing the deformation with increasing roll angle. The removal of the moments of inertia accentuates this effect.

The rebound phase follows, during which elastic energy stored in the structure is released and converted back into kinetic energy. Rebounds, generally undesirable, extend the duration of acceleration pulses experienced by occupants. When examining 15-degree roll angles with moments of inertia, the kinetic energy decreases more gradually, not reaching its lowest point until 175 ms, displaying minimal rebounding. The prolonged time for kinetic energy to reach its lowest point as roll angles increase signifies a slower absorption of impact energy, potentially leading to occupant injuries. The 10-degree case exhibits a similar pattern.

However, in the absence of moments of inertia, the rebounding phase becomes more pronounced, diminishing as roll angles increase. Following the impact at a 0-degree angle, the section undergoes a substantial vertical bounce. When a roll angle is introduced, the rebound no longer solely occurs in the vertical direction; instead, it exhibits other directional components, thereby reducing the emphasis on the rebound.

The dissipation of impact energy primarily occurs through large plastic deformations of fuselage structures during impact accidents, although the energy-absorbing capabilities of the main fuselage structures differ. Figure 12.7 displays the energy vs. time curves for various fuselage structures when moments of inertia are applied, and Table 12.2 lists the time of steady state and the energy absorbed by the frames for the four different cases, with and without moments of inertia. Due to limitations in space, in Appendix H, corresponding plots are available for drop cases where moments of inertia are not applied (refer to Figure H.2).

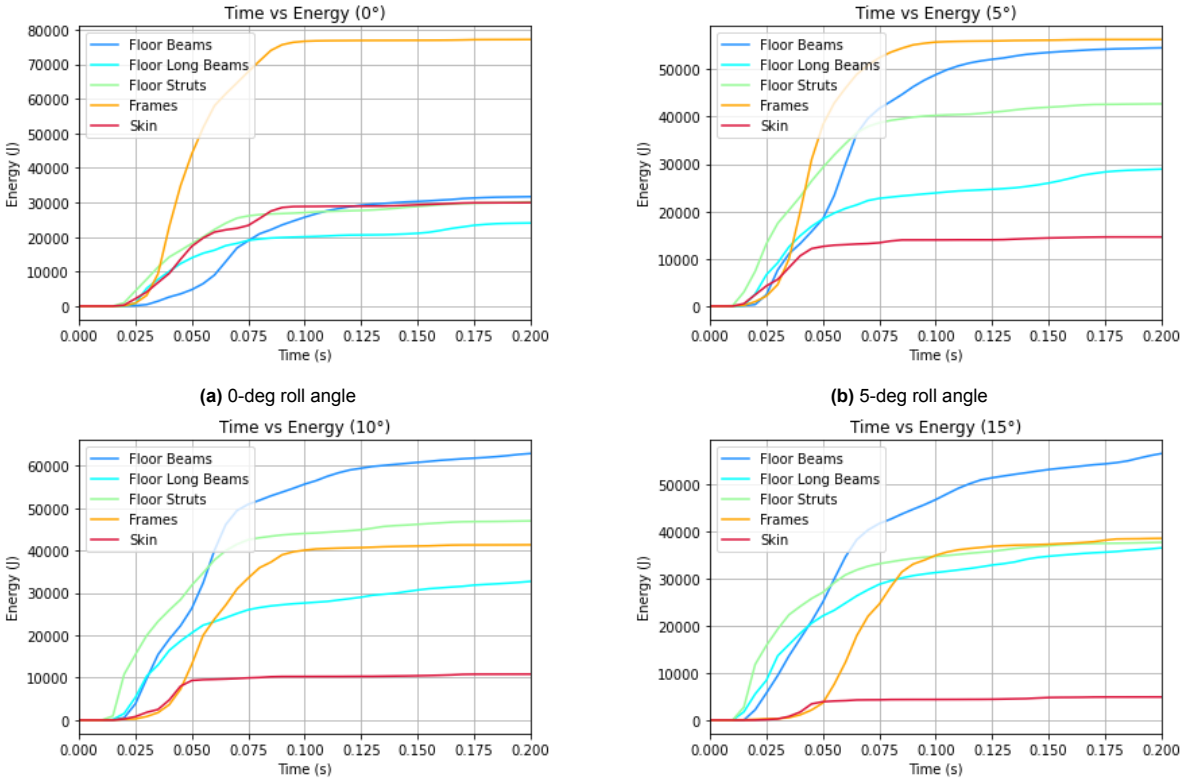

(a) 0-deg roll angle

(b) 5-deg roll angle

(c) 10-deg roll angle

(d) 15-deg roll angle

Figure 12.7: Energy absorption of main structures of fuselage section with different roll angles

Upon analyzing both Figure 12.7 and H.2, it becomes apparent that the floor struts, located right above the impact area when roll angles are introduced, function as the primary energy-absorbing structure during the initial impact stages, exhibiting a swifter increase in absorption as the roll angle increases. Subsequently, in the 0-degree case, the absorption shifts to the fuselage skin and frames, with the frames proving to be the most prominent energy absorber due to unique design features. In cases with elevated roll angles, rapid lateral deformation transfers the absorbed energy from the struts to the floor beams and longitudinal beams. Notably, the energy absorption of the floor components continues to rise beyond that of the frames, without stabilizing, especially evident in the 10 and 15-degree roll angle cases. Figures 12.7 and H.2 suggest that energy absorption stabilizes around 125 ms for the 0-degree roll angle case and around 185 ms for the 5-degree roll angle case. In contrast, for the 10 and 15-degree roll angle cases, energy absorption continues to increase even after 200 ms, suggesting the necessity of bigger time step to capture the entire analysis.

However, the absence of moments of inertia leads to substantial differences between cases. In corresponding perpendicular drop tests, energy absorbed by floor components is considerably higher, attributed to intense rear deformation of the floor beams and longitudinal beams upon impact. The incorporation of moments of inertia constraints the lateral deformation, leading to less overall floor distortion. Also, as mentioned earlier, moments of inertia result in distributed energy absorption throughout the entire section. Conversely, without moments of inertia, impact energy concentrates on the left part of the section during increased left roll angles. This amplifies the energy absorbed by floor components situated directly above the impact area, while notably diminishing the energy absorption by frames.

The gradual reduction in energy absorbed by frames with increasing roll angles is evident in Table 12.2, with a more pronounced reduction when moments of inertia are removed. Additionally, the time for each component's internal energy to reach stability increases, especially in cases without moments of inertia, indicating a delayed stabilization of the fuselage section's deformation during the crash.

Table 12.2: Time of steady state and energy absorbed by frames, with and without moments of inertia

Condition	Roll angle	Time of steady state	Energy absorbed by frames
Inertia	0-deg	100 ms	78kJ
	5-deg	110 ms	57kJ
	10-deg	150 ms	41kJ
	15-deg	200 ms	39kJ
No Inertia	0-deg	100 ms	75kJ
	5-deg	110 ms	52kJ
	10-deg	125 ms	30kJ
	15-deg	150 ms	22kJ

12.4. Angle Impact on the DRIs and SEVs

Figures 12.8 to 12.10 depict the spatial positioning of the Dynamic Response and Severity Indexes along the fuselage section, incorporating moments of inertia.

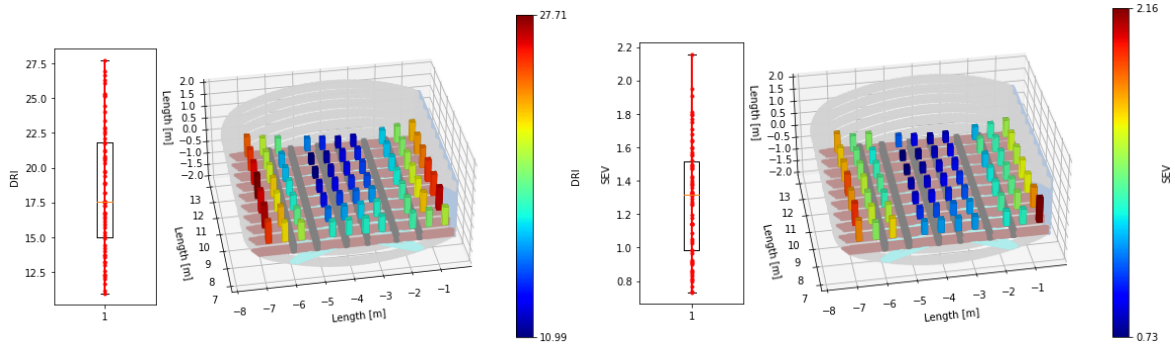

(a) Spatial variation of the DRI **(b)** Spatial variation of the SEV

Figure 12.8: Spatial variation of the DRI and SEV with moments of inertia, for the 5 degrees case

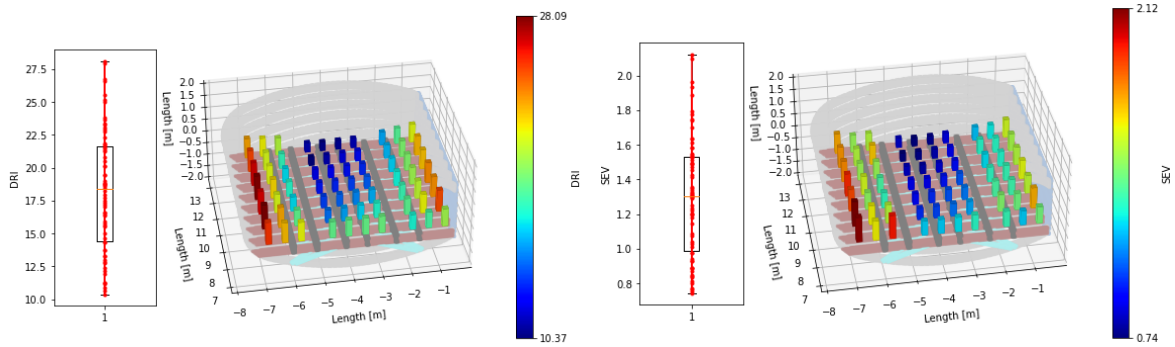

(a) Spatial variation of the DRI **(b)** Spatial variation of the SEV

Figure 12.9: Spatial variation of the DRI and SEV with moments of inertia, for the 10 degrees case

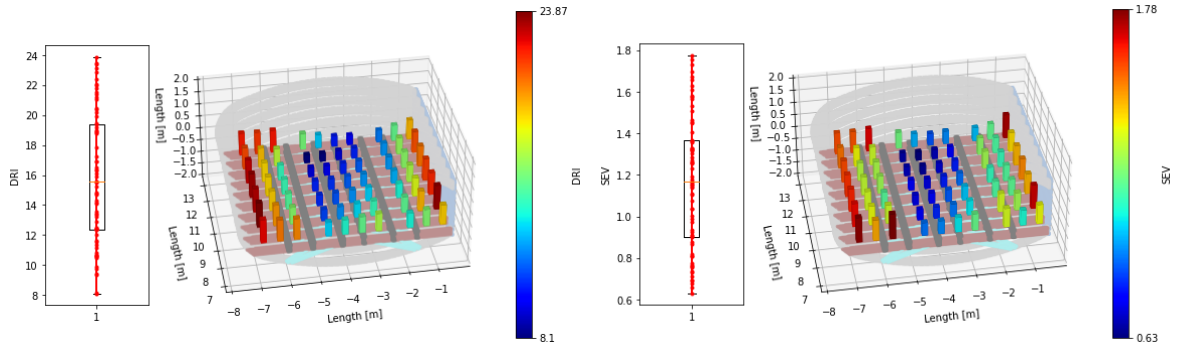

(a) Spatial variation of the DRI

(b) Spatial variation of the SEV

Figure 12.10: Spatial variation of the DRI and SEV with moments of inertia, for the 15 degrees case

Correspondingly, Figures H.3 to H.5 in Appendix H showcase the scenarios without the application of moments of inertia. Specifically, for the 0-degree angle case, refer to Figure 11.6 and 7.11 with and without moments of inertia, respectively.

A discernible correlation emerges when examining each passenger injury criterion alongside the magnitude deformations of each section from Figures 12.2 and H.1. A consistent pattern is evident upon impact, characterized by slightly more deformation at the rear end, resulting in reduced DRIs, and increased stiffness at the front, leading to higher DRI values.

In drop test cases with increased roll angles, higher DRI values are observed on the left side compared to the right side, aligning with the kinematics of the drop test itself. The introduction of roll angles causes the section to impact on a more localized region, particularly the left part, inducing high accelerations for passengers above the initial crashed region.

When moments of inertia counteract the rotation of the section upon impact, energy absorption is more evenly distributed throughout the entire section. This results in more uniform accelerations between the left and right parts, as reflected in Figure 12.10 for the 15 degrees case. In contrast, without moments of inertia, the post-impact behavior involves a rotation to the right side, leading to a gradual reduction in accelerations (and consequently DRIs) from left to right, as illustrated in Figure H.5, for the 15 degrees case without moments of inertia.

However, relying solely on Dynamic Response Indixes for an effective assessment of section crashworthiness during roll angles proves insufficient. In earlier drop tests, the predominant components were the vertical velocity introduced at the onset, coupled with gravitational acceleration. Subsequent lateral accelerations experienced by passengers resulted from fuselage leaning upon impact and side loads due to section rebound—factors slightly considered when plotting the Severity Indexes. While these lateral accelerations were nearly negligible in comparison to the vertical component, in more complex crash scenarios, lateral accelerations become more pronounced, particularly along the x direction (from left to right) in the current case.

This heightened emphasis on side accelerations leads to more discernible differences between DRIs and SEVs in these more intricate situations. Whereas DRI was previously deemed sufficient for crashworthiness assessment, now the significance of SEV becomes more pronounced. It is essential not to overlook the analysis of DRIs, but in such instances, SEV takes on greater importance. Nonetheless, a well-balanced consideration of both injury criteria provides a more nuanced assessment of the structure.

Finally, Table 12.3 summarizes key values from DRIs and SEVs, encompassing averages, maximums, medians, and minimums, along with computational time.

Notably, an interesting pattern surfaces in the average values of DRI and SEV for the 0, 5, and 10-degree cases, remaining relatively consistent with and without the addition of moments of inertia. However, for the 15 degrees case, these averages show a significant reduction, accompanied by a noteworthy decrease in maximum and minimum DRI and SEV. This reduction aligns with the kinetic energy analysis, indicating a decrease in energy dissipation rate and maximum deformation with an increase in roll angle.

Table 12.3: DRI and SEV comparison for different roll angles

Cond.	Angle	DRI				SEV				Comp. Time
		Avg	Max	Median	Min	Avg	Max	Median	Min	(h)
Inertia	0-deg	18.63	26.94	18.42	11.44	1.27	1.83	1.34	0.76	3.83
	5-deg	18.49	27.71	17.53	10.99	1.28	2.16	1.31	0.73	3.56
	10-deg	18.24	28.09	18.36	10.37	1.30	2.12	1.31	0.74	3.53
	15-deg	15.83	23.87	15.54	8.10	1.17	1.78	1.17	0.63	3.59
No Inertia	0-deg	18.95	28.97	19.09	11.93	1.29	2.00	1.30	0.77	6.54
	5-deg	18.40	31.45	17.60	11.70	1.28	2.22	1.25	0.77	3.49
	10-deg	18.57	27.71	18.60	10.99	1.29	2.16	1.31	0.73	3.44
	15-deg	14.16	27.02	12.34	8.40	1.03	1.83	0.93	0.60	3.81

The concentration of impact energy on the left part of the section further diminishes effective energy-absorbing areas on the right side, decreasing even further the rate at which the energy is being dissipated by the overall structure. The lower rate of dissipation will imply softer contact with the ground, and, consequently, reduced acceleration pulses felt by the occupants, which explains the overall reduction in DRIs and SEVs.

12.5. Key Findings and Implications

Similarly to the case study conducted on conventional airplane design and outlined in the Literature, the addition of roll angles revealed distinct failure modes within the FV fuselage sections, marked by the formation of plastic hinges in fuselage frames, floor beams, and oblique struts. This led to the preservation of the structural integrity of the Flying-V's cabin floor, while maintaining occupant survival space at least 85% of the original. A lack of crushing space due to the fuselage's ovalization could further diminish the occupant survival space below this threshold for increased roll angles but, fortunately, the heightened overall stiffness accompanied with the fuselage's ovalization hindered this possibility. Nonetheless, structural integrity does not necessarily guarantee improved passenger acceleration sustainability, prompting subsequent analysis of DRIs and SEVs.

As anticipated, left roll angles directed impact energy towards the left side, resulting in increased maximum peak acceleration on that flank and a corresponding decrease on the right. However, the introduction of roll angles led to a reduction in average DRI and SEV values, with this effect becoming more pronounced at higher angles.

These observations yield both favorable and unfavorable outcomes: the introduction of roll angles can elevate the risk of injury to passengers directly above the point of impact. This localized impact initiation concentrates stress in a smaller region, resulting in higher DRIs and SEVs, which could prove fatal in extreme cases. Conversely, passengers farther away from the impact area might experience increased chances of survival.

Furthermore, whereas fuselage frames were previously the primary energy absorption components in perpendicular impact cases, the introduction of roll angles redirected energy absorption toward floor components, leading to higher plastic deformation. This shift could raise problems especially in maintaining occupants' egress paths.

Lastly, the prior introduction of moments of inertia proved beneficial during vertical drop tests. However, it's important to recognize that the same conclusion may not necessarily apply to more intricate scenarios. In the present analysis, the inclusion of moments of inertia mitigated post-impact rotation, resulting in a more uniform distribution of passenger accelerations through the dispersal of impact energy. Nevertheless, it's crucial to acknowledge that if a more complex FEM model of the Flying-V were available and identical drop tests were conducted, the structure might exhibit different deformations. This analysis only served as a preliminary crashworthiness assessment upon introducing roll angles, with the reduced modelling approach lacking adequate empirical validation due to time constraints. Thus, further research is needed to validate and enhance the comprehension of the observed behavior. It was primarily utilized to underscore differences in section behavior upon the removal of moments of inertia from other sections, without drawing definitive conclusions about its effectiveness.

13

Pitch Angles Landing Assessment on FV Fuselage Crashworthiness

In traditional vertical drop tests or when introducing roll angles into the crash scenarios, the fuselage centerline maintains a horizontal orientation. Previous Chapters illustrated that, by employing the implicit moments of inertia approach, the dynamics of subsequent sections of the Flying-V are approximately considered without the need for a physical representation of the models. Notably, structural deformations, as well as variations in DRIs and SEVs, more closely resemble those observed in full passenger fuselage cases.

Taking a progressive step, this Chapter introduces a variable centerline orientation. Instead of remaining horizontal, a pitch is introduced, and drop tests are conducted with 5-degree increments, up to 15 degrees, as specified in the crashworthiness requirements during the Literature Study. By scrutinizing the crashworthiness of the full passenger fuselage model of the Flying-V under varying pitch angles, this case study aims to provide an understanding of how different orientations affect crash responses. Subsequently, the implicit moments of inertia approach will be re-evaluated.

The Chapter commences with an introduction in Section 13.1, setting the stage for the forthcoming analysis. A visual inspection of crash sections is presented in Section 13.1.1, followed by an energy analysis in Section 13.1.2. To bolster the examination, reactions forces and acceleration distribution along the fuselage length are studied in Section 13.1.3 and Section 13.1.4, respectively. The impact of angle variation on DRIs and SEVs is subsequently analyzed in Section 13.1.5. To ensure the robustness and precision of the implicit moments of inertia approach, a verification and validation plan is outlined in Section 13.2, and identical analysis conducted for the full passenger model are again performed. Due to the disparities in outcomes observed between the full passenger fuselage and the reduced model utilizing applied moments of inertia, Section 13.3 introduces another reduced modelling technique briefly mentioned in the Literature. Finally, Section 13.4 provides a platform for discussing the obtained results.

13.1. Impact of Pitch Angle on the Integrity of the Full Passenger Fuselage

This initial analysis focuses on examining the impact angle with the rigid ground by performing drop tests. The fuselage pitch is deliberately rotated during descent to introduce varying pitch angles, thereby enhancing the fidelity of the investigation.

A series of four analyses were performed. The first involved a direct impact perpendicular to both the ground and the fuselage section, a scenario previously explored in Chapter 9 when studying the full passengers' model. Subsequent simulations featured incremental pitch angles of 5°, 10°, and 15°. Throughout these simulations, a consistent initial velocity of 7.9 m/s (26 ft/s) was maintained.

For a more detailed information on the geometrical and numerical aspects of the full passengers' fuselage section, refer to Section 9.1.

13.1.1. Visual Inspection of the Crash Sections

This section presents numerical analyses to evaluate how the pitch angle affects the damage behavior of the fuselage section. The test specimens collided with the ground at pitch angles of approximately 5°, 10°, and 15°. Figures 13.1, 13.2, and 13.3 depict the moments before and after the impact for each respective case, where the impact initiation between the fuselage section and the ground can clearly be seen.

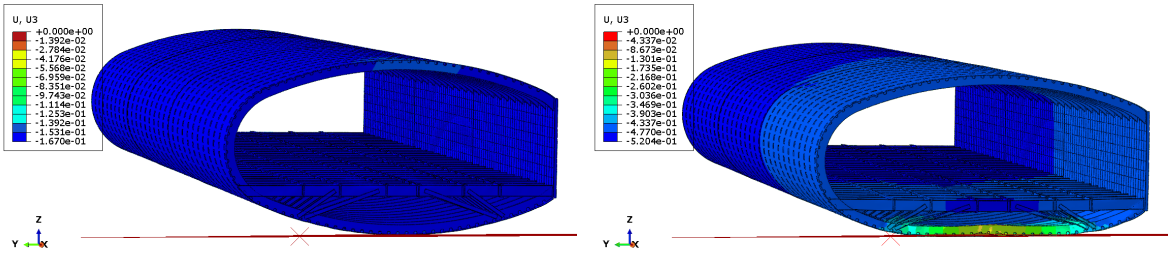

(a) Before the impact (0.02s) **(b)** After the impact (0.06s)

Figure 13.1: 5° pitch angle impact with the ground

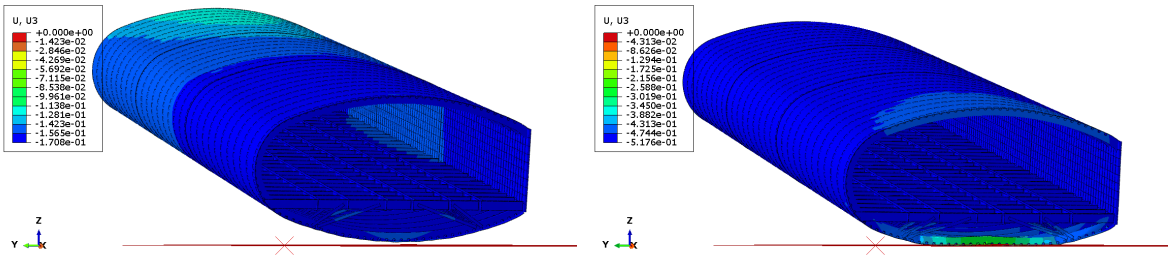

(a) Before the impact (0.02s) **(b)** After the impact (0.06s)

Figure 13.2: 10° pitch angle impact with the ground

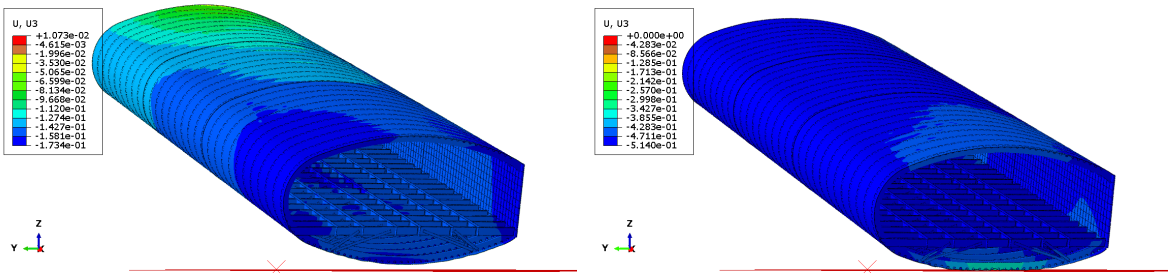

(a) Before the impact (0.02s) **(b)** After the impact (0.06s)

Figure 13.3: 15° pitch angle impact with the ground

As emphasized in the right depiction of each Figure, the imbalance in fuselage sections resulted in impact initiation on a very small area and, as the pitch angle increases, this impact area diminishes progressively, leading to increasing stresses.

This can also be inferred in Figure 13.4, the instant when the rear portion of the fuselage section makes contact with the ground in each scenario. Higher deformations at the front part of the cargo floor illustrates the effect of smaller initial impact areas.

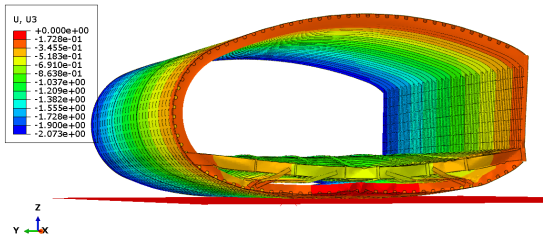

(a) 5° case (0.18s)

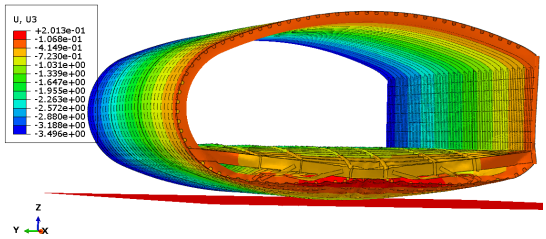

(b) 10° case (0.28s)

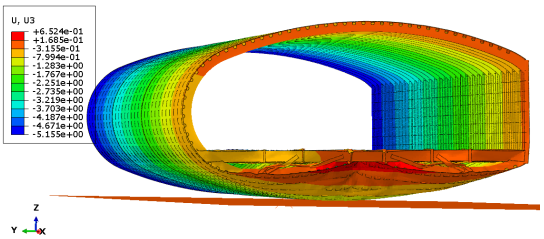

(c) 15° case (0.38s)

Figure 13.4: Step frames when the rear section impacts the ground

As mentioned earlier, a numerical analysis was previously conducted to simulate the collision between the fuselage section and the ground without any pitch angle. Shown in Figure 13.5, a relatively uniform damage occurred across all lower frames and reinforcements in the perpendicular impact between the rigid ground and the fuselage section.

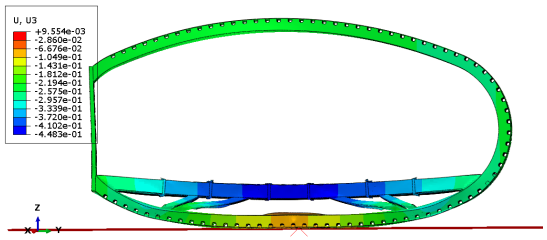

(a) 0° impact front view

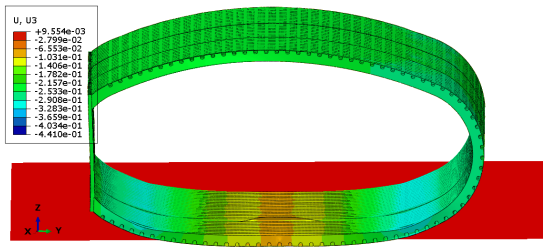

(b) 0° impact without floor

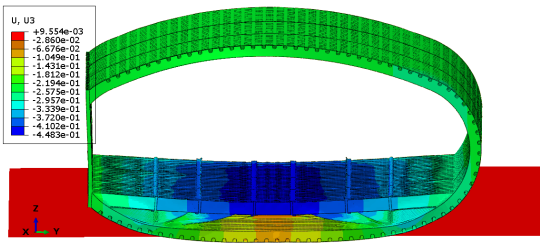

(c) 0° impact diagonal view

Figure 13.5: Perpendicular ground collision (0.06s)

13.1.2. Energy Analysis

Figure 13.6 provides a summary of the damage energy graphs for all the configurations as computed by the Abaqus code. The computation of damage energies involved assessing the cumulative dissipated damage energy for each element. The graph in Figure 13.6a illustrates that the 100 kJ damage energy threshold was attained at distinct time steps for the four analyzed configurations. Specifically, the configuration without any impact angle reached the 100 kJ damage energy mark around 0.03 seconds, whereas the other configurations reached this level at a later time, experiencing even further delay in reaching the threshold due to the increase in pitch angle.

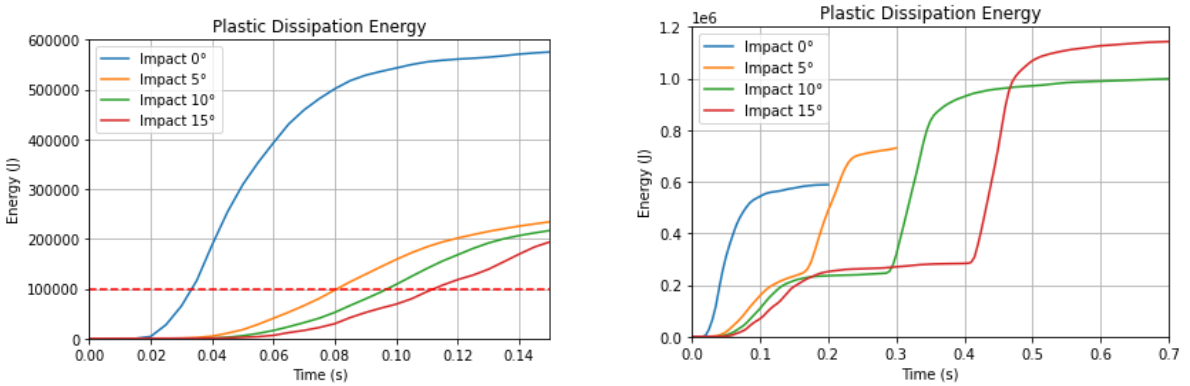

(a) Initial time range up to 0.15 seconds

(b) Whole time range of the drops

Figure 13.6: Influence of the pitch angles in plastic dissipation energy

These trends were expected, as the damaged area in the case of the perpendicular impact was considerably more extensive during the initial moments of the fuselage contact with the ground, resulting in rapid energy dissipation.

Figure 13.6b illustrates the plastic energy dissipation over the entire time span for each case. As the pitch angle increases, the dissipation of impact energy takes longer, attributed to the gradual contact of the fuselage with the ground, contrasting the simultaneous impact seen in the case of perpendicular collisions. Higher pitch angles result in increased angular momentum, requiring more energy to be dissipated due to plastic deformation. Moreover, the curves in Figure 13.6b for drop tests involving pitch angles exhibit a stepped shape. This characteristic is attributed to the full fuselage being divided into three subdivisions - back, engine, and front - interconnected using tie constraints in Abaqus. During rotation, the front part gradually makes contact with the ground, absorbing energy through plastic deformation. Subsequently, in a gradual sequence, the engine part follows suit, succeeded by the back part. This step-like pattern in the curves reflects the sequential impact and plastic deformation of each fuselage subdivision during the drop tests.

Figure 13.7 displays cross-sections of the deformed fuselage sections assessed at specific time intervals: 80 ms, 100 ms, and 110 ms for configurations with impact angles of 5°, 10°, and 15°, respectively, and 30 ms for the configuration with a perpendicular ground impact.

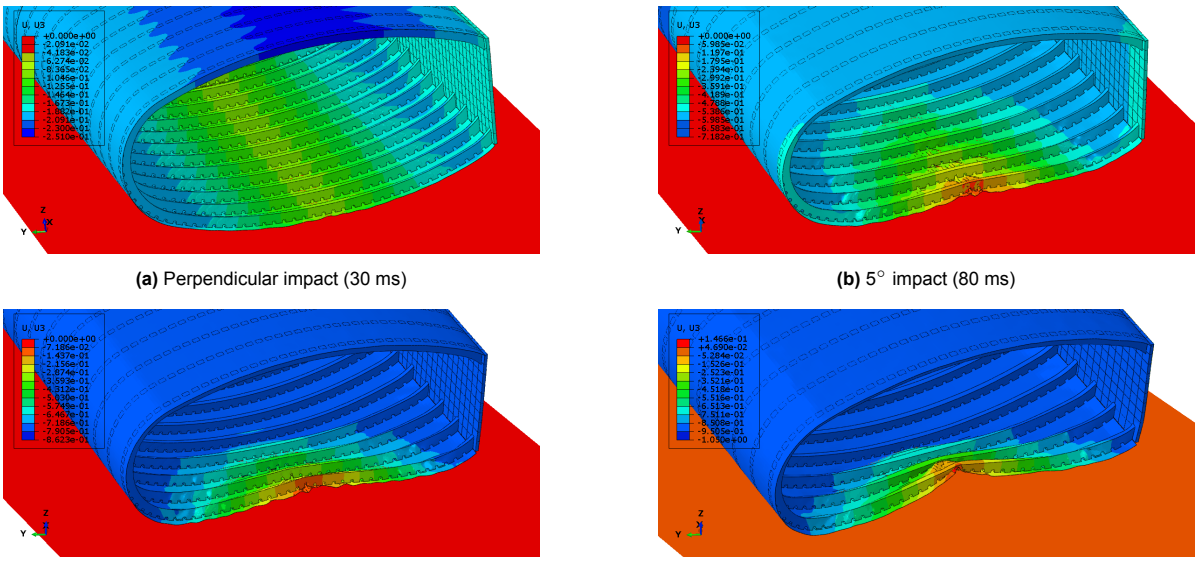

(a) Perpendicular impact (30 ms)

(b) 5° impact (80 ms)

(c) 10° impact (100 ms)

(d) 15° impact (110 ms)

Figure 13.7: Early stages of impact in the sub-cargo area, with a total dissipated plastic energy of 100 kJ. The removal of the floor enhances clarity for better comprehension.

As already remarked, under these conditions, where the dissipated plastic energy amounted to 100 kJ (as indicated in Figure 13.6a), a comparison between Figure 13.7a and Figures 13.7b, 13.7c and 13.7d reveals a substantially more extensive damaged area in the configuration with the perpendicular impact, contrasting with the configurations involving impact angles.

Proceeding further, Figure 13.8 illustrates the temporal variation of kinetic energy for all the cases. The drop tests commence with the specimens positioned a few millimeters above the ground, elucidating the initial increase in kinetic energy observed in all simulations.

The analysis applied to the variation in energy dissipation among all the specimens can be extended to the examination of kinetic energy curves. When incorporating pitch angles and considering an equivalent amount of damage energy, the predominant absorption of kinetic energy occurs primarily in the outermost front frames and reinforcements. This results in more pronounced deformations in this region compared to a perpendicular impact, where damage in the sub-cargo area appears to be distributed almost uniformly along the length of the fuselage section but concentrated in the central area of the subfloor, leading to smaller deformations.

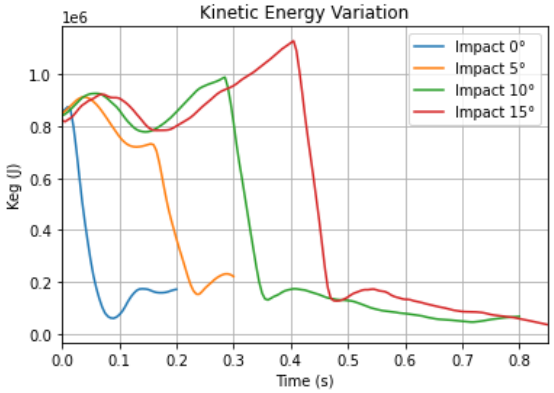

Figure 13.8: Kinetic energy histories of fuselage section with different pitch angles

In non-perpendicular impact scenarios, the kinetic energy absorbed and subsequently dissipated as plastic energy by the structure appears to result in more hazardous damage extending beyond the subfloor area. This extended damage has the potential to significantly impact the passenger area, particularly in the presence of higher pitch angles. The increased angular momentum created by the pitch angle further accelerates the fuselage section, contributing to the overall increase in kinetic energy of the sections and a more forceful ground impact. On the other hand, the 0 degrees impact case results in a faster energy absorption. This is evident in the steep slope of the kinetic energy variation curve, leading to the solution reaching equilibrium much sooner than other cases, around 200 ms.

Finally, the rebound phase occurs, where elastic energy stored in the structure is released and converted back into kinetic energy or dissipated through vibrations in the case of material failure. From Figure 13.8, it is evident that for the perpendicular ground impact case, the rebound is higher, potentially prolonging the duration of acceleration pulses experienced by occupants.

Advancing further, Figure 13.9 illustrates the energy absorption by components throughout the crash duration for all four distinct impact angles. Once again, the curves for drop tests involving pitch angles exhibit a stepped shape, as previously explained. Notably, an intriguing trend emerges: the energy absorption by components rises with an increase in pitch angle. The rotation of the fuselage around the same contact point results in structural components farther from the rotation point possessing higher angular momentum. Consequently, these components deform more, absorbing more impact energy due to a more forceful ground impact. Across all cases, frames emerge as the structural component that absorbs the most impact energy. In contrast, the floor beams exhibit less deformation for perpendicular impacts, gradually increasing as the impact angle rises. Figure 13.4 sheds light on this observation: upon ground impact, the frames undergo drastic deformation, impacting the structural components of the floor, particularly the floor longitudinal beams. Due to the intense impact and the elongated shape of the floor longitudinal beams, they subsequently deform and continue to vibrate, with accentuated vibration at higher angles, leading to a lack of convergence when a pitch angle is introduced.

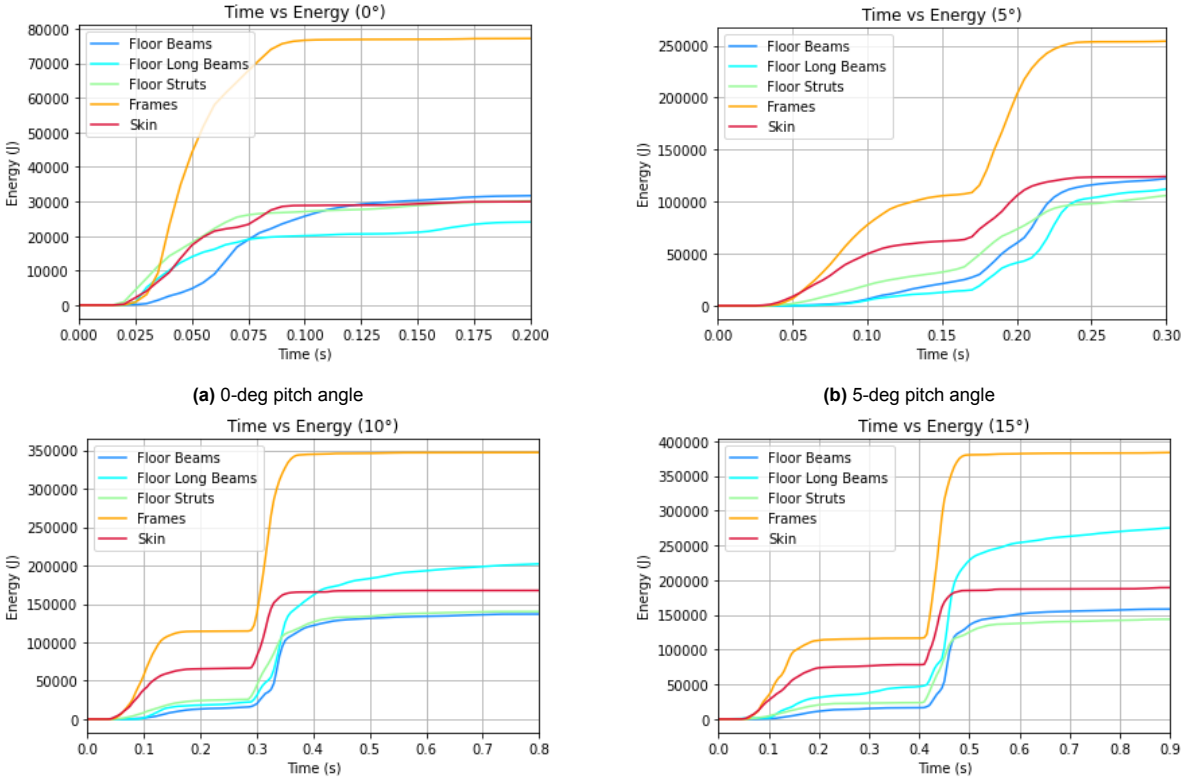

(a) 0-deg pitch angle

(b) 5-deg pitch angle

(c) 10-deg pitch angle

(d) 15-deg pitch angle

Figure 13.9: Energy absorption of main structures of fuselage section with different pitch angles

13.1.3. Force vs Time

Continuing along the same line of thought, Figure 13.10 illustrates the trends of force versus time for the four examined configurations. The force, measured as the reaction force in vertical z-direction on the rigid plane, exhibits distinctive behaviors across these configurations.

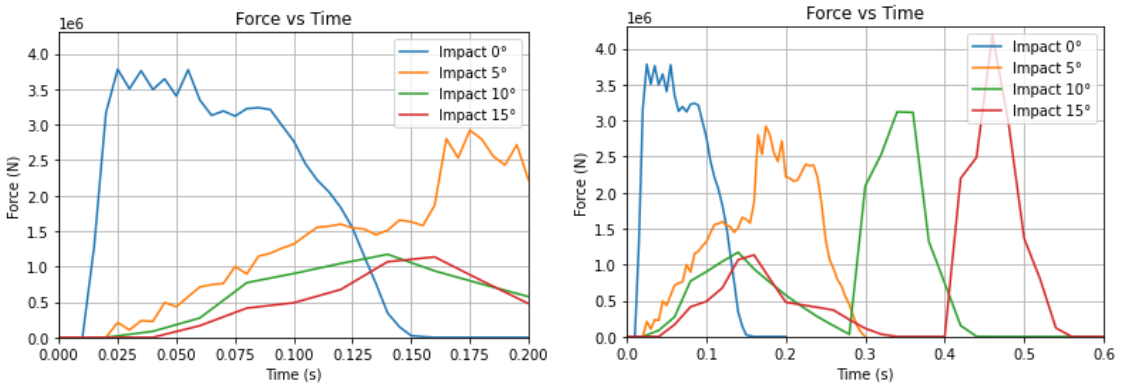

(a) Initial time range up to 0.2 seconds

(b) Whole time range of the drops

Figure 13.10: Time-dependent force profiles for the four different scenarios

In the scenario of the zero-impact angle configuration, an early peak force of approximately 3750 kN was recorded in the analysis at 0.025 seconds, Figure 13.10a. Conversely, configurations with increased pitch angles reached lower peak forces, with values of 3000 kN at 0.17 seconds for the 5° case and 3200 kN at 0.35 seconds for the 10° case. The 15° case, however, deviated from this pattern, displaying higher reaction forces of approximately 4300 kN at 0.46 seconds, as seen in Figure 13.10b.

These observed behaviors are indicative of the deformations occurring in all configurations. Specifically, the configuration experiencing a perpendicular impact underwent a more abrupt but longer deformation, as the impact energy was distributed along the entire length of the fuselage. Consequently, the residual stiffness at the onset of the impact event remained significant, resulting in a force peak that remained relatively constant for almost 0.1 seconds (blue line in Figure 13.10a). On the contrary, configurations with increased pitch angles experienced sudden deformations on one edge, leading to an immediate degradation of stiffness and the absence of force peaks in the initial stage of the impact event (refer to the other curves in Figure 13.10b). The force peaks were encountered at later stages, and in the case of the 15° impact, the rotational motion kinematics contributed to an even more forceful impact with the ground at a later time.

13.1.4. Acceleration Distribution along the Fuselage Length

In Figure 13.11, depicting the front fuselage section for configurations with impact angles of 5°, 10°, and 15°, four specific nodes have been designated as control points for acceleration measurements. These identical locations were chosen as control points for the fuselage model experiencing a perpendicular impact. This choice facilitates a comparative analysis of the impact angle's influence on the distribution of accelerations along the length of the fuselage.

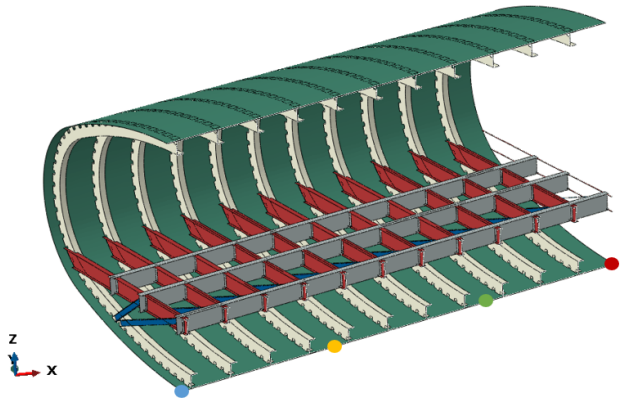

Figure 13.11: Node positions along the front fuselage length

Figure 13.12 depicts the acceleration along the z-direction over time at the specific control points identified in Figure 13.11, offering insights into the impact dynamics of the four configurations. Figure 13.12a illustrates accelerations for the perpendicular impact, while Figures 13.12b, 13.12c, and 13.12d depict accelerations for the 5°, 10°, and 15° impact angle configurations, respectively.

In the case of the normal impact event, all control points displayed non-zero acceleration from the outset, affirming that the impact force uniformly influenced the entire fuselage length right from the beginning. Conversely, in configurations with impact angles, the initial acceleration of the first control point was comparatively higher than that of the other control points. This observation suggests that, for these configurations, the impact force initially acted on a smaller area during the initial phases of the impact event. Nevertheless, it's noteworthy that both the first and second points in the drop test with a 10° pitch angle exhibited similar accelerations during the initial ground contact.

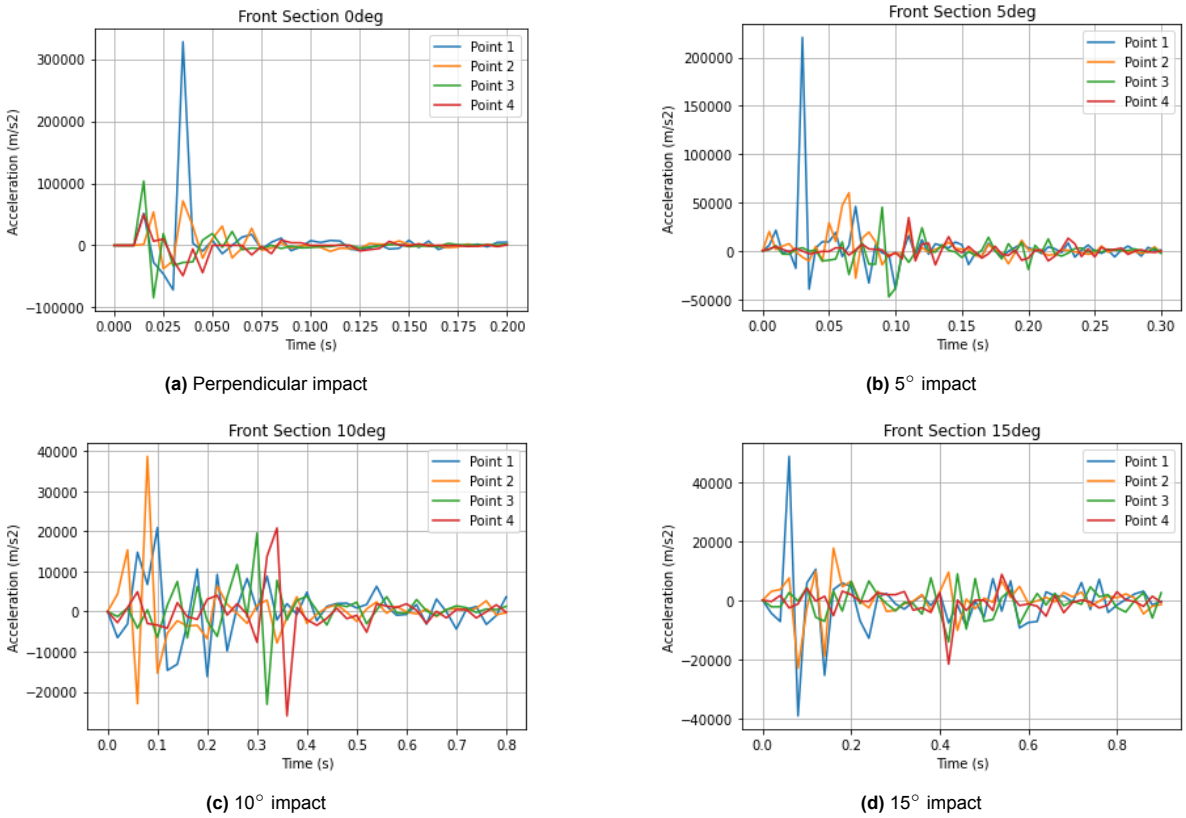

(a) Perpendicular impact

(b) 5° impact

(c) 10° impact

(d) 15° impact

Figure 13.12: Acceleration of four different control points along the front section of the fuselage

Additionally, due to the relatively condensed length dimensions of the front passengers' fuselage, understanding the impact of the pitch angles becomes more challenging, so the accelerations of three reference points spanning the entire passengers' fuselage—including the front, engine, and back sections—were also plotted for a comprehensive understanding of the impact dynamics (see Figure 13.13).

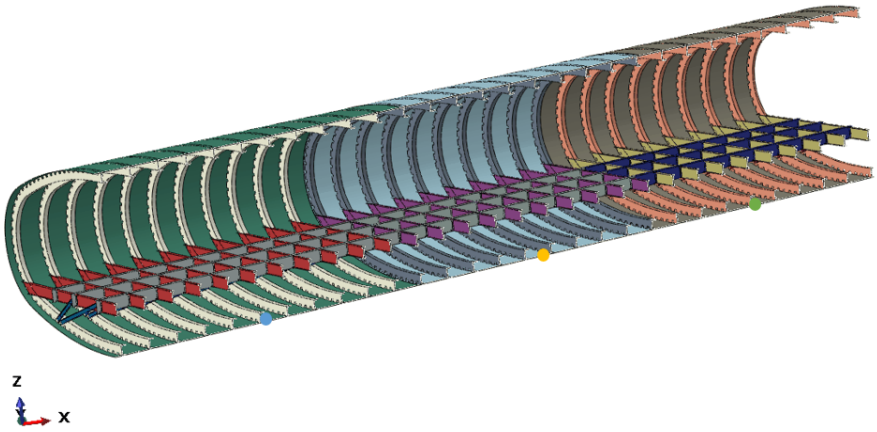

Figure 13.13: Node positions along the full passengers' fuselage length

The previously mentioned observations are reiterated in a clearer manner this time, as the points are more widely spaced (refer to Figure 13.14). In the case of a perpendicular impact, all three points make contact with the ground more or less simultaneously. However, with an increase in pitch angles, the time at which each point touches the ground prolongs, especially for points located farther away from the initial point of contact.

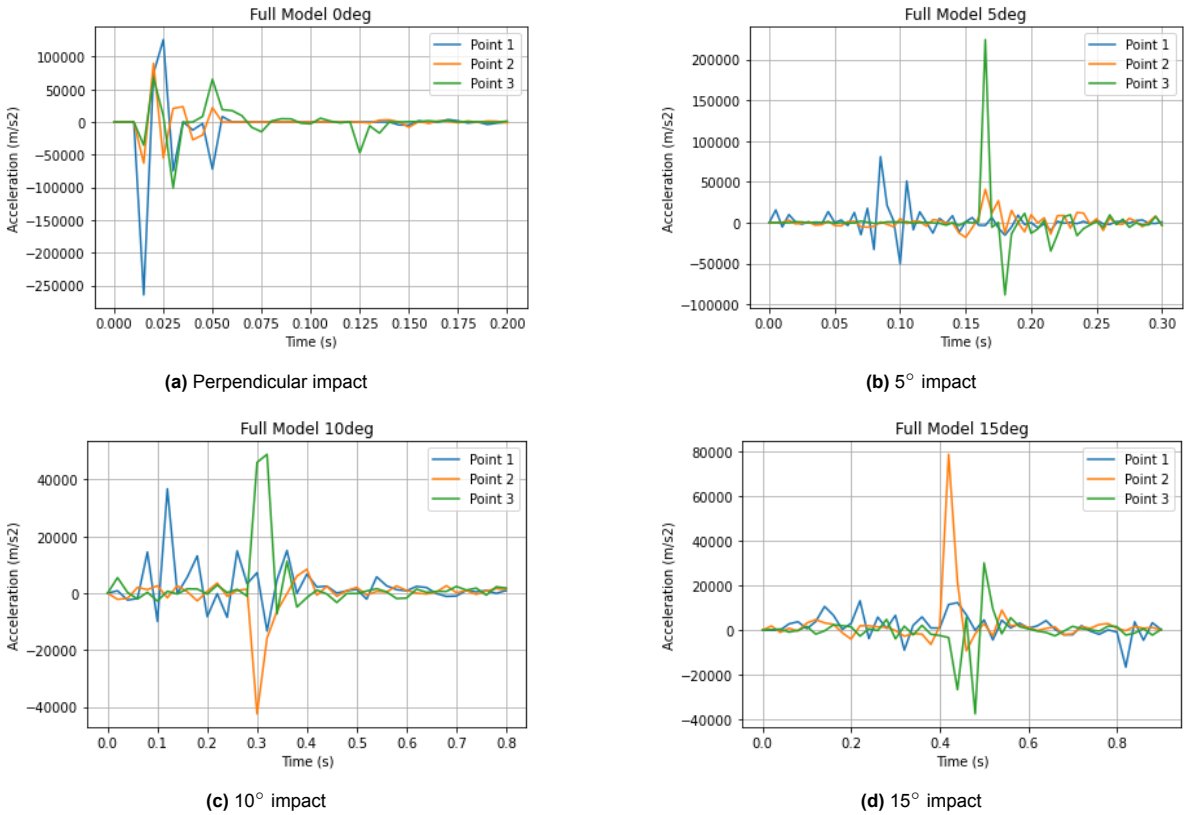

(a) Perpendicular impact

(b) 5° impact

(c) 10° impact

(d) 15° impact

Figure 13.14: Acceleration of four different control points along the full passengers' fuselage

13.1.5. Angle Impact on the DRIs and SEVs

Figures 13.15, 13.16 and 13.17 illustrates the spatial variation of DRIs and SEVs for pitch angles of 5, 10, and 15 degrees, respectively. The results for the 0-degree case were previously discussed and are depicted in Figure 9.9.

To accommodate space limitations, the magnitude displacement corresponding to these impact scenario cases are presented in Figure I.1 from Appendix I. The defined limit for magnitude displacement corresponds to the maximum value observed in the 15-degree pitch angle case, occurring at the fuselage's end due to the initial angle. For a more concise analysis, Figure I.2 also displays the maximum and minimum displacement values for each specific case.

Regarding the 0-degree case, the impact surface comprised lower frames and reinforcements that contacted the ground simultaneously, resulting in relatively uniform damage longitudinally. This uniformity led to rapid energy absorption, reducing DRIs and SEVs compared to other cases.

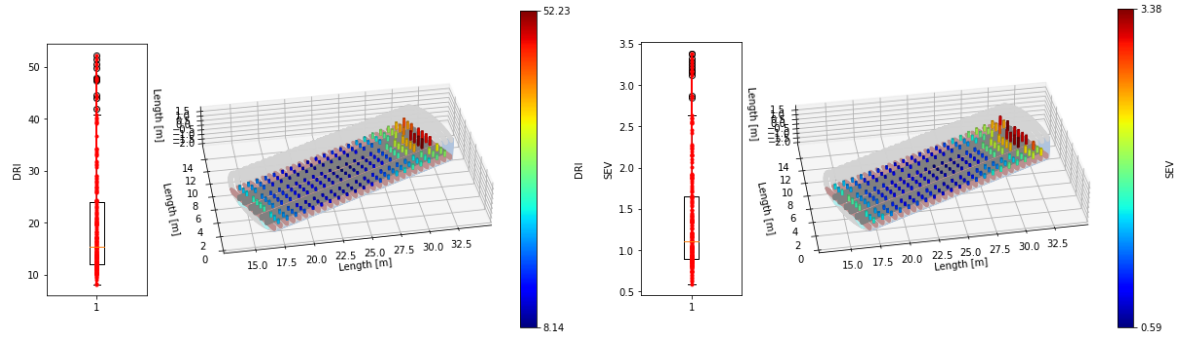

(a) Spatial variation of the DRI

(b) Spatial variation of the SEV

Figure 13.15: Spatial variation of the DRI and SEV along the full passengers' fuselage section, with 5° pitch angle

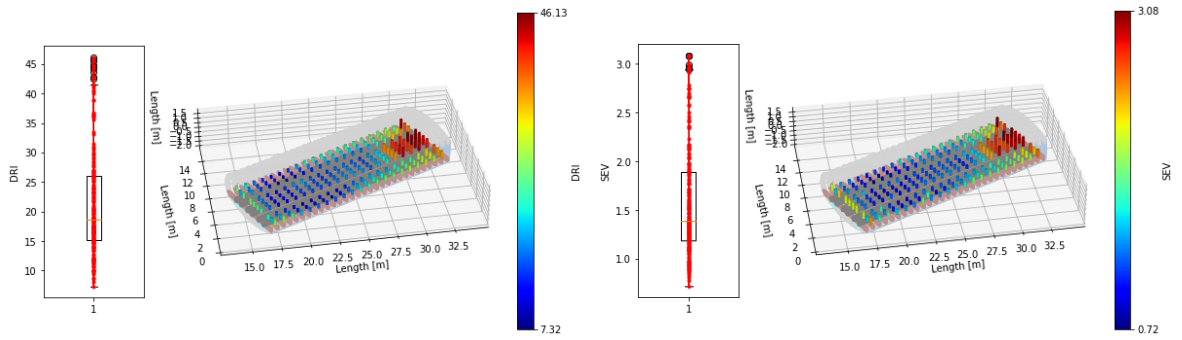

(a) Spatial variation of the DRI **(b)** Spatial variation of the SEV

Figure 13.16: Spatial variation of the DRI and SEV along the full passengers' fuselage section, with 10° pitch angle

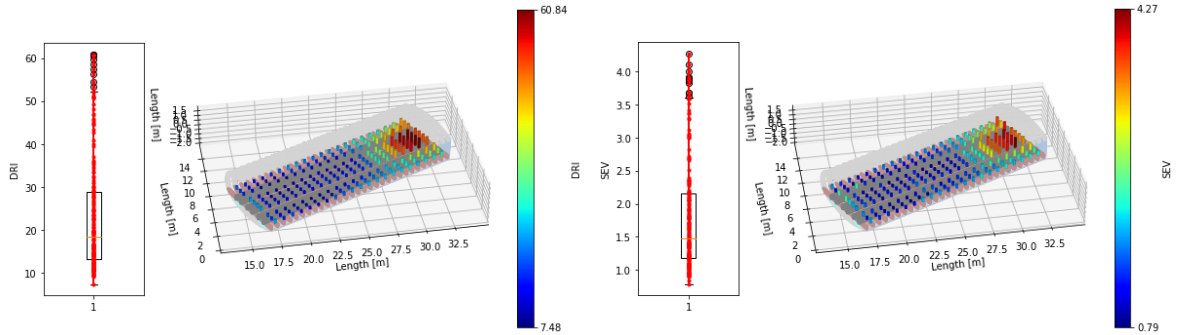

(a) Spatial variation of the DRI **(b)** Spatial variation of the SEV

Figure 13.17: Spatial variation of the DRI and SEV along the full passengers' fuselage section, with 15° pitch angle

The higher plastic deformation in the fuselage's middle enhanced energy absorption, further reducing DRIs. On the contrary, increased stiffness near the sides resulted in less structural deformation, raising DRIs. As the SEV considers the DRI in its calculation and the primary impact component is in the vertical z direction, the SEV follows the same trend as the DRI.

For pitch angles of 5 to 15 degrees, additional angular momentum from the fuselage sections' rotation around the contact point accelerates the fuselage, resulting in stronger impacts with the ground, particularly in regions farther from the rotation point. Analyzing DRIs and SEVs, especially at the sections' end, visually confirms this observation. Notably, the 5-degree case yields a higher maximum DRI and SEV index value than the 10-degree case. This seemingly counterintuitive result is explained by the more localized deformation in a smaller end impact area in the 5-degree case, leading to higher accelerations locally. Conversely, the 10-degree case extends the impact area slightly further back.

Contrary to previous trends, introducing pitch angles causes higher DRI and SEV values in the middle longitudinal areas rather than sideways near the spar and lateral frames, mainly at the fuselage's back end. This shift is attributed to the very high velocities reached at the section's end, resulting in strong impact forces and substantial deformations of structural elements. The limited space between frames and the floor structure cannot contain the large plastic deformations, ultimately impacting floor structural elements and subjecting passengers to excessive accelerations. Finally, the first row for cases with pitch angles exhibits higher DRI and SEV values due to impact initiation in a small area, as observed in Figures 13.4 and 13.7.

Table 13.1: DRI and SEV comparison for different pitch angles

Pitch Angle	**DRI**				**SEV**				**Comp. Time (h)**
-	Avg	Max	Median	Min	Avg	Max	Median	Min	-
0-deg	19.57	29.68	19.06	13.00	1.34	2.13	1.44	0.84	9.31
5-deg	19.47	52.23	15.44	8.14	1.37	3.38	1.11	0.59	25.41
10-deg	21.51	46.13	18.63	7.32	1.58	3.08	1.39	0.72	43.80
15-deg	23.28	60.84	18.38	7.48	1.79	4.27	1.48	0.79	44.68

13.1.6. Reflection on the Results

Previous research on the crashworthiness of the Flying-V aircraft identified an existing gap in evaluating its ability to withstand tail impacts and rigid body rotation. In comparison to traditional aircraft fuselages, the Flying-V's fuselage is notably more robust and rigid. In the event of a tail-impact crash landing, one potential scenario is the outer wings of the FV sustaining damage or detaching from the main body. While this could potentially enhance crashworthiness by dissipating energy, the absence of a FEM model for the outer wings and the lack of analysis on potential separation hindered further investigation. This aspect stands as a recommendation for future research endeavors. Moreover, the increased stiffness and strength of the Flying-V's fuselage section led to an analysis of the effects of rigid body dynamics.

Indeed, diverging from traditional vertical drop tests, where initial fuselage-ground contact led to considerably broader damage areas, configurations with pitch angles showcased heightened deformations at the front section of the cargo floor. This highlighted the impact of smaller initial impact zones, with amplified effects observed at steeper pitch angles.

Perpendicular drop tests revealed a predominant engagement of lower frames and reinforcements with the ground simultaneously, resulting in longitudinally uniform damage, aligning with previous modelling approaches. This trend increased the risk of injuries sideways, near the stiffer areas of the spar and lateral frames, with improved survival prospects in the central region.

However, the introduction of pitch angles resulted in heightened angular momentum, accelerating the fuselage section and intensifying ground impact, necessitating greater energy dissipation due to plastic deformation. Consequently, energy absorption was predominantly localized in the outermost back frames and reinforcements, leading to more pronounced deformations in this area and extending hazardous damage beyond the subfloor region. The high velocities attained at the section's end, coupled with restricted space between frames and the floor structure, were insufficient to accommodate significant plastic deformations, ultimately impacting floor structural elements and subjecting passengers to excessive accelerations, thereby raising safety concerns.

These damages could potentially be mitigated if the fuselage were not elliptically shaped. A rounded shape would enhance the crushing space beneath the floor, allowing for more extensive frame deformation before potentially affecting the passenger area. Although literature on the crashworthiness of conventional airplanes was reviewed, conclusive studies regarding possible passenger injuries were lacking. Therefore, further exploration of the effects of fuselage ovalization and subsequent rigid body dynamics could be further conducted in future research.

Also, previous study introduced alternative conceptual designs for the Flying-V, particularly focusing on adjustments to the crushable elements beneath the floor. While the chosen design for continued crashworthiness assessment exhibited better performance in vertical drop tests, another design incorporating additional crushable elements could potentially be considered more survivable when subjected to pitch angles. This would naturally increase the complexity of the fuselage section and subsequent simulations, demanding an extensive analysis of previously explored design concepts under varying pitch angles. However, such detailed investigation was not deemed necessary for the current study, nor is it proposed for subsequent research.

While this analysis offers initial insights into the effects of rigid body dynamics and identifies potential areas of concern, it only represents a fraction of the entire Flying-V aircraft. Nevertheless, the analysis falls short in considering the overall V-shape of the Flying-V due to its one-sided representation. Furthermore, due to time constraints and the absence of horizontal velocity, no conclusions were drawn regarding the inherent yaw angle of the Flying-V, which could introduce side loads to passengers as a result of misalignment of passenger seats compared to traditional aircraft configurations. This aspect also stands as a recommendation for future research.

13.2. Reduced Model Analysis: An Assessment of the Viability of the Implicit Moments of Inertia Technique

After evaluating the crashworthiness of the entire passenger fuselage under various pitch angles, the next phase involves assessing the practicality of the previously suggested extended/reduced model. This section has been previously tested for conventional vertical drop tests and when subjected to roll angles. As basis for comparison, the extended model, both with and without applied moments of inertia, was compared to the same perpendicular drop test conducted on the full passenger fuselage model. Nonetheless, in the prior analyses, the section's centerline remained horizontal, resulting in favorable outcomes such as reduced computational time and improved simulation realism.

In the current scenario, the same methodology is employed, utilizing the extended model positioned near the fuselage's midsection (refer to Figure 13.18a). Two reference points are again strategically placed on each side of the reduced section using a distributed coupling technique, attaching them to the lateral surfaces (see Figure 13.18b). This distributed coupling accommodates the inherent deformation of secondary nodes, particularly those forming the lateral surfaces, ensuring simulation fidelity. The moments of inertia of the aft and forward sections of the passengers' fuselage are then applied to their corresponding reference points.

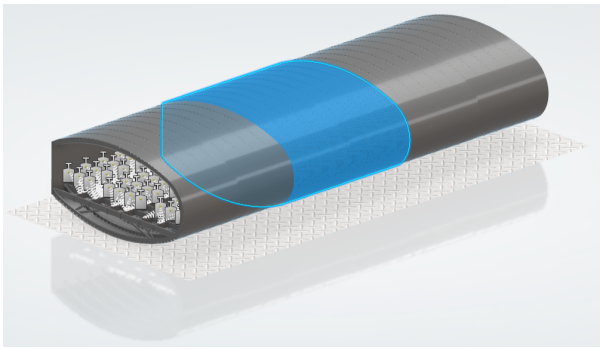

(a) Passengers' fuselage, with special attention to the midsection

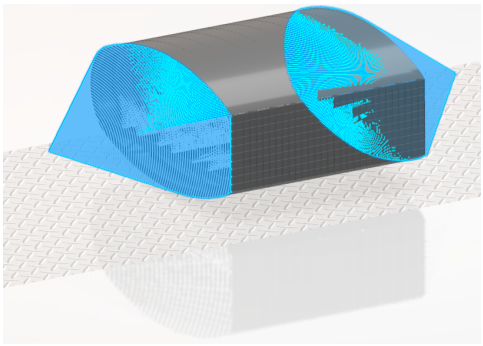

(b) Reference points attached to the lateral surfaces

Figure 13.18: Full and reduced model employed in the validation

However, the current landing scenario presents a slightly more complex situation. Due to the reduced length of the extended model compared to the full passenger fuselage (approximately three times smaller), a straightforward introduction of a pitch angle cannot be conducted for the reduced model and the associated drop tests. To overcome this challenge, a new validation approach is implemented.

13.2.1. Validation Approach

To authenticate this approach, the impact velocity for the midsection was determined through analytical calculations. Subsequently, drop tests for the reduced section were simulated at 0°, 5°, 10°, and 15° angles, incorporating the computed impact velocities. The resulting DRIs and SEVs were then juxtaposed with those acquired from drop tests of the complete model's engine section at the corresponding angles. This methodology facilitated an examination of the impact of moments of inertia and yielded valuable insights for potential adjustments in the future.

Analytical formulation

To determine the impact velocity of the reduced model, a rigid body rotation of the entire passengers' fuselage was taken into account, revolving around a point of contact with the ground. For clarity, three states were considered:

- **State 1:** the moment just before the passenger fuselage made contact with the ground, incorporating a specific angle (see state 1 in Figure 13.19).
- **State 2:** the moment immediately after the passenger fuselage came into contact with the ground (state 2 in Figure 13.19).
- **State 3:** the moment just before the entire fuselage touched the ground, now in a parallel orientation to it (state 3 in Figure 13.19).

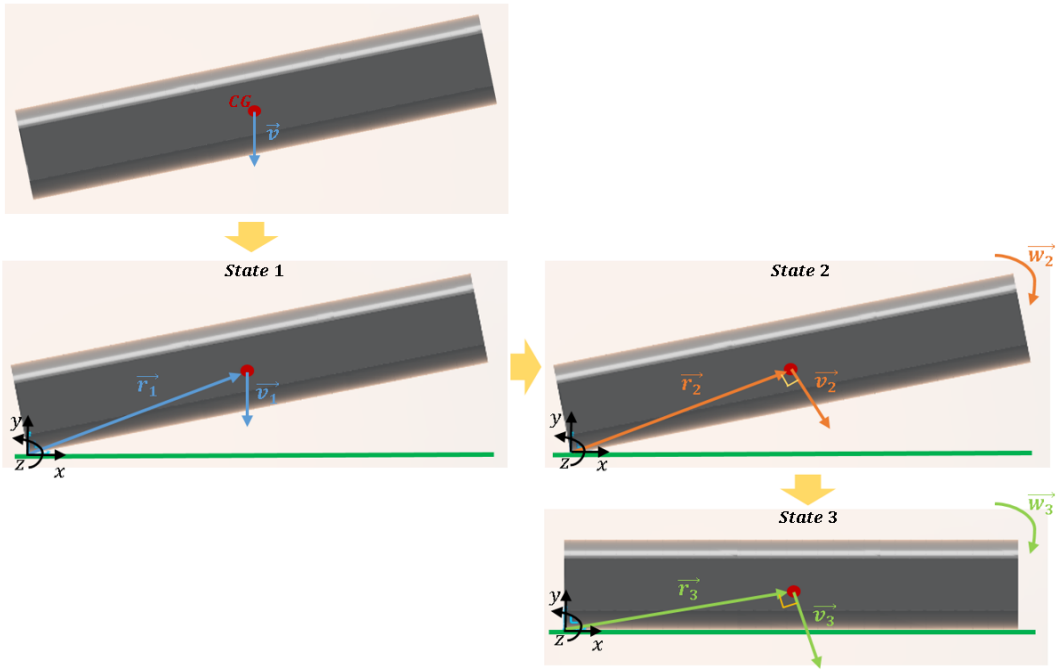

Figure 13.19: All the steps considered in the rigid body rotation of the passengers' fuselage

Between states 1 and 2, the impact was presumed to be perfectly plastic, and the conservation of angular momentum is applied. Subsequently, between states 2 and 3, the conservation of energy is invoked.

State 1 to 2

Similar to how linear momentum connects the mass and velocity of a rigid body, angular momentum is a vector quantity that relates the angular velocity of a rigid body to its moments of inertia [54]. This connection is conserved, meaning that the total angular momentum of a closed system (where no external torque is applied) remains constant.

The definition of angular momentum for a rigid body b is established with respect to a reference frame attached to the body and moving with it. Unlike linear momentum, angular momentum is influenced by the chosen origin [54].

Assuming a body-fixed reference frame with the origin at O, the angular momentum over the body's volume can be calculated as:

$$\mathbf{h}^b = \int_V \overrightarrow{r} \times \rho(\overrightarrow{r})\overrightarrow{v}\, dV \tag{13.1}$$

Here, $\overrightarrow{v}$ represents the velocity of any infinitesimal particle of the body.

By solving this integral and utilizing the definitions of the first and second moments of inertia of the body, the angular momentum can be expressed as:

$$\overrightarrow{H}^b = -\overrightarrow{v}_O \times \mathbf{c} + \mathbf{I}\overrightarrow{\omega}^b \Leftrightarrow \overrightarrow{H}^b = -\overrightarrow{v}_O \times \int_V \overrightarrow{r}\rho(\overrightarrow{r})dV + \mathbf{I}\overrightarrow{\omega}^b \tag{13.2}$$

where $\overrightarrow{v}_O$ is the velocity of the origin of the reference system attached to the rigid body, and $\overrightarrow{\omega}^b$ is the angular rate of the body frame concerning the inertial one expressed in the body frame.

Knowing that the system's mass is given by $m = \int_V \rho(\mathbf{r})dV$, and considering the conservation of angular momentum, one observes the following between states 1 and 2:

$$\overrightarrow{H}_{O_1} = \overrightarrow{H}_{O_2} \Leftrightarrow$$

$$(\overrightarrow{r}_1 \times \overrightarrow{v}_1)m + \mathbf{I}_{CG} \cdot \overrightarrow{w}_1 = (\overrightarrow{r}_2 \times \overrightarrow{v}_2)m + \mathbf{I}_{CG} \cdot \overrightarrow{w}_2 \tag{13.3}$$

where $\overrightarrow{r}_1 = \overrightarrow{r}_2$ and $\overrightarrow{w}_1 = 0$, due to zero body's rotation in the initial state. $\overrightarrow{r}_1$ and $\overrightarrow{r}_2$ denote the distances between the point of contact (origin of the local coordinate system) and the center of gravity (CG) of the passengers' fuselage for angles of 5°, 10°, and 15° (see Figure 13.19). These vector values, as well as the mass m of the whole passengers' fuselage, were directly extracted from the 3DEXPERIENCE platform (Table 13.2).

Angle	$\mathbf{r}_x\ (m)$	$\mathbf{r}_y\ (m)$	$\mathbf{r}_z\ (m)$
5°	0	9.34	2.45
10°	0	9.09	3.26
15°	0	8.77	4.04
Mass		$27252.9\ kg$	

Table 13.2: Mass and location of the fuselage's CG for different angles

$\mathbf{I}_{CG}$ defines the Inertia Matrix for the center of gravity of the passengers' fuselage in relation to the local coordinate system. So, to extract meaningful results for this analysis, it is essential to consider the local coordinate system, centered at the ground contact point.

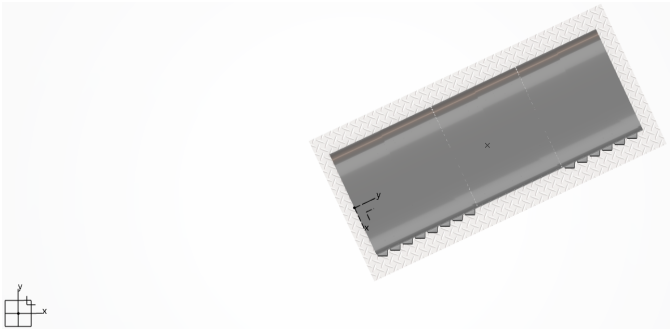

Figure 13.20: Upper view of the 3DEXPERIENCE model.The global coordinate system can be seen on the left, while the local coordinate system is depicted at the center

The local coordinate system undergoes a 65° counterclockwise rotation about the z-axis (refer to Figure 13.20), requiring the application of a rotation matrix.

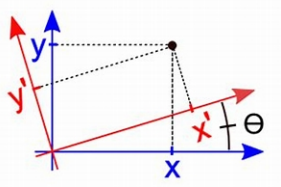

Figure 13.21: Rotation of axes in two dimensions

Considering the matrix that rotates a given coordinate system with x and y axes counterclockwise by an angle θ (see figure 13.21), denoted as:

$$\mathbf{R}_\theta = \begin{bmatrix} \cos\theta & \sin\theta \\ -\sin\theta & \cos\theta \end{bmatrix} \tag{13.4}$$

The new rotated coordinate system is calculated as:

$$u'_i = R_\theta . u_j \tag{13.5}$$

Substituting θ with 65° yields the specific rotation matrix:

$$\mathbf{R}_{65^\circ} = \begin{bmatrix} 0.423 & 0.906 \\ -0.906 & 0.423 \end{bmatrix} \tag{13.6}$$

In matrix notation, the same principle applies, and the transformation of a second order tensor between coordinate systems using the rotation matrix is expressed as:

$$I'_{ij} = R_{ij} I_{lm} R_{mj} \tag{13.7}$$

Here:

- I'_{ij} represents the transformed tensor. In this case, $\mathbf{I}_{CG}$ is related to the local coordinate system.
- R_{ij} is the rotation matrix.
- I_{lm} is the original second-order tensor, more specifically $\mathbf{I}_{CG}$ of the passengers' fuselage related to the global coordinate system. It was directly obtained from 3DEXPERIENCE for various angles (0°,5°,10°, and 15°).
- Finally, R_{mj} represents the transpose (inverse) of the rotation matrix.

Replacing equation 13.7 with the respective values, the Inertia Matrices, expressed in units of $kg{\cdot}m^2$, can be computed as follows:

$$\mathbf{I}_{CG_5} = \begin{bmatrix} 816066.40 & 0 & 0 \\ 0 & 135006.60 & -68906.67 \\ 0 & -68922.86 & 916865 \end{bmatrix} \quad \mathbf{I}_{CG_{10}} = \begin{bmatrix} 816064.86 & 0 & 0 \\ 0 & 152912.14 & -135735.54 \\ 0 & -135767.45 & 898959 \end{bmatrix}$$

$$\mathbf{I}_{CG_{15}} = \begin{bmatrix} 816067.26 & 0 & 0 \\ 0 & 182150.76 & -198441.05 \\ 0 & -198487.60 & 869718 \end{bmatrix}$$

Finally, solving for $\overrightarrow{w}_2$ for different angles (by substituting the relevant values into equation 13.3), and knowing that:

$$\overrightarrow{v} = \overrightarrow{r} \times \overrightarrow{w} \tag{13.8}$$

the values of $\overrightarrow{w}_2$ and $\overrightarrow{v}_2$ for 5°, 10° and 15° can be taken out.

Angle	$\mathbf{w}_{2_x}\ (rad/s)$	$\mathbf{w}_{2_y}\ (rad/s)$	$\mathbf{w}_{2_z}\ (rad/s)$	$\mathbf{v}_{2_x}\ (m/s)$	$\mathbf{v}_{2_y}\ (m/s)$	$\mathbf{v}_{2_z}\ (m/s)$
5°	1.17	0	0	0	2.87	−10.92
10°	1.14	0	0	0	3.71	−10.35
15°	1.10	0	0	0	4.43	−9.63

Table 13.3: $\overrightarrow{w}_2$ and $\overrightarrow{v}_2$ components for different angles

State 2 to 3

During the transition from states 2 to 3, and under the assumption of non-slipping rolling of the fuselage, a portion of the body's energy will manifest as translational and rotational kinetic energy about the center of mass, while the remainder will manifest as potential energy. This assumption is made under the condition that the overall energy of the system remains conserved, yielding the following:

$$T_2 + \sum U_{2\to3} = T_3 \Leftrightarrow$$
$$\frac{1}{2} m \overrightarrow{v}_2^2 + \frac{1}{2} \overrightarrow{\omega}_2^T \mathbf{I}_{CG} \overrightarrow{\omega}_2 + \Delta y\, mg = \frac{1}{2} m \overrightarrow{v}_3^2 + \frac{1}{2} \overrightarrow{\omega}_3^T \mathbf{I}_{CG0} \overrightarrow{\omega}_3 \tag{13.9}$$

In this context, $\mathbf{I}_{CG0}$ represents the Inertia Matrix corresponding to the scenario where the passenger's fuselage aligns parallel to the ground (0° angle). This matrix is defined as:

$$\mathbf{I}_{CG_0} = \begin{bmatrix} 816066.63 & 0 & 0 \\ 0 & 128980.37 & -68906.67 \\ 0 & -68922.86 & 922890 \end{bmatrix} kgm^2 \tag{13.10}$$

By substituting the values of $\overrightarrow{v}_2$ and $\overrightarrow{\omega}_2$ from Table 13.3 into equation 13.9 and incorporating the variations of y (seen in Figure 13.22) provided in Table 13.4 for different angles, we can isolate the angular velocity $\overrightarrow{\omega}_3$ just before the impact with the ground at a 0° angle.

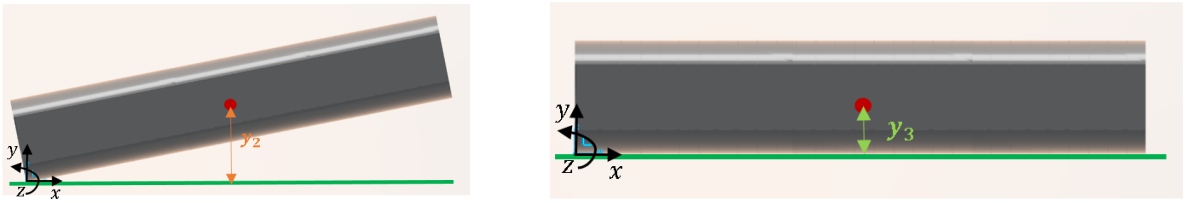

Figure 13.22: Y component for state 2 and 3

$\Delta\theta$	$\Delta y\ (m)$
$5° \to 0°$	0.82
$10° \to 0°$	1.63
$15° \to 0°$	2.40

Table 13.4: Δy from state 2 to 3 for different angles' variation

Additionally, the calculation of $\overrightarrow{v}_3$ is determined using equation 13.8, with the given information that $\overrightarrow{r}_0 = (0, 9.52, 1.63)\ m$.

Ultimately, the resultant values for $\overrightarrow{\omega}_3$ and $\overrightarrow{v}_3$ at 5°, 10° and 15° can be determined (Table 13.5).

Angle	$\mathbf{w}_{3_x}\ (rad/s)$	$\mathbf{w}_{3_y}\ (rad/s)$	$\mathbf{w}_{3_z}\ (rad/s)$	$\mathbf{v}_{3_x}\ (m/s)$	$\mathbf{v}_{3_y}\ (m/s)$	$\mathbf{v}_{3_z}\ (m/s)$
5°	1.22	0	0	0	1.99	−11.65
10°	1.25	0	0	0	2.04	−11.90
15°	1.26	0	0	0	2.5	−12

Table 13.5: Linear and angular velocity components for state 3

Reduced Model

The previous velocities and CGs locations were computed for the entire passenger fuselage. In contrast, the simplified model focuses on a smaller portion, specifically the middle engine section (Figure 13.23).

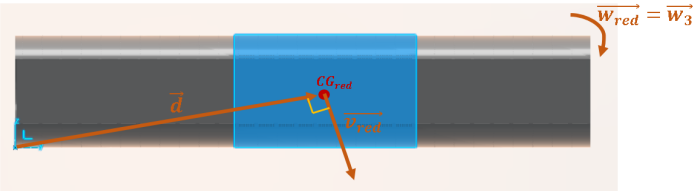

Figure 13.23: Depiction of the reduced model and velocity vectors applied to it

Given the model's uniform circular motion, the angular velocity stays constant, and it is reasonable to assume that the angular velocity of the reduced model, $\overrightarrow{\omega}_{red}$, is equal to $\overrightarrow{\omega}_3$. By extracting the center of gravity location of the engine section directly from 3DEXPERIENCE ($\overrightarrow{r}_{red} = (0, 10.37, 1.63)\ m$) and considering the relationship:

$$\overrightarrow{v}_{red} = \overrightarrow{r}_{red} \times \overrightarrow{\omega}_{red},$$

the ultimate velocities at impact for various angles can then be determined.

Angle	$\mathbf{v}_{red_x}\ (m/s)$	$\mathbf{v}_{red_y}\ (m/s)$	$\mathbf{v}_{red_z}\ (m/s)$
$5°$	0	2	-12.7
$10°$	0	2	-13
$15°$	0	2.1	-13.1

Table 13.6: Velocity components of the reduced model upon hitting the ground

13.2.2. Visual Inspection of the Crash Scenarios

After calculating the velocity components upon impact for each scenario, vertical drop tests were carried out on the extended/reduced model. In Figures 13.24, 13.25 and 13.26, the left-side images showcase the maximum deformation of the reduced model sections at various pitch angles. Concurrently, the right side depicts the corresponding maximum deformation of the full passenger fuselage's engine section, providing a basis for comparison. It is noteworthy that in the cases of 10 degrees and 15 degrees, the analytically calculated velocity for the reduced model remains constant. Similarly, the deformations for the engine section also exhibit close similarity, leading to the decision to simultaneously consider both cases.

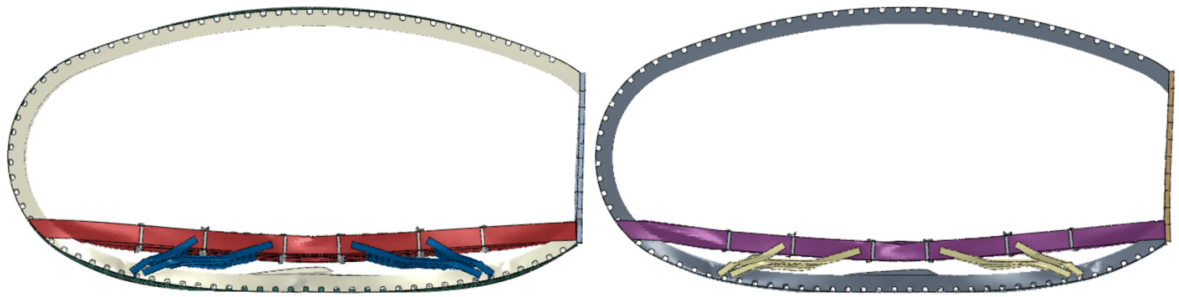

(a) Maximum deformation of the reduced model **(b)** Maximum deformation of the engine (extended) section

Figure 13.24: Maximum deformation for the perpendicular impact cases. The right one corresponds to the engine section of the full passenger model

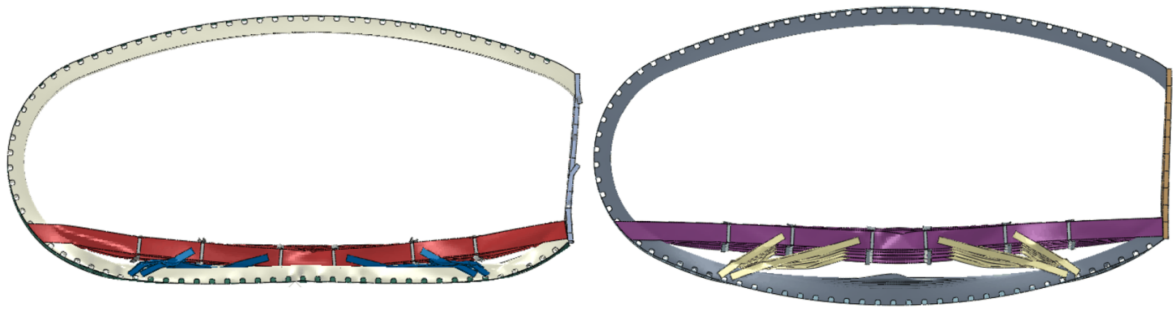

(a) Maximum deformation of the reduced model **(b)** Maximum deformation of the engine (extended) section

Figure 13.25: Maximum deformation for the 5 degrees impact cases. The right one corresponds to the engine section of the full passenger model

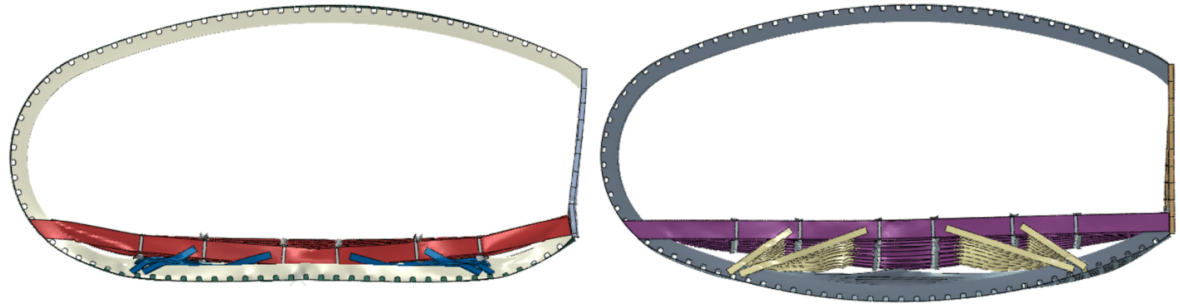

(a) Maximum deformation of the reduced model **(b)** Maximum deformation of the engine (extended) section

Figure 13.26: Maximum deformation for the 10 and 15 degrees impact cases (both deformations were very similar). The right one corresponds to the engine section of the full passenger model

For the 0 degrees case previously examined in Chapter 11, moments of inertia for all components of the FV shown in Figure 5.4 were utilized. However, for the current scenario, only the moments of inertia of the back and front sections of the passenger fuselage were taken into account. Subsequently, as will be demonstrated later, the results closely align with those of the preceding case.

One of the prior conclusions indicated that the spatial variation of the DRIs and SEVs in the engine section, considering both the full passenger model and the extended model with applied moments of inertia for all FV parts, exhibited a similar trend. Also, examining the case where moments of inertia for the back and front parts of the fuselage section were considered reveals that the maximum deformations are remarkably similar in the case of perpendicular impact of the passenger fuselage section, as qualitatively observed in Figure 13.24. This further affirms the efficacy of employing moments of inertia for straightforward vertical drop tests.

However, for the reduced model section with analytically applied velocities during impacts at 5 and 10/15 degrees, the deformations are significantly greater compared to their counterparts in the full fuselage section (see Figure 13.25 and 13.26). Nevertheless, these results were somewhat anticipated, given the simplified methodology that solely considers the moments of inertia of other parts without accounting for mass. The approach captures the kinematics of other parts to some extent but lacks physical representation, resulting in zero absorption of impact energy by the back and front sections.

13.2.3. Energy Analysis

In the preceding analysis, wherein pitch angles were introduced across the entire passenger fuselage and the model rotates upon hitting the ground, the sequence entails the front section absorbing initial impact energy, succeeded by the engine section, and finally, the rear part. The impact surface progressively increases with the rotating angle, resulting in a slower energy dissipation, as depicted in Figure 13.6b: 0.3s for the 5-degree case and 0.5s and 0.6s for the 10° and 15° angles, respectively.

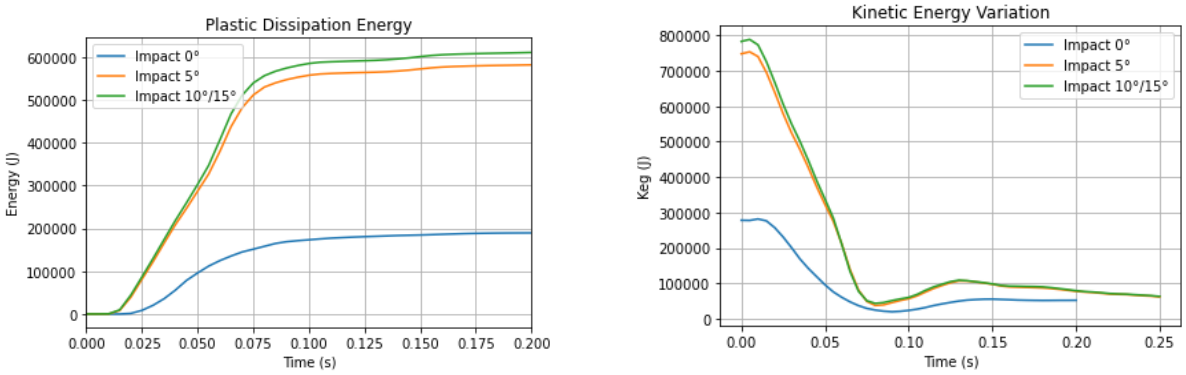

(a) Plastic dissipation variation **(b)** Kinetic energy histories

Figure 13.27: Reduced model variation of kinetic and plastic dissipation energies for different pitch angles

In contrast, for the reduced model case, the impact occurs all at once with only a small section available to absorb the entirety of the energy. This leads to a much rapid energy absorption (0.125s for the 5° and 10°/15° cases). For the perpendicular impact case of the reduced and full models, the energy absorption variation curves follow the same trend (energy is fully absorbed around 0.15s).

Moving forward, Figure 13.27b illustrates the kinetic energy curves for all analyzed cases. Given by $K_{eg} = \frac{1}{2}mv^2$, the mass for all instances remains constant, but the velocity increases notably with the introduction of a pitch angle. This results in more than double the initial kinetic energy (given the squared nature of velocity) compared to the perpendicular case. Moreover, higher pitch angles exhibit a more pronounced rebound. Although the crushable length starts the same, at the analysis' conclusion, it is entirely occupied by the deformed floor and frame components for non-perpendicular impact cases. This leads to a more accentuated plastic deformation, consequently also storing more energy through elastic means. As a result, the total resultant kinetic energy after the rebound (local maximum post the point of maximum deformation) is greater for higher impact velocities.

The energy absorption by components is visually represented in Figure 13.28. Notably, the curves for drop tests with increased velocity, accounting for angular momentum when introducing a pitch angle, display a steeper shape and signify a greater amount of energy being absorbed by components when compared to the perpendicular drop test. Consistently across all cases, frames emerge as the structural components that absorb the highest impact energy. Similar to the energy absorption by components of the full passenger model depicted in Figure 13.9, the floor beams exhibit less deformation for perpendicular impacts, with deformation gradually increasing as the impact velocity rises. This pattern might be attributed to the intense deformation experienced by frames upon collision, influencing the structural elements of the floor, particularly the floor longitudinal beams. The stepped pattern is now nonexistent due to the lack of gradual energy absorption by the front and back sections. Intriguingly, in the 10°/15° case, approximately 250 kJ of energy is absorbed by the frames, a figure nearly identical to the energy level observed during the second curve rise in Figure 13.9d. This suggests that the energy absorption, previously distributed across the broader engine and rear parts and following the impact of the front part with the ground, as indicated by the initial rise of the curve, is now concentrated solely within the engine section. Consequently, this concentration of energy leads to significant deformations evident in the current case. Similar deductions can be made for the 5° case.

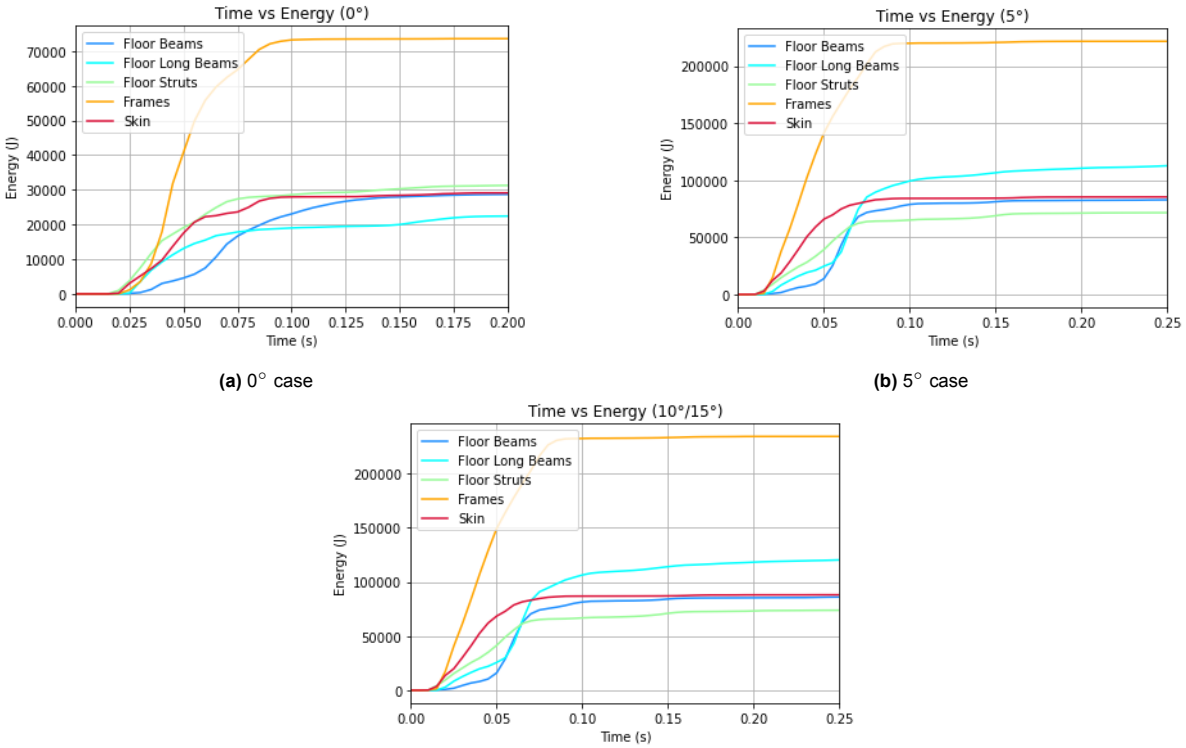

(a) 0° case

(b) 5° case

(c) 10°/15° case

Figure 13.28: Energy absorption of main structures of reduced model with different pitch angles

13.2.4. Angle Impact on the DRIs and SEVs

Figures 13.29, 13.30, and 13.31 delineate the spatial evolution of DRIs at various impact velocities for the 0, 5, and 10/15-degree cases, respectively. To enhance comparability, the engine section counterpart from the full passenger model is juxtaposed for reference.

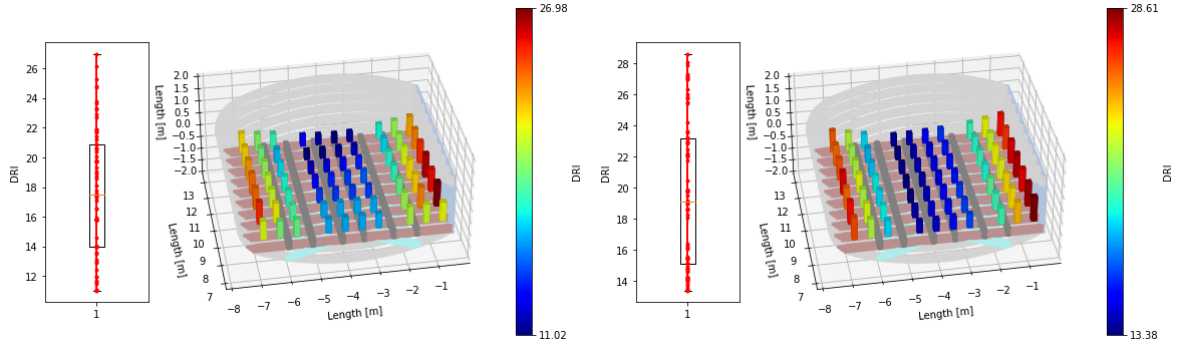

(a) Reduced/extended model **(b)** Engine (extended) section of the full passenger model

Figure 13.29: Spatial variation of the DRI for the 0 degrees case

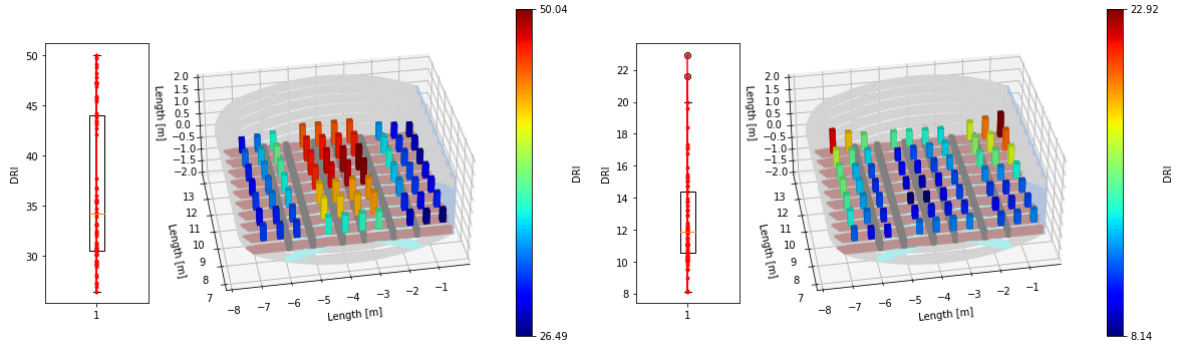

(a) Reduced/extended model **(b)** Engine (extended) section of the full passenger model

Figure 13.30: Spatial variation of the DRI for the 5 degrees case

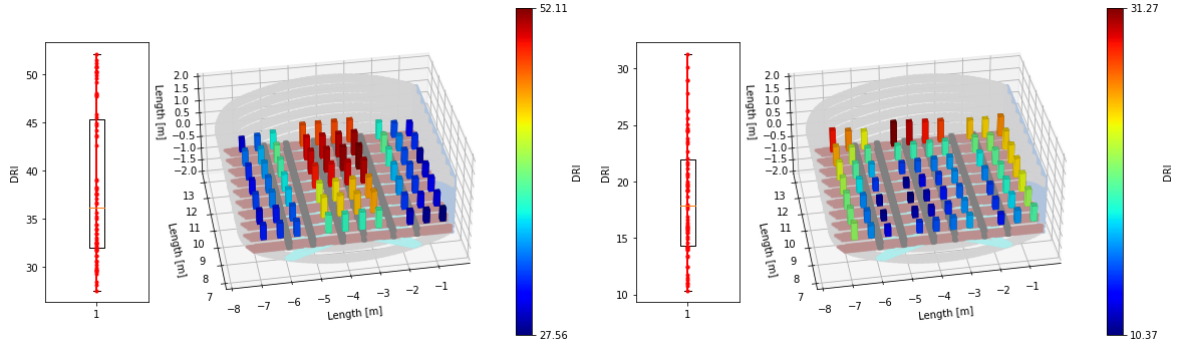

(a) Reduced/extended model **(b)** Engine (extended) section of the full passenger model

Figure 13.31: Spatial variation of the DRI for the 10 and 15 degrees case. Results were deemed very similar

Examining the 0-degree case, a commendable correlation between the two figures can be observed, with a slight DRI increase in the reduced model's front part. The impact surface involves lower frames and reinforcements making simultaneous ground contact, resulting in relatively uniform longitudinal damage.

The heightened plastic deformation in the fuselage's middle augments energy absorption, leading to reduced DRIs. Conversely, increased stiffness towards the sides results in less structural deformation, yielding higher DRIs.

Upon introducing pitch angles of 5 to 15 degrees, the augmented final impact velocity incorporates additional angular velocity from the fuselage section's rotation. This intensifies ground impacts, substantially elevating DRI values for the reduced model. The accentuated increase is notable at the rear, primarily owing to the horizontal velocity component added to the crash scenarios. The introduction of velocities due to pitch angles results in higher DRI values in the middle longitudinal areas rather than the sides near the spar and lateral frames. This shift stems from the exceedingly high velocities attained, generating robust impact forces and considerable deformations of structural elements. The constrained space between frames and the floor structure proves inadequate for containing extensive plastic deformations, consequently affecting floor structural elements and exposing passengers to excessive accelerations.

In stark contrast, the DRI variation for the full model engine counterpart unfolds differently. The initial impact of the full passenger model's front section absorbs some impact energy, with the deformation peak occurring at the rear part. The middle engine section benefits from a degree of "protection" provided by the adjacent sections, resulting in modest DRIs. It's only in the last row of the engine section, before the initiation of the back part, that an increase in DRIs can be observed.

The spatial variation of the SEVs for both the reduced model and its engine counterpart are illustrated in Figures 13.32, 13.33, and 13.34. Given that the SEV incorporates the DRI in its calculation and the primary impact component is in the vertical z direction, the SEV exhibits a consistent trend with the DRI. The observations mentioned earlier can be directly applied to the SEV results as well.

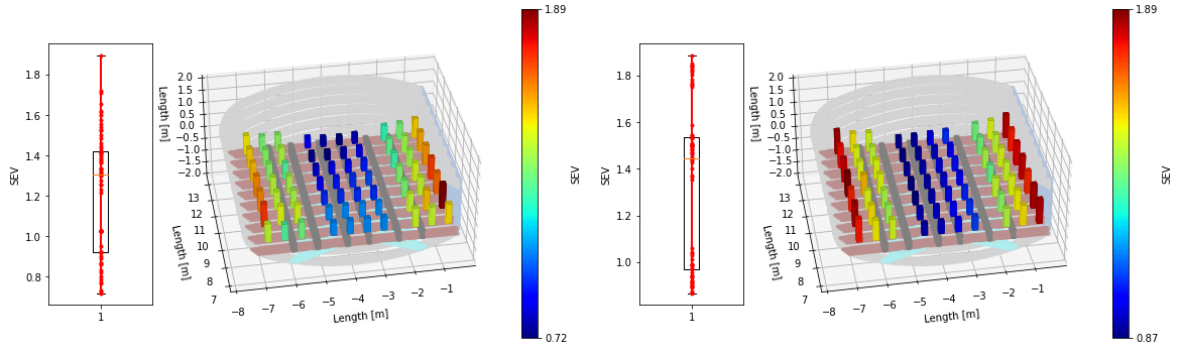

(a) Reduced/extended model **(b)** Engine (extended) section of the full passenger model

Figure 13.32: Spatial variation of the SEV for the 0 degrees case

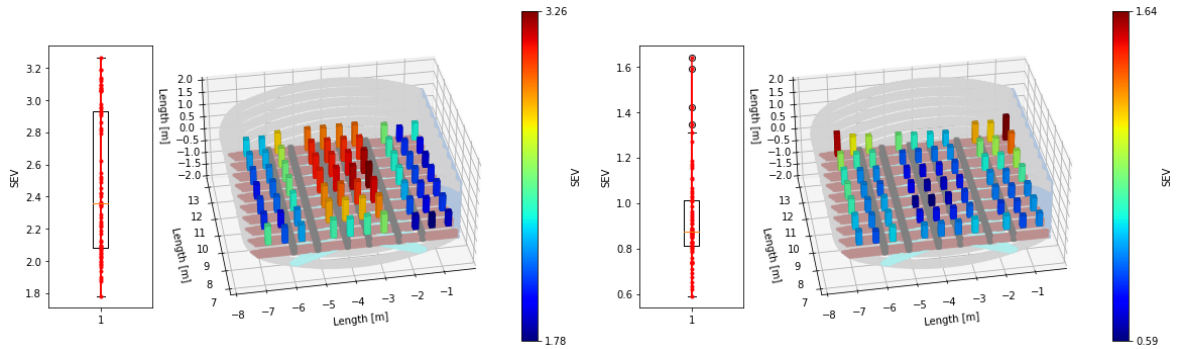

(a) Reduced/extended model **(b)** Engine (extended) section of the full passenger model

Figure 13.33: Spatial variation of the SEV for the 5 degrees case

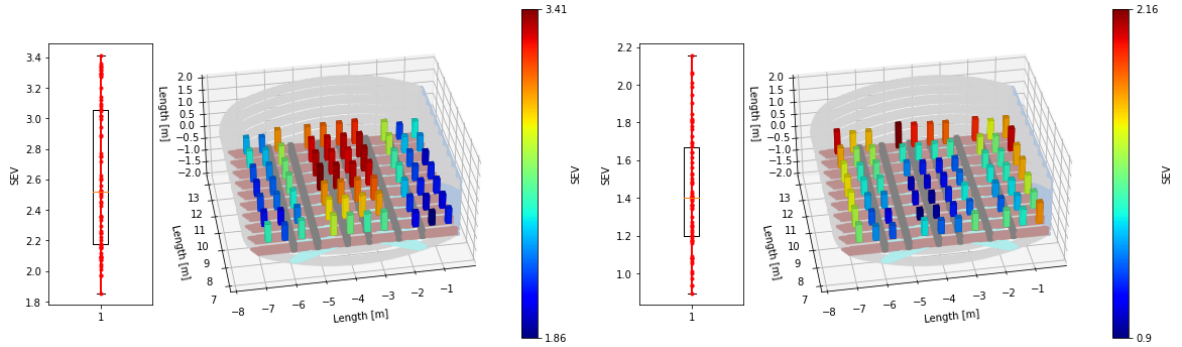

(a) Reduced/extended model

(b) Engine (extended) section of the full passenger model

Figure 13.34: Spatial variation of the SEV for the 10 and 15 degrees case. Results were deemed very similar

Table 13.7 presents a summary encompassing the average, maximum, median, and minimum values for both Dynamic Response and Severity Indexes, considering both the reduced modelling technique and the engine section of the full passenger section.

Table 13.7: DRI and SEV comparison for different pitch angles

Model	Angle	DRI				SEV				Comp. Time
		Avg	Max	Median	Min	Avg	Max	Median	Min	(h)
Reduced	0-deg	17.81	26.98	17.48	11.02	1.22	1.89	1.31	0.72	3.56
	5-deg	36.65	50.04	34.29	26.49	2.48	3.26	2.36	1.78	4.51
	10/15-deg	38.31	52.11	36.12	27.56	2.61	3.41	2.52	1.86	4.47
Engine	0-deg	19.65	28.61	19.09	13.38	1.33	1.89	1.44	0.87	-
	5-deg	12.75	22.92	11.86	8.14	0.93	1.64	0.87	0.59	-
	10/15-deg	18.62	31.27	17.91	10.37	1.44	2.16	1.40	0.90	-

Notably, distinct patterns emerge in both DRIs and SEVs with increasing pitch angles. The engine section exhibits a nuanced trend, characterized by a slight decrease followed by an increase in both DRI and SEV values. Conversely, the reduced modelling technique demonstrates a notable upswing in DRI and SEV values as pitch angles rise. The significant escalation in injuria criteria values with rising pitch angles for the reduced modelling technique is closely tied to the absence of FEM representations for the back and front sections of the passengers' fuselage. In the absence of such inclusion, these sections do not actively participate in energy absorption upon impact, resulting in a deviation from the gradual energy absorption observed in the full passenger fuselage scenario.

The analytical methodology proposed in Section 5.1, while based on simplifications, remains informative. However, even with increased precision, different outcomes would be anticipated. This prompts a critical examination of the viability of the reduced modelling approach when introducing a variable centerline orientation, deviating from the horizontal orientation observed in cases involving perpendicular drop tests or roll angles.

13.3. Alternative Simplified Modelling Technique: Introducing Submodelling

In lieu of the previously employed implicit moments of inertia technique, an alternative methodology has been proposed to address more extreme crash scenarios. Described in the Literature, this approach involves initially conducting a drop test on the entire existing passenger model with a substantially coarser mesh, seen in Figure 13.35a, effectively reducing the computational time required for the analysis. Subsequently, the same drop test is replicated using the submodelling technique, with a further refinement focused on the section of interest, in this case, the engine part (Figure 13.35b). The results obtained from the subsequent sections of the full model drop test are then interpolated onto the free edges of the engine model, significantly enhancing the overall precision of the outcomes. This technique underwent testing solely under the most severe drop conditions, involving 15 $^{\circ}$ pitch angle. The additional cases were considered unnecessary to validate the effectiveness of the alternative approach.

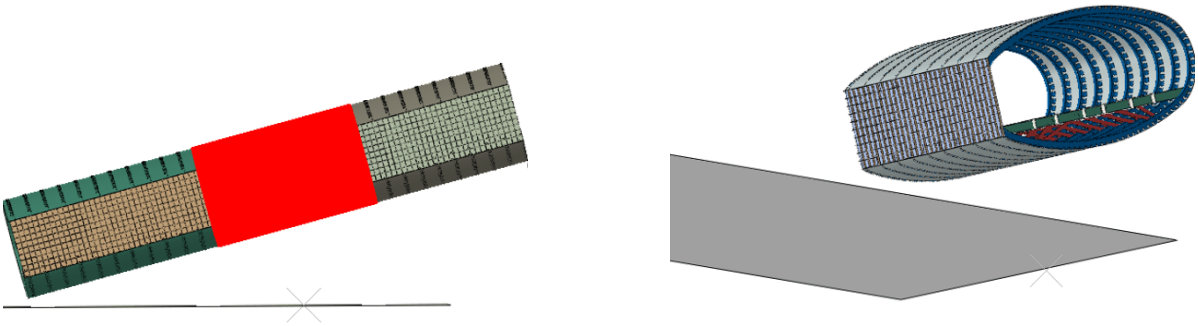

(a) Engine section location in the full passenger model

(b) Engine section used for submodelling

Figure 13.35: FEM model of the engine section and its location in the full passenger model

13.3.1. Visual Inspection of the Crash Scenarios

Upon visually examining the crash sections generated from the drop test with a 15-degree pitch angle, depicted in Figures 13.36 and 13.37, along with assessing displacement values for both the maximum deformation step and at conclusion of the analysis, a striking similarity emerges.

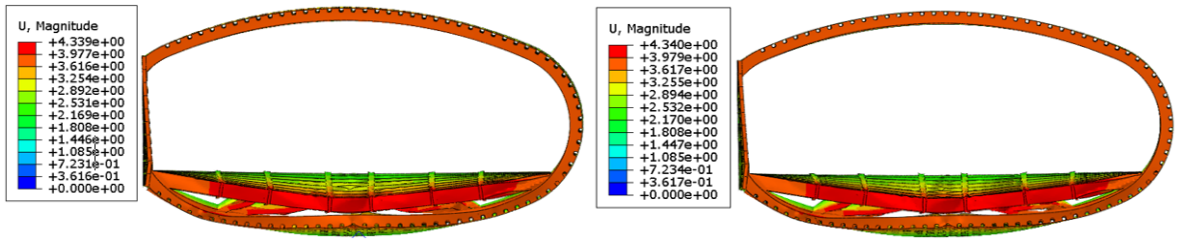

(a) Maximum deformation of the submodel

(b) Maximum deformation of the engine (extended) model

Figure 13.36: Back views showcasing maximum deformation for the two cases (0.48s). The right one corresponds to the engine section of the full passenger model

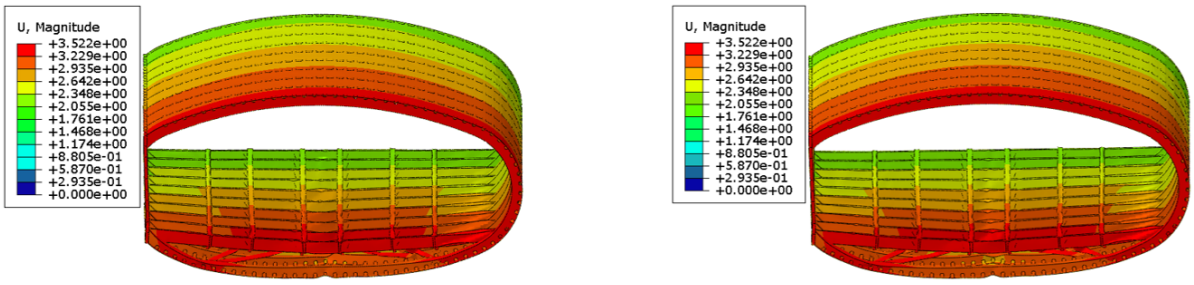

(a) Displacement variation for the submodel

(b) Displacement variation for the engine (extended) model

Figure 13.37: Back views showcasing dsplacement variation at the end of the analysis. The right one corresponds to the engine section of the full passenger model

The color-coded representation aligns consistently in both simulations, revealing heightened displacement at the back due to increased rotations further from the rotation forward point, and a gradual reduction in displacement towards the front. In contrast to prior outcomes utilizing the implicit moments of inertia technique, which resulted in floor components harshly impacting frames and producing entirely distinct crash sections, the submodelling approach aptly captures the dynamics of the engine section. This is achieved by bypassing the FEM representation of subsequent sections, leading to a substantial reduction in computational time—a aspect that will be further explored later.

13.3.2. Energy Analysis

Figures 13.38a and 13.38b provide an insight into the variations in kinetic energy and plastic dissipation energy for both the submodel and the full passenger model.

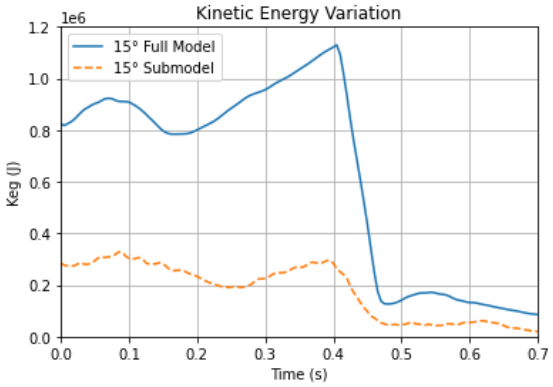

(a) Kinetic energy histories

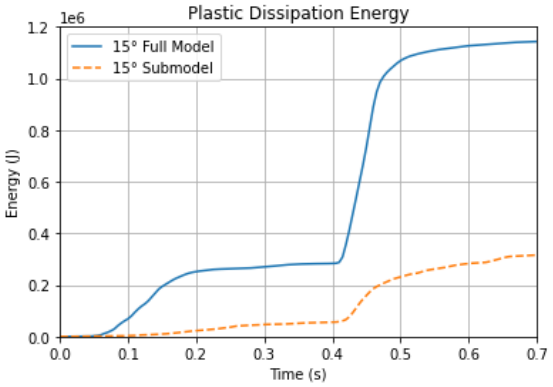

(b) Plastic dissipation energy

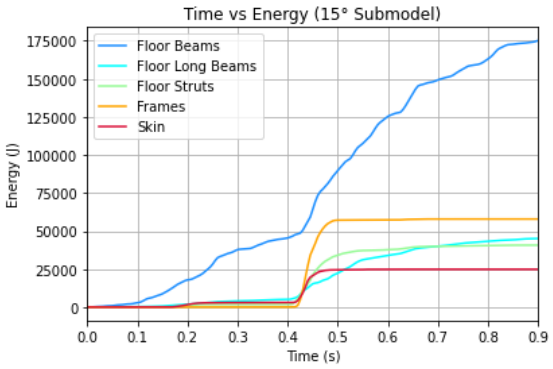

(c) Energy absorption of main structures

Figure 13.38: Energy analysis for the submodelling approach

Notably, there exists a considerable difference in mass, with the submodel exhibiting an initial kinetic energy approximately one-third of that observed in the full passenger model. Despite this distinction, both curves exhibit similar trends: an initial increase in kinetic energy as the specimens are positioned slightly above the ground before impact, followed by a slight decrease during the moment of rear section impact with the ground. Subsequently, there is a notable increase in kinetic energy attributed to the angular momentum induced by the rotation of the model, reaching a peak around 0.4 seconds for both cases. The distribution of angular velocity, proportional to the distance from the point of rotation, leads to distinct velocity peaks. In the full passenger model, the maximum velocity occurs at the extreme of the back section, while in the submodel, it occurs at the end of the engine section. The greater distance of the rear section from the point of rotation results in a substantially higher increase in kinetic energy for the full passenger model, leading to a more forceful impact with the ground. This disparity explains the steeper curve observed up to the point of maximum deformation, reached around 0.48 seconds. A slight rebound phase ensues, followed by a subsequent decrease in kinetic energy until reaching near-zero values. Figure 13.38b highlights the substantial increase in size of the full passenger model compared to the engine section, resulting in a significant rise in the energy that can be dissipated. The maximum energy dissipated occurs when both models make full contact with the ground.

Moving forward, Figure 13.38c delineates the energy absorbed by the main structural components in the submodelling case. When comparing it to its counterpart in the full model (Figure 13.9d), noticeable distinctions arise. These include the diminished energy absorption by the skin and the seemingly unrealistic energy absorbed by the floor beams. This discrepancy may stem from the fact that the nodes on the free edges of the engine section, used to interpolate the results from the full model drop test, primarily belong to the skin and floor beams, potentially resulting in the impractical outcomes.

13.3.3. DRIs and SEVs Variation

To conclude the submodelling analysis, Figures 13.39 and 13.40 illustrate the spatial variation of the Dynamic Response and Severity Indexes for both cases under examination.

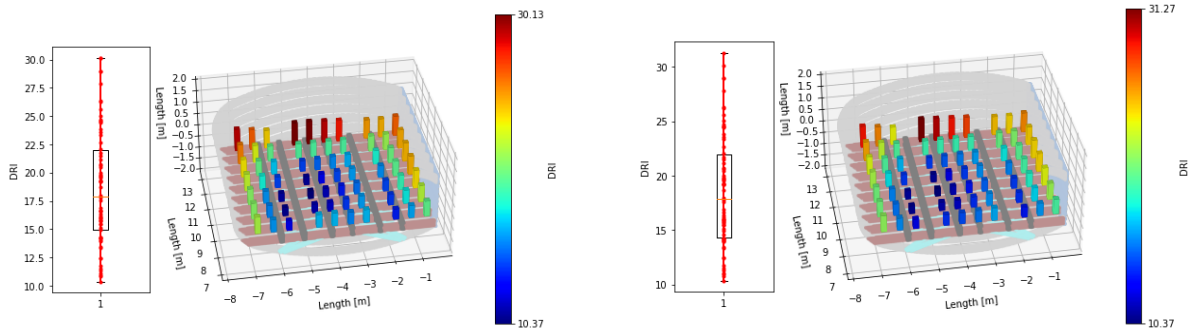

(a) Submodel **(b)** Engine (extended) section of the full passenger model

Figure 13.39: Spatial variation of the DRI

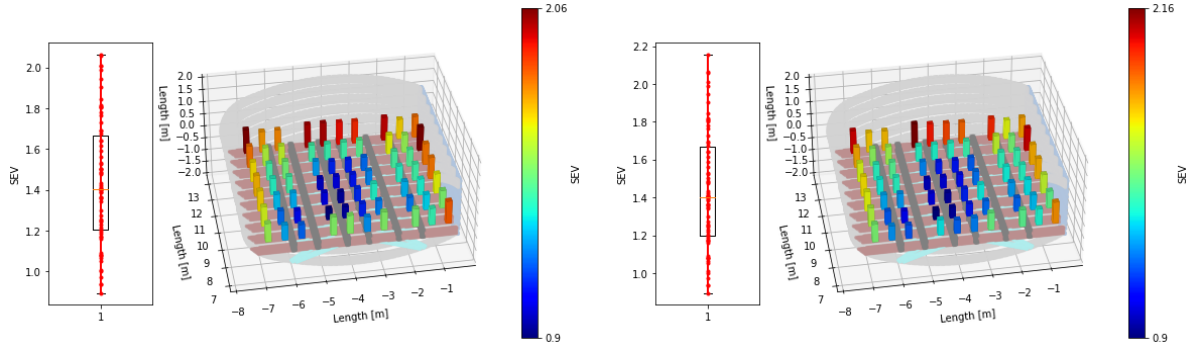

(a) Submodel **(b)** Engine (extended) section of the full passenger model

Figure 13.40: Spatial variation of the SEV

As previously mentioned, the initial impact of the full passenger model's front section absorbs a portion of the impact energy, culminating in the deformation peak at the back part. The middle engine section benefits from a degree of "protection" offered by the adjacent sections, resulting in the observed modest DRIs and SEVs. Notably, it's only in the last row of the engine section, just before the initiation of the rear part, that an increase in DRIs and SEVs is observed. This pattern is consistently captured using the submodelling technique, and the values presented in Table 13.8 further affirm the resemblance between the results. As a noteworthy observation, the computational time for the submodel already encompasses the duration required to conduct the full passenger drop test with a rough mesh and the subsequent engine drop test with a refined mesh. This integration results in an almost halved computational time compared to its counterpart.

Table 13.8: DRI and SEV comparison for modelling techniques

Model	Angle	DRI				SEV				Comp. Time
		Avg	Max	Median	Min	Avg	Max	Median	Min	(h)
Submodel	15-deg	18.43	30.13	17.65	10.37	1.36	2.06	1.34	0.90	23.62
Engine	15-deg	18.62	31.27	17.91	10.37	1.44	2.16	1.40	0.90	44.68

While the implicit modelling technique considers the moments of inertia of all Flying-V parts, providing a rough estimation of their dynamics, its precision diminishes when conducting more complex drop tests, such as those involving pitch angles, leading to imprecise and unrealistic results. On the other hand, the submodelling technique delivers high precision coupled with a substantial reduction in computational time. However, it is essential to emphasize that a comprehensive FEM representation of a more complex model is requisite before employing the submodelling technique.

13.4. Discussion on the Results

Previously, the addition of moments of inertia yielded better outcomes and faster simulation times for perpendicular drop tests. However, upon introducing a varying centerline orientation rather than the horizontal, the results significantly diverged from those obtained using a more complex FEM model. The validation approach, based on numerous simplifications, likely influenced this disparity in results.

Firstly, the impact was assumed to be perfectly plastic, disregarding any losses of kinetic energy resulting from rebound or other forms of energy dissipation. There was a tentative consideration for a rough penalty factor to address potential kinetic energy reduction due to structural rebound. However, inclusion of this factor yielded only marginal improvements, still significantly diverging from the comparison case, and so it wasn't deemed essential.

Secondly, and most crucially, the simplified methodology relied solely on moments of inertia without considering mass. This, combined with the absence of FEM representation for other sections of the full passenger fuselage, resulted in zero energy absorption by those sections. Whereas in perpendicular drop test cases, simultaneous contact of lower frames and skin with the ground led to similar longitudinal deformation patterns, introducing pitch angles led to gradual ground contact. The lack of FEM models and subsequent absence of energy absorption by subsequent sections connected to the engine hindered the viability of the outcomes significantly. Consequently, it can be concluded that the proposed methodology, despite remaining informative, did not function well upon introducing varying centerline orientation.

On the other hand, the submodelling approach offered high precision with a substantial reduction in computational time. However, it's crucial to underscore the need for a comprehensive FEM representation of a more complex model before employing submodelling. While this remained a preliminary analysis demonstrating the capabilities of the submodelling approach, it is recommended to first create proper FEM representations for the remaining sections of the Flying-V in the future. Then, to better assess the crashworthiness of the FV, drop tests can be conducted with a coarse overall mesh to identify critical regions. Subsequently, critical areas could be subjected to a more detailed assessment using the submodelling technique.

This page intentionally contains no content.

V

Back Matter

This page intentionally contains no content.

Summary, Conclusions and Recommendations

This report serves as a documentation of the activities, results, and analyses undertaken throughout the M.Sc. thesis research project. The primary goal was to investigate the viability of simplified modelling approaches, aiming to capture the essential kinematics of various sections of the Flying-V without necessitating physical representation. This research specifically focused on assessing the crashworthiness of the Flying-V, particularly in the face of unique and more complex crash scenarios. Subsequently, a set of research sub-questions was derived from this objective. In the 'Conclusions' section of this Chapter, each of these sub-questions will be addressed, providing an overview of the attained results. Furthermore, based on these findings, recommendations for potential future research directions will be presented.

Summary

In the initial exploration of crashworthiness for the Flying-V aircraft, a systematic investigation unfolded, involving various modelling approaches. The study began with an examination of the crashworthiness characteristics of the Flying-V, focusing on a non-linear, explicit-dynamic finite element model developed in previous work. This model served as the foundational framework for subsequent analyses.

Validation of the optimal section design was performed through drop tests at a minimum vertical impact velocity of 26 ft/s, in line with Literature standards. Results demonstrated agreement with prior data, particularly regarding energy dissipation by components.

Spatial variations in the Dynamic Response Index (DRI) were explored, revealing asymmetry in the fuselage section. The Severity Index (SEV) was introduced to address DRI limitations, offering a more comprehensive assessment by considering combined effects of various accelerations. While correlations between SEV and DRI trends were noted, further exploration, especially regarding lateral impacts and out-of-plane displacements, was acknowledged. This groundwork set the stage for further studies on impact scenarios and potential passenger side loads.

As the analysis delved into more dynamically complex scenarios, expanding the computational domain to encompass larger fuselage sections became essential for a more reliable study while maintaining computational efficiency. This necessity led to the examination of an extended Flying-V fuselage section, doubling the size of the baseline model. The analysis provided good insights into the complex relationship between passenger distribution, structural configuration, and overall structural behavior. Significant findings included an imbalance in weight distribution, particularly pronounced in the extended section, leading to asymmetrical floor deformations. Attempts to address this imbalance, such as removing the last row, resulted in challenges regarding weight concentration and center of gravity shifts.

Spatial fluctuations in DRIs and SEVs consistently revealed minimal values in the middle area and elevated values on the sides, suggesting potential areas of concern. Comparison with the baseline model indicated a slight increase in DRI values for the extended model with 7 passenger rows and a more significant increase for the extended model with 6 passenger rows. However, the extended fuselage with 7 rows exhibited deformation patterns consistent with those of the baseline model.

The unrestricted edges of both models led to unrealistic buckling effects and more significant lateral contractions and expansions, implications which were more pronounced in the extended section, resulting in undesirable crushing and twisting behaviors. This, in turn, contributed to an uneven distribution of DRIs and SEVs longitudinally, particularly near the free back cross section. To address these issues and achieve more uniform deformation, as well as improve distributions of DRIs and SEVs along the fuselage sections, a modification was proposed. Specifically, the deformation in the longitudinal direction was constrained to zero at the two free cross sections, aiming to mitigate unrealistic effects caused by uncontrolled lateral deformations and enhance the overall accuracy of the simulation.

Visual inspections revealed a notable difference in the deformed state of sections with and without boundary conditions. The forward lean observed without constraints was successfully mitigated, demonstrating the efficacy of the introduced modification in maintaining perpendicularity to the ground. Also, a better understanding emerged when examining accelerations at a common point, emphasizing the role of boundary conditions in reducing magnitude acceleration and ensuring a more realistic structural response, similar to the one obtained if the sides were constrained by other structural elements. The introduction of sliding boundary conditions ultimately enhanced the predictive capabilities of simulations, providing insights into the structural behavior of fuselage sections under controlled deformation conditions. However, a notable disparity persisted in the energy absorbed by components between the baseline and extended models, despite initial assumptions that the introduction of boundary conditions would address this issue. Furthermore, there remained an opportunity for further exploration into the impact of introducing additional structural elements to restrict lateral deformations.

This was tackle upon introducing subsequent back and front sections on each side of the extended model, located near the engine of the Flying-V and, in order to assess the consistency of fuselage deformations, the results obtained were compared to the ones with sliding boundary conditions. Additionally, for a more comprehensive analysis of potential Flying-V crash scenarios without oversimplifying them, and for the subsequent validation of a reduced modelling technique introduced in the Literature, the crashworthiness assessment had to be extended to the full passenger fuselage. It was concluded, upon analysing the crash sections and the longitudinal distribution of the DRIs and SEVs of the engine section, that the incorporation of structural components in both the rear and front sections of the complete passenger fuselage not only enhanced the stability of the engine section but also yielded outcomes akin to those observed with sliding boundary conditions. This underscored the important role of lateral constraints in achieving consistent structural responses during impact.

An overall variation in terms of DRIs, SEVs and energy absorptions for all the modelling approaches touched upon so far was then studied. Also, the assessment expanded further to include the computational time used for each model. The baseline section led to the least damaged sustained by the passengers compared to the other counterparts coupled with reduced computational time (5.37h), and it was deemed sufficient to assess the crashworthiness of the Fying-V when considering conventional vertical drop tests. However, as the analysis delved into more dynamically complex scenarios, expanding the computational domain to encompass larger fuselage sections became essential for a more reliable study.

Comparing the extended models, the 7 rows one performed better in overall reduction of the DRIs and SEVs, but it exhibited longer computational times compared to the 6 rows twin, attributed to increased deformation of the floor components (6.54h vs. 3.54h). The decrease in computational time of the extended 6 rows model, even less than the baseline model, was due to less plastic deformation suffered by its structural components, leading to a rapid overall simulation of the drop tests. Nonetheless, it was discontinued for modelling more realistic Flying-V crash scenarios due to the unrealistic passenger lay-out, not consistent with the frames spacing.

Introducing the sliding boundary conditions proved logical to minimize possible unrealistic deformation but, as a downside, increased the overall stiffness of the model by constraining the structural distortion in other directions. This was felt by the overall increase in DRI and SEVs compared to the other models counterparts, with a maximum when introducing the BC into the extended model. An unbalanced increase in computational time compared to its counterparts (67.24h) aggravated even further the possible use of this approach to further assess the crashworthiness, falling short in the study. Nonetheless this modelling approach gave good insights to the overall study of the Flying-V section.

Finally the full fuselage section, with approximately three times the length of the extended fuselage, obtained a slight increase in DRIs and SEVs. However, due to its increased FEM model, it gave the most realistic results for the studies taken so far. Not only performed well in terms of computational time (9.3h), it will prove essential for future studies onto other possible FV crash scenarios without oversimplifying, serving also as a validation for future reduced modelling techniques.

After juxtaposing the various modelling approaches, taking into consideration factors such as computational time, result realism, energy efficiency, and passenger safety, the consensus favored the extended model with seven passenger rows, which demonstrated an optimal equilibrium between efficiency and result authenticity while maintaining simulation simplicity. This selected model served as the foundational framework for the subsequent implicit modelling technique proposed, with later results being compared to the ones from the full fuselage section for viability purposes.

By leveraging the use of moments of inertia, the vertical drop tests were further optimized. A comparative analysis between extended model accounting for the moments of inertia of other sections of the Flying-V and the full passenger fuselage model was undertaken.

It was seen that the incorporation of moments of inertia prevented the twisting behavior that previously resulted in undesirable backward lean of the floor elements and introduced a more uniformly bent behavior at the front part. This methodology brought the section closer to the impact behavior observed by the engine section of the full passenger model, both in terms of visual inspecting the crash sections and spatial variation of DRIs and SEVs. By avoiding the complexities of a more intricate model and the associated computational times, this simplified approach appeared to yield more realistic results for simple vertical drop tests. Also, the introduction of moments of inertia further reduced the simulation time for the extended section (from 6.54h to 3.83h), aligning with expectations as fewer floor deformations resulted in a faster solver solution.

Expanding on this investigation, and since aircraft crashes don't typically involve a straightforward vertical descent but instead often occur with varying degrees of rolling inclination, the subsequent study focused on evaluating the crashworthiness performance of fuselage sections under varying roll angle impact conditions (with increments of 5 degrees up to 15 degrees). Given that the centerline maintained a horizontal orientation in both vertical and roll analyses, and due to the positive effects of integrating moments of inertia near the fuselage cross sections previously highlighted, it was considered advantageous to revisit the extended 7-rows model further enhanced with additional moments of inertia to capture the dynamics of other Flying-V sections. Nonetheless, the results for the drop tests without the addition of moments of inertia were also conducted in parallel and their outcomes compared. In the end, the structural integrity of the cabin floor was maintained, ensuring occupant survival space remained at least 85% of the original space post-crash. Left roll angles resulted in increased peak acceleration on the left side and a decrease on the right side. The timing of acceleration pulses changed with higher roll angles, influencing seat behavior and potentially leading to left side seat collapse. Moments of inertia mitigated rotation, dispersing impact energy uniformly and reducing the risk of injuries to occupants. The influence of moments of inertia on the right side was more pronounced, emphasizing their role in maintaining consistency in acceleration patterns across different roll angles. In contrast, the absence of moments of inertia concentrated impact energy on the left part, diminishing overall energy absorption. The study revealed the significance of SEV in complex crash scenarios, particularly when lateral accelerations become pronounced. Also, the reduction in average DRI and SEV values at higher roll angles aligned with the kinetic energy analysis, indicating a decrease in rate of energy dissipation and a softer contact with the ground. This reduction in DRIs and SEVs emphasized the need to account for the specific crash dynamics induced by roll angles in the crashworthiness evaluation. Moreover, while fuselage frames traditionally served as the main energy-absorbing components in perpendicular impact scenarios, the introduction of roll angles has redirected energy absorption towards floor components, resulting in increased plastic deformation. This alteration may pose challenges, particularly in ensuring the maintenance of occupants' egress routes.

Lastly, a variable centerline orientation was implemented and the crashworthiness of the FV fuselage was assessed for different pitch angles, also with 5 degrees increments up to 15 degrees. The drop tests were once again conducted for the full passenger fuselage and later compared to the case of the extended model with moments of inertia. Due to the more intricate kinematics and to ensure the robustness and precision of the implicit moments of inertia approach, a comprehensive verification and validation plan was outlined, where, by making use of the conservation of angular momentum and energy, the velocities upon impact were analytically calculated for the extended section. Visual inspection of crash scenarios provided valuable insights into the deformation patterns of both the reduced model and the full passenger fuselage under different pitch angles. The contrast between the two models, particularly at elevated pitch angles, unveiled notably greater deformations in the reduced model. Additionally, examining the spatial evolution of DRIs and SEVs provided crucial insights into the structural behavior of both the reduced model and the full passenger fuselage, highlighting apparent trends. Whereas the full passenger model exhibited distinct behavior with a more gradual increase in DRIs and SEVs, the reduced model exhibited a substantial increase in DRI and SEV values with rising pitch angles. Nonetheless, these outcomes were already anticipated, considering the simplified methodology that solely relied on moments of inertia without accounting for mass, leading to a lack of physical representation and impact energy absorption by the back and front parts.

As an alternative to the implicit moments of inertia method, the submodelling technique was proposed to address extreme crash scenarios. It involved conducting an initial drop test on the entire model with a coarser mesh, followed by replicating the test using submodelling focused on refining the engine section. Visual inspection of crash scenarios with a 15-degree pitch angle, coupled with the study of the spatial variation of DRIs and SEVs, revealed a striking similarity in outcomes between the submodel and the full passenger model, indicating the submodelling approach's efficacy in capturing engine section dynamics while reducing significantly the computational time.

Conclusions

In conclusion, reflecting on the research questions, criteria such as the spatial variation of DRIs and SEVs, energy analysis, and visual inspection of crash sections were crucial in selecting an appropriate modelling approach for evaluating the crashworthiness of the Flying-V. The assessment also considered the computational time used for each model, which was deemed of tremendous importance. The baseline section exhibited the least passenger damage and reduced computational time, making it suitable for assessing crashworthiness in conventional vertical drop tests. However, as the analysis progressed to dynamically complex scenarios, expanding the computational domain to include larger fuselage sections became essential for a more reliable study.

Introducing sliding boundary conditions logically minimized unrealistic deformation but increased overall model stiffness, leading to an unbalanced increase in computational time and hindering its suitability for further crashworthiness assessment. Alternatively, adding adjacent structural elements normalized longitudinal deformations, as observed in the engine section inside the full passenger model. This extended FEM model, despite increased complexity, offered more realistic results, proving essential for future studies on various FV crash scenarios without oversimplification.

Nonetheless, after comparing the various modelling approaches, the consensus favored the extended model with seven passenger rows as it demonstrated an optimal balance between efficiency and result authenticity while maintaining simulation simplicity. This model served as the foundational framework for subsequent proposed simplified modelling techniques, with results compared to those from the full fuselage section for viability purposes. For vertical drop tests, incorporating moments of inertia brought the section closer to the impact behavior observed in the engine section of the full passenger model, providing more realistic results and reducing simulation time.

The subsequent study focused on evaluating crashworthiness performance under varying roll and pitch angle impact conditions. For the roll analysis, the addition of moments of inertia were preferred based on outcomes from vertical drop tests, proving essential in mitigating rotation and dispersing impact energy uniformly. However, only a preliminary assessment of the simplified modelling approach was conducted, necessitating a more intensive analysis.

For pitch angles, a verification and validation plan was delineated to ensure the robustness and accuracy of the implicit moments of inertia approach. Yet, the proposed methodology, despite being informative, raised concerns about its feasibility under varying centerline orientations. The implicit modelling technique, which provided a rough estimation of subsequent parts' dynamics of the Flying-V, resulted in imprecise and unrealistic outcomes, necessitating a thorough evaluation of the reduced modelling approach for intricate drop tests involving pitch angles.

As an alternative, the submodelling technique offered precision with a substantial reduction in computational time. Nevertheless, it is imperative to conduct a comprehensive finite element model representation of a more complex model before employing such an approach.

Recommendations for Future Work

The development of the Flying-V aircraft introduces a significant challenge, especially in ensuring its crashworthiness during emergency landings. The Literature review indicates a limited scope of crashworthiness studies concerning unconventional aircraft designs, particularly those relying on conventional vertical drop tests for assessment. However, the unique geometry and mass distribution of the Flying-V can result in landing scenarios with diverse horizontal, rotational, and vertical components which cannot be adequately replicated by standard vertical drop tests.

To address this challenge, the current research aimed to evaluate the crashworthiness of the Flying-V by implementing different impact angles, both in terms of roll and pitch, as part of testing the proposed simplified modelling technique's viability. Nonetheless, it was also noted that the FV inherently includes a yaw angle, resulting in a deviation in the alignment of passenger seats when compared to traditional aircraft. Consequently, the initial proposal was to optimize the seat orientation by studying the effect of the misalignment and the introduction of side loads to passengers by conducting crash events with horizontal velocity and a pitch angle of 15 degrees. Unfortunately, due to time constraints, such tests could not be conducted, and the full potential of the study on assessing lateral injuries sustained by passengers was not fully realized. This stands as a recommendation for future research.

Additionally, the current research revealed that the implicit moments of inertia approach provided reliable outcomes for simple drop tests but fell short for more complex crash scenarios. The verification and validation approach employed were deemed oversimplified, potentially contributing to significant result differences. Further investigation into the use of this simplified method and a more robust validation assessment is warranted.

The concept of using moments of inertia to account for the kinematics of other sections of the Flying-V emerged from the lack of proper finite element model representations for those sections. The literature study explored weight and moments of inertia methods, but these primarily relied on analytical formulations, introducing imprecision to the outcomes. To comprehensively assess the crashworthiness of the Flying-V, there is a compelling need to create a FEM model, ideally representing the entire aircraft. Sucessive simulations with a coarse overall mesh should be performed to identify critical regions of the Flying-V. Subsequently, by leveraging the submodelling technique briefly explored in the current work, these critical areas could then be subjected to a more detailed assessment.

Bibliography

[1] URL: https://www.planecrashinfo.com/.

[2] MIL-STD 1290. *Light fixed and rotary-wing aircraft crash resistance*. Dept. of Defense, 1988.

[3] Pintar F A et al. *Worldsid assessment of far side impact countermeasures*. Annu Proc Assoc Adv Automot Med.

[4] Airbus A350. *Proposed ESF D-30 on CS 25.785(d) - installation of angled seats (applicable to Airbus A350-941)*. July 2014. URL: https://www.easa.europa.eu/en/document-library/product-certification-consultations/proposed-esf-d-30-cs-25785d.

[5] Ira Herbert Abbott, Von Doenhoff Albert Edward, and Ira Herbert Abbott. "6". In: *Theory of wing sections: Including a summary of Aerofoil Data*. Dover, 1959, pp. 111–123.

[6] A. Adams, C. K. Thorbole, and H. M. Lankarani. "Scale modelling of aircraft fuselage: An innovative approach to evaluate and improve crashworthiness". In: *International Journal of Crashworthiness* 15.1 (2010), pp. 71–82. DOI: 10.1080/13588260903047663.

[7] Federal A Administration. *Aviation Rulemaking Advisory Committee; Transport Airplane and Engine Issues; New Task*. June 2015. URL: https://www.federalregister.gov/documents/2015/06/04/2015-13542/aviation-rulemaking-advisory-committee-transport-airplane-and-engine-issues-new-task.

[8] Federal A Administration. *The Federal Register*. 2022. URL: https://www.ecfr.gov/current/title-14/chapter-I/subchapter-C/part-25.

[9] Federal A Administration. *Transport Aircraft Crashworthiness and Ditching Working Group Report to FAA*. Sept. 2018. URL: https://www.faa.gov/regulations_policies/rulemaking/committees/documents/index.cfm/document/information/documentID/3743.

[10] Federal Aviation Administration. "Transport Airplane Cabin Interiors Crashworthiness Handbook". In: *U.S. Department of Transportation* (May 2009). DOI: https://www.faa.gov/documentLibrary/media/Advisory_Circular/AC_25-17A_CHG-1.pdf.

[11] European Union Aviation Safety Agency. *CS-25 Amendment 27 - review of Aeroplane Performance Requirements for Air Operations and regular update of CS-25*. Jan. 2023. URL: https://www.easa.europa.eu/en/document-library/certification-specifications/cs-25-amendment-27.

[12] Airbus. *Aircraft Characteristics: Airport Operations & tech data*. URL: https://www.airbus.com/en/airport-operations-and-technical-data/aircraft-characteristics.

[13] John D. Anderson and Mary L. Bowden. *Introduction to flight*. McGraw-Hill, 2022.

[14] PhD Andrea Isfeld. *Reducing computational demands in Abaqus with submodeling*. Sept. 2022. URL: https://www.inceptra.com/reducing-computational-demands-in-abaqus-with-submodeling/.

[15] SAE ARP. "Performance Standards for Oblique Facing Passenger Seats in Transport Aircraft". In: *SAE International* (May 2016).

[16] G. Bourget. "The effect of landing gear implementation on Flying V aerodynamics , stability and controllability". In: (2020).

[17] Pedro D. Bravo-Mosquera, Fernando M. Catalano, and David W. Zingg. "Unconventional aircraft for Civil Aviation: A Review of Concepts and Design Methodologies". In: *Progress in Aerospace Sciences* 131 (2022), p. 100813. DOI: 10.1016/j.paerosci.2022.100813.

[18] J. W. Brinkley and J. T. Shaffer. *Dynamic simulation techniques for the design of escape systems: Current applications and Future Air Force Requirements*. Aerospace Medical Research Laboratory - Wright-Patterson Air Force Base, 1971.

[19] Alan Byar and Tein-Min Tan. “A crashworthiness study of a Boeing 737 Fuselage Section”. PhD thesis. Drexel University, 2003.

[20] Viano D C. *Biomechanical response and injuries in blunt lateral impact*. STAPP Conference Proceedings, 1989.

[21] J. M. Cavanaugh et al. *Biomechanical response and injury tolerance of the pelvis in twelve sled side impacts*. 1990.

[22] J. M. Cavanaugh et al. *Injury and response of the thorax in side impact cadaveric tests*. 1993.

[23] M. B. P. Claeys. “Flying V and Reference Aircraft Structural Analysis and Mass Comparison”. PhD thesis. TUDelft, 2018, pp. 1–107.

[24] J. W. Coltman et al. *Aircraft crash survival design guide*. Vol. 2. U.S. Army Aviation Research and Technology Activity (AVSCOM), Aviation Applied Technology Directorate, 1989.

[25] TU Delft. *Technology*. URL: https://www.tudelft.nl/en/ae/flying-v/technology.

[26] Marco Desiderio. “Flying-V Crashworthiness: a Preliminary Assessment”. PhD thesis. TUDelft, 2023, pp. 1–106.

[27] Marco Desiderio et al. “Crashworthiness of the Flying-V Aircraft Concept with Vertical Drop Test Simulations”. In: *ASIDIC* (2023). DOI: 10.31224/3034.

[28] T P Dotman. *A Structural Sizing Methodology for the Wing-Fuselage of the Flying-V (M.Sc. Thesis)*. Delft, Dec. 2021.

[29] T. P. Dotman. “A Structural Sizing Methodology for the Wing-Fuselage of the Flying-V”. PhD thesis. TUDelft, 2021, pp. 1–238.

[30] Flight Safety Foundation. *Survival factors*. Oct. 2017. URL: https://flightsafety.org/asw-article/survival-factors/.

[31] A. Ruiz Garcia. “Aerodynamic Model Identification of the Flying-V using Wind Tunnel Data”. PhD thesis. TUDelft, 2019.

[32] Venkateswarlu Gattineni and Venukumar Nathi. “Implant and submodeling techniques for detailed finite element study of inserts in Composites”. In: *MethodsX* 6 (2019), pp. 2076–2087. DOI: 10.1016/j.mex.2019.09.012.

[33] M. Guida et al. “Review on the design of an aircraft crashworthy passenger seat”. In: *Progress in Aerospace Sciences* 129 (2022), p. 100785. DOI: 10.1016/j.paerosci.2021.100785.

[34] Scott Hamilton. *Don’t look for commercial BWB airplane any time soon, says Boeing’s future Airplanes head*. Mar. 2018. URL: https://leehamnews.com/2018/04/03/dont-look-for-commercial-bwb-airplane-any-time-soon-says-boeings-future-airplanes-head/.

[35] J. M.T. Horwitz. “Parametric Design of the Flying-V Winglets for Improved Lateral-Directional Stability and Control”. PhD thesis. TUDelft, 2021, pp. 1–61.

[36] John R. Humm et al. “Responses and injuries to PMHS in side-facing and oblique seats in horizontal longitudinal sled tests per FAA emergency landing conditions”. In: *SAE Technical Paper Series* (2016). DOI: 10.4271/2016-22-0006.

[37] K E Jackson. “Impact testing and simulation of a crashworthy composite fuselage concept”. In: *International Journal of Crashworthiness* 6.1 (2001), pp. 107–122. DOI: 10.1533/cras.2001.0166.

[38] Karen E. Jackson, Edwin L. Fasanella, and Sotiris Kellas. “Development of a scale model composite fuselage concept for improved crashworthiness”. In: *Journal of Aircraft* 38.1 (2001), pp. 95–103. DOI: 10.2514/2.2739.

[39] Karen E. Jackson, Edwin L. Fasanella, and Karen H. Lyle. “Crash Certification by Analysis – Are We There Yet?” In: *NASA* ().

[40] G Kay. “Failure modeling of titanium-6al-4v and 2024-T3 aluminum with the johnson-cook material model”. In: *Tech. rep. Washington DC, USA: Federal Aviation Administration* (Sept. 2002). DOI: 10.2172/15006359.

[41] Rowan Koenderink. “Design Methodology for Unconventional Engine Mounting Structures, Including Crashworthiness Assessment”. PhD thesis. TUDelft, 2024, pp. 1–92.

[42] R. Liebeck. “Design of the blended-wing-body subsonic transport”. In: *40th AIAA Aerospace Sciences Meeting & Exhibit* (2002). DOI: 10.2514/6.2002-2.

[43] Nikki van Luijk. “Constrained aerodynamic shape optimisation of the Flying V Outer Wing”. In: *TUDelft* (2023). DOI: 10.2514/6.2023-3250.vid.

[44] M. R. Maltese et al. *Response corridors of human surrogates in lateral impacts*. 2002.

[45] Elisabeth Martin. *Statistical summary of commercial jet airplane accidents*. URL: https://skybrary.aero/sites/default/files/bookshelf/32664.pdf.

[46] USAF MIL-S-9479B. “Military Specification: Seat System, Upward Ejection, Aircraft, General Specification”. In: *EverySpec* (Mar. 1971).

[47] Haolei Mou, Yuejuan Du, and Tianchun Zou. “Effects of different roll angles on civil aircraft fuselage crashworthiness”. In: *Advances in aircraft and spacecraft science* 2.4 (2015), pp. 391–401. DOI: 10.12989/aas.2015.2.4.391.

[48] Haolei Mou, Jiang Xie, and Zhenyu Feng. “Research status and future development of crashworthiness of civil aircraft fuselage structures: An overview”. In: *Progress in Aerospace Sciences* 119 (2020), p. 100644. DOI: 10.1016/j.paerosci.2020.100644.

[49] Benjamin C. Moulton and Douglas F. Hunsaker. “Simplified mass and inertial estimates for aircraft with components of constant density”. In: *DigitalCommons@USU* (Jan. 2023), pp. 1–40. DOI: 10.2514/6.2023-2432.vid.

[50] Airbus NEO. *Special condition on installation of oblique seats - applicable to Airbus A330 NEO*. July 2017. URL: https://www.easa.europa.eu/en/document-library/product-certification-consultations/special-condition-installation-oblique-seats.

[51] N. van Oene. “Landing Gear Design Integration for the TU Delft Initiator”. PhD thesis. TUDelft, 2019.

[52] Wilco Oosterom and Roelof Vos. “Conceptual design of a flying-V aircraft family”. In: *AIAA AVIATION 2022 Forum* (2022). DOI: 10.2514/6.2022-3200.

[53] M. Palermo. “The Longitudinal Static Stability and Control Characteristics of a Flying V Scaled Mode”. PhD thesis. TUDelft, 2019.

[54] Vincenzo Pesce et al. “Chapter Five - Attitude dynamics”. In: *Modern spacecraft guidance, navigation, and control: From system modeling to AI and innovative applications*. Elsevier, 2023, pp. 207–252.

[55] M Phillippens et al. “Neck Injury Criteria for Side-Facing Aircraft Seats”. In: *DOT/Federal Aviation Administration* (2011).

[56] R. Van der Pluijm. “Cockpit Design and Integration into the Flying V”. PhD thesis. TUDelft, 2021, pp. 1–70.

[57] Alan Poston. “Human Engineering Design Data Digest”. In: *Tech. rep. United States Department of Defence* (Apr. 2000).

[58] Priya Prasad and Harold J. Mertz. “The position of the United States delegation to the ISO Working Group 6 on the use of HIC in the automotive environment”. In: *SAE Technical Paper Series* (1985). DOI: 10.4271/851246.

[59] Federal Register. *Special Conditions: Boeing Model 787-8 Airplane*. Sept. 2007. URL: https://www.federalregister.gov/documents/2007/09/26/E7-18942/special-conditions-boeing-model-787-8-airplane-crashworthiness.

[60] Aniello Riccio et al. “An insight on the crashworthiness behavior of a full-scale composite fuselage section at different impact angles”. In: *Aerospace* 6.6 (2019), pp. 1–14. DOI: 10.3390/aerospace6060072.

[61] Airbus S.A.S. 2016.

[62] SAEJ885. 1980.

[63] Dennis F. Shanahan. “Basic principles of helicopter crashworthiness”. In: *NATO OTAN* (1993). DOI: 10.21236/ada267099.

[64] Stephen Soltis. “Seat Dynamic Performance Stand Range of Sizes”. In: *US Department of Transportation - FAA*. DOT/FAA/CT-TN90/23 (1990), pp. 1–21.

[65] E. L. Stech and P. R. Payne. *Dynamic models of the human body*. Aerospace Medical Research Lab, 1969.

[66] Ralf Sturm and Martin Hepperle. “Crashworthiness and ditching behaviour of blended-wing-body (BWB) aircraft design”. In: *International Journal of Crashworthiness* 20.6 (2015), pp. 592–601. DOI: 10.1080/13588265.2015.1068997.

[67] Aero Toolbox. *Sweep angle and supersonic flight*. Sept. 2022. URL: https://aerotoolbox.com/intro-sweep-angle/.

[68] Egbert Torenbeek. “Synthesis of subsonic airplane design”. In: *Delft University Press* (1982). DOI: 10.1007/978-94-017-3202-4.

[69] R. C. J. Voeten. “Flying-V: A design methodology for unconventional engine mounting structures”. PhD thesis. TUDelft, 2022, pp. 1–176.

[70] N Yoganandan et al. *Biomechanics of side impact: injury criteria, aging occupants, and airbag technology*. J Biomech 40, 2007.

[71] N Yoganandan et al. *Oblique lateral impact biofidelity deflection corridors from Post Mortem Human Surrogates*. Stapp Car Crash J 57, 2013.

[72] N Yoganandan et al. *Thoraco-abdominal deflection responses of post mortem human surrogates in side impacts*. Stapp Car Crash J 56, 2012.

[73] Lifang ZENG et al. “Mechanism analysis of hysteretic aerodynamic characteristics on variable-sweep wings”. In: *Chinese Journal of Aeronautics* 36.5 (2023), pp. 212–222. DOI: 10.1016/j.cja.2023.01.002.

[74] Richard E. Zimmermann and Norman A. Merritt. *Aircraft crash survival design guide*. Vol. 1. U.S. Army Aviation Research and Technology Activity (AVSCOM), Aviation Applied Technology Directorate, 1989.

[75] Tianchun Zou, Haolei Mou, and Zhenyu Feng. “Research on effects of oblique struts on crashworthiness of composite fuselage sections”. In: *Journal of Aircraft* 49.6 (2012), pp. 2059–2063. DOI: 10.2514/1.c031867.

This page intentionally contains no content.

VI

Appendix

This page intentionally contains no content.

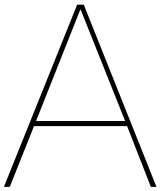

Additional Occupant Injury Criteria for Oblique Seats

Body Part	Injury Criterion
Head	(1) HIC ≤ 1000 (AS8049B Section 5.3.9.4) in the event of head contact with seats, or other structure (including airbags),① *or* (2) HIC 15 ≤ 700 (49 CFR 571.208) in the event of head contact with an airbag *only* ② ① Following a test, calculate HIC. If this value is ≤1000, the test is successful. If HIC is > 1000, and contact is made with the seat or other structure, regardless of airbag usage, the test has failed. ② Use of HIC 15 is permitted as an alternate to HIC if the ATD head only contacts an airbag and makes no head contact with the seat or other structure. ATD head contact with the seat or other structure, through the airbag, or contact subsequent to contact with the airbag requires the use of HIC. HIC 15 is not applicable if head contact has occurred. The following evaluations of the test data should be used to determine if head contact has occurred: a. A review of the dynamic test videos and evaluation of the ATD head path movement, head contact, and head reaction at contact should be made. There should be a noticeable change in the head movement at the time of contact. A review and evaluation of the ATD head acceleration plots (x, y, z and resultant) should be made. The resultant ATD head acceleration plot during the time period in which the critical HIC calculation was made should show an abrupt change in the head acceleration.
Neck	Nij (49 CFR 571.208) (1) Nij shall be below 1.0, where Nij =Fz/Fzc + My/Myc, and Nij critical values: (a) Fzc = 1530 pounds (6805 N) tension (b) Fzc = 1385 pounds (6160 N) compression (c) Myc = 229 foot-pounds (310 Nm) in flexion (d) Myc = 100 foot-pounds (136 Nm) in extension (2) In addition, peak Fz shall be below 937 pounds (4168 N) in tension and 899 pounds (3999 N) in compression. (3) Rotation of the head about its vertical axis relative to the torso is limited to 105 degrees in either direction from forward-facing. (4) Concentrated loading on the neck is unacceptable during any phase of the test. The intent is that the neck should not be a load path in any ATD contact with the seat system, never the initial point of contact and for neck movement to be in unison with the head and shoulders. In particular, the front of the neck should

Body Part	Injury Criterion
	never be contacted, however incidental contact, such as a sliding motion against a flat surface, or a headrest, during rebound may be acceptable. [Visual evidence and loading data shall be collected during the test to show that neck contact is non-injurious.]
Shoulder	(1) Where upper torso straps are used, tension loads in individual straps shall not exceed 1750 pounds (7784 N). If dual straps are used for restraining the upper torso, the total strap tension loads shall not exceed 2000 pounds (8896 N). (2) The upper torso restraint straps (where installed) shall remain on the ATD's shoulder during the impact.
Thorax	Significant contact between the thorax and seat system structure is not permitted during initial impact, except for intentional contact with an airbag or shoulder restraint. For example, contact with a corner or protrusion would be significant contact and be unacceptable. Sliding along a smooth wall is not significant contact and could be acceptable, provided all other injury criteria is met. Rebound contact that produces an x direction acceleration exceeding 20g for more than 3ms is not permitted.
Abdomen	Significant contact between the abdomen and seat structure is not permitted except for intentional contact with an airbag or seat cushion.
Spine	(1) The lumbar spine force (Fz) cannot exceed 1200 pounds (5338 N) tension and 1500 pounds (6673 N) compression. (2) Spine forces and moments shall be recorded using a six axis load cell and shall be reported. This data is collected for knowledge gathering. There are no pass/fail criteria associated with this data except as noted above for Fz.
Pelvis	(1) The pelvic restraint shall remain on the ATD's pelvis during the impact and rebound phases of the test. Provided that the pelvic restraint remains on the ATD's pelvis, trapping of the belt between the ATD leg and the pelvis is acceptable. (2) Any part of the load-bearing portion of the bottom of the ATD pelvis shall not translate beyond the edges of its seat's bottom seat-cushion supporting structure.
Femur	(1) Where leg contact with seats or other structure occurs, the axial compressive load in each femur does not exceed 2250 pounds (10008 N). (2) Axial rotation of the upper leg shall be limited to 35 degrees in the strike direction from the nominal seated position. Evaluation during rebound is not biofidelic and need not be considered.
All	Contact between the head, pelvis, torso, or shoulder area of one ATD with the adjacent-seated ATD's head, pelvis, torso, or shoulder area is not allowed. Contact during rebound is allowed.

B

SEV: Graphic Approximation Technique

By utilizing the graphic approximation technique illustrated in Figure B.1, it is possible to obtain the rise time, plateau duration, and acceleration values (g) along the x and y axes at a specific time based on acceleration-time plots derived from measurements or computations [46].

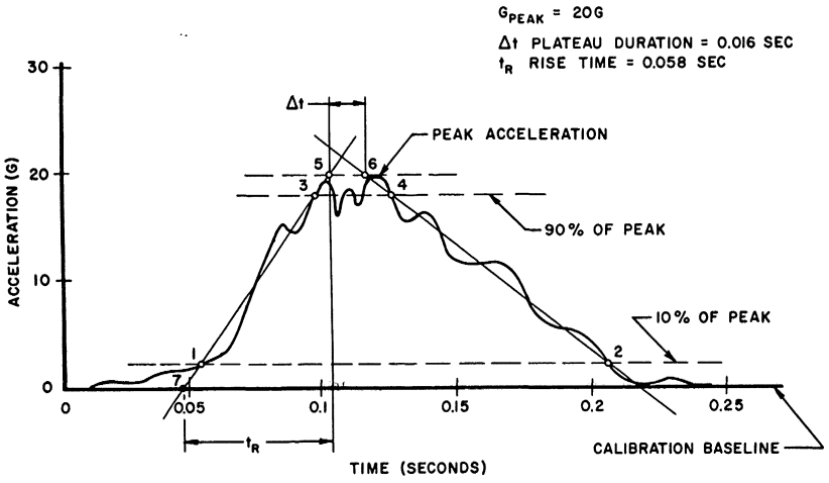

Figure B.1: Graphic Approximation Example [46]

1. Establish the calibration baseline, correcting for any gravity bias acceleration.
2. Establish the maximum (peak) acceleration magnitude.
3. Construct a reference line parallel to the calibration baseline at a magnitude equal to 10 percent of the peak acceleration. The intersection of this line with the acceleration time plot defines points 1 and 2 in Figure B.1.
4. Construct a second reference line parallel to the calibration baseline at a magnitude equal to 90 percent of the peak acceleration. The intersection of this line with the acceleration time plot defines points 3 and 4 in Figure B.1.
5. Construct the onset line defined by the straight line through points 1 and 3.
6. Construct the offset line defined by the straight line through points 2 and 4.
7. Construct a line parallel to the calibration baseline, through the peak acceleration. The time interval defined by the intersections of this line with the constructed onset and offset lines (points 5 and 6) is the plateau duration (Δ_t).

8. Locate the intersection of the constructed onset line with the calibration baseline (point 7). The time interval defined by points 7 and 5 is the rise time (T_R).

9. For a given plot of accelerations in the x and y axes, the specific g values are graphically obtained from the constructed onset and offset lines for the specific time at which the summation vector of acceleration is the greatest. An example is shown on Figure B.2.

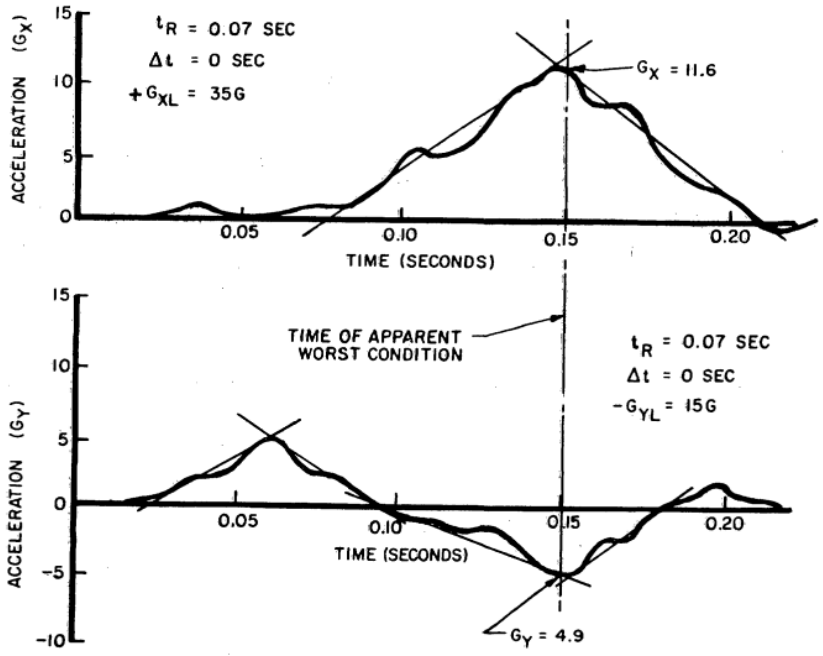

Figure B.2: Multiaxial Acceleration Environment Example [46]

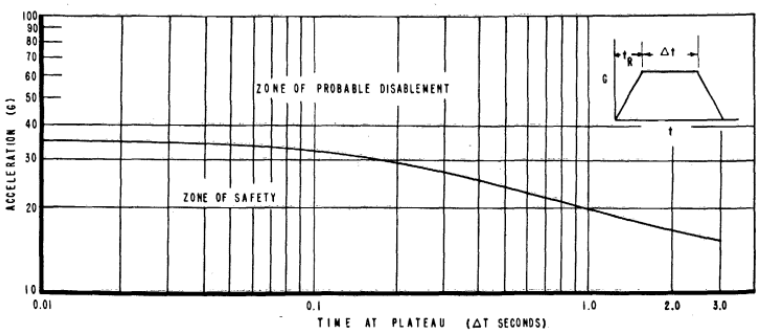

Δt (SEC)	0-.03	.06	.084	.13	.15	.19	.22	.27	.32	.38	.45	.52	.61	.73	.87	1.0	1.22	1.5	1.92	2.45	3.0
G	35	34	33	32	31	30	29	28	27	26	25	24	23	22	21	20	19	18	17	16	15

Figure B.3: Acceleration Limit ($+G_{xL}$) (Rise Time $\geq .03$ Sec) [46]

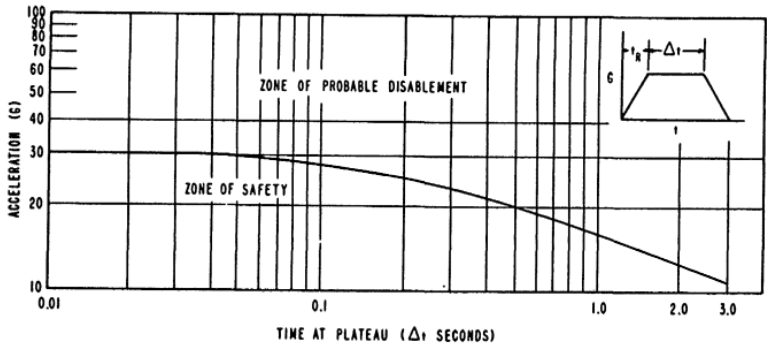

Δt (SEC)	0-.03	.05	.08	.11	.15	.2	.23	.30	.33	.38	.45	.6	.75	.9	1.0	1.2	1.5	1.9	2.5	3.0
G	30	29	28	27	26	25	24	23	22	21	20	19	18	17	16	15	14	13	12	11

Figure B.4: Acceleration Limit ($-G_{xL}$) (Rise Time $\geq .03$ Sec) [46]

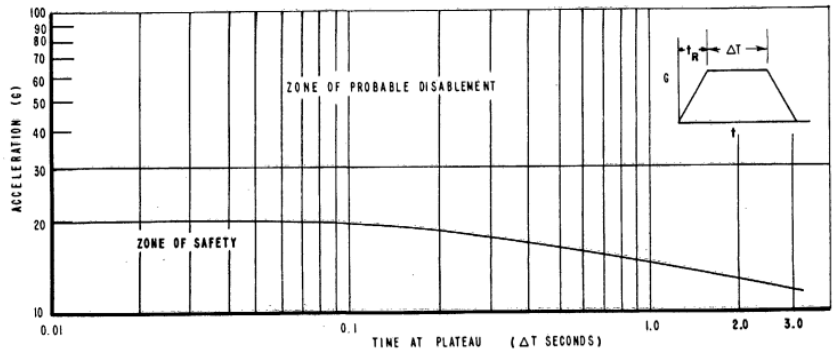

Δt (SEC)	0-.03	.085	.15	.25	.36	.52	.75	1.1	1.6	3.0
G	20	19.5	19	18	17	16	15	14	13	11.5

Figure B.5: Acceleration Limit ($\pm G_{xL}$) (Rise Time $\leq .03$ Sec) [46]

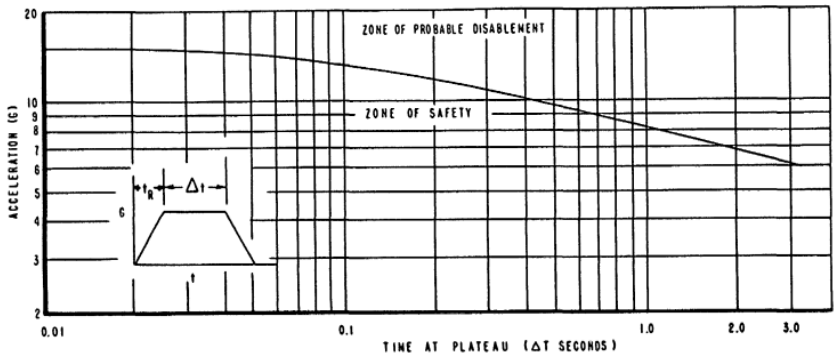

Δt (SEC)	0-.03	.06	.11	.18	.28	.41	.62	.86	1.8	3.0
G	15	14	13	12	11	10	9	8	7	6

Figure B.6: Acceleration Limit ($\pm G_{yL}$) (Any Rise Time) [46]

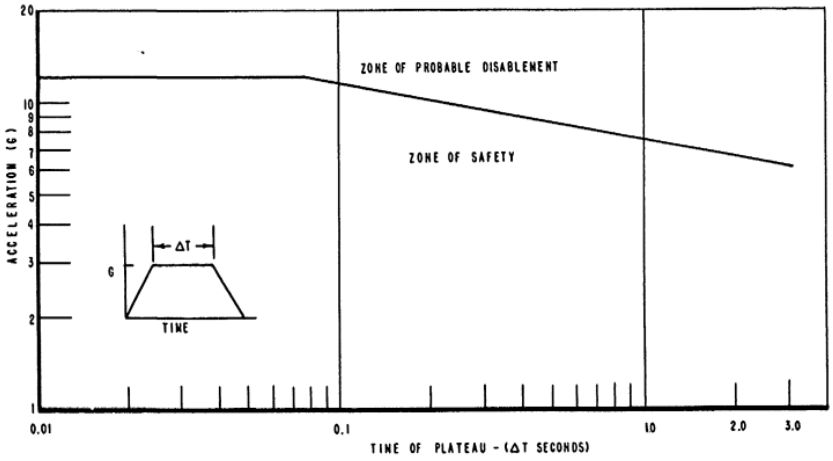

PLATEAU	DURATION MSEC	80	126	208	360	666	1340	3000
	MAGNITUDE G	12	11	10	9	8	7	6

Figure B.7: Acceleration Limit for $(-G_z)$ (Rise Time $\geq .04$ Sec) [46]

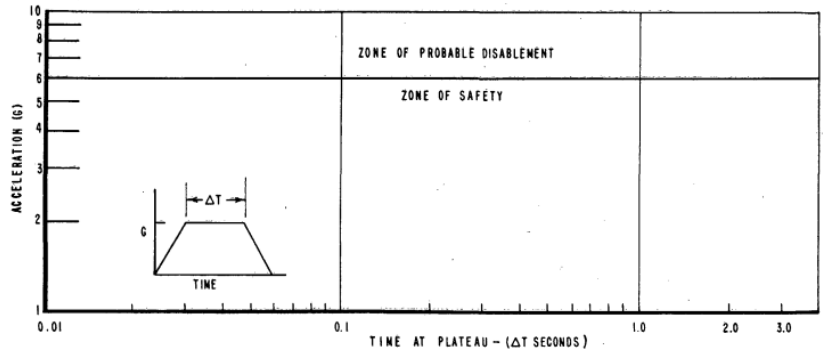

PLATEAU	DURATION M SEC	0-3000
	MAGNITUDE G	6

Figure B.8: Acceleration Limit for $(-G_z)$ (Rise Time $< .04$ Sec) [46]

C

Flying-V's Horizontal Approach Speed

Once acceptable vertical velocity for crashworthiness analysis has been established, the question remains: should the horizontal component of the velocity also be considered and if so, what should be then the velocity vector used when the horizontal component is added to the analyses?

This matter was also discussed in the proposed special conditions issued by the FAA for the Boeing 787 [59]. Back then, a commentator suggested that the special conditions should incorporate a requirement for a full scale drop test involving a forward velocity vector. This test would aim to simulate a condition representative to a wheels-up landing, with the combined effect of both vertical and horizontal velocity elements taken into account to assess the loads on the passengers and crew.

The FAA examined both the airframe's longitudinal loading situations and the combined longitudinal and vertical loading situations of the 787 aircraft during crash scenarios that could be survived, as well as during emergency landings with various wheels up landing gear setups. According to the FAA [59], the primary factors that govern how the aircraft responds to impacts in the longitudinal direction – mainly deformation, mass, and friction – remain largely unaffected by the shift from a metal-based to a composite-based fuselage structure. Because of the similarities between the 787 and the existing aircraft fleet in relation to these conditions, the FAA has concluded that these specific conditions would focus only on evaluating the 787's performance under vertical impact conditions.

However, concerning the Flying-V, the issue doesn't lie from the material employed in the aircraft's structure, but rather from its design. The constant cross-sectional shape of the wings' fuselage in the FV results in a specific angle relative to the direction of landing. This aspect could challenge the feasibility of conducting only vertical drop tests for such an innovative design.

To guarantee compliance with the C/D category of the International Civil Aviation Organization (ICAO), an upper limit is imposed on the approach speed, denoted as V_{appmax}. This constraint is necessary to ensure that the wing loading of the Flying-V is adequately maintained. The approach speed is calculated using Equation C.1 [52]:

$$V_{\text{app}} = \sqrt{\frac{W_{\text{MLW}}}{S} \frac{2}{\rho_0} \frac{1}{C_{L_{app}}}} \tag{C.1}$$

In this equation, the density ρ_0 corresponds to sea-level conditions ($1.225kg/m^3$) as the approach speed is based on indicated airspeed. The landing weight, W_{MLW}, is defined as 76% of the takeoff weight, which aligns with the average case for the reference aircraft as per Airbus specifications [12]. While emergencies can occur at any point during a flight, for the sake of simplicity, this average weight will be considered.

For all members of the Flying-V aircraft family, the maximum lift coefficient in the approach configuration, C_{Lapp}, was set by Oosterom [52] at 0.73. This value was derived from the detailed study of the Flying-V's landing gear conducted by Bourget [16]. Even thought, to analyse the crashworthiness, the landing gear is in the retracted position, again, for ease of understanding, the same lift coefficient will be used.

Upon substituting the values derived from Oosterom's study [52] into Equation C.1, the calculated velocity for the FV-1000 amounts to 147 knots (75.6 m/s or 248 ft/s).

Bourget [16] and Pluijm [56] considered an approach speed of $V_{\text{approach}} = 140\text{kts} = 72\text{m/s}$, identical to the landing speed of an A350-900 [61]. Following an optimization process built on certain presumptions, Oosterom [52] managed to reduce the approach velocity to 137 knots (70.7 m/s or 231 ft/s). Given that the soundness of these assumptions was not verified in Oosterom's research, a more conservative approach will be adopted here, considering 147 knots (248 ft/s) as the magnitude of the velocity vector.

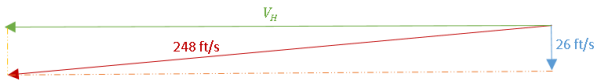

Figure C.1: Components of the velocity vector

Knowing the vertical velocity and the magnitide of the velocity vector, the horizontal velocity V_H can easely be calculated using Equation C.2:

$$V_{\text{H}} = \sqrt{248^2 + 26^2} = 246.6\text{ft/s} \tag{C.2}$$

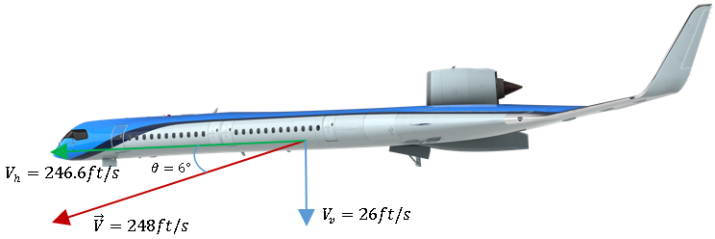

Figure C.2: Lateral view of the FV with the velocity vector used [25]

This was also the horizontal impact velocity used by Sturm et al. [66] when analysing the crashworthiness and ditching behaviour of Blended wing Body (BWB) aircraft design. For the crash simulations, Sturm chose an airplane setup with retracted landing gear. This crash scenario is considered one of the most severe yet survivable situations, as the fuselage structure must fully absorb the vertical portion of the kinetic energy through deformation [66]. A horizontal impact speed of 75 m/s (246 ft/s) was applied along with an aircraft angle of 15°. The vertical velocity used by Sturm was 9 m/s (30 ft/s) which aligns with the impact scenario outlined in the "crashworthiness" special condition for the Boeing 787 aircraft [59].

Figure C.3 presents a sequence of outcomes derived from the crash simulation done by Sturm [66]. Initially, the aircraft's rear section makes contact with the ground, prompting an initiation of pitch-down motion. This rotational movement defines the crash dynamics up to a point 450 ms following the initial impact. Throughout this period, the aircraft remains without contact with the ground. Subsequently, the centerbody enters the ground impact phase. The rotation is halted once the entire lower fuselage establishes contact with the ground at approximately 690 ms. Subsequent to this, the sliding phase starts. As long as the aircraft's sliding motion remains uninterrupted by any obstructions, the potential for increased passenger acceleration loads is not anticipated.

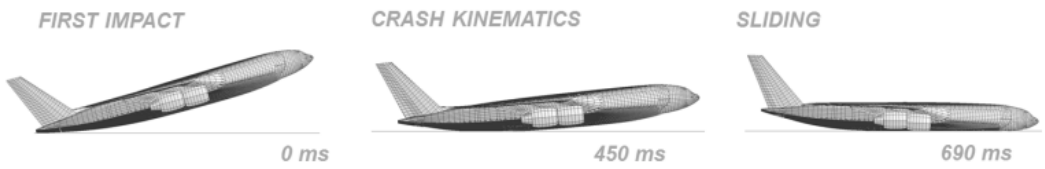

Figure C.3: Crash kinematics of the NACRE BWB aircraft [66]

D

Aircraft Impact Attitudes Envelopes

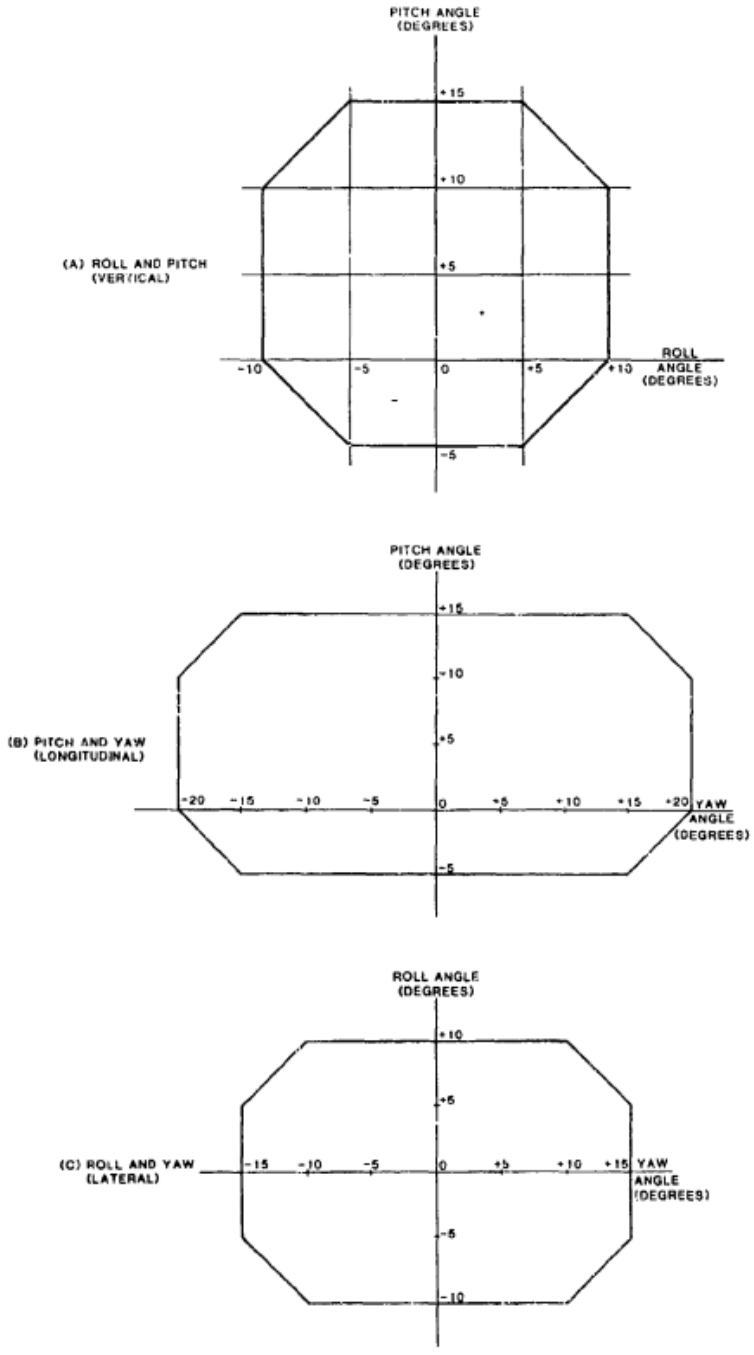

Figure D.1: Aircraft Impact Attitudes Envelopes [24]

E

FV-1000 Aircraft Floor Plan and Plugs' Dimensions

This section of the appendix displays the floor plan created by Oosterom [52] for the FV-1000 aircraft and the length of fuselage plugs.

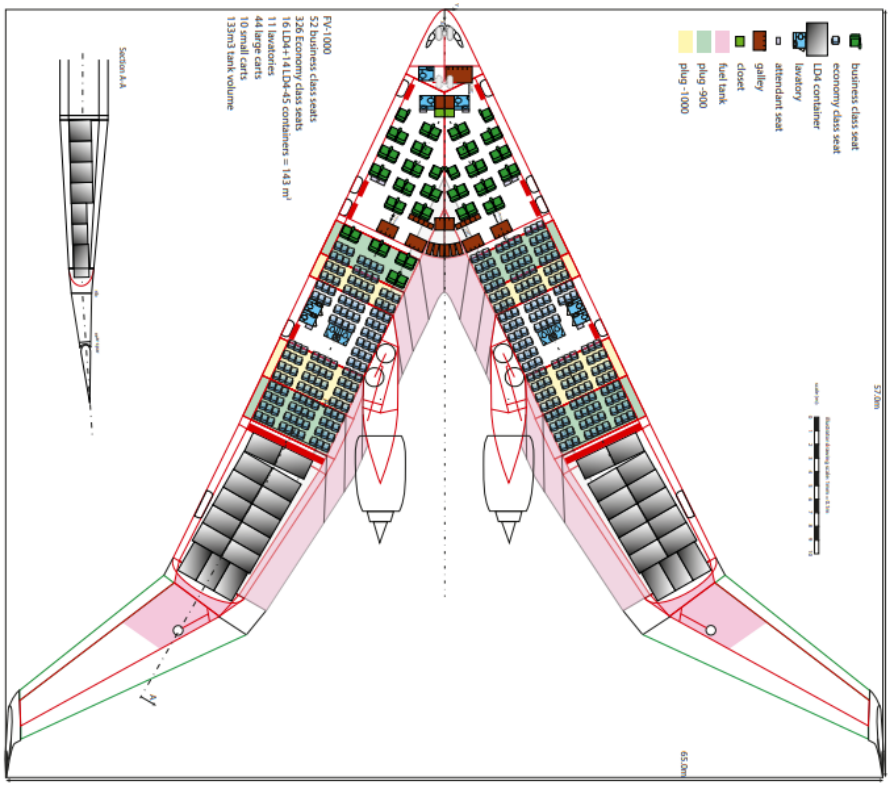

Figure E.1: Floor layout of the FV-1000 airplane, illustrating the plugs to create an FV-800 or FV-900 version [52]

Table E.1: Length of fuselage plugs to build a family of Flying-V aircraft [52]

plug		frames	length (m)
-900	front	4	2.67
	aft	5	3.33
-1000	front	3	1.88
	aft	5	3.12

F

Inertial Estimates for the Outer-Wing of the Flying-V

Aircraft's mass and inertial properties are required to estimate the dynamics and handling characteristics of aircraft [49]. Yet, determining these properties can be challenging due to their dependence on factors such as the aircraft's external shape, internal structure, systems, and mass distribution within the airframe. The mass and inertial properties of aircraft are commonly estimated through the utilization of computer-aided design software or determined through a variety of experimental methods. In the case of the outer wing of the FV, due to its complex geometry and assuming it has constant density, a method for quickly predicting the mass and inertial properties proposed by Moulton et al. [49] was used.

While assuming a constant density may seem restrictive, the technique used offers a valuable means to estimate mass properties of intricate internal structures. The impact of geometric features such as sweep, taper and airfoil geometry of the outerwing is included in the analysis.

F.1. Generalized Mass Properties

F.1.1. Volume, Mass, and Weight

The volume of an object can be determined by integrating the space enclosed by its geometry, expressed as a volume integral

$$V = \iiint_V dV \tag{F.1}$$

The mass of an object with uniform density is merely given by

$$m = \rho V \tag{F.2}$$

and the weight W of an object is

$$W = mg \tag{F.3}$$

Here, g represents the gravitational constant. Assuming constant density allows us to fully define the mass characteristics of an object using its volume, along with either its mass, density, or weight [49].

F.1.2. Center of Gravity

The position of the center of gravity (CG) for an object can be calculated based on its mass distribution. In the case of an object with uniform density, the moments along each axis can be expressed as volume integrals

$$M_{yz} = \rho \iiint_V x dV \tag{F.4}$$

$$M_{xz} = \rho \iiint_V y dV \tag{F.5}$$

$$M_{xy} = \rho \iiint_V z dV \tag{F.6}$$

The coordinates of the object CG relative to the object origin can then be computed from

$$\bar{x} \equiv \frac{M_{yz}}{m} \tag{F.7}$$

$$\bar{y} \equiv \frac{M_{xz}}{m} \tag{F.8}$$

$$\bar{z} \equiv \frac{M_{xy}}{m} \tag{F.9}$$

F.1.3. Mass Moment of Inertia

The mass moment of inertia of an object can be represented in tensor form as

$$[\mathbf{I}] = \begin{bmatrix} I_{xx} & -I_{xy} & -I_{xz} \\ -I_{yx} & I_{yy} & -I_{yz} \\ -I_{zx} & -I_{zy} & I_{zz} \end{bmatrix} \tag{F.10}$$

where the individual moments and products of inertia for an object with uniform density can be calculated using volume integrals

$$I_{xx} = \rho \iiint_V \left(y^2 + z^2\right) dV \tag{F.11}$$

$$I_{yy} = \rho \iiint_V \left(x^2 + z^2\right) dV \tag{F.12}$$

$$I_{zz} = \rho \iiint_V \left(x^2 + y^2\right) dV \tag{F.13}$$

$$I_{xy} = I_{yx} = \rho \iiint_V (xy) dV \tag{F.14}$$

$$I_{xz} = I_{zx} = \rho \iiint_V (xz) dV \tag{F.15}$$

$$I_{yz} = I_{zy} = \rho \iiint_V (yz) dV \tag{F.16}$$

F.2. Component Properties

The mass and moment-of-inertia characteristics of an entire aircraft can be approximated by combining the contributions of each individual component that constitutes the complete aircraft.

Here it is included a more general estimate to calculate the mass properties of an airplane wing, assuming that it is a solid of constant density. The same methodology can then be applied considering the geometric values of the outerwing of the Flying-V.

F.2.1. General Wing Segment

A method was developed by Moulton et al. [49] to estimate the volume, mass, and inertial properties of an individual wing segment. For wings with greater complexity, this process can be iterated for each wing segment, and the outcomes combined, akin to summing the influences of multiple components on the aircraft.

Geometry and Coordinate Definitions

Each wing segment can be characterized by specific parameters, such as span b, root chord c_r, tip chord c_t, root airfoil thickness τ_r, tip airfoil thickness τ_t, airfoil thickness distribution, sweep angle Λ, and dihedral angle Γ. Within a given wing segment, the sweep and dihedral angles are assumed to remain constant, while the chord and airfoil thickness are considered to vary linearly with respect to the spanwise location. Throughout this analysis, impact of wing twist is disregarded, as it typically exerts minimal influence on the mass properties of the wing when compared to the other listed parameters.

For objects with simple geometries, the location of the center of gravity is known due to the symmetry of each geometry. Hence, the origin for each object is easily defined at the center of gravity. In the case of a finite wing, a coordinate system will be established that is distinct from the wing's center of gravity, as the center of gravity of the wing is not known beforehand [49].

In the current analysis, the coordinate system for a wing segment is depicted in Figure F.1. The coordinate frame's origin is situated at the wing-root quarter-chord, while the z-axis is aligned with the chord-line, extending outward from the root.

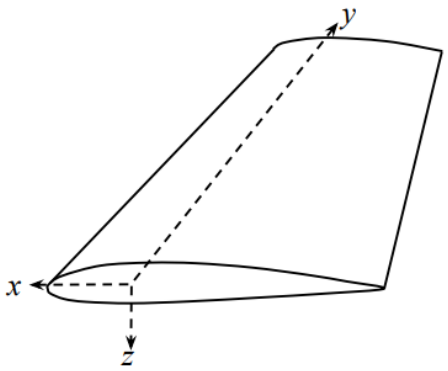

Figure F.1: Drawing of the wing-segment coordinate frame [49]

Wing sweep refers to the wing's chordwise tilting in the xy-plane, illustrated in Figure F.2. A positive sweep angle shifts the wing tip towards the rear, while a negative sweep angle moves the wing tip forward. The sweep angle is determined by the angle between the y-axis and a line connecting the quarter-chords of the root and tip, as depicted in Figure F.2.

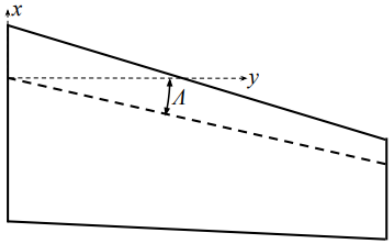

Figure F.2: Quarter chord sweep angle [49]

Wing dihedral refers to the rotation of the wing around the aircraft's x axis, as illustrated in Figure F.3. When the dihedral angle is positive, it raises the wingtip relative to the wing root, whereas a negative dihedral (anhedral) angle lowers the wingtip relative to the wing root.

It's important to note that the dihedral angle is not defined in relation to the wing-segment coordinate frame but rather with respect to the aircraft coordinate frame.

Dihedral essentially signifies a rotation of the wing coordinate frame concerning the aircraft coordinate frame. This distinction is necessary because later on, the wing-segment coordinate frame will be rotated by the dihedral angle and shifted within the aircraft coordinate frame. As a result, the effects of dihedral will not be factored into the wing's mass and inertia properties. However, they will be accounted for once the inertia of the entire aircraft is taken into consideration.

In the case of the Flying-V, the outer wing doesn't possess a dihedral angle. The same is not true for the case of the winglet.

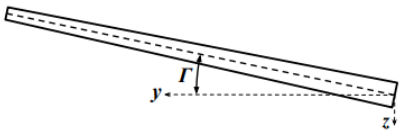

Figure F.3: Dihedral is a rotation of the wing coordinate system about the aircraft coordinate frame x axis [49]

The chord c and the airfoil maximum thickness in percent chord τ_m are assumed to vary linearly from root to tip of the wing segment

$$c(y) = (c_t - c_r)\,\frac{y}{b} + c_r \tag{F.17}$$

$$\tau_m(y) = (\tau_t - \tau_r)\,\frac{y}{b} + \tau_r \tag{F.18}$$

The maximum thickness of the wing at any point along its span is determined by both the local airfoil's maximum thickness and the local chord, according to

$$t_m(y) = \tau_m(y)c(y) \tag{F.19}$$

Both $\tau_m(y)$ and $c(y)$ are allowed to vary linearly, but $t(y)$ may be nonlinear.

The choice of airfoil used in the wing segment significantly impacts the wing's mass properties. In this analysis, it is assumed that the mass properties of the airfoil are primarily influenced by its thickness distribution, and any effects due to camber are considered negligible.

To facilitate the analysis, an airfoil coordinate system was established and can be seen in Figure F.4. The coordinates of the airfoil are denoted with subscripts x_a and y_a.

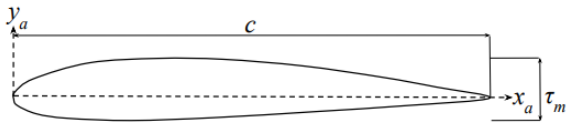

Figure F.4: Airfoil coordinate frame [49]

The thickness distribution of an airfoil as a function of the percentage of the chord length, denoted by $\tau(x_a/c)$, can be expressed as the product of the maximum thickness τ_m and the thickness distribution function $\mu(x_a/c)$

$$\tau\left(\frac{x_a}{c}\right) = \tau_m \mu\left(\frac{x_a}{c}\right) \tag{F.20}$$

In the current analysis, it is assumed that the thickness distribution function $\mu(x_a/c)$ remains constant across the wing segment, while allowing the maximum thickness τ_m to vary linearly, as indicated in Equation F.18. The presented methodology can accommodate any arbitrary thickness distribution $\mu(x_a/c)$.

The thickness distribution under consideration is the NACA 4-digit series distribution [5], which can be expressed as follows

$$\mu\left(\frac{x_a}{c}\right) = a_0\sqrt{\frac{x_a}{c}} + a_1\left(\frac{x_a}{c}\right) + a_2\left(\frac{x_a}{c}\right)^2 + a_3\left(\frac{x_a}{c}\right)^3 + a_4\left(\frac{x_a}{c}\right)^4 \tag{F.21}$$

This thickness distribution exhibits great flexibility and is capable of accommodating a broad spectrum of airfoil shapes beyond the NACA 4-digit series. Allowing arbitrary values for these coefficients does not compromise the generality of the model. Table F.1 presents specific coefficient values that can be utilized to replicate the thickness distribution of various airfoils, including those that do not conform to the NACA 4-digit thickness distribution.

Table F.1: NACA 4-digit series coefficients for various airfoil thickness distributions [49]

Airfoil	a_0	a_1	a_2	a_3	a_4
Traditional NACA 4-Digit Series	2.969	-1.260	-3.516	2.843	-1.015
NACA 4-Digit Series with closed trailing edge [29]	2.980	-1.320	-3.286	2.441	-0.815
Clark Y (with $\tau_m = 0.117$)	2.947	-1.102	-3.975	3.533	-1.399
Selig S1010	0.0001	9.998	0.087	-1.922	14.381
Diamond with τ_m at $x/c = 0.5$	0.479	-0.948	14.248	-26.970	13.234

Taking these definitions into account, a wing segment can be fully characterized by its span b, root chord c_r, tip chord c_t, root airfoil thickness τ_r, tip airfoil thickness τ_t, sweep angle Λ, and dihedral angle Γ, and airfoil thickness distribution $\mu(x_a/c)$. Figure F.5 depicts a single wing segment with all these geometric parameters represented. The span length b is defined parallel to the y-axis.

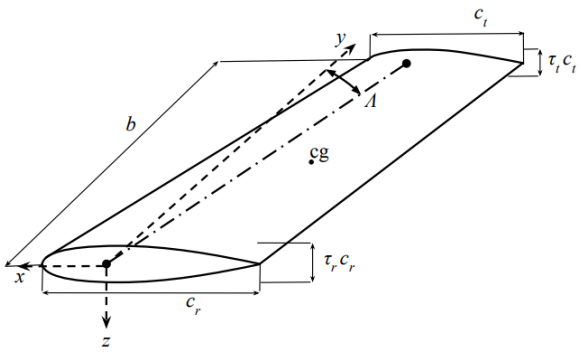

Figure F.5: Airfoil coordinate frame [49]

Volume and Center of Gravity

To determine the mass and inertial properties of the wing, the integrals presented in Eqs. F.1, F.4-F.6, and F.11-F.16 must be computed. These integrals are volume integrals and involve terms of the form $x^i y^j z^k$ where i, j, and k are all positive integers.
The wing's volume is confined within the wing-segment coordinate frame, encompassing the region

$$0 \leq \hat{x} \leq 1 \tag{F.22}$$

$$0 \leq \hat{y} \leq 1 \tag{F.23}$$

$$0 \leq \hat{z} \leq 1 \tag{F.24}$$

where the change of variables

$$\hat{x} = \frac{1}{4} - \frac{x}{c(\hat{y})} \tag{F.25}$$

$$\hat{y} = \frac{y}{b} \tag{F.26}$$

$$\hat{z} = \frac{1}{2} - \frac{z}{\tau_m(\hat{y})\mu(\hat{x})c(\hat{y})} \tag{F.27}$$

has been implemented, leading to the following derivatives

$$d\hat{x} = -\frac{dx}{c(\hat{y})} \tag{F.28}$$

$$d\hat{y} = \frac{dy}{b} \tag{F.29}$$

$$d\hat{z} = -\frac{dz}{\tau_m(\hat{y})\mu(\hat{x})c(\hat{y})} \tag{F.30}$$

Note that the negative signs in the derivatives for x and z are used in the appendical derivations to flip the integrand direction from 1 through 0 to 0 through 1, as shown here [49].
Using this change of variables, the local chord and maximum airfoil thickness described in Eqs. F.17 and F.18 can be expressed as follows

$$c(\hat{y}) = (c_t - c_r)\,\hat{y} + c_r \tag{F.31}$$

$$\tau_m(\hat{y}) = (\tau_t - \tau_r)\,\hat{y} + \tau_r \tag{F.32}$$

As the dimensional x and $c(\hat{y})$ values in Eq. F.25 are defined within the wing segment coordinate system, the symbol $\hat{x}$ represents the local airfoil chordwise ratio x_a/c. Hence, the general thickness distribution described in Eq. F.20 can be formulated as a function of both the spanwise location and the chordwise coordinate

$$\tau(\hat{x}, \hat{y}) = \tau_m(\hat{y})\mu(\hat{x}) \tag{F.33}$$

Regarding the thickness distribution of NACA 4-digit airfoils

$$\mu(\hat{x}) = a_0\sqrt{\hat{x}} + a_1\hat{x} + a_2\hat{x}^2 + a_3\hat{x}^3 + a_4\hat{x}^4 \tag{F.34}$$

Due to the thickness distribution definition in the chordwise direction, the z bounds depend on the chordwise coordinate x. Furthermore, considering the definition of linear changes in chord and airfoil thickness, the x and z bounds rely on the spanwise coordinate y. Employing these bounds in Eq. F.1 and performing integration, the volume of the wing segment is given by

$$V = S_{0,0,0} = \frac{b}{12}\kappa_a v_0 \tag{F.35}$$

where

$$\kappa_a \equiv \tau_r\left(3c_r^2 + 2c_r c_t + c_t^2\right) + \tau_t\left(c_r^2 + 2c_r c_t + 3c_t^2\right) \tag{F.36}$$

The value of parameter ν_0 relies on an integral that is a function of the thickness distribution. For a wing employing the NACA 4-digit thickness distribution,

$$v_0 = \frac{1}{60}\left(40a_0 + 30a_1 + 20a_2 + 15a_3 + 12a_4\right) \tag{F.37}$$

To calculate the wing segment's center of gravity, it is necessary to evaluate the volume integrals as provided in equations F.4–F.6.
Since the sweep affects the x coordinate of the wing's mass, the sweep angle needs to be taken into consideration during the computation of M_{yz}. The moment M_{yz} can then be determined by applying the shift $-ytan\Lambda$ due to sweep to the x coordinate, which gives

$$M_{yz} = \rho\iiint_V (x - y\tan\Lambda)dV = \rho\iiint_V xdV - \rho\tan\Lambda\iiint_V ydV \tag{F.38}$$

Mouton et al. [49] highlighted that there is no requirement to incorporate sweep into the integrations for M_{xz} or M_{xy} in equations F.5 and F.6. This is due to the absence of an x term in these integrals and the fact that sweep has no influence on the y or z coordinates of mass within the wing segment. Because sweep affects the right wing differently than the left wing [49], the distinction in solutions for left and right wings will be addressed by introducing a specific definition

$$\delta \equiv \begin{cases} 1, & \text{right wing} \\ -1, & \text{left wing} \end{cases} \tag{F.39}$$

By solving the integrals necessary to calculate M_{yz}, M_{xy}, and M_{xz}, the following values are obtained

$$M_{yz} = \rho \left[S_{1,0,0} - \tan\Lambda S_{0,1,0} \right] = -\rho \frac{b}{240} \left[3\kappa_b v_1 + 4b\kappa_c v_0 \tan\Lambda \right] \tag{F.40}$$

$$M_{xz} = \rho\delta S_{0,1,0} = \rho\delta \frac{b^2}{60} \kappa_c v_0 \tag{F.41}$$

$$M_{xy} = \rho S_{0,0,1} = 0 \tag{F.42}$$

where

$$\kappa_b \equiv \tau_r \left(4c_r^3 + 3c_r^2 c_t + 2c_r c_t^2 + c_t^3 \right) + \tau_t \left(c_r^3 + 2c_r^2 c_t + 3c_r c_t^2 + 4c_t^3 \right) \tag{F.43}$$

$$\kappa_c \equiv \tau_r \left(3c_r^2 + 4c_r c_t + 3c_t^2 \right) + 2\tau_t \left(c_r^2 + 3c_r c_t + 6c_t^2 \right) \tag{F.44}$$

In the case of a wing that utilizes the NACA 4-digit thickness distribution,

$$v_1 = \frac{1}{60} \left(56a_0 + 50a_1 + 40a_2 + 33a_3 + 28a_4 \right) \tag{F.45}$$

By incorporating Eq. F.35 into Eq. F.2 and utilizing the outcome along with Eqs. F.40–F.42 in Eqs. F.7–F.9, the position of the center of gravity concerning the wing origin can be determined by

$$\bar{x} \equiv \frac{M_{yz}}{m} = -\frac{3\kappa_b v_1 + 4b\kappa_c v_0 \tan\Lambda}{20\kappa_a v_0} \tag{F.46}$$

$$\bar{y} \equiv \frac{M_{xz}}{m} = \delta b \frac{\kappa_c}{5\kappa_a} \tag{F.47}$$

$$\bar{z} \equiv \frac{M_{xy}}{m} = 0 \tag{F.48}$$

As anticipated by Moulton et al. [49], the z coordinate of the center of gravity (CG) is zero due to the neglection of twist and camber. Additionally, it is worth mentioning that sweep exclusively impacts the x coordinate of the CG, as expected.

Inertia Tensor

The inertia tensor of the wing segment can be calculated concerning the origin of the wing-segment coordinate system shown in Figure F.5. This computation involves employing the volume integrals provided in equations F.11–F.16 with suitable limits [49]. By applying the shift resulting from sweep, we obtain the inertia tensor about the origin of the wing segment

$$[\mathbf{I}]_o = \rho \iiint_V \begin{bmatrix} y^2+z^2 & -(xy) & -(xz) \\ -(xy) & x^2+z^2 & -(yz) \\ -(xz) & -(yz) & x^2+y^2 \end{bmatrix} dV$$
$$+\rho \iiint_V \begin{bmatrix} 0 & -\left(-y^2\tan\Lambda\right) & -(-yz\tan\Lambda) \\ -\left(-y^2\tan\Lambda\right) & y^2\tan^2\Lambda - 2xy\tan\Lambda & 0 \\ -(-yz\tan\Lambda) & 0 & y^2\tan^2\Lambda - 2xy\tan\Lambda \end{bmatrix} dV \tag{F.49}$$

By solving the previous volume integral, F.49 yields the following outcome

$$[\mathbf{I}]_o = \begin{bmatrix} I_{xx_o} & -I_{xy_o} & -I_{xz_o} \\ -I_{yx_o} & I_{yy_o} & -I_{yz_o} \\ -I_{zx_o} & -I_{zy_o} & I_{zz_o} \end{bmatrix} \tag{F.50}$$

where

$$I_{xx_o} = \rho\left(S_{0,2,0} + S_{0,0,2}\right) = \rho\frac{b}{3360}\left(56b^2\kappa_f v_0 + \kappa_g v_3\right) \tag{F.51}$$

$$I_{yy_o} = \rho\left(S_{2,0,0} + S_{0,0,2} + S_{0,2,0}\tan^2\Lambda - 2S_{1,1,0}\tan\Lambda\right)$$

$$= \rho\frac{b}{10080}\left[84b\left(2b\kappa_f\tan^2\Lambda + \kappa_d\tan\Lambda\right)v_1 + 49\kappa_e v_2 + 3\kappa_g v_3\right] \tag{F.52}$$

$$I_{zz_o} = \rho\left[S_{2,0,0} + \left(\tan^2\Lambda + 1\right)S_{0,2,0} - 2S_{1,1,0}\tan\Lambda\right]$$

$$= \rho\frac{b}{1440}\left[12b\left\{2b\left(\tan^2\Lambda + 1\right)\kappa_f v_0 + \kappa_d v_1\tan\Lambda\right\} + 7\kappa_e v_2\right] \tag{F.53}$$

$$I_{xy_o} = I_{yx_o} = \rho\delta\left(S_{1,1,0} - S_{0,2,0}\tan\Lambda\right) = -\rho\delta\frac{b^2}{240}\left[4b\kappa_f v_0\tan\Lambda + \kappa_d v_1\right] \tag{F.54}$$

$$I_{xz_o} = I_{zx_o} = \rho\left(S_{1,0,1} - S_{0,1,1}\tan\Lambda\right) = 0 \tag{F.55}$$

$$I_{yz_o} = I_{zy_o} = \rho\delta S_{0,1,1} = 0 \tag{F.56}$$

and

$$\kappa_d \equiv \tau_r\left(c_r + c_t\right)\left(2c_r^2 + c_r c_t + 2c_t^2\right) + \tau_t\left(c_r^3 + 3c_r^2 c_t + 6c_r c_t^2 + 10c_t^3\right) \tag{F.57}$$

$$\kappa_e \equiv \tau_r\left(5c_r^4 + 4c_r^3 c_t + 3c_r^2 c_t^2 + 2c_r c_t^3 + c_t^4\right) + \tau_t\left(c_r^4 + 2c_r^3 c_t + 3c_r^2 c_t^2 + 4c_r c_t^3 + 5c_t^4\right) \tag{F.58}$$

$$\kappa_f \equiv \tau_r\left(c_r^2 + 2c_r c_t + 2c_t^2\right) + \tau_t\left(c_r^2 + 4c_r c_t + 10c_t^2\right) \tag{F.59}$$

$$\kappa_g \equiv \tau_r^3\left(35c_r^4 + 20c_r^3 c_t + 10c_r^2 c_t^2 + 4c_r c_t^3 + c_t^4\right) + \tau_r^2\tau_t\left(15c_r^4 + 20c_r^3 c_t + 18c_r^2 c_t^2 + 12c_r c_t^3 + 5c_t^4\right)$$

$$+\tau_r\tau_t^2\left(5c_r^4 + 12c_r^3 c_t + 18c_r^2 c_t^2 + 20c_r c_t^3 + 15c_t^4\right) + \tau_t^3\left(c_r^4 + 4c_r^3 c_t + 10c_r^2 c_t^2 + 20c_r c_t^3 + 35c_t^4\right) \tag{F.60}$$

In the context of a wing employing the NACA 4-digit thickness distribution,

$$v_2 = \frac{1}{980}\left(856a_0 + 770a_1 + 644a_2 + 553a_3 + 484a_4\right) \tag{F.61}$$

$$\begin{aligned} v_3 = {} & \frac{2}{5}a_0^3 + a_0^2 a_1 + \frac{3}{4}a_0^2 a_2 + \frac{3}{5}a_0^2 a_3 + \frac{1}{2}a_0^2 a_4 + \frac{6}{7}a_0 a_1^2 + \frac{4}{3}a_0 a_1 a_2 + \frac{12}{11}a_0 a_1 a_3 + \frac{12}{13}a_0 a_1 a_4 \\ & + \frac{6}{11}a_0 a_2^2 + \frac{12}{13}a_0 a_2 a_3 + \frac{4}{5}a_0 a_2 a_4 + \frac{2}{5}a_0 a_3^2 + \frac{12}{17}a_0 a_3 a_4 + \frac{6}{19}a_0 a_4^2 + \frac{1}{4}a_1^3 + \frac{3}{5}a_1^2 a_2 \\ & + \frac{1}{2}a_1^2 a_3 + \frac{3}{7}a_1^2 a_4 + \frac{1}{2}a_1 a_2^2 + \frac{6}{7}a_1 a_2 a_3 + \frac{3}{4}a_1 a_2 a_4 + \frac{3}{8}a_1 a_3^2 + \frac{2}{3}a_1 a_3 a_4 + \frac{3}{10}a_1 a_4^2 \end{aligned}$$

$$+\frac{1}{7}a_2^3 + \frac{3}{8}a_2^2 a_3 + \frac{1}{3}a_2^2 a_4 + \frac{1}{3}a_2 a_3^2 + \frac{3}{5}a_2 a_3 a_4 + \frac{3}{11}a_2 a_4^2 + \frac{1}{10}a_3^3 + \frac{3}{11}a_3^2 a_4 + \frac{1}{4}a_3 a_4^2 + \frac{1}{13}a_4^3 \tag{F.62}$$

Due to the relationship between mass, volume, and density as expressed in Eq. F.2, applying Eq. F.2 in conjunction with the volume relation provided in Eq. F.35 enables us to express the tensor components in terms of mass rather than density

$$I_{xx_o} = m\left[\frac{56b^2\kappa_f v_0 + \kappa_g v_3}{280\kappa_a v_0}\right] \tag{F.63}$$

$$I_{yy_o} = m\left[\frac{84b\left(2b\kappa_f v_0 \tan^2\Lambda + \kappa_d v_1 \tan\Lambda\right) + 49\kappa_e v_2 + 3\kappa_g v_3}{840\kappa_a v_0}\right] \tag{F.64}$$

$$I_{zz_o} = m\left[\frac{12b\left\{2b\left(\tan^2\Lambda + 1\right)\kappa_f v_0 + \kappa_d v_1 \tan\Lambda\right\} + 7\kappa_e v_2}{120\kappa_a v_0}\right] \tag{F.65}$$

$$I_{xy_o} = I_{yx_o} = -\delta bm\left[\frac{4b\kappa_f v_0 \tan\Lambda + \kappa_d v_1}{20\kappa_a v_0}\right] \tag{F.66}$$

$$I_{xz_o} = I_{zx_o} = I_{yz_o} = I_{zy_o} = 0 \tag{F.67}$$

The derivation of the κ parameters presented here relies on integrals that assume the wing segment varies linearly in chord and thickness distribution [49].
On the other hand, the ν parameters in this derivation come from integrals that are dependent on the thickness distribution [49].
The inertia components provided in Eqs. F.51–F.56 and F.63–F.67 can be utilized in Eq. F.50 to calculate the inertia tensor concerning the origin of the wing-segment coordinate frame. However, to incorporate the inertial components of the wing segment in determining the overall aircraft's inertia, it becomes valuable to have knowledge of the inertial components of the wing segment relative to the center of gravity (CG) of the wing segment.
According to the parallel axis theorem, the inertia tensor about an arbitrary point $[\mathbf{I}]_1$ is related to the inertia tensor about the center of gravity $[\mathbf{I}]$ with the following expression

$$[\mathbf{I}]_1 = [\mathbf{I}] + m\left[(\mathbf{s}\cdot\mathbf{s})[\mathbf{E}] - \mathbf{s}\mathbf{s}^T\right] \tag{F.68}$$

where **s** represents the vector from the center of gravity to the point of interest, and $[\mathbf{E}]$ denotes a 3×3 identity matrix. This relationship can be rearranged to determine the inertia about the wing-segment center of gravity (CG) based on the inertia about the origin of the wing-segment coordinate system

$$[\mathbf{I}] = [\mathbf{I}]_o - m\left[(\mathbf{s}\cdot\mathbf{s})[\mathbf{E}] - \mathbf{s}\mathbf{s}^T\right] \tag{F.69}$$

s denotes the vector from the wing-segment center of gravity (CG) to the wing-segment origin,

$$\mathbf{s} = -\left\{\begin{array}{c}\bar{x}\\ \bar{y}\\ \bar{z}\end{array}\right\} \tag{F.70}$$

For any given wing segment, the vector **s** can be calculated using equations F.46–F.48. By applying Eq. F.70 in Eq. F.69 and simplifying the expression, the inertia tensor of the wing segment relative to the wing segment center of gravity (CG) can be determined by

$$[\mathbf{I}] = [\mathbf{I}]_o - m\left[\begin{array}{ccc}\bar{y}^2+\bar{z}^2 & -\bar{x}\bar{y} & -\bar{x}\bar{z}\\ -\bar{x}\bar{y} & \bar{x}^2+\bar{z}^2 & -\bar{y}\bar{z}\\ -\bar{x}\bar{z} & -\bar{y}\bar{z} & \bar{x}^2+\bar{y}^2\end{array}\right] \tag{F.71}$$

G

A Preliminary Analysis: Counteracting the Engine Weight

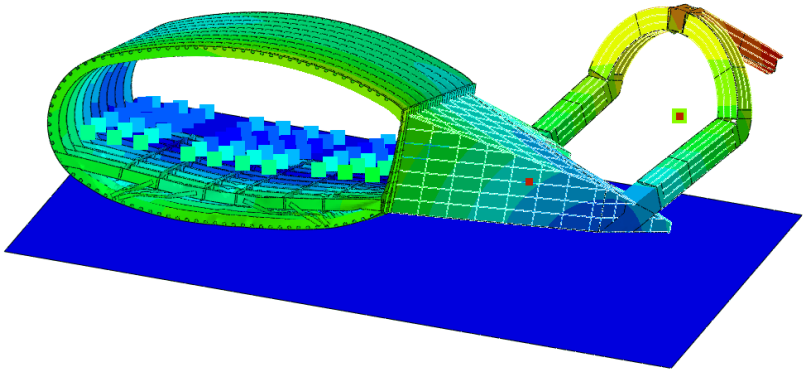

(a) Model without taking into account the moments of inertia of other sections of the Flying-V. Red dots are representative of the engine and landing gear masses

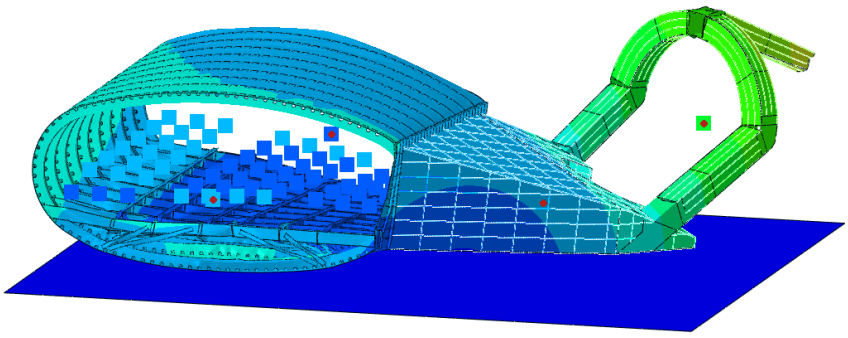

(b) Model taking into account the moments of inertia of other sections of the Flying-V. Red dots are representative of the engine and landing gear masses, as well as the reference points where the moments of inertia are being applied

Figure G.1: Engine and landing gear masses location

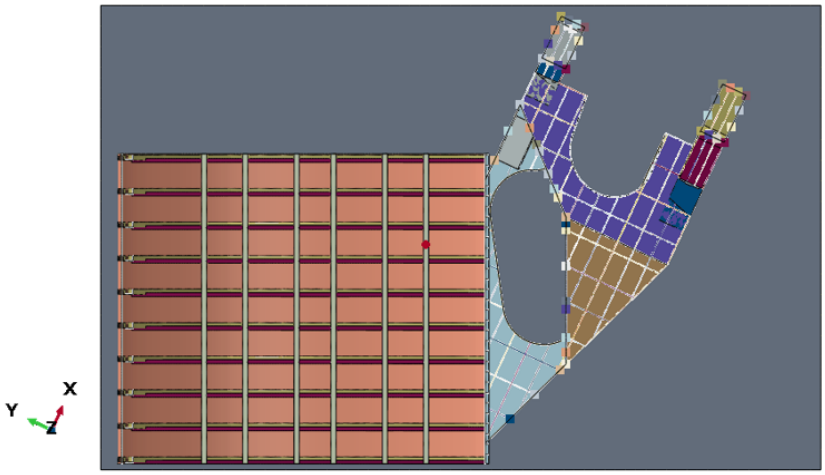

Figure G.2: Position of the structural center of mass of the model. Denoting that the engine and landing gear masses aren't being considered

Table G.1: DRI and SEV comparison for engine models with and without moments of inertia

Models	DRI				SEV				Comp. Time (h)
-	Avg	Max	Median	Min	Avg	Max	Median	Min	-
Engine	19.40	30.84	18.27	13.62	1.52	3.65	1.42	0.96	13.99
Engine Inertia	19.22	26.90	18.00	12.42	1.50	3.07	1.41	0.97	35.52

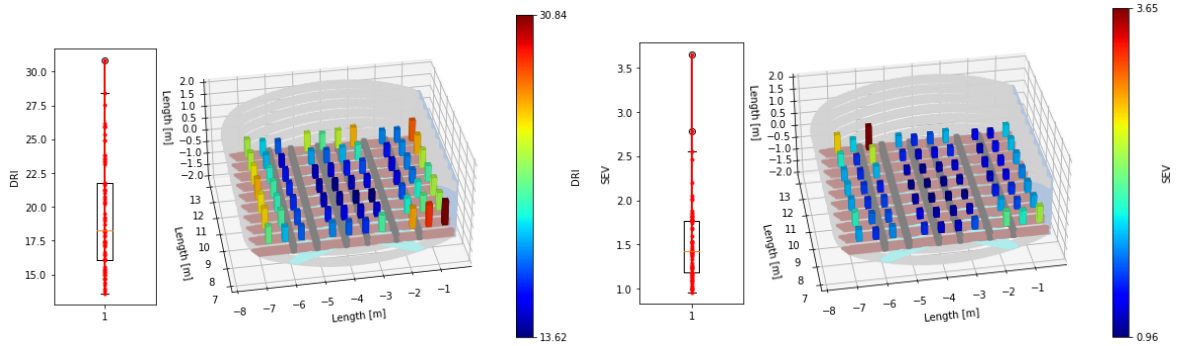

(a) Spatial variation of the DRI

(b) Spatial variation of the SEV

Figure G.3: Spatial variation of the DRI and SEV without moments of inertia, for the model with engine

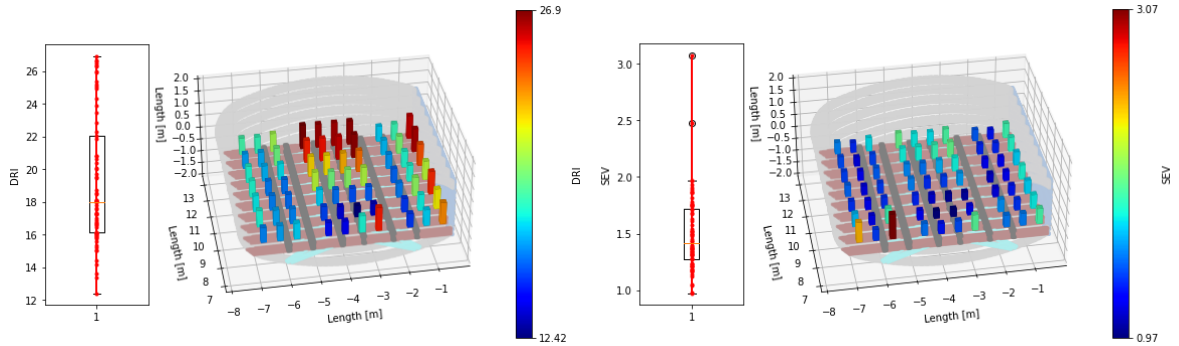

(a) Spatial variation of the DRI

(b) Spatial variation of the SEV

Figure G.4: Spatial variation of the DRI and SEV with moments of inertia, for the model with engine

Roll Analysis of the Section Without Moments of Inertia: Extra Results for Comparison

H.1. Visual Inspection of the Crash Sections

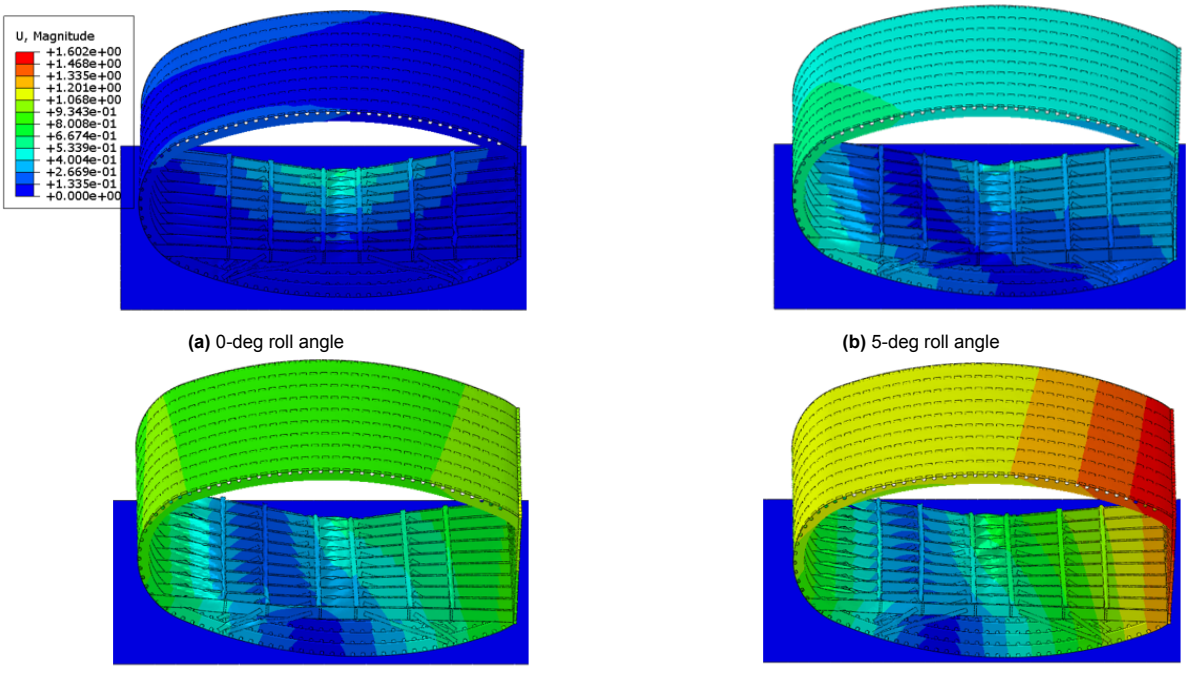

(a) 0-deg roll angle

(b) 5-deg roll angle

(c) 10-deg roll angle

(d) 15-deg roll angle

Figure H.1: Displacement variation of fuselage section at 200 ms, without moments of inertia

H.2. Energy Analysis

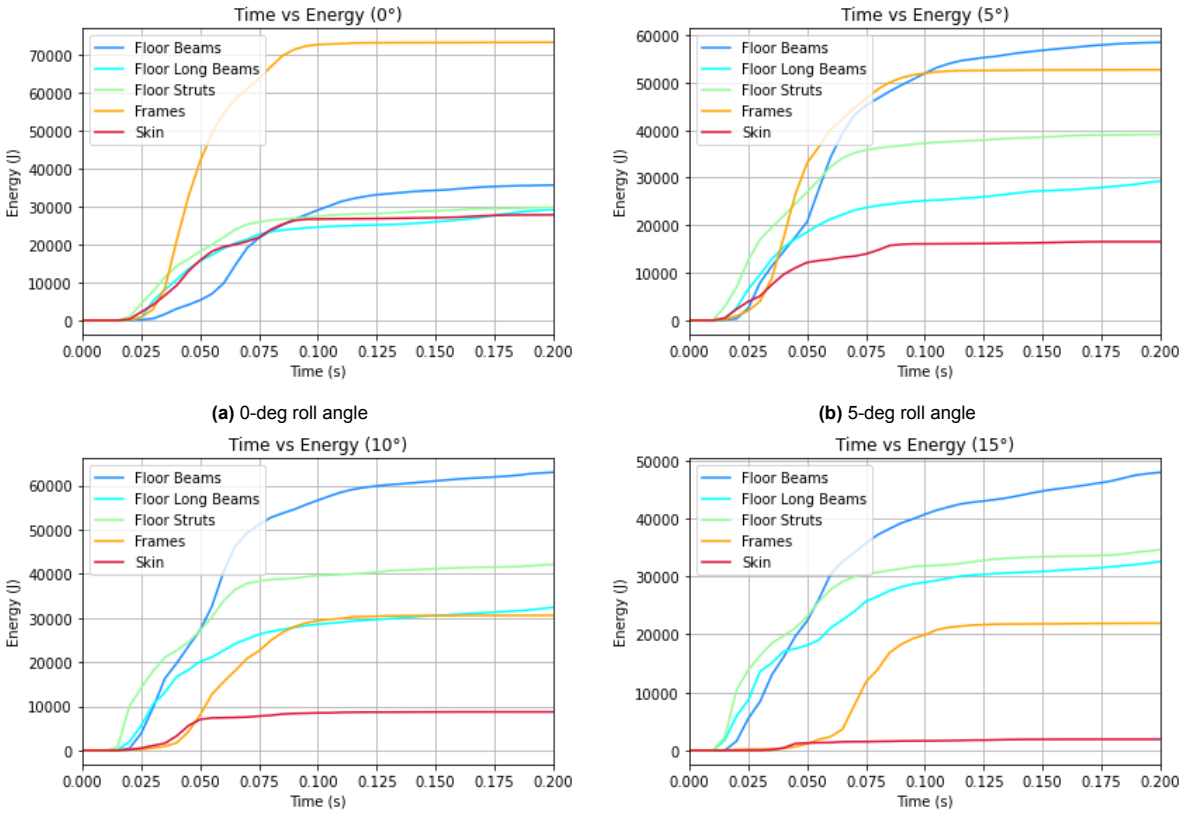

(a) 0-deg roll angle

(b) 5-deg roll angle

(c) 10-deg roll angle

(d) 15-deg roll angle

Figure H.2: Energy absorption of main structures of fuselage section with different roll angles, without moments of inertia applied

H.3. Angle Impact on the DRIs and SEVs

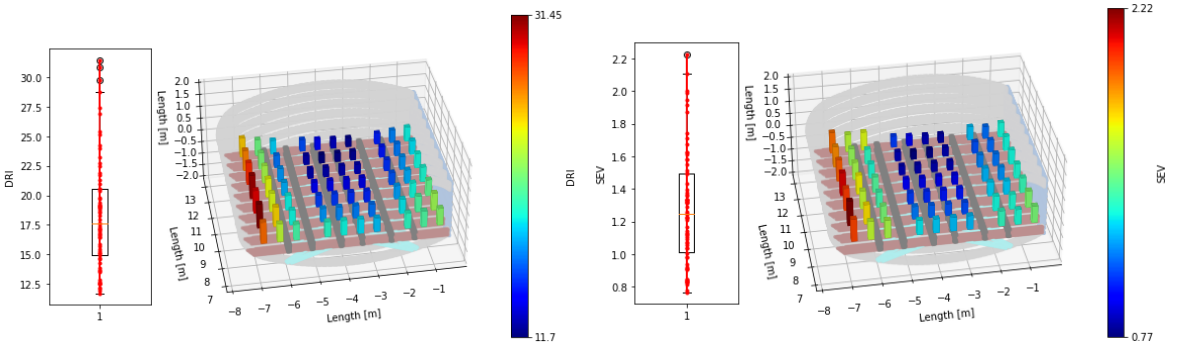

(a) Spatial variation of the DRI

(b) Spatial variation of the SEV

Figure H.3: Spatial variation of the DRI and SEV without moments of inertia, for the 5 degrees case

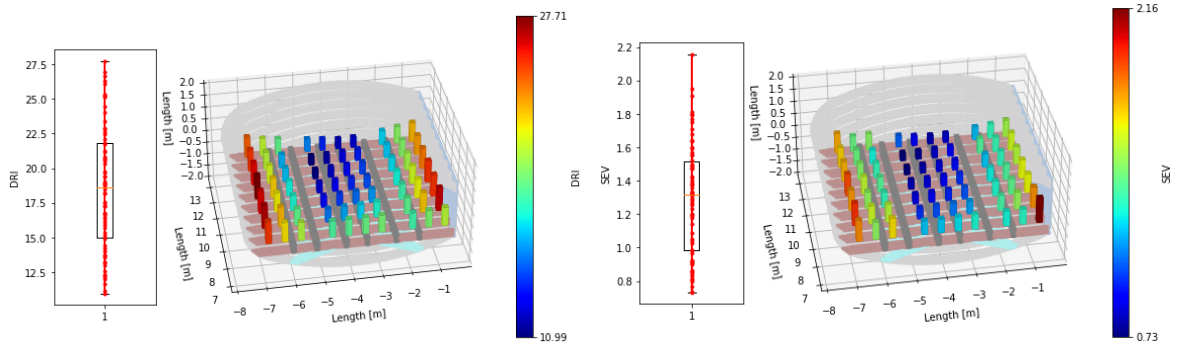

(a) Spatial variation of the DRI **(b)** Spatial variation of the SEV

Figure H.4: Spatial variation of the DRI and SEV without moments of inertia, for the 10 degrees case

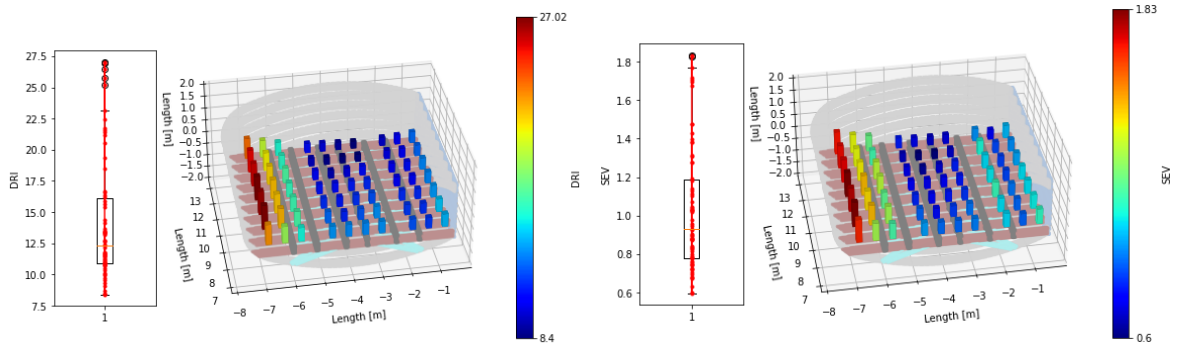

(a) Spatial variation of the DRI **(b)** Spatial variation of the SEV

Figure H.5: Spatial variation of the DRI and SEV without moments of inertia, for the 15 degrees case

Pitch Analysis: Extra Results for Comparison

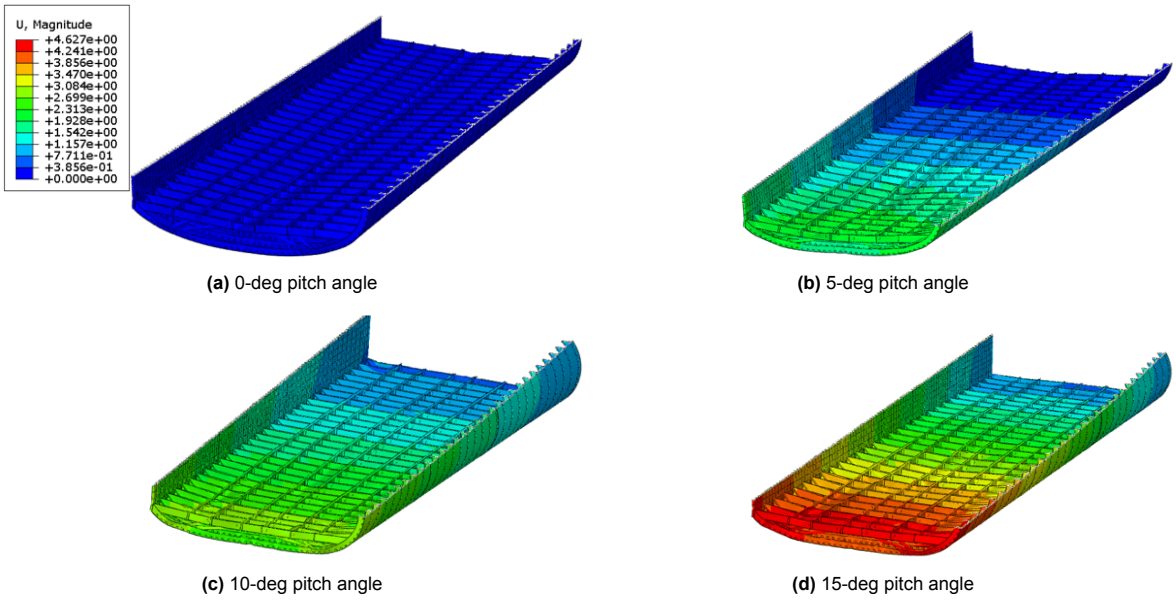

(a) 0-deg pitch angle

(b) 5-deg pitch angle

(c) 10-deg pitch angle

(d) 15-deg pitch angle

Figure I.1: Displacement variation of full passenger model, with displacement limits from the 15 degrees case

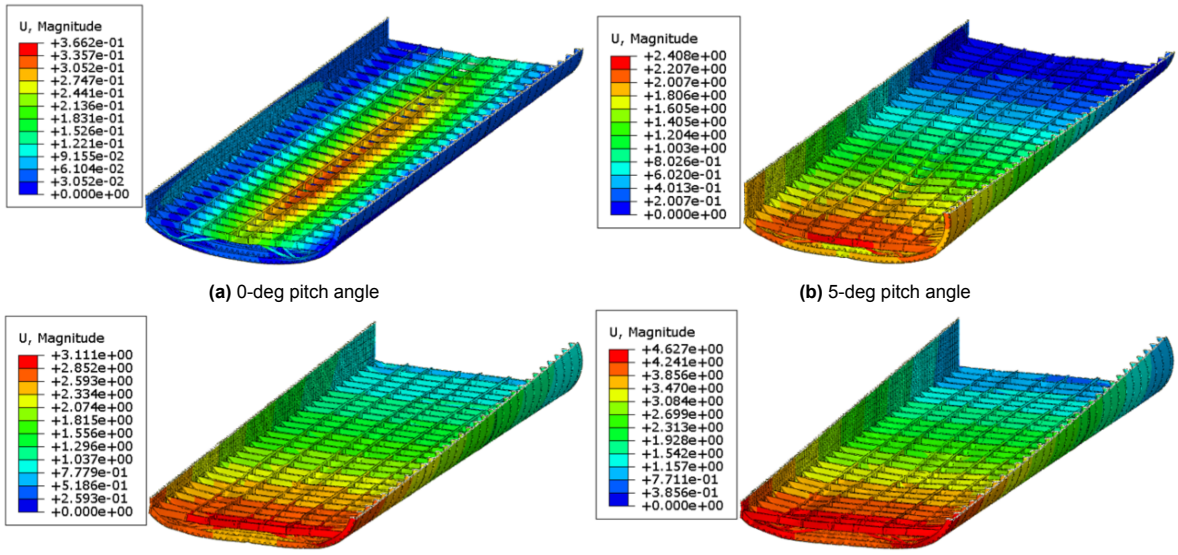

(a) 0-deg pitch angle

(b) 5-deg pitch angle

(c) 10-deg pitch angle

(d) 15-deg pitch angle

Figure I.2: Displacement variation of full passenger model